THE UNIVERSITY OF
SYDNEY

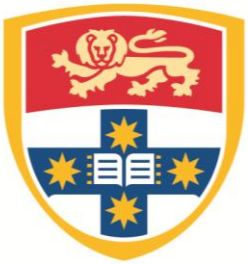

THE UNIVERSITY OF
SYDNEY

A Numerical and Experimental Investigation on the Thermal Structure of Oxy-fuel Combustion

Shogo Sayama

Supervisors: Professor Assaad R. Masri and Dr Matthew Dunn

This thesis is submitted in fulfilment of the requirements
for the degree of **Master of Philosophy**

The School of Aerospace, Mechanical
and Mechatronic Engineering
The University of Sydney
Australia

13 August 2014

Declaration

I hereby declare that the work presented in this thesis is solely my own work and that to the best of my knowledge the work is original, except where otherwise indicated in the text of this thesis by reference to the author or by acknowledgement of the source of the work. No part of this work has been submitted for any other degree or diploma. A final version of this thesis was proof read by a processional proof reader, resulting in some minor non-technical grammatical corrections.

Signature 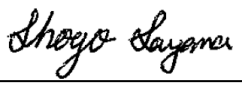

Acknowledgements

This Master of Philosophy was supervised by Professor Assaad Masri and Dr Matthew Dunn. I would like to thank my supervisors, without whose guidance and support, none of this work would have been possible. In particular, weekly meetings and personal teaching with Dr Matthew Dunn helped improve my research and enhance my interest in combustion research significantly.

Also, I have appreciated the support of Mr Samuel Priestly, an undergraduate student. He gave me great help in fabricating the counter-flow burner. I would not have finished on schedule without his valuable assistance.

Further, I would like to thank all co-workers in the Sydney University Clean Combustion Laboratory. Their advice and comments in the laboratory and group seminars encouraged me to improve my research. The presentations they gave in group seminars heightened my interest and widened my knowledge on combustion.

Lastly, I thank all of the people whom I have met in Australia for a wealth of great experiences and their help in improving my English skills.

Abstract

This thesis presents a numerical and experimental investigation on the characteristics of oxy-fuel combustion utilising CH_4 as a fuel. An emphasis is placed on investigating the thermal structure and the impact of the oxidiser diluent on oxy-fuel flames. The numerical portion of this thesis sheds light on off-stoichiometric temperature peaking (OTP), which is a phenomenon whereby the flame temperature does not peak at exactly stoichiometry, but rather near stoichiometry. Specifically, OTP in equilibrium calculations (0D OTP) and opposed-flow diffusion flame simulations (1D OTP) is explored for N_2, CO_2 and H_2O diluted flames examining the significance of reactivity, dissociation, diffusivity, conductivity, finite-rate chemistry, heat release, and specific heats. Results from both 0D OTP and 1D OTP analysis indicate that all investigated flames possess some degree of OTP, with the CO_2 diluted oxidiser case displaying the largest degree of OTP. Parametric analysis utilising concepts of imaginary species and post-simulation equilibrium calculations are shown to be valuable tools to determine the dominant mechanism causing OTP for the different simulation results examined. Experimentally, the development and application of a planar hydroxyl radical (OH) laser induced fluorescence thermometry technique to a laminar oxy-fuel counter-flow diffusion flame is presented. The resulting temperature profiles obtained by a spectrally integrated two-line technique are found to agree well with the simulated thermal structure to within a 2% difference. Further, this thesis also presents the detailed design of a counter-flow burner and laser pulse stretcher for the application Raman scattering in oxy-fuel flames for future experiments.

Nomenclature

Roman

Symbol	Definition
A	*Cross Section Area, Einstein A Coefficient*
a	*Strain Rate or Collisional Broadening Coefficient*
b	*Collisional Broadening Coefficient*
B	*Einstein B Coefficient*
c	*Speed of Light in Vacuum*
C_p	*Specific Heat Capacity per Unit Mass*
C_{pm}	*Specific Heat Capacity per Unit Mole*
D	*Diffusion Coefficient*
d	*Particle Diameter or Laser Beam Diameter*
E	*Laser Energy or Laser Energy per Unit Area*
EI_{CO}	*Emission Index of CO*
f	*Focus Length*
$f_{\#}$	*F Number of Lens*
F_L	*Fluence, J/m^2*
F_y	*Quantum Yield*
g	*Gain or Spectral Line Width*
G	*Gibbs Free Energy*
h	*Specific Enthalpy or Planck' Constant*
IS_{CO2}	*IS_{CO2} has Completely the Same Thermo-chemical Data as that of CO_2 and no Reactivity with Molecular Weight Being 45.*
IS_{H2O}	*IS_{H2O} has Completely the Same Thermo-chemical Data as that of H2O and no Reactivity with Molecular Weight Being 19.*
K_g	*Total Number of Species*
L	*Optical Propagation Path Length or Separation Distance of Opposed-flow Burner*
$\dot{M}$	*Mass Flow Rate*
m	*Magnification*
m	*Magnification*

M^2	*Degree of Multimode*
n	*Mole Fraction*
$\dot{Q}$	*Heat Transfer, W*
Q	*The Number of Molecules in Ground State*
q_p	*Heat Release per Unit Mass*
$\dot{Q}_{rad}$	*Heat Loss due to Radiation, J/m^3-s*
r	*Distance from the Origin in Radial Coordinate*
R	*Ratio of Two-Line*
R	*Universal Gas Constant*
R_{bs}	*Reflectivity of Beam Splitter*
S	*Signal Intensity*
T	*Temperature*
t	*Time*
T_{ad}	*Adiabatic Flame Temperature*
u	*Velocity*
V	*Diffusion Velocity, Volume*
W	*Molecular Weight*
x	*Distance from the Origin in x coordinate or Mole number*
X	*Mole Fraction*
y	*Distance from the Origin in y-coordinate*
Y	*Mass Fraction*
y_L	*Laser Sheet Height*
Y_{O2_oxi}	*O_2 Mass Fraction in Oxidiser*
Z_p	*Partition Function*
Δz	*Laser Sheet Thickness*

Greek

Symbol	Definition
γ	*Cross Section of Raman Scattering*
η	*Quantum Efficiency*
λ	*Thermal Conductivity or Wavelength*
μ	*Viscosity*
ξ	*Mixture Fraction*

ξ_n	*Normalised Mixture Fraction*
ρ	*Density*
σ	*Standard Deviation, Cross Section of Scattering*
τ	*Optical Delay Time*
ϕ	*Equivalence Ratio or the Number of Incident Photon*
ϕ_n	*Normalised Equivalence Ratio*
$\dot{\omega}$	*Chemical Production Rate, mole/m^3-s*
Ω	*Solid Angle*

Subscript

Symbol	Definition
0	*Stagnation Plane in Opposed-flow Flame*
c	*Probed Volume*
F	*Fuel Stream*
i	*Species i*
k	*Species k or Reaction k*
m	*Mole Based Unit*
n	*Normalised*
O	*Oxidiser Stream or Oxygen*

Abbreviations

0D OTP: Zero Dimensional Off-stoichiometric Temperature Peaking

1D OTP: One-Dimensional Off-stoichiometric Temperature Peaking

ADU: Analogue to Digital Unit

CARS: Coherent Anti-stokes Raman Spectroscopy

CCD: Charge Coupled Device

CCS: Carbon Capture and Storage

DM: Diatomic Mechanism

EOC: Enhanced Oil Recovery

FWHM: Full Width at Half Maximum

HPEC: HP Equilibrium Calculation

ICCD: Intensified Charge Coupled Device

IPCC: Intergovernmental Panel on Climate Change

LIF: Laser Induced Fluorescence

LIPF: Laser Induced Pre-dissociative Fluorescence

MI: Matrix Inversion

MTF: Modulation Transfer Function

NPM: N2 reaction Prohibited Mechanism

PECP: Post-Equilibrium Calculation Process

PECPT: PECP Only Extracting Temperature Information

PIV: Particle Image Velocimetry

PLIF: Planar Laser Induced Fluorescence

PSF: Point Spread Function

SNR: Signal to Noise Ratio

SSM: Single Step Mechanism

TEM: Transverse Electromagnetic Mode

TPEC: TP Equilibrium Calculation

TSM: Two Step Mechanism

List of Figures and Tables

Contents

Chapter 1
Introduction

It is generally well accepted within the scientific community that due to the anthropogenic activity of burning fossil fuels, the levels of CO_2 in the atmosphere have increased, leading to global warming [1]. Although the emission of CO_2 is due to many sectors, such as transportation and chemical manufacturing, by far the largest emitting sector for CO_2 emissions is electrical power generation [2]. Alternative energy sources, such as nuclear power and renewable energy sources, including solar, wind, geothermal and tidal energy, are expected to become increasingly prevalent and play a crucial role in the solution of the global warming issue and future energy demand. Presently, renewable energy generation methods cannot meet the near-term energy demand for various reasons, such as supply and demand issues, technology still being in development and limited installation capabilities. As a result, in the present and near future, energy demands will inevitably be met by utilising conventional fossil fuel combustion.

As a near-term solution to the minimisation of CO_2 emissions, carbon capture and storage (CCS) schemes have been proposed to be applied to existing fossil fuel burning power stations. Ideally, CCS realises zero CO_2 emissions from fossil fuel power plants via isolation of CO_2 from exhaust streams and subsequent storage of the separated CO_2. Applying CCS to fossil fuel power plants is an attractive option to obtain near-term reduction in global CO_2 emissions, as it could be applied by retrofitting existing fired power stations as well as leveraging existing power station designs with much of the existing power-generating infrastructure being utilised.

Although there are technical hurdles in many areas that remain to be overcome for the successful introduction of CCS in fossil fuel fired power plants, the combustion side of the technology when employing an oxy-fuel style CCS system requires further research. In the oxy-fuel realisation of CCS, the combustor is fed a mixture of fuel, O_2 and diluent (typically CO_2 and/or H_2O) with the combustion products being ideally solely a mixture of H_2O and CO_2. This allows the easy separation of the H_2O from the CO_2 through precipitation, providing a sequestration ready stream of high purity CO_2.

As the oxy-fuel mode of combustion replaces the N_2 in the oxidiser stream, which is used as a diluent with CO_2 or H_2O, a significant variation in the combustion properties results due to the different reactivity, radiative thermodynamics and diffusive properties of CO_2 and H_2O compared to N_2. This significant change in the flame diluent properties significantly influences the bulk flame properties, resulting in significant differences in flame stability, pollutant emissions and flame structure between oxy-fuel flames and conventional air-fuel flames.

Despite the practical importance, significant advances in the understanding of the nature of oxy-fuel combustion with CO_2 and H_2O diluted flames are still required. To this end, this thesis aims to investigate and further the understanding of oxy-fuel combustion by specifically studying the thermal structure of laminar oxy-fuel flames relative to conventional air-fuel flames. A particular focus is made on oxy-fuel combustion utilising CH_4 as a fuel, due to its relevance as the primary fuel constituent in high efficiency CNG fire power stations.

This study utilises both numerical and experimental investigations, where the numerical simulations are used to investigate specific details of the thermal structure of oxy-fuel combustion, such as peak temperatures for different mixtures and off-stoichiometric peaking. Experimentally a temperature measurement technique suitable for the potentially high temperatures found in oxy-fuel flames that utilises non-invasive laser induced fluorescence (LIF) of the OH is developed and applied.

This thesis consists of seven chapters including the introduction chapter; background, methodology, thermo-chemical analysis of oxy-fuel combustion, analysis of oxy-fuel laminar diffusion flames, thermal structure measurement of oxy-fuel laminar flames and conclusions and recommendations. Chapter 2 provides a review of the background knowledge on oxy-fuel combustion, laminar flame modelling and laser diagnostics. In chapter 3, the techniques and apparatus used in the present study are explored, in particular the theory and procedure of OH LIF thermometry is explored. Also in chapter 3, the novel design of the counter-flow burner and a new laser pulse stretcher topology is explored in detail. Chapter 4 investigates the thermo-chemical coupling structure in oxy-fuel combustion, primarily using 0D constant pressure adiabatic equilibrium calculations. In chapter 5, the thermal structure of CO_2 diluted laminar flames are

examined relative to conventional air-fuel laminar flames in the counter-flow diffusion flame geometry. The physics behind the OTP in 1D opposed-flow flames are also explored, since OTP analysis techniques have only been developed at this stage in literature for 0D systems. Chapter 6 provides the results and discussion of thermal structure measurements of oxy-fuel flames. The procedure to determine the operating conditions and the validation of laser measurement system applied in the present study are also explored in detail in this chapter. In the last chapter, the contributions made by this study are summarised briefly and some recommendations for future studies are outlined.

Chapter 2
Background

This chapter reviews the state-of-art background material for the subsequent chapters in this thesis. Specifically, the following topics are explored in detail: oxy-fuel combustion, laminar flame modelling, zero dimensional off-stoichiometric temperature peaking (OTP), laser diagnostics and image processing and optical devices.

2.1 Oxy-fuel Combustion

Oxy-fuel combustion is seen as one of the major options for CO_2 capture in clean combustion technologies of the future. In this section, the motivation and the alternative methods of oxy-fuel systems are explored in detail. Oxy-fuel combustion potentially possesses new parameters that designers can utilise to optimise the combustion system. Typically, the oxidiser dilution degree is limited in the low diluent fraction case to a certain range due to material temperature limits used in the combustor or furnace, whilst flame stability limits become a limiting factor in the high diluent fraction case [3-6]. When N_2 is directly replaced with CO_2 or H_2O in oxy-fuel combustion systems, the flame characteristics deviate considerably from conventional air-fuel flames even if the diluting degree is the same as that in air. This significant effect of N_2 replacement with CO_2 or H_2O on the fundamental flame characteristics is an important motivation for the study of the fundamental nature of oxy-fuel combustion, which is a common underlying theme throughout this thesis. In the last part of this chapter, the current research trends in oxy-fuel combustion are examined and discussed. For reference, a conceptual sketch of oxy-fuel combustion mode is shown in **Fig.1**.

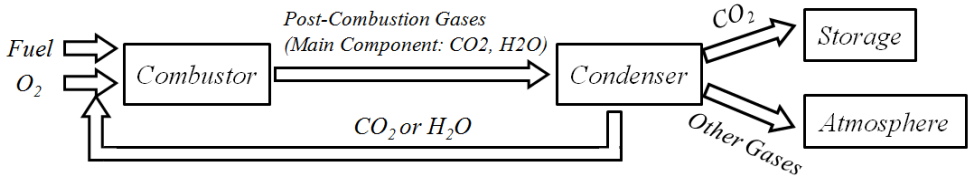

Fig.1. Principle of oxy-fuel combustion modes.

2.1.1 Motivation to Study

The IPCC's latest report [1] states that the average surface temperature of the earth has increased by 0.74 K since the start of the industrial age. The most significant anthropogenic contributor to global warming in twentieth and twenty-first century can be attributed to the increased amount of CO_2 arising from fossil fuel combustion, a large proportion of which is due to electrical power generation. Community, regulatory and industrial concerns regarding the impact of CO_2 emissions have been increasing in recent years with alternatives that significantly reduce CO_2 emissions such as CCS being promoted. CCS system is a broad descriptor that is used to describe the many systems that capture a portion of the CO_2 emissions from a combustion process, such as a power plant's combustion of coal. These CO_2 emissions are prevented from being emitted into the atmosphere by sequestering them in deep saline aquifers, subterranean oil fields, deep sea lakes or chemical bound into carbonate rock forms [7-9].

A key to the high efficiency, hence success, of CCS systems is that the combustion exhaust stream features a high fraction of CO_2. To this end, oxy-fuel combustion is considered to be one of the most promising combustion modes to operate efficient CO_2 capturing systems. In oxy-fuel combustion, the N_2/O_2 oxidiser stream (air) is replaced by the CO_2/O_2 or H_2O/O_2 oxidiser stream. Assuming complete combustion with idealised global single step chemistry, the post-combustion gases in the oxy-fuel combustion mode consist of only CO_2 and H_2O, which simply requires removal of water through precipitation for CO_2 isolation. The concept of the oxy-fuel combustion was initially proposed by Abraham and his co-workers as a method of enhanced oil recovery (EOR) [10]. In this application, the CO_2 rich stream is found to be a good injectant for the EOR process since CO_2 becomes supercritical at typical oil reservoir pressures and temperatures of 10 to 30 MPa and 30°C to 110°C respectively [11-13].

Conventionally, the term 'oxy-fuel combustion' refers to a combustion mode that is enhanced by the addition of oxygen above those found in normal air-fuel combustion modes. However, more recently, the term 'oxy-fuel combustion' has also been applied to situations where oxygen concentrations in oxidisers are elevated and a diluent such as CO_2 or H_2O is employed rather than N_2. In the present work, the term 'oxy-fuel combustion' is used to represent the case where the oxidiser stream is a mixture of

CO_2/O_2 or H_2O/O_2, (e.g. the oxidiser stream does not contain $N_{2)}$. In addition, it is noted that the term 'N_2 diluted combustion' is used as a generic term, which includes conventional air-fuel flames and flames that feature elevated levels of O_2 in the N_2 diluted oxidiser stream.

2.1.2 Comparison Study with Mono-Ethanol Amine Scrubbing

Amine scrubbing of combustion gases is another promising method that can be utilised to limit the emission of CO_2 from combustion processes into the atmosphere. In the amine scrubbing method, conventional air-fuel combustion is initially conducted and then the flue gas is post-processed for CO_2 isolation utilising amine. In the amine scrubbing method, the CO_2 is retrieved from the post-flame gas via the following reaction:

$$CO_2 + 2RNH_2 \text{ (Amine)} \rightarrow RNHCOO^- + RNH_3^+$$

The 'R' in this reaction designates a generic alkyl group. The remaining flue gas (nitrogen, etc.) exhausts to the atmosphere and the amine solution flows to the regenerator. After sending the amine solution to the regenerator, the endothermic reverse reaction takes place by the addition of heat:

$$RNHCOO^- + RNH_3^+ + \text{heat} \rightarrow CO_2 + 2RNH_2 \text{ (Amine)}.$$

Due to this reverse reaction, CO_2 is separated from the amine and the amine can be recycled. The main drawback of this amine scrubbing scheme is the need for the large amounts of energy required to liberate CO_2 from the amine. In addition, the concentration of amine in the solution is limited due to corrosion concerns, and consequently the main component of amine solutions is water. As the primary constituent of the amine solution is water, a significant amount of energy is wasted by heating the water in the CO_2-amine liberation process. For reference, a conceptual sketch of amine scrubbing is shown in **Fig.2**.

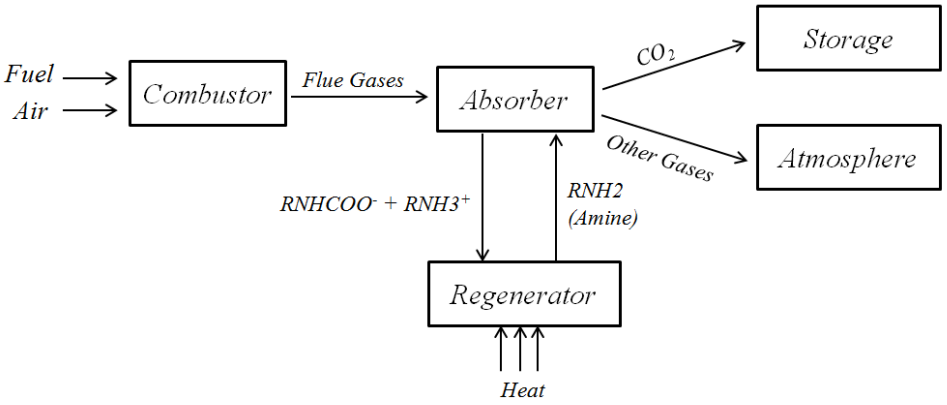

Fig.2. A conceptual sketch of amine scrubbing system.

There have been some comparative studies between amine scrubbing schemes and oxy-fuel combustion scheme from economic and performance perspectives presented in literature [14-16]. From the literature, there is not a distinctive and clear advantage for either method at the present stage of progress for either amine or oxy-fuel methods to achieve cost effective and practical CCS. It is noted that although amine scrubbing requires a significant amount of energy to liberate the CO_2 from the amine in the regenerator, the oxy-fuel combustion mode also requires a significant amount of energy for the cycle to separate the pure O_2 from the air to be utilised as the oxidiser in the oxidiser stream. A common energy requirement of both amine scrubbing and oxy-fuel cycles is the need to liquefy the CO_2 for efficient transport to the sequestration site.

2.1.3 CO_2 or H_2O Dilution

Temperature distribution is a significant factor for the designs of combustors. If the operating temperature in the combustor, for example the exhaust gas temperature, is significantly varied by changing the composition of the reactants, modification of combustor design is generally required. To minimise the modification of the currently existing combustors, the dilution degrees of CO_2 or H_2O are tailored in oxy-fuel systems such that the combustion gas temperature is close to that of ordinary air combustion. Liu et al. [17] studied this temperature control method with regard to coal combustion and found roughly 70% CO_2 dilution by volume provides good agreement with standard air-fuel combustion temperatures.

In addition to minimising the necessity for a re-design or retrofit, temperature control via CO_2 or H_2O dilution provides a route for significantly decreased NO_x emissions. Although N_2 and hence NO_x do not feature in an idealised oxy-fuel system, some degree of N_2 in the system is always present in practical systems due to air infiltration into the pre-combustion system, N_2 present in the fuel and imperfect separation of O_2 from air is often of concern in practical combustion facilities. This presence of N_2 in the system means that the minimisation of NO_x formation must be considered in the design, which is typically achieved via temperature control. Ditaranto et al. [3] reported that even with a small residual fraction of N_2 in the oxidiser stream, significant NO_x emissions can be produced in the oxy-fuel combustion mode due to the potentially high temperatures produced in oxy-fuel combustion. However, when sufficient CO_2 or H_2O dilution is coupled with the system, the flame temperature is significantly reduced and then NO_x emissions due to residual N_2 can be lower relative to ordinary air-fuel combustion [4].

At the other extreme, the upper limit of CO_2 or H_2O dilution is also of interest in design. The upper limit on the diluent fraction is determined by flame stability. It is generally known that with more than 70% CO_2 dilution (by volume), robust combustion is difficult to stabilise in turbulent jet flame [5], while Kutne et al. [6] has reported oxy-fuel flames with 80% CO_2 dilution (by volume) stabilised by a combination of swirl and partial premixing.

2.1.4 Nature of Oxy-fuel Combustion

Ideally, to minimise the retrofitting process of power plants the characteristics of the oxy-fuel combustion operation should be matched to those of the conventional air-fuel mode of operation. However, it is not possible to find such a condition that matches all aspects of flame properties between air-fuel and oxy-fuel combustion. This is due to the differences in several physical properties such as reactivity, molecular weight and diffusivity between N_2, CO_2, and H_2O.

Taking adiabatic flame temperature, ignition delay time and flame speed as representative flame characteristics, the difficulty encountered in matching these flame

characteristics from air-fuel and oxy-fuel combustion is examined. The constant pressure adiabatic flame temperature is shown in **Fig.3**, simulations of the zero dimensional constant pressure auto-ignition evolution are presented in **Fig.4** and freely propagating laminar premixed flame simulations are shown in **Fig.5**. The data presented in **Figs. 3-5** is for illustrative purposes, greater detail on the specifics of these simulations will be covered in subsequent sections and chapters of this thesis. In all these simulations, methane was used as the fuel and five different oxidiser compositions examined: air ($21\%O_2+79\%N_2$), $21\%O_2+79\%CO_2$, $25\%O_2+75\%CO_2$, $32\%O_2+68\%CO_2$ and $39\%O_2+61\%CO_2$. The initial temperature and pressure was set to be 300 K and one atm in equilibrium calculations and freely propagating laminar premixed flame simulations. An initial temperature of 1,200 K and one atm was used in the constant pressure auto-ignition simulations. In **Fig.3**, the T_{ad} of oxy-fuel combustion with $32\%O_2+68\%CO_2$ is similar in magnitude to that of air over the entire equivalence ratio range. Since the temperature in a furnace is one of the key parameters, the oxidiser condition of $32\%O_2+68\%CO_2$ can be a good candidate oxidiser composition for matching air-fuel operating conditions. However, for the $32\%\ O_2+68\%\ CO_2$ oxidiser case, the ignition delay time is shorter and the burning velocity significantly smaller relative to that of air combustion as is shown in **Fig.4** and **Fig.5**. To match the ignition delay time of air, an oxy-fuel oxidiser mixture of $25\%O_2+75\%CO_2$ is required and to match the flame speed, an oxidiser mixture of $39\%O_2+61\%CO_2$ is required. However, the T_{ad} for both of these oxidiser conditions is significantly different from the T_{ad} of air-fuel combustion.

As with the adiabatic flame temperature, the ignition delay time and flame speed is related to the flame stability. Consequently, it can be concluded that there is always a compromise in the selection of the oxidiser composition that relates to the stable operation of oxy-fuel combustion compared to air-fuel combustion.

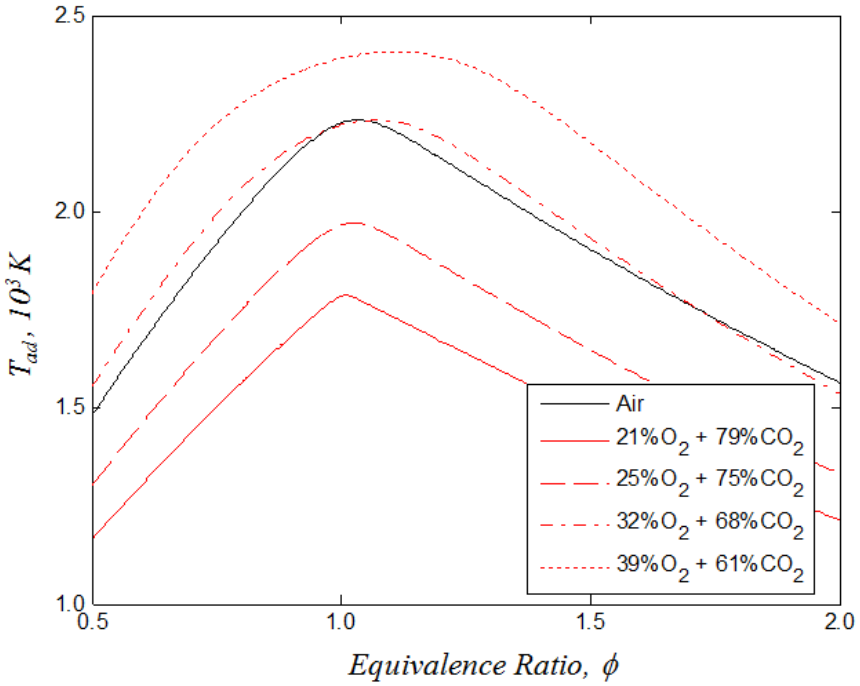

Fig.3. T_{ad} distributions with various oxidisers. The initial temperature and pressure was set to be 300 K and one atm.

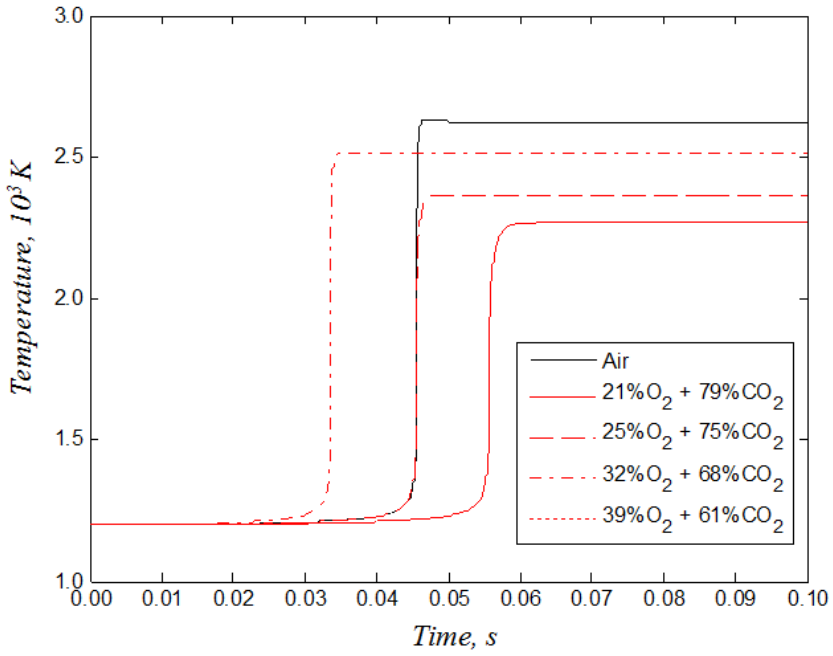

Fig.4. Results of constant pressure auto-ignition simulation with different oxidisers at stoichiometric conditions. The initial temperature and pressure was set to be 1,200 K and one atm.

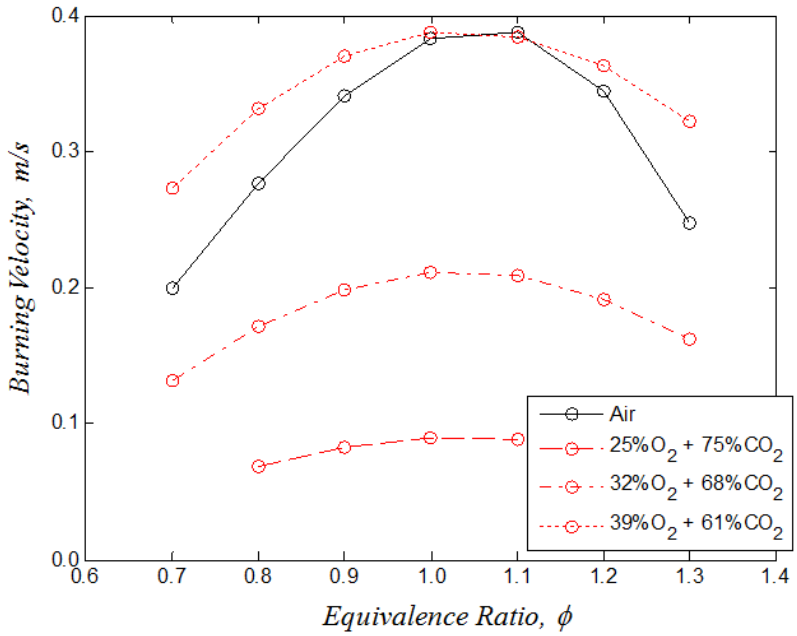

Fig.5. Burning velocities with various oxidisers. The initial temperature and pressure was 300 K and one atm. Numerical results indicate that for the 21%O_2 + 79% CO_2 oxidiser case a laminar flame cannot be sustained using standard numerical parameters.

2.1.5 Current Research Trend and Understandings

There are numerous studies in literature related to oxy-fuel combustion [18-28]. While most studies focus on the CO_2 diluted flame case, there are also several studies that examine the H_2O diluted oxy-fuel case [25-28]. In addition, studies for O_2 enriched flames and the flames diluted by the slight addition of CO_2 or H_2O with other diluents, such as N_2 and Ar [29-31], have been reported. Examples of studies looking at utilising high fractions of CO_2 or H_2O in the diluent are reported in [5, 19].

2.2 Laminar Flame Modelling

The kinetic, diffusive and thermodynamic properties of oxy-fuel combustion are explored in Chapters 4 and 5 using zero dimensional (0D) reactors and laminar flames. In this section the underlying theory, models and equations solved for laminar flames and reactors are introduced.

2.2.1 Kinetic Mechanisms

To numerically investigate and analyse oxy-fuel combustion, several kinetic mechanisms of varying complexity are employed in this study. The most frequently used mechanism for hydrocarbon flame is the GRI-Mech 3.0 mechanism (GRI 3.0), which contains 325 reactions and 53 species [32]. In the GRI 3.0, C_3 oxidation and NO formation are included. The use of GRI 3.0 has provided reasonable agreements, with experimental results over a wide range of conditions indicating that it is a sufficiently detailed and predictive chemical mechanism [33, 34]. At the other extreme, global reaction schemes are the simplest reaction models, with one example being the single step mechanism (SSM) developed by Westbook and Dryer [35]. With a SSM, the flame fundamentally consists of only fuel, oxidiser and products (CO_2 and H_2O). For methane-air combustion, such a SSM results in $CH_4 + 2O_2 \rightarrow CO_2 + 2H_2O$. While single step reaction mechanisms have a very low computational cost, the accuracy and range of applicability is significantly smaller compared to more detailed mechanisms such as GRI 3.0. Due to the inaccuracies of SSMs and the high computational cost of detailed mechanisms such as GRI 3.0, reduced mechanisms that utilise steady state and partial equilibrium assumptions have also been developed, such as the four step mechanism developed by Bilger and Starner [36]. Such reduced mechanisms are capable of predicting a reasonable agreement with experimental results in terms of extinction point, temperature and post-combustion composition, including minor species concentration such as O, OH, HO_2, H_2O_2 over an extensive strain rate range (2 to 300 s^{-1}) in a counter-flow configuration [36].

In recent years, the use of simplified reaction models in 0D reactor and 1D laminar flame simulations is not necessary owing to the rapid increase in computational processing power over recent years, allowing detailed mechanisms such as GRI 3.0 to be used on desktop computers. Simplified reaction models are still of considerable importance in that they can be used as tools to aid the analysis of combustion phenomenon, allowing the isolation of particular factors in flame simulations. One example of such an investigation that utilises a reduced mechanisms for flame analysis is that of Law et al. [37], where a single step reaction mechanism is utilised to clarify the roles that the dissociation of CO_2 and H_2O play in off-stoichiometric peaking of the adiabatic flame temperature. Another example that exploits a reduced mechanism for

analysis purposes is that of Katta et al. [38], where a single step reaction model with a large reaction rate coefficient was utilised for the evaluation of finite-rate chemistry effects on the size and shape of outer structures in jet diffusion flames of hydrogen with buoyancy-influenced toroidal vortices roll.

2.2.2 Transport Models

Diffusion also plays an important role in combustion phenomena. As with reaction models, there are several diffusion models for speeding up computation, understanding the diffusion role in flame and obtaining highly accurate results. Three commonly utilised diffusion models that are used in combustion computations are: multi-component diffusion, mixture averaged diffusion and Lewis number controlled diffusion. Multi-component diffusion mode is the model that yields results closest to the actual phenomenon; correspondingly, it is the most complex to implement, requires the largest amount of fundamental property data and is the most computationally expensive. Derived from kinetic theory [39], the multi-component diffusion coefficient D_{ij} of the species *i* in species *j* for ordinary (Fickian) diffusion is given as:

$$D_{ij} = X_i \frac{W_{mix}}{W_j} (F_{ij} - F_{ii}) \tag{1}$$

where

$$[F_{ij}] = [L_{ij}]^{-1}.$$

The component of $[L_{ij}]$ are determined from:

$$[L_{ij}] = \sum_{k=1}^{K_p} \frac{X_k}{W_i D_{ik}} [W_j X_j (1 - \delta_{ik}) - W_i X_i (\delta_{ij} - \delta_{jk})]$$

where δ_{mn} is the Kronecker delta function. It is noted that the multi-component diffusion coefficients are not the same as the binary diffusivity for the same pair of species if the mixture is not a binary mixture.

As multi-component transport can be excessively costly in some simulations such as DNS that employs detailed chemistry and can also lead to numerical instabilities in some situations due to its complexity, mixture averaged diffusion is often employed as an alternative to address these problems with typically only a small accuracy penalty. The mixture averaged diffusion coefficient D_{im} of i-th species can be expressed as:

$$D_{im} = \frac{1 - Y_i}{\sum_{j \neq i}^{K_p} (X_j / D_{ji})}. \quad (2)$$

In addition Lewis number controlled models often referred to as "unity Lewis number" diffusion models are also frequently employed. In the Lewis number controlled diffusion model, the mass diffusivity of some or all of the species in flame are set to be equal to thermal diffusivity of either the mixture or the respective species thermal diffusivity. The study of a hydrogen-air flame by Katta et.al [38] is an example of one of the many "flavours" of Lewis number controlled diffusion models that have been implemented in literature. Katta et.al [38] examine a number of combinations of diffusion models and reaction models, with one diffusion model taking the local diffusion coefficient $D_{i\text{-}N2}$ of the species i to be equal to $D_{H2\text{-}N2}$ or $D_{O2\text{-}N2}$ depending on the location in the flame. Considering such a diffusion model that varies with axial distance through the flame, Barlow and et.al [40] determined that there is an evolution from a scalar structure dominated by molecular diffusion to one by turbulent transport in piloted methane/air jet flames.

In addition to the choice of the diffusion model, it is also necessary to consider whether Soret and Dufour effects are accounted for in the model or not. The Soret effect is the transfer of mass due to thermal gradients whilst the Dufour effect is the transfer of energy due to concentration gradients. The significance of the Soret effect has been examined in hydrogen/air flame using counter-flow premixed and diffusion flames and freely propagating flame simulations by Yang et.al [41]. The study reported that except for the freely-propagating planar flame, the diffusion of H_2 due to the Soret effect increased the fuel concentration entering the flame structure and as such modified the mixture stoichiometry and flame temperature, leading to a substantial increase of the flame speed for the lean mixtures and a decrease in flame sped for rich mixtures. Soret diffusion of H was found to alter the concentration and distribution of H in the reaction zone, which in turn can affect the individual reaction rates.

2.2.3 Reactors and Burners

2.2.3.1 Equilibrium State

The equilibrium calculation seeks the solution in which the Gibbs energy of mixture becomes a minimum under given temperature and pressure with the conservation law of species. The spontaneous phenomenon with infinite time in an absence of external treatment leads to the Gibbs free energy minimum. Hence, the obtained result is referred to as equilibrium state. The Gibbs free energy, *G*, is mathematically represented in the form:

$$G = RT \sum_{i=1}^{K_g} \left(\frac{x_i G_i^0}{RT} + x_i \frac{\ln x_i}{\sum x_i} + x_i \ln P \right) \tag{3}$$

where *R* is universal gas constant, *T* is temperature, *P* is pressure, *x* is mole number, G^0 is the molar Gibbs free energy at 1 atm and K_g is the total number of species. When an equilibrium calculation is conducted with the total enthalpy of the system held constant, the obtained temperature is called the adiabatic flame temperature. Equilibrium calculations are a zero dimension simulation where no spatial or temporal dimensions are included in the calculation. The equilibrium solution is only determined only by the ambient temperature, pressure and the reactant composition. Due to their simplicity, equilibrium calculations are often used as an initial step for the fundamental understanding of combustion of the fuel of interest and the obtained T_{ad} is frequently utilised as criteria to understand flame temperature [42-45].

2.2.3.2 Closed Zero Dimensional Reactors (Auto-ignition Chemistry)

The zero dimensional (0D) reactors utilised in the studies in this thesis are assumed to be adiabatic with chemically inert walls and no inlets or outlets. The reactants are assumed to be spatially homogeneously distributed in the reactor and there is no temperature or composition gradients within the mixture, thus thermal and mass diffusion in the reactor are not considered. The chemical reactions are assumed to occur at each and every location within the reactor at the same rate. A single temperature,

pressure and vector of species concentrations at each time step sufficiently describe the evolution of the thermo-chemistry state vector in the reactor. Although an enormous amount of information is obtained from a single OD reactor simulation, a single characteristic value that can be obtained from such simulations is the ignition delay time. There are several methods to define the ignition delay time, in most cases the ignition delay time is calculated based on the time at which the rate of change of temperature (*dT/dt*) reaches a maximum, another definition often used in compression ignition simulations and auto-ignition simulations where the fuel exhibits multistage ignition is to take the ignition delay as the point where the rate of change OH is a maximum. The simulation of closed zero dimensional reactors can be operated with constant pressure or constant volume. Constant pressure simulations are more relevant to boiler and combustor applications, where as constant volume calculations are more relevant to internal combustion engine applications. For reference, the governing equations for constant pressure are shown below:

$$\frac{dT}{dt} = \frac{\left(\frac{\dot{Q}}{V}\right) - \sum(h_{m_i}\dot{\omega}_\iota)}{\sum([i]C_{pm_i})} \tag{4}$$

$$\frac{d}{dt}[i] = \dot{\omega}_\iota - [i]\left(\frac{\sum \dot{\omega}_\iota}{\sum[i]} + \frac{1}{T}\frac{dT}{dt}\right) \tag{5}$$

where $[i]$ is molar concentration of species i, $\dot{Q}$ is heat transfer rate, C_{pm} is molar specific heat capacity, h_m is enthalpy per unit mole and $\dot{\omega}$ is species production rate. Equation (4) is derived from conservation of mass, whilst equation (5). is derived from a conservation of species. A typical auto-ignition solution for a constant pressure reactor is shown in **Fig.6**. Due to the relative simplicity of 0D auto-ignition reactor simulations, they are often used as an initial step in understanding auto-ignition phenomenon as well as the evaluation and development of chemical kinetic mechanisms from shock tube experiments [46-49].

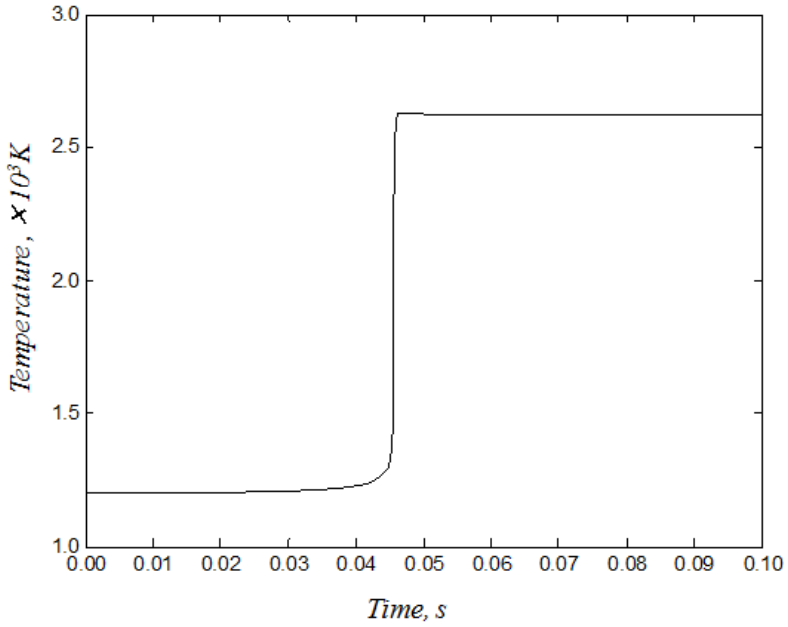

Fig.6. A typical result of closed zero dimensional reactor with constant pressure (1 atm). The calculation utilises a stoichiometric methane-air mixture, with an initial temperature of 1200K.

2.2.3.3 Freely Propagating Premixed Flame Simulation

In freely propagating premixed flame simulations it is assumed that the flame is planar and one dimensional. Radial transport is assumed to be negligible, whilst molecular transport and thermal conduction in the axial direction are accounted for. Freely propagating flame simulations are usually conducted to obtain the characteristic flame speed of the gas mixture, the premixed laminar flame speed. The laminar flame speed is defined as the reactant flow speed entering the flame in the steady state condition where the flame becomes stationary with a fixed coordinate system such that the reactant flow velocity is equal to the flame propagation velocity. The flame speed is one of the most useful parameters to characterize the combustion of fuel-oxidizer mixtures due to the flame speed being strongly correlated to the flammability which is related to flame extinction and instability. The flammability limit defined by Spalding [50] is a state at which steady propagation of the one-dimensional, planar premixed flame in the infinite domain fails to be possible. Another characteristic of freely propagating flames is that it is a conservative system in that the downstream temperature is relaxed to the adiabatic flame temperature. This is because the freely propagating flame assumes there is no molecular transport or loss of enthalpy in the radial direction, in addition it is assumed

that in the ideal case there is no heat loss mechanisms such as wall conduction or radiation.

To obtain the results of freely propagating flame simulations, equations (6), (7) and (8) are numerically solved.

The continuity equation, or conservation of mass:

$$\dot{M} = \rho u A \tag{6}$$

The energy equation or conservation of energy:

$$\dot{M}\frac{dT}{dx} - \frac{1}{c_p}\frac{d}{dx}\left(\lambda A\frac{dT}{dx}\right) + \frac{A}{c_p}\sum_{k=1}^{K}\rho Y_k V_k C_{pk}\frac{dT}{dx} + \frac{A}{C_p}\sum_{k=1}^{K}\dot{\omega}_k h_k W_k V_k + \frac{A}{c_p}\dot{Q_{rad}} = 0 \tag{7}$$

The species transport equation or species evolution equation:

$$\dot{M}\frac{dY_k}{dx} + \frac{d}{dx}(\rho A Y_k V_k) - A\dot{\omega}_k W_k = 0 \quad (k = 1, \ldots., K_g) \tag{8}$$

2.2.3.4 Opposed-Flow Flame Simulation

The opposed flow flame simulations model a flow consisting of two opposing nozzles separated by a finite separation distance which results in a flat flame stabilised between the two nozzles. A conceptual sketch of the opposed flow flame configuration is shown in **Fig.7**. The stagnation plane in the non-reacting case is determined by momentum balance of two streams and can be a reasonable approximation in the reacting case. Both premixed and non-premixed flames can be applied to the opposed-flow field. When both opposed streams are premixed, two premixed flames are formed, one on either side of the stagnation plane. At the other extreme, when the one stream is fuel and the other oxidiser, a diffusion flame is produced on the oxidiser side of the

stagnation plane for hydrocarbon flame. The most attractive element of this opposed-flow simulation is that the three-dimensional flow flame can be treated mathematically as one dimension by some assumptions. The first assumption is that the radial velocity varies linearly with radial distance at a given axial position. The second assumption is that the pressure field in this system is represented by:

$$P = P_0 - \frac{1}{2}(P'r^2) + F(x) \tag{9}$$

where *r*: radial coordinate, *x*: axial coordinate, P_0: stagnation pressure, *P'*: the radial pressure gradient eigenvalue and *F(x)*: the pressure variation in the axial direction. The last assumption is that the temperature and species have no radial variation in the axial direction. From an experimental perspective, these three assumptions can be realised if the velocity profiles for both of the nozzles at the exit plane is sufficiently close to a flat top profile [51]. The set of equations governing the 1D laminar opposed flow case were first reported by Kee, et al [52] and are given below:

$$\frac{\partial(\rho u)}{\partial x} + \frac{1}{r}\frac{\partial(\rho v r)}{\partial r} = 0 \tag{10}$$

where u and v are the axial and radial velocity components:

$$\rho u\frac{dT}{dx} - \frac{1}{C_p}\frac{d}{dx}\left(\lambda\frac{dT}{dx}\right) + \frac{\rho}{C_p}\sum_{k=1}^{K} Y_k V_k c_{pk}\frac{dT}{dx} + \frac{1}{C_p}\sum_{k=1}^{K}\dot{\omega}_k h_k + \frac{1}{c_p}\dot{Q_{rad}} = 0 \tag{11}$$

$$\rho u\frac{dY_k}{dx} + \frac{d}{dx}(\rho Y_k V_k) - \dot{\omega}_k W_k = 0 \quad (k = 1, \ldots, K_g) \tag{12}$$

Another characteristic of opposed flow flame configuration is that it is not sufficient to characterise the simulations by solely the inflow compositions, an additional parameter the strain rate is required. The presence of aerodynamic straining in the system is a significant difference compared to freely propagating flames causing opposed flow flames to not be conservative, resulting in peak flame temperatures that are usually lower than the adiabatic flame temperature.

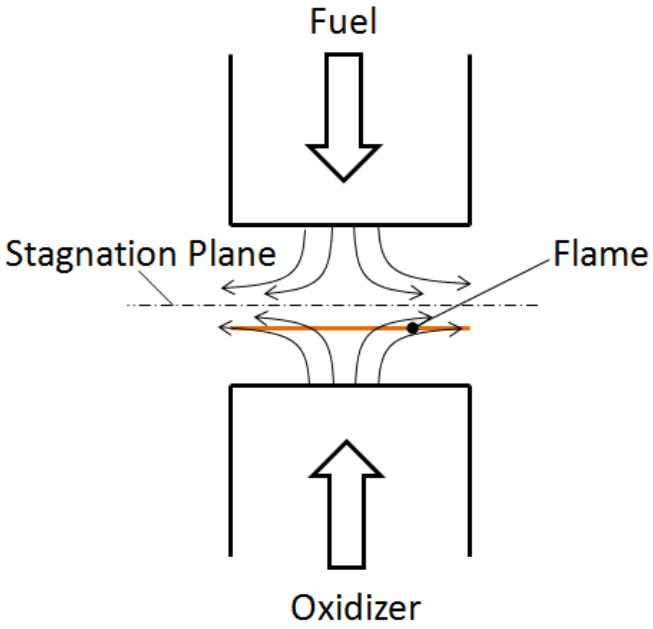

Fig.7. A conceptual sketch of a counter-flow burner.

Flame shear and stretching caused by flame surface motion and unsteadiness are suppressed in the opposed flow burner configuration as the flame is flat and laminar, only perturbations by aerodynamic straining are possible. Due to this, opposed flow flames are frequently used for the evaluation of the flame response to aerodynamic straining [33, 53-57]. The zero strain rate case is also possible to be evaluated by extrapolations of results from low strain to zero strain [55, 56]. The physical meaning of the strain rate is the velocity gradient, or equivalently, the inverse value of the flow time. The simplest method to determine the representative strain rate in the specified flow field is:

$$a = \frac{V_F + V_O}{L} \tag{13}$$

where V_F and V_O are a mean flow speed at the opposed ends respectively. A more detailed definition of the strain rate is often used:

$$a = \frac{2V_O}{L}\left(1 + \frac{V_F\sqrt{\rho_F}}{V_O\sqrt{\rho_O}}\right) \tag{14}$$

This definition of the global strain rate is similar to the axial velocity gradient on the oxidizer size just ahead of stagnation plane. Equation 9 takes into account the density difference between the two opposed streams as well as the progressive deviation of the velocity distribution from being uniform at the nozzle exit to a stagnation surface in the cold flow [58] limit. Furthermore, the maximum axial velocity gradient, i.e., $(du/dx)|_{max}$ on the fuel side just before the flame can also be used as representative strain rate. Chelliah et.al [59] reported that the strain rate at extinction by this definition is relatively insensitive to the boundary conditions of the flow.

Flame properties such as burning velocity, flame thickness and flame temperature structure vary with the global strain rate. For premixed flames, these variations with strain-rate are relatively small, whilst for diffusion flames they can vary significantly [60, 61]. For diffusion flames, the flame position does not vary significantly with strain rate [62] and thus the permissible time for reaction at each point is reduced as strain rate increases. For premixed flames the flame position typically varies with strain rate and thus the reaction time scale for reaction does not vary significantly with strain rate until the flame is sufficiently close to a stagnation plane.

It has been shown to be advantageous to analyse the structure of diffusion flames in terms of a conserved scalar [63-65]. One of the most useful conserved scalar definitions that is utilised extensively in this thesis is the mixture fraction ξ. The mixture fraction is defined as the mass fraction of mixture that originates from the fuel stream at the particular point of interest, taking a value of 0 at oxidizer outlet and 1 at fuel outlet. The mixture fraction at stoichiometry is here designated ξ_{st} as is customary. To calculate the mixture fraction at any point in the domain the following formulation proposed by Bilger et al. [63] is often used:

$$\xi = \frac{2(Y_C - Y_{C,2})/W_c + (Y_H - Y_{H,2})/2W_H - (Y_O - Y_{O,2})/W_O}{2(Y_{C,1} - Y_{C,2})/W_c + (Y_{H,1} - Y_{H,2})/2W_H - (Y_{O,1} - Y_{O,2})/W_O} \qquad (15)$$

Where the *Y*'s are the elemental mass fractions of carbon, hydrogen and oxygen; *W*'s are atomic weights; and the subscripts 1 and 2 refer to the fuel stream and oxidizer stream, respectively. This formulation assumes the Lewis numbers for all species equal

to unity, i.e., equal thermal and mass diffusivity. In analysing experimental data, it is common to drop the oxygen term from equation (15) resulting in the following expression:

$$Z = \frac{2(Y_C - Y_{C,2})/W_c + (Y_H - Y_{H,2})/2W_H}{2(Y_{C,1} - Y_{C,2})/W_c + (Y_{H,1} - Y_{H,2})/2W_H}. \quad (16)$$

This equation (16) yields results nearly identical to the Bilger formulation (15), but with a reduced sensitivity to experimental noise and interferences [66, 67].

2.2.4 Laminar Flame Models to Turbulent Flame Models

The study of laminar flames is not only relevant to laminar flames but also to turbulent flames as many experimental studies have found that under certain conditions the structure of a turbulent flame can be parameterised by a laminar flame. Such experimental findings form the basis for many turbulent numerical modelling methods such as flamelet models [68] which assume that steady laminar counter-flow flames exhibit a scalar structure similar to unsteady distorted mixing layers in a turbulent flow field. Therefore the counter-flow geometry can also be used as a tool to study chemistry model and molecular transport effects in turbulent flames.

In the terms of turbulent flame simulation methods that do not use pre-computed tabulations, such as PDF calculations and direct numerical simulation (DNS), reduced kinetic models are employed more frequently than detailed reaction models such as GRI 3.0. This is because reactive turbulent flows using these large detailed mechanisms still feature a significant computational cost; this is despite recent extraordinary increases in the speed of computers and the availability of efficient computational techniques. The miss-application of the assumptions of infinitely fast reactions, single step reactions or reduced kinetic mechanisms in turbulent flame simulations can also lead to errors in the prediction of stability limits due to finite-rate chemistry effects [69].

2.3 Off-stoichiometric Peaking of Adiabatic Temperature (0D OTP)

This section provides an overview of the fundamental physics of 0D OTP primarily developed by Law et.al [37] , together with a discussion on the significance of 0D OTP to oxy-fuel combustion.

2.3.1 The Physics of 0D OTP

It is generally known in the combustion field that the adiabatic temperature, T_{ad} of a flame generally does not peak at stoichiometry, but rather near stoichiometry. For instance the maximum T_{ad} in methane-air combustion is seen at an equivalence ratio, ϕ, of 1.04 for an initial temperature of 300K and ambient pressure of 1atm. This phenomenon is called zero dimensional off-stoichiometric temperature peaking (0D OTP). The nature of 0D OTP has been previously explored by Law et.at [37]. which clarified some of the differing descriptions for OTP in literature. In their work the skewness of T_{ad} in ϕ space was evaluated considering the heat release per unit mass, q_p, and the specific heat capacity, C_p at specific value of ϕ. For reference the q_p and C_p of methane-fuel combustion is shown in **Fig. 8** as a function of ϕ. Whilst C_p monotonically increases with ϕ, leading to a shift of the temperature peak to the lean side of stoichiometry, the q_p holds a parabolic curve with a peak at a slightly rich side of stoichiometry, which drives the rich shifting of the temperature peak. The consequent temperature peak position is determined such that these two shifting phenomena are balanced. More accurately, the temperature peaks such that:

$$\frac{\frac{d}{d\emptyset}q_p(\emptyset)}{q_p(\emptyset)} = \frac{\frac{d}{d\emptyset}C_p(\emptyset)}{C_p(\emptyset)} \tag{17}$$

Fig. 9 shows the q_p related term, i.e., left hand side of equation (17), as well as the C_p related term, the right hand side of equation (17) in ϕ space. The crossing condition between the two curves in **Fig. 9** represents the mixture of maximum T_{ad}.

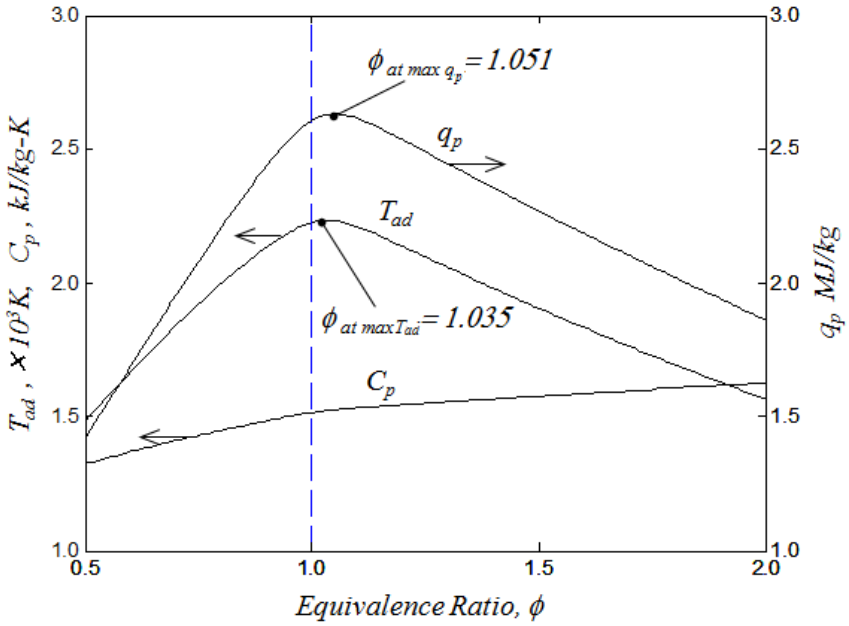

Fig.8. Off-stoichiometric peaking of adiabatic flame temperature with air-methane mixtures at initial temperature of 300 K and ambient pressure of one atm.

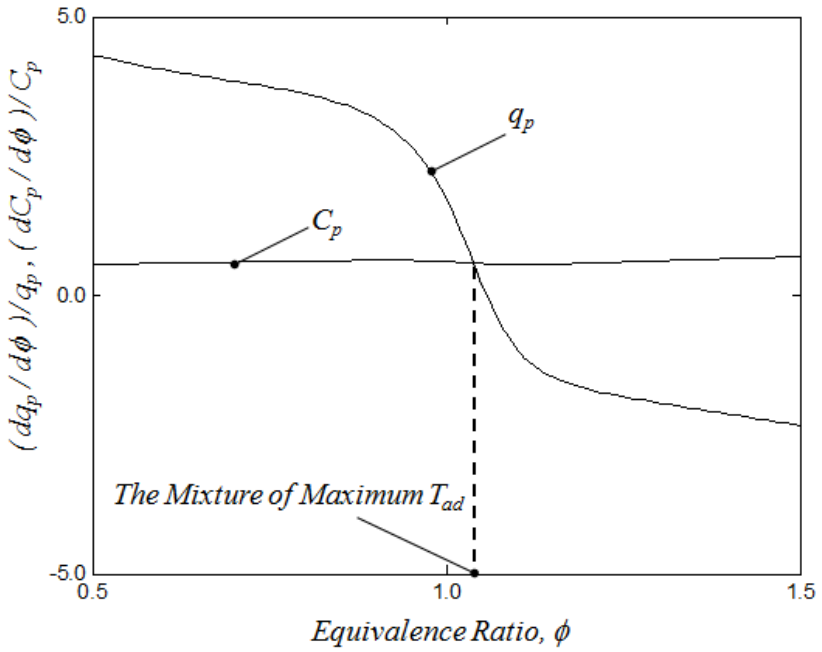

Fig.9. **The relationship of the driving forces for 0D OTP in terms of, q_p and C_p .**

Law et al. [37] also identifies the cause of the rich side of off-stoichiometric peaking of the q_p which is dominant factor of the rich shifted 0D OTP typically found in hydrocarbon flames. By employing a dissociation frozen mechanism in which any dissociation reactions, such as $CO_2 \rightarrow CO + O_2$ are suppressed from GRI 3.0, allowing a methodology to examine the influence of dissociation on 0D OTP was developed [37]. **Fig. 10** shows the calculation results with this dissociation frozen mechanism and GRI 3.0. The q_p with the dissociation frozen mechanism peaks at stoichiometry in contrast with GRI 3.0. Therefore it can be concluded that dissociation does play a dominant role in the rich shift of the q_p peak. Also since the gap between the zero dissociation and full mechanism in the q_p represents the dissociation degree at an individual equivalence ratio, it can be observed that the dissociation occurs to a greater degree at stoichiometry than at the slightly rich side of stoichiometry and as a result the q_p and consequent T_{ad} of methane-air combustion peaks in the rich mixture condition.

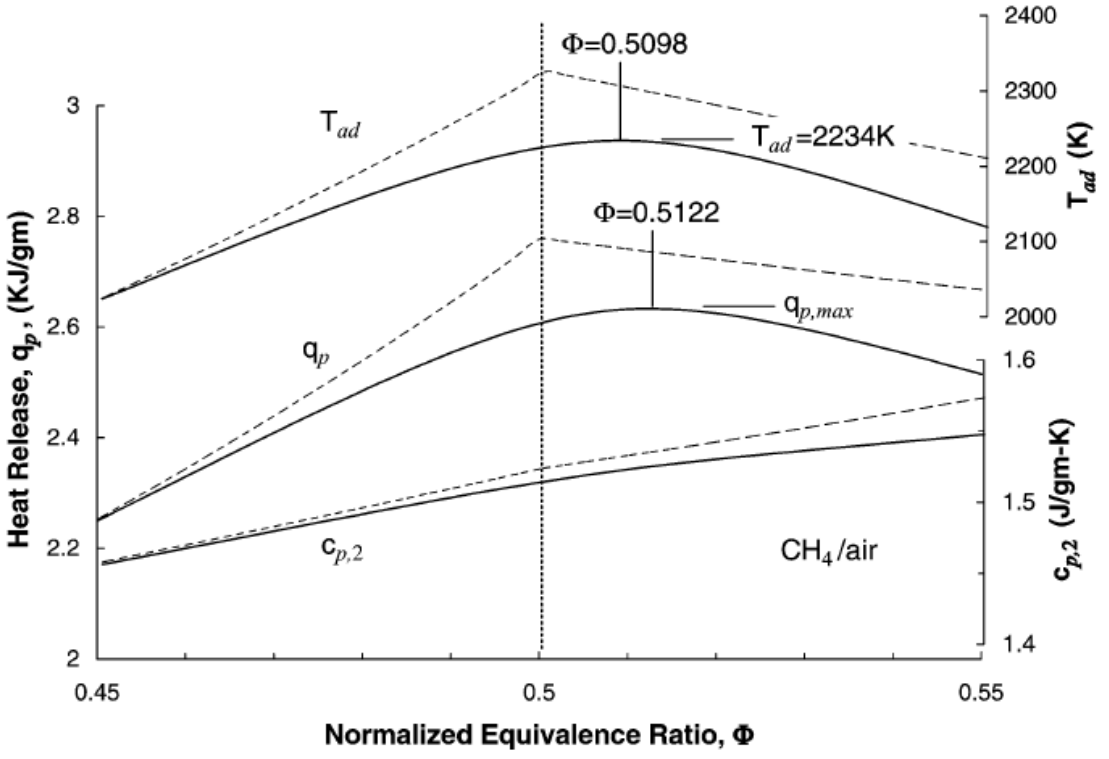

Fig.10. T_{ad}, q_p and C_p of the methane-air combustion for the full GRI 3.0 mechanism and the dissociation frozen mechanism. The graph is from [37]. The normalised equivalence ratio is defined as $\phi/(\phi+1)$. Dash lines: dissociation frozen mechanism, Solid lines: GRI 3.0.

2.3.2 Significance of 0D OTP in Oxy-fuel Mode Fire Stations

In determining operation condition of firing power plants, the post-combustion gas temperature is a primary factor from both a performance and environmental perspective. In conventional air-fuel flames, the net-equivalence ratio in the furnace is varied to realize the desired temperature. However, equivalence ratio control is generally not possible in the oxy-fuel combustion mode as oxy-fuel combustion system must remain close to near-stoichiometric burning. In oxy-fuel combustion the inclusion of O_2 in the post-combustion gas means some energy is consumed wastefully since the supply of pure O_2 requires significant energy consumption. Due to this fact the degree of the CO_2 or H_2O dilution is typically varied as the primary temperature controlling parameter in oxy-fuel combustion.

Keeping the above in mind it can be said that one of the most sophisticated temperature control strategies in oxy-fuel based firing plants is to control the primary temperature by the dilution degree with equivalence ratio adjustments around stoichiometry used as fine tuning mechanism. Since oxy-fuel combustion replaces the N_2 in oxidizer stream with CO_2 or H_2O the C_p of the resultant mixture is different in terms of physical properties from conventional N_2 diluted flames. Also as the presence of CO_2 and H_2O enhances dissociation effects which impact the heat release structure, hence the 0D OTP characteristics of oxy-fuel flames is expected to be varied from those of N_2 diluted flames. Due to the significance of 0D OTP in oxy-fuel scheme and expectation of characteristic variation from conventional flames, the study of the 0D OTP structure for oxy-fuel combustion is one of the primary objectives of this study. The results obtained in this study can be a guide for the determination of the operational conditions used in practical applications and industry.

2.4 Laser Diagnostic Techniques

Laser diagnostics in modern experimental combustion science are of considerable utility due to their remote, non-intrusive and in-situ characteristics combined with the potential for high temporal and spatial resolution. In this section, three representative spectroscopic techniques are briefly reviewed and then the OH LIF thermometry

techniques employed in the present research are discussed in greater detail. A review of the current state-of-the-art knowledge regarding the application of laser diagnostics to oxy-fuel combustion is also provided.

2.4.1 Rayleigh Spectroscopy

The elastic scattering of light, i.e. scattering with no shift in wavelength, can be classified as either Rayleigh scattering or Mie scattering. Rayleigh scattering is based on the interaction of light with molecules while Mie scattering is based on the interaction of light with particles. More accurately, the distinction between the two resides in size the molecule or particle and the wavelength of the incident light through the relation: $d/(2\lambda) < 0.05$, where d is the diameter of the molecule or particle and λ is the incident wavelength. Rayleigh scattering arises from the oscillating dipole moment induced by incident laser light quanta. A detailed description of the theory of Mie scattering and Rayleigh scattering can be found in literature [70, 71]. Advantageous features of Rayleigh scattering include its signal strength and simplicity of the experimental setup. However as there is no frequency shift in Rayleigh process and thus Rayleigh signal, interference from background scattering as well as Mie scattering can easily corrupt the Rayleigh scattering signal. Typically for high quality Rayleigh scattering measurements significant attention is needed to paid to eliminate spurious background reflections as well as judicious flame/flow selection to avoid soot, droplets and particles. Temperature measurement via Rayleigh scattering requires information on the constituents at probed volume since Rayleigh scattering cross section varies with composition. The signal intensity of the Rayleigh scattering signal S can be mathematically represented by:

$$S = kE\sigma_{eff}\sum[i] \tag{18}$$

where k is a constant which accounts for a geometry of collection optics and a detection efficiency, E is the incident laser energy, $[i]$ is a number density of species i and σ_{eff} is an effective cross section at proved volume. The effective cross section is:

$$\sigma_{eff} = \sum X_i \sigma_i \tag{19}$$

where X_i is a mole fraction of species *i* and σ_i is a Rayleigh cross section of species *i*. In Rayleigh scattering thermometry, the ideal gas equation of state is typically incorporated into the above two equations to determine temperature assuming the pressure is known. Example applications using Rayleigh scattering to determine temperature can be found in the following references [72-74].

2.4.2 Raman Scattering

Raman scattering is an inelastic scattering interaction of light with molecules and is often termed rotational, vibrational, ro-vibrational or electronic depending on the nature of energy level transitions which occur in the molecule and the photon energy of the interacting light. From a classical viewpoint, Raman scattering is driven by the polarizability variation due to the electron positions in molecules. The resultant Raman scattering signal when down shifted in frequency is termed stokes and the other anti stokes for historical reasons. The detailed physics of Raman scattering from both a classical and quantum perspective is well elucidated in literature [70, 75]. Although Raman scattering is shifted from the excitation wavelength and hence somewhat immune from the scattering interferences that plague Rayleigh scattering measurements the main drawback of Raman scattering is its very low signal level. Due to the very low signal levels, Raman scattering is typically limited to clean flames with low interference levels from flame luminosity and soot. In practical devices, sufficient optical access to obtain sufficient signal levels is often a challenge to achieve using Raman scattering. As Raman scattering requires only a single laser to monitor all major species in flames, Raman scattering is often utilised in the combustion field to determine the thermo-chemical state of laboratory scale flames. The Raman scattering signal intensity from species *i* can be represented in the form;

$$S_i = P_i \, f_i(T) \, E \, \gamma_i \, [i] \tag{20}$$

where *P* is a constant which depends on the wavelength, optics geometry and collection efficiency, $f(T)$ is a bandwidth factor which accounts for a temperature-dependent

distribution of molecules in their allowed quantum states and γ is a cross section of Raman scattering.

To processes the raw Raman signals to species concentrations, there are mainly two options; the Spectral Fitting Method which is based on libraries of theoretical spectra and Matrix Inversion (MI) [76] tMI is based on utilising species spectral responses that that are not highly spectrally resolved and are determined based on extensive calibration measurements in heated flow and flames to determine the temperature dependent system response. A hybrid spectral fitting MI has been introduced by Fuest et.al [77]. The hybrid method utilizes simulated spectral libraries, and namely integrates simulated spectrums over regions corresponding to on-chip binning for determination of temperature dependence matrix elements in MI method instead of conducting extensive calibration leading to a much higher precision in the measurements.

2.4.3 LIF

Fluorescence is the process of light emission from a high energy state in an atom or molecule to a lower energy state with the same electronic spin state (the same multiplicity). In contrast emission of light form a high energy state to a lower energy state with a different electronic spin state is termed phosphorescence. In general fluorescence lifetimes are in the range of nanoseconds to microseconds and are typically much shorter than the phosphorescence life times which are generally in the range of microseconds to seconds. A complicating factor in making quantitative LIF measurements is collisional quenching. It is not true that all excited molecules emit fluoresce photons, indeed the primary energy transfer path for excited state molecules is de-excitation through collisional quenching. The physics behind collisional quenching is explained in [70, 78, 79]. To circumvent the quenching disturbance to the experimental data, some prior calibration measurements can be taken. One of them is a direct pre-measurement of collisional quenching cross section of monitored molecules, which can be seen in [80]. The difficulty of this method is need for extensive pre-experiments as quenching cross section varies with collision partners. The LIPF (Laser Induced Pre-dissociative Fluorescence) may also be a good way for reduction of the collisional effect as the time scale of pre-dissociation is smaller than that of collisional quenching, as is shown in [81]. Especially, LIPF has more advantages at higher pressure fields, since LIPF signal intensities are almost constant as far as the pre-

dissociation lifetime is sufficiently short, while the quantum yield for linear fluorescence decreases significantly with increasing pressure. Mathematical formulation of LIF signal intensities is not mentioned here since the more detailed exploration of LIF is conducted in the methodology chapter.

2.4.4 OH LIF Thermometry

Temperature is one of the most significant parameters in combustion, since it governs chemical reaction rates and equilibrium states. Due to the significance of temperature, several laser based thermometry techniques have been developed and applied such as LIF based thermometry. One of the most substantial advantages of LIF based thermometry is the feasibility of planar imaging, that is, spatially resolved images can be obtained. In general, Coherent Anti-stokes Raman Spectroscopy (CARS) measurements are applied as a point measurement. However recent advances in the technique have extended it to line and planar configurations in flames using picosecond and femtosecond lasers [82, 83]. In terms of accuracy, CARS based measurements typically provide the highest accuracy [84]. Spontaneous Raman spectroscopy can be applied in a point or line measurement configuration. However, due to the relatively weak signal intensity, the small scattering cross section and the sensitivities to spectral interferences from sources such as PAH and soot precursors its application as a universal thermometry technique is challenging [85]. Laser absorption method is limited to line-of-sight integrated measurements and thus lack the spatial resolution required for measurements in turbulent flames [86]. Rayleigh scattering can be applied as a planar imaging technique. However, the local composition must be known in order to determine the effective scattering cross section [72]. The primary disadvantage of LIF based thermometry techniques is the necessity to specify certain spectroscopic parameters, such as the fluorescence yield, electronic quenching and the fluorescence quantification model.

Some example target species that have been employed in LIF based thermometry are OH [87-90], NO [91-93], O_2 [94], CH [95] and indium [96-100]. Care must be taken in the selection of the environment the LIF thermometry technique is applied to as well as the target species. The OH radical and vibrationally hot O_2 are present only around the flame front and high temperature regions, the CH radical is narrowly distributed in

vicinity of the flame front and NO (seeded into a reactive flow system) is present relatively in a large region in both the unburned and the post-flame gas. Thus far, OH has been most frequently employed in LIF thermometry due to its high concentration in the high temperature region of the flame, its strong signal, easy accessibility of electronic transition by the frequency-doubled conventional dye laser with rhodamine and its well-known spectroscopic characteristics.

There are many different methods to apply OH LIF based thermometry. Spectral fitting, two-line peak and two-line integration methods are explored here as representative example. In spectral fitting techniques, an excitation-emission scan of the laser wavelength is implemented over numerous lines in the ro-vibrational manifold of interest. The shape of obtained LIF-emission laser wavelength can then be compared to the theoretical emission-absorption wavelength spectrum, with the shape of the spectral profile being dependent on temperature, thus allowing temperature to be obtained by seeking the best fit condition between experimental and theoretical profiles. In two-line peak thermometry, two lines in the manifold of interest are selected and then signal intensity at the two wavelengths is detected in the experiment. As the spectral profile depends on temperature, the ratio of two signal intensities also relies on temperature at the probed volume. These two measurement techniques have been widely applied in literature, as seen in [87-90]. In contrast, the two-line area method is a relatively new idea. As with the two-line peak method, two lines are selected but spectral profiles of the two lines are scanned, and then the signals are spectrally integrated in individual lines. The ratio of the integrated value at each line is relevant to temperature, and thus temperature at probed volume can be obtained. Kostka et al. [101] reported that the integration scheme improved the measurement accuracy by as much as threefold in their experiment.

2.4.5 Application to CO_2 Diluted Flames

The application of laser diagnostics to CO_2 diluted flames encounters some challenges due to the distinctive and unique properties of CO_2. For instance, CO_2 has a higher refractive index relative to air, which can cause beam steering effects when laser or signal light passes through an interface between air and high CO_2 content flows, while it was reported that beam steering was not significant with a 68% CO_2 mixture by

Sevault et al. [5]. Specifically for Raman spectroscopy, the Raman crosstalk of CO_2 with O_2 leads to uncertainty in O_2 monitoring, especially when the O_2 fraction is low. Similarly, Raman rotational bands of H_2 near CO_2 Raman bands can also be affected. In CO_2 diluted flames the impact of the shift of the radical pool must be considered at higher temperatures, which can lead to some advantages compared to conventional N_2 diluted flames. For example, the detection of CO Raman spectra can be achieved with high SNR, while in conventional air-breathing flames the CO Raman suffers from low signal levels and interferences from N_2. Greater details of the challenges and advantages of the application of Raman scattering to CO2 diluted vs. conventional air-breathing flames are outlined in [5]. In LIF and CARS based, methods as the influence of CO_2 being the dominant collisional partner needs to be accounted for. As CO_2 features a significantly more complicated energy structure compared to N_2, measuring, modelling and understanding the collisional behaviour of CO_2 vs. N_2 is typically far more complex.

2.5 Image Processing/Optical Devices

In this section, a set of underlying concepts on optical devices and units that are used in laser diagnostics are given such as: lasers, collection systems such as cameras and collection lenses, and laser pulse stretchers. To successfully execute laser diagnostics, it is of considerable importance to design and arrange optical systems in an appropriate way. This section outlines the necessary theory in order for this to occur.

2.5.1 Lasers

2.5.1.1 Required Laser Wavelength in Diagnostics

Most lasers employed in combustion diagnostics are performed at visible or ultraviolet (UV) wavelengths for specific reasons. Firstly, most imaging devices, such as Charge Coupled Device (CCD) cameras, work most efficiently at visible wavelengths. In addition, some scattering phenomena used in diagnostics, such as Raman and Rayleigh scattering, enhance scattering efficiency with a decrease in the incident laser

wavelength. Further, excitation wavelengths for electronic transitions of major species in flames generally resides in UV-visible regimes.

2.5.1.2 Laser Survey

There are currently numerous laser types on the market, while the lasers available for diagnostics are limited due to wavelengths and signal intensities required in applications to combustion environments. The Nd:YAG laser and dye laser are explored here as representative, primarily motivated by the fact that these lasers are the ones used in the present study.

Nd:YAG Laser:

A Nd:YAG laser emits laser beams in trivalent neodymium ions, Nd^{3+} housed in an yttrium aluminium garnet ($Y_3Al_5O_{12}$) crystalline host material. A Nd:YAG laser essentially emits fixed frequency light, while it can be tuned within a quite narrow frequency when injection seeded. The primary fundamental wavelength that Nd:YAG lasers typically operate at is 1,064 nm. A Nd:YAG laser is often used with harmonic generation, allowing additional wavelengths to be generated such as 532 nm (Second Harmonic Generation), 355 nm (Third Harmonic Generation) and so on. For instance, the frequency-doubled Nd:YAG laser beam of 532 nm is frequently employed in particle image velocimetry (PIV), Rayleigh and Raman scattering, and for pumping tuneable lasers. The repetition rate of Nd:YAG lasers pumped by a flash-lamps is typically a few tens of Hz and pulse energies are hundreds of mili-joules at 532 nm. One of the challenges in applying Nd:YAG lasers with flash-lamp pumping is that the repetition rates are not sufficiently high to capture temporal evolution in detail in most turbulent combustion fields.

Q-switching is a technique used for producing very high power, so termed “giant” laser pulses with Nd:YAG lasers. In normal lasing operation, gain or population inversion is reduced during lasing actions since stimulated emission depletes the upper laser level. Thus, it is difficult to create intense pulses. In Q-switched laser operation, a significantly large population inversion is initially realised by holding the Q of the cavity down (suppressing lasing), and then rapidly raising the Q of the cavity (rapid lasing). The Q of a cavity here refers to the ratio of the radiation energy stored in the

cavity to the power loss. By this rapid Q value control, the laser pulse with Q-switching obtains very high instantaneous power levels. Most Q-switching systems are realised by a Pockels cell.

Dye Laser:

In contrast with the Nd:YAG laser, the dye laser can be tuned over relatively large spectral range. Complex organic molecules are employed as the lasing media in dye lasers, due to their closely packed vibrational-rotational transitions, while there are only discrete atomic energy states in the active medium in Nd:YAG lasers. In addition, it is generally know that flash-lamp-pumped dye lasers provide very high pulse energies of a few joules per pulse. Due to the adjustability of wavelengths and high pulse energy, flash-lamp pumped dye lasers are extensively employed in Raman spectroscopy diagnostics. At the other extreme, dye lasers pumped either by frequency-doubled Nd:YAG lasers or N_2, Cu, Ar lasers features low pulse energies. However, dye laser pumped by other lasers gives rises to better laser quality and equivalently narrower spectral line width. Consequently, narrow band laser pumped dye lasers are applied to LIF measurements in combustion.

2.5.1.3 Spatial Resolution of Laser Beam

A characteristic of focused laser beams is that they are significantly dependent on the transverse mode structure of the beam, that is, the number of transverse electromagnetic modes (TEM). A laser beam with single mode (TEM_{00}) holds a Gaussian intensity profile and is generally considered diffraction-limited. The two subscript number of TEM represents vertical and horizontal mode number respectively. Multimode beams shows higher divergence and poorer focusing characteristics than that of single mode beams. The degree of the multimode characteristic of a laser beam can also be represented by the M^2 value. The unity of the M^2 value refers to diffraction-limited beams and the M^2 value increases with multimode degree. Most scientific lasers have M^2 value of 1–2, while the Nd:YAG lasers explored above hold M^2 values of tens to hundreds (Note that the Nd:YAG laser has M^2 value less than 3). The spatial resolution of laser beams focused by an ideal focussing lens with focal length f can be formulated in the form:

$$d_0 = \frac{4\, f\, \lambda\, M^2}{\pi d} \tag{21}$$

where d_0, d and λ is the focused laser beam diameter, laser diameter before focusing and laser beam wavelength. The diameters mentioned here are defined such that the laser beam intensity drops to e^{-2} of the maximum. As is obvious from the equation, the spatial resolution of focused laser beams is M^2 times diameter of diffraction-limited.

2.5.1.4 Laser Sheet Formation

In a typical application such as Planar Laser Induced Fluorescence a laser beam is focused into a thin sheet. There are several methods to realise this sheet formation. One of the most common strategies is conducted with a plano-convex spherical lens and cylindrical telescope. The example is shown in **Fig.11**. The spherical lens is used to focus the laser beam near the centre of the field of view of the camera, and typically has a focal length of 500 to 1000 mm for an increase of the Rayleigh range. The Rayleigh range is the distance along the beam from the focus to the point where the beam diameter is $\sqrt{2}$ times the diameter at the focus. Equivalently, the Rayleigh range is a parameter representing the distance over which the laser beam thickness is essentially the same as the focal point. The cylindrical telescope comprises a plano-convex lens and a larger plano-convex lens. The first lens may be replaced with plano-concave lens to avoid a real focus and consequent air breakdown. The laser sheet height is determined by the height of the second cylindrical lens and then the larger lens, which is expensive, is needed when large laser sheets are created. Thus, the second lens is frequently omitted and allows the divergence of the laser beam in such situations, while the laser intensity profile varies in the propagation direction due to the divergence of the laser beam.

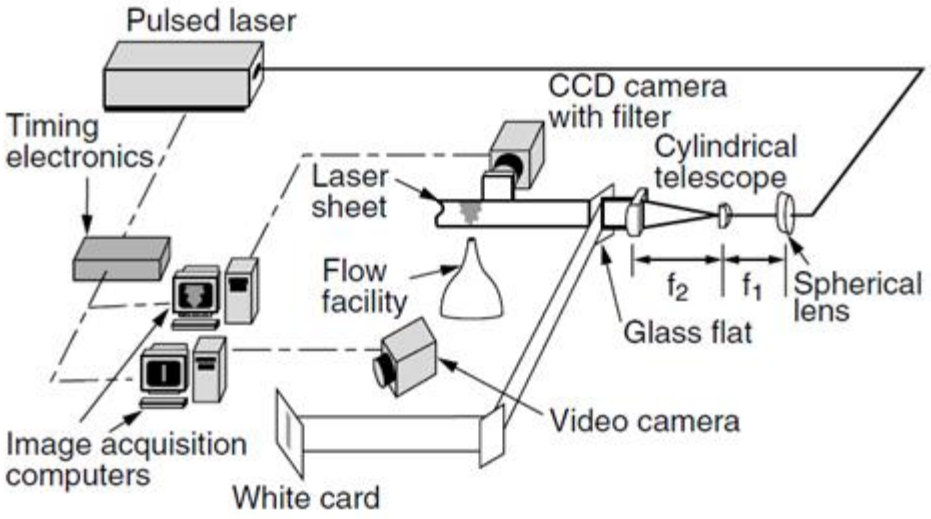

Fig.11. Schematic of typical planar imaging experiments from [102].

2.5.2 Collection Optical System

2.5.2.1 Relation Between Collection Optical System and Signal Intensity

A schematic view of a typical optical collection system is shown in **Fig.12**. The probed volume in flow is illuminated by a laser sheet of height y_L and thickness Δz. The optical system is assumed to be an array sensor, for example, a CCD camera, and a collection lens of focal length f and aperture diameter D. The pixel width and height of the camera are δx and δy respectively. Each pixel images a region in the flow of $\Delta x = \delta x/m$, $\Delta y = \delta y/m$, where m = y_i/y_o is the magnification and y_i and y_o are as defined in **Fig.12**. The obtained signal is spatially integrated in the z direction over a distance of sheet thickness Δz. Now, assuming that a pulsed laser light sheet is illuminated with a local fluence F_L (J/m^2), the number of photons collected by each pixel, S_{pp}, is represented by:

$$S_{pp} = \frac{F_L}{h\nu}\Delta V \frac{d\sigma}{d\Omega} n \Delta\Omega \eta_t \qquad (22)$$

where h is a Planck's constant, ν is a laser frequency, $\Delta V = \Delta x \Delta y \Delta z$ is a volume imaged by each pixel, $d\sigma/d\Omega$ is a differential scattering cross section, n is the number density of the scattering medium, $\Delta\Omega$ is the solid angle subtended by the lens, and η_t is the transmission efficiency of the collection optics (pixel collection efficiency, lens and

spectral filters). The solid angle has a relation with the magnification and *f* number ($f_\# = f/D$) of the lens in the form:

$$\Delta\Omega = \frac{\pi}{4}\frac{m^2}{(f_\#)^2(m+1)^2} \tag{23}$$

Assuming the laser sheet is uniform (i.e., the fluence is constant), the fluence can be approximated as $F_L = E_L/y_L$, where E_L is the laser energy. Now, combining the above two equations and substituting $\Delta x = \delta x/m$ and $\Delta y = \delta y/m$, the S_{pp} is:

$$S_{pp} = \frac{E_L}{h\nu}\frac{\delta x \delta y}{y_L}\frac{d\sigma}{d\Omega}\left(\frac{\pi}{4}\frac{1}{(f_\#)^2(m+1)^2}\right)n\eta_t \tag{24}$$

From this equation, it can be observed that the collected photon number per pixel increases with m and the distance of camera from the object while the solid angle subtended by the collection lens decreases. This is because the Δx and Δy increase with a decrease of the magnification, leading to light collection from a large region of the flow per pixel. In addition, although the laser sheet is assumed to feature the same fluence here, the laser sheet needs to be expanded to cover the larger field of view when moving the camera farther away. In order to consider this effect, equation (24) is converted with the condition of $y_L = y_o$ in the form ($y_L = N_p\delta y/m$):

$$S_{pp} = \frac{E_L}{h\nu}\frac{y_i}{(N_p)^2}\frac{d\sigma}{d\Omega}\left(\frac{\pi}{4}\frac{1}{(f_\#)^2(m+1)^2}\right)n\eta_t \tag{25}$$

where N_p is the number of pixels in one column of the camera. This equation contains much important information for collection optical system design. First, the signal is independent of Δz, which is how tightly the sheet is focused, while the signal increases with the incident laser energy. The independence of the Δz comes from the fact that while the fluence is increased by tighter focusing, the number of molecules scattering incident light is reduced. Second, the signal is weakened as the number of pixels is increased because the scattered lights are collected from the smaller region of the flow. This indicates the importance of physical pixel size in signal to noise ratio (SNR).

However, it is also of considerable importance to remember that as the pixel size increases the spatial resolution is reduced. Equation (25) also shows that the S_{pp} is proportional to $m/(m+1)^2$. This relation of m and S_{pp} is shown in **Fig.13**. It is understood that as the signal reaches maximum value at a unity magnification, the signal level falls off on either side. In addition, the signal intensity is inversely proportional to $f_{\#}^2$. This strong dependence of $f_{\#}$ is the exact reason many applications utilise lenses with low $f_{\#}$ as collection lenses. Generally for PLIF, Rayleigh scattering measurements and Raman scattering in reactive flows lenses with $f_{\#}$ of less than 3 are employed to obtain get sufficient SNRs, whilst for PLIF application $f_{\#}$'s are typically less than 5.

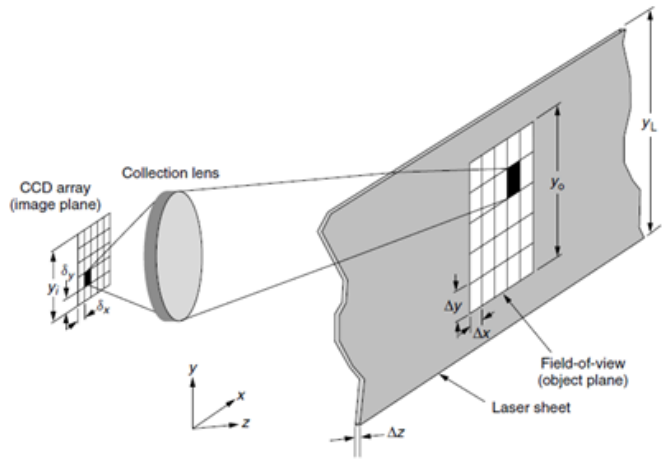

Fig.12. A conceptual sketch of planar laser imaging of a flow field using an array detector, from [102].

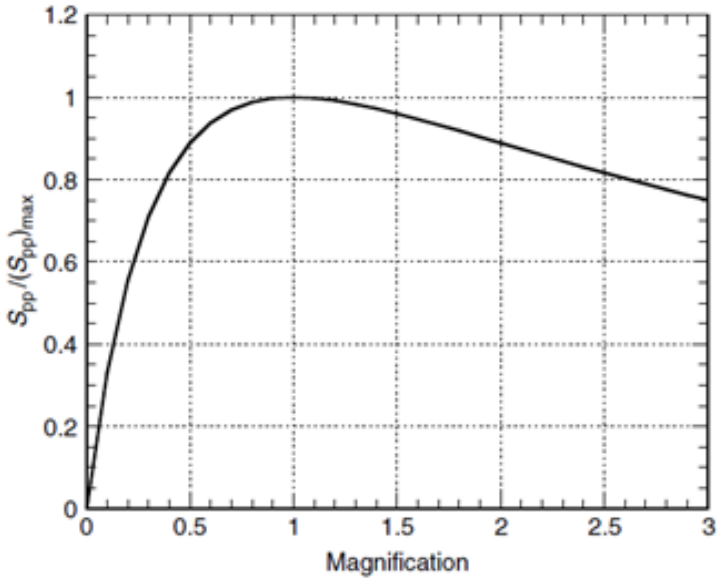

Fig.13. Relative variation of photons per pixel (s_{pp}) versus magnification for a typical planar imaging experiment. The graph is from [102].

2.5.2.2 Spatial Resolution

It is challenging to precisely and accurately quantify spatial resolution in optical collection systems, while knowledge of the spatial resolution is of considerable importance in diagnostics applications. In most cases, the spatial resolution of the collection optics is regarded as the area in the flow that single pixels in camera images or smallest resolvable bar pattern or a resolution target in resolution test chart, as shown in **Fig. 14** (1951 USAF). These methods are sufficient for some diagnostic applications, but may not be adequate for the other experiments, such as a detailed structure study in flame since the thickness of flame is generally sub-millimetre.

One of the more sophisticated methods to evaluate spatial resolution in the system in detail is to measure the size of the so-called ‘blur spot’. The imaging system resolution is dependent on the characteristics of most components in the system: collection lenses, array detectors and illumination sources. For simplicity, the discussion here is limited to the case where the laser sheet is sufficiently thinner than the depth-of-field of the collection optics. In such a situation, the spatial resolution is dependent only on camera specification and the size and shape of the point spread function (PSF). The PSF refers

to the intensity profile at the image plane produced by imaging an infinitesimally small point source of light. The image projected on the image plane is generally considered as the convolution of the PSF with the irradiance distribution of the probed object. The diameter of PSF is called the blur spot. As is obvious, a large blur spot means poor resolution and will deteriorate the measurements. In addition, the PSF will be the Airy disc function in the ideal optical system (the diffraction limit). The study conducted by Clemens et al. is a good example of quantifying the resolution by blur spot [102].

Another possible method to quantify the blurring effect of the optical system is Modulation Transfer Function (MTF). There are not many studies putting the MTF into practice [103-106]. The MTF represents the amplitude response of the imaging system to a sine wave patter. To define the MTF more accurately, let the maximum and minimum irradiance of a sine wave object be R_{0max} and R_{0min}, respectively and the contrast of the object, C_0, be:

$$C_0 = \frac{R_{0max} - R_{0min}}{R_{0max} + R_{0min}}. \tag{26}$$

Also, the contrast of image is denoted by:

$$C_0 = \frac{R_{imax} - R_{imin}}{R_{imax} + R_{imin}} \tag{27}$$

where *i* refers to the image. The MTF with spatial frequency is then defined as

$$MTF(s) = \frac{C_i}{C_o} \tag{28}$$

Thus, the unity MTF means an infinitesimally small resolution in the system. Some studies were already conducted for clarifying the relation between MTF and how accurately the imaging system of interest captures the scalar structure in flow [105, 107].

Fig.14. An example of resolution test chart (1954 USAF). This 1954 USAF was set by US Air Force.

2.5.3 Image Arrays

2.5.3.1 CCD Cameras and ICCD Cameras

CCD array and image-intensified CCD (ICCD) array are some of the most frequently used image detectors for scientific purposes. There have been significant advances over the last few decades in CCD camera technologies, leading to uniform pixel response in cameras with almost negligible non-linearity. CMOS based camera technologies have also been advanced and the frame speed as well as the low cost of CMOS cameras are quite attractive. However, CMOS cameras still struggle with the problem of non-linear responses for each pixel, which makes quantitative measurements difficult and thus, CCD cameras are still a major tool in scientific imaging. In the following, CCD and ICCD cameras are explored briefly.

A CCD camera consists of a photodiode unit, transfer unit and amplification unit. Initially, a photodiode unit detects photons and converts the photons to charge (electrons). These electrons are transferred to an amplification unit by a transfer unit. In the amplification unit, the charge is converted to a voltage signal. The CCD array can be categorised into two illumination types: front and back illumination. The quantum efficiency, which is a ratio between the number of the photoelectrons created and incident photons, is different between these two illumination schemes. Front illuminated CCD array generally has relatively lower quantum efficiency of 10–50% at visible and near-IR wavelengths, and virtually zero at UV and mid-IR wavelength. On the other hand, back illuminated CCD array possesses higher efficiency of around 90% in the visible wavelengths and 20% at the UV wavelengths, although back illuminated

CCD arrays are typically more expensive and typically cannot be electrically gated or shuttered at the same speed as front illuminated detectors..

ICCD cameras are employed often for very short exposure time measurements (a few nanoseconds), such as for diagnostics with low signal light level s with high continuous background light levels. A common image intensifier consists of a photocathode, a micro-channel plate, a phosphor screen, and a mechanism to couple the screen to the CCD. An image intensifier also has a gating function, which is useful to suppress background luminosity in very luminous flows, such as sooting flames. Since scattering phenomena generally takes place during the order of several nanoseconds for typical Nd:YAG nanosecond excitation, a short duration gating enables reduction of the background signal at no expense of interested signals. It is noted that intensification in ICCD cameras does not reduce shot noise but rather intensification reduces the proportion of dark noise and readout noise to the resultant signals by amplifying the incident signals. Since intensification reduces the proportion of the readout noise and dark noise to the resultant signals, the primary noise source is typically a combination of shot noise and electron multiplication noise in sufficiently amplified signals.

2.5.3.2 Software Binning and Hardware Binning

CCD cameras generally have two types of binning methods: a hardware binning and software binning. Hardware binning is a scheme in which electrons stored in each pixel are summed up with a specified size before an amplifier section reads the electrons. Due to the pre-process in each pixel, the number of readings is reduced with the degree being proportional to a specified binning size. Consequently, the total readout noise is smaller than no binning imaging in principle. At the other extreme, software binning scheme sums up electrons over a specified size after an amplifier section reads the electrons. As is obvious from the procedure of software binning, a software binning requires reading processes every single pixel. Hence, there is no difference in the total readout noise in one frame between in presence and absence of a software binning, but rather the signal level is increased as well as the readout noise in the new software binned super-pixel which generally results in an increased SNR but not as large an increase as hardware binning.

2.5.3.3 Photo Transfer Curves

Consider a situation in which a detector detects sufficiently large number of photons to readout noise and dark current noise, for example, where photon shot noise dominates detector noise. Based on this assumption and the fact that photon shot noise obeys the Poisson distribution, the conversion gain g can be determined in the following way.

The gain g is a constant for conversion of camera output signals (ADU) to actual physical numbers of electrons (e^{-1}) generated by incident photons interacting with CCD array. It has a unit of electrons per ADU (e^{-1}/ADU) and is defined by:

$$\eta\Phi = gS \tag{29}$$

where η is a quantum efficiency (photoelectrons per unit incident photon), Φ is a number of incident photons during camera exposure period, S is a camera output digital signal. Since $\eta\Phi$ is directly proportional to S, their errors are also directly proportional by the same constant and thus:

$$\sigma_{\eta\Phi} = g\sigma_S \tag{30}$$

where $\sigma_{\eta\Phi}$ and σ_s is a standard deviation of $\eta\Phi$ and S respectively. For a Poisson distribution, standard deviation is simply the square root of the mean and thus:

$$\sigma_{\eta\Phi} = (\overline{\eta\Phi})^{1/2}.$$

Substitute this to (30):

$$(\overline{\eta\Phi})^{1/2} = g\sigma_S$$

Using equation (29):

$$(\overline{gS})^{1/2} = g\sigma_S$$

and thus:

$$g = \frac{\bar{S}}{\sigma_S^2} \tag{31}$$

As is understood from the equation (31), the g appears as a gradient in a graph of mean v. variance of output signals. The graph is referred to as photon transfer curve. The gain of the cameras used in the present study was also measured using the relation of the equation (31). The result and measurement system is shown in Appendix 5.

2.5.4 Laser Pulse Stretchers

Pulse durations of laser beam are determined predominantly by the duration of effective pumping, intra-resonator energy extraction rates in the laser unit. Despite its fixed characteristic value of pulse duration in laser systems, there are many applications that require a temporal extension of the laser pulse duration for a reduction of the instantaneous beam intensity at no expense of total pulse energy. Spontaneous Raman scattering spectroscopy is such an exact example. The Raman scattering cross sections of combustion relevant species are relatively small and thus a high energy input is required at a probed volume to obtain reasonable SNRs. However, once the large energy laser inputs are realised in the measurement system, the strong optical emission from the plasma spark overwhelms the weak Raman signal and disturbs chemical reactions at the probed volume. In this context, a laser pulse stretcher is needed in Raman spectroscopy to avoid gas breakdown. There are several methods to temporally stretch laser pulses, such as optical pulse stretching, pulse stretching by intra-cavity non-linear materials, electronic pulse stretching and pulse stretching by dispersion. Due to its high frequency of use and easiness to implement, optical pulse stretching method is focussed upon here.

Optical pulse stretching is normally achieved by a combination of beam splitters and mirrors. The most basic geometry is a ring cavity, which is reported by Kojima [108]. The schematic view is shown in **Fig.15**. The ring cavity traps and stores a portion of the laser pulse and the pulse leaks slightly every single leg. As a consequence, the output beam from laser pulse stretcher is temporally stretched and reduced in maximum intensity. The parameters that determine the output temporal beam profiles are a reflectivity (R_{bs}) of beam splitter in the cavity and an optical delay time (τ), that is, a period of time for one leg, which is controlled by the optical propagation path length L in the cavity. The output laser beam, $D(t)$, is mathematically represented by:

$$D(t) = R_{bs}Q(t) + (1-R_{bs})^2\,Q(t-\tau) + (1-R_{bs})^2\,R_{bs}Q(t-2\tau) + \cdots + (1-R_{bs})^2\,R_{bs}^{n-1}Q(t-n\tau) + \cdots \quad (32)$$

where t is time evolution since an entry of laser pulse to the cavity and $Q(t)$ is the original laser pulse from laser unit. In this laser pulse stretcher, there is a reduction limit of laser pulse per cavity. To show the maximum reduction ratio in single cavity, the

initial term and second term in equation (32) are plotted as a function of R_{bs}. The objective of using a laser pulse stretcher is to decrease maximum laser intensity. Keeping this in mind, please see **Fig.16**. While the first term is decreased as R_{bs} is decreased from unity, the second term is increased. However, the trend is opposite from 0.38 ($\cong (3-\sqrt{5})/2$) onwards. Consequently, it is understood that the maximum reduction ratio by single-ring cavity is 0.38.

For reference, the output signals with the R_{bs} = 0.3, 0.38 and 0.45 are also show in **Fig.17, 18** and **19**, assuming the temporal and spatial profile of the original laser pulse is Gaussian with total energy of 1.0 J, temporal full width at half maximum (FWHM) of 8 ns and spatial FWHM of 7 mm. Due to the 38% reduction limit per cavity, the multiple cavities are normally required in Raman spectroscopy. In the basic method to determine each optical delay time in cavities, the optical delay times of each cavity set to be $\tau_1=dt$, $\tau_2 = 2\tau_1$, $\tau_3 = 4\tau_1\ldots$, and $\tau_n=2^{n-1}\tau_1$, where subscript *n* represents *n-th* cavity and *dt* represents temporal FWHM of original laser pulse. The doubling of the optical delay time every ring cavity is necessary for a suppression of each pulse overlapping.

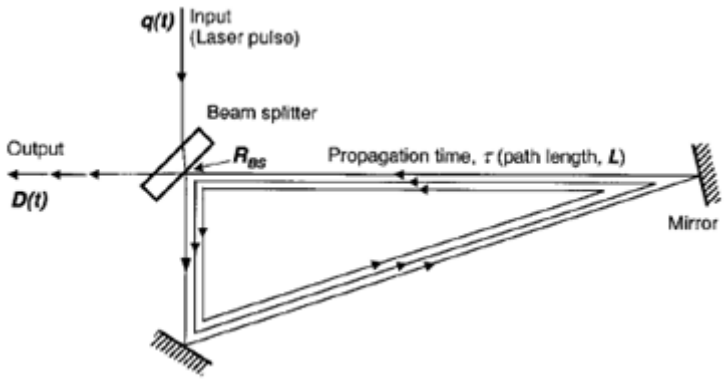

Fig.15. Schematic of the basic right-triangle ring cavity used as a pulse stretcher. The input laser pulse is divided into multiple smaller output pulses that are extracted through a partially transmitting beam splitter.

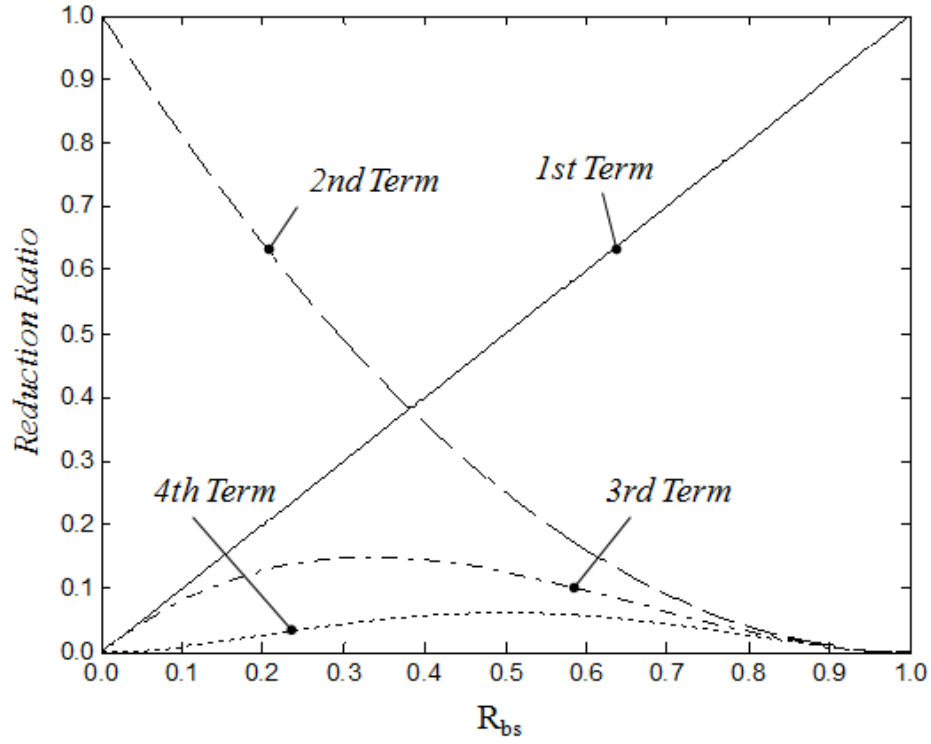

Fig.16. The reduction ratio of each term in equation (32).

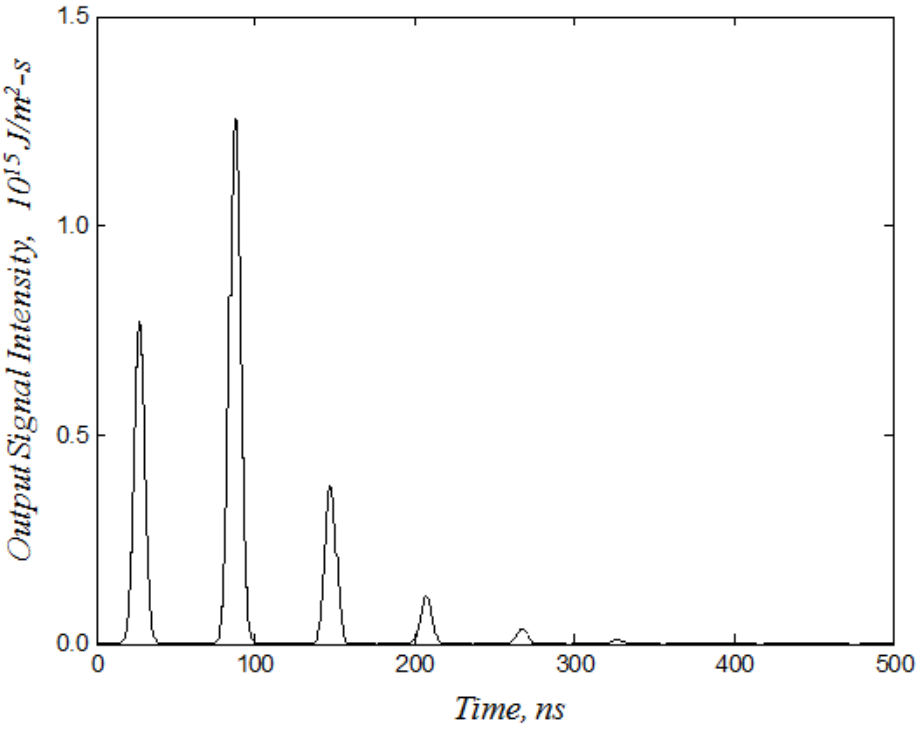

Fig.17. Temporal Profile after laser pulse stretcher with R_{bs} of 0.30 at a centre of the beam.

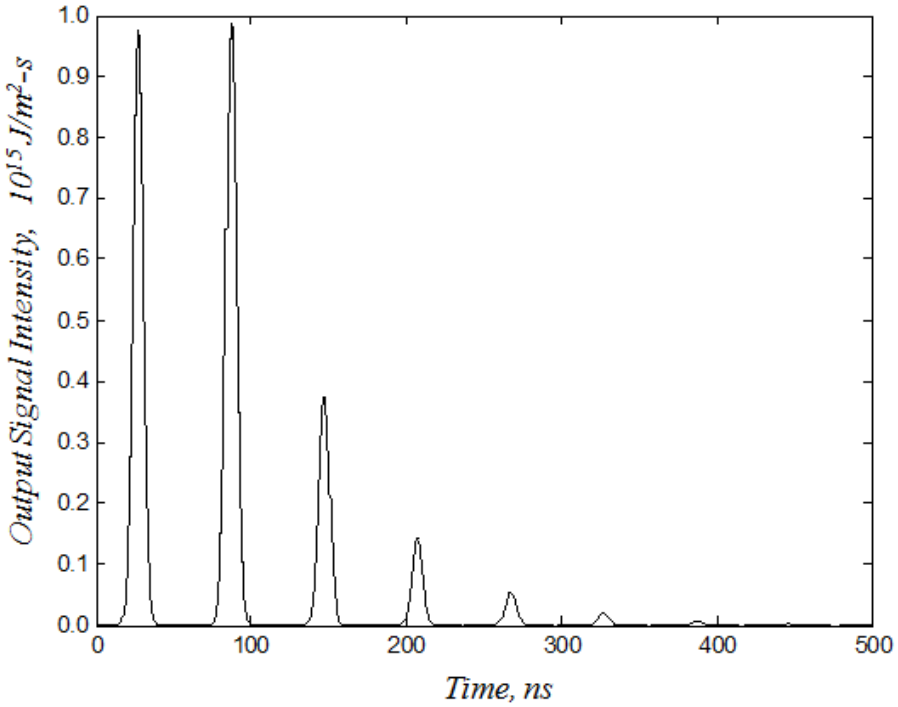

Fig.18. Temporal profile after laser pulse stretcher with R_{bs} of 0.38 at a centre of the beam.

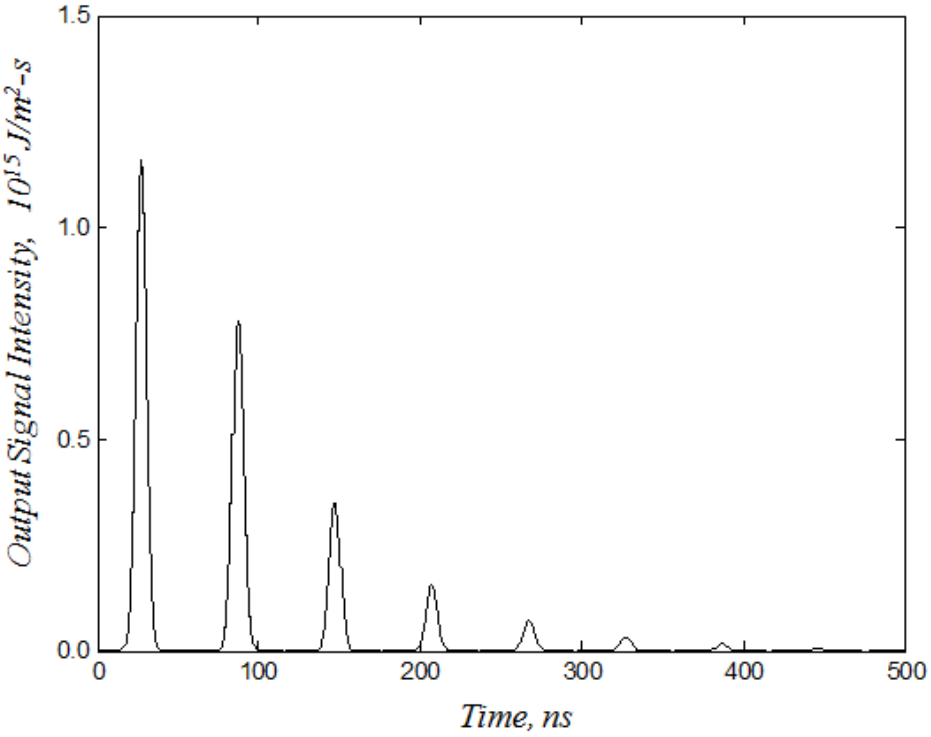

Fig.19. Temporal profile after laser pulse stretcher with R_{bs} of 0.45 at a centre of the beam.

Chapter 3
Methodology

This chapter provides information on the software, apparatus and techniques used in the present simulations and experiments. In addition, the definitions of some characteristic parameters used in the following chapter are detailed here.

3.1 Simulations

CANTERA 2.0 [109] was employed for zero and one-dimensional reactors and CHEMKIN PRO [110] was utilised for counter-flow diffusion flame. CANTERA 2.0 [109] is a free software and thus the all simulations were initially implemented with CANTERA 2.0 [109]. However, CANTERA 2.0 [109] shows some bugs and errors with Soret effect being activated. Due to the bug, CHEMKIN PRO [110] was used for solving counter-flow diffusion flame rather than CANTERA2.0 [109]. In all simulations in this study, CH_4 was used as the fuel.

Counter-flow diffusion flames needs appropriate tolerance and grid quality for high quality results. Also, the separation distance in counter-flow configuration (distance between opposed nozzles) also must be set reasonably. The determination procedures of these parameters are explored in the following. In addition, the post-processing scheme to calculate heat release in both constant pressure adiabatic flame temperature and opposed-flow diffusion flame are also explored. Further, normalised equivalence ratio, mixture fraction, normalised mixture fraction and strain rate are defined here as well.

3.1.1 Tolerance and Mesh Quality for Simulation

CHEMKIN [110] uses TWOPNT program [111] for finding steady state solutions from a set of governing differential equations. The TWOPNT [111] allows users to specify the relative tolerance and absolute tolerance. These tolerance values determine the quality of the results. As these tolerances get smaller, the quality of the result is enhanced and the necessary computational time is increased. As such, it is required to find a good trade-off point with the solution being insensitive to these tolerance values

as well as the computation time being acceptable. To seek this trade-off point, the counter-flow air-methane flame simulation was conducted with different sets of the tolerance values at 200s-1. Based on this result, the relative and absolute tolerances were set to be 1.0×10^{-5} and 1.0×10^{-9} respectively in this study.

In CHEMKIN [110], the grid properties are determined by initial grid number, adaptive gradient and curvature. In simulation, the grid is initially distributed evenly with the grid number being the specified value. Using this grid, rough solution of the simulation is obtained. After this the grid, it is refined only where the significant variation of temperature and composition is observed in the rough solution, such as in the precinct region of flame. The finesse in the refining process depends on the user-specified adaptive gradient and curvature. The final solution with the refine grid is computed using the previously obtained rough solution as an initial guess. The initial grid number determines only the maximum spatial grid length. On a basis of this fact, the initial grid was determined so that the maximum initial spatial grid length was 0.05 mm, which is reasonably small. Utilising this value as an initial grid number, the opposed-flow simulation with air mode was implemented at 400 s^{-1}, varying the adaptive gradient and curvature values. As the strain rate is increased, the necessary grid quality is higher and hence the relatively higher strain rate was chosen here. From this result, the curvature and gradient was set to be 0.2 and 0.02 respectively in this study.

3.1.2 Separation Distance in Opposed-flow Flame Simulation

For opposed-flow flame simulations, additional care must be taken on separation distance. If the separation distance between opposing nozzles is too small, the resultant flame structure can be narrower, irrespective of strain rates due to the too-close proximity of flame to stagnation plane in space. Therefore, the sensitivity of the solution to separation distance was examined with air-fuel mode, and 71% CO_2 contained oxy-fuel mode (by volume) at 15 s^{-1}. The relatively low strain rate was chosen here since flame thickness is wider with a decrease of strain rate. Based on this sensitivity analysis, the separation distance was set to be 20 mm.

3.1.3 The Method for Obtaining Heat Release and Cp

In constant pressure adiabatic equilibrium calculation, the enthalpy gap between products and reactants at an initial temperature (300 K) represents heat release of the combustion, q_p. The specific heat capacities of products at initial temperature and adiabatic flame temperature are averaged over and the result was used as representative C_p. The procedure is summarised in **Fig.20 (a)**. The calculation fashion to get q_p and C_p at each mixture fraction in counter-flow flame is summarised in **Fig.20 (b)**. In contrast with adiabatic flame calculation, external thermal energy input via diffusion/convection and conduction are present, and thus the external energy input needs to be added to the heat of reaction. The specific heat capacities of products at initial temperature and resultant temperature are averaged over at individual mixture fraction, and the result was used as representative C_p.

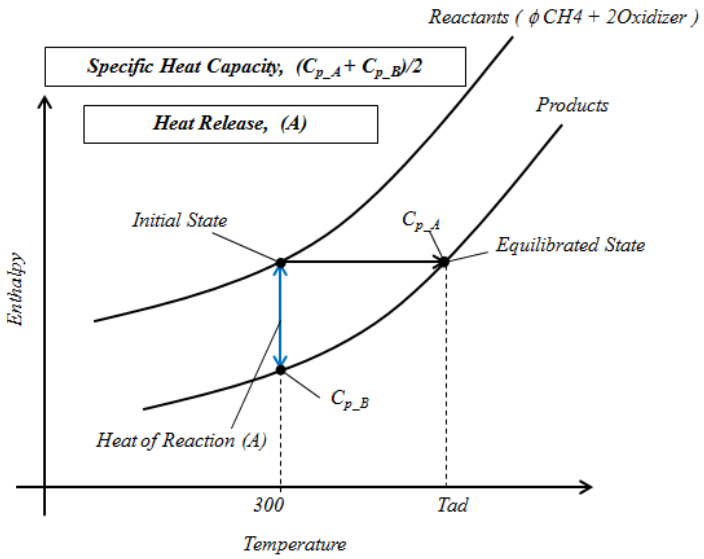

(a)

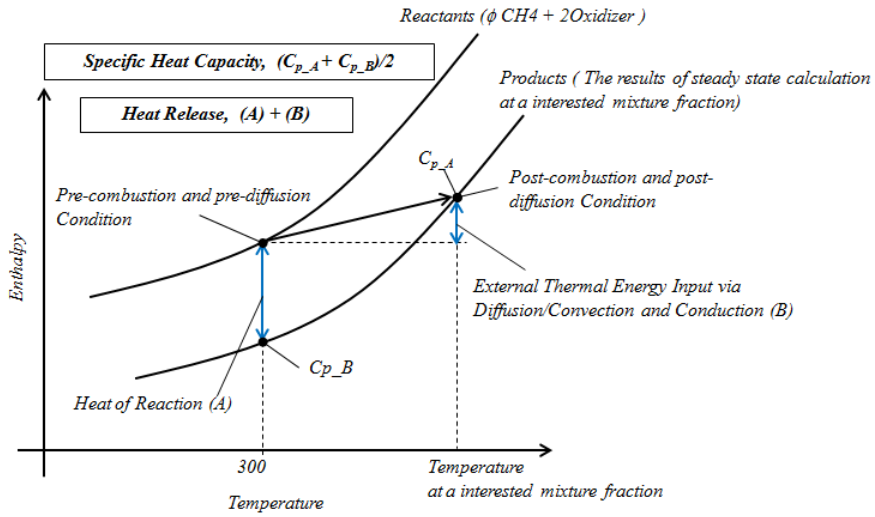

(b)

Fig.20. The summary of determination of qp and Cp from the results of equilibrium calculation. (b) The summary of determination of qp and Cp from the counter-flow flame simulation.

3.1.4 Normalised Equivalence Ratio

Normalised equivalence ratio, ϕ_n, was used to evaluate thermo-chemical structures in chapter 4. The normalised equivalence ratio ϕ_n is defined by:

$$\phi_n = \frac{\phi}{1+\phi}. \tag{33}$$

This normalised equivalence ratio spans from 0 to 0.5 for lean condition and from 0.5 to unity for rich condition. In other words, the normalised equivalence ratio can suppress an asymmetrical nature of the definition of ϕ in that lean combustion is represented from 0 to 1, but rich combustion from one to infinity. Since the present research is one of the structural studies, it is preferable to remove the definition-based asymmetric feature in evaluation processes. However, as equivalence ratio ϕ is a much more frequently used definition, the ϕ was also used as necessary.

3.1.5 Mixture Fraction and Normalised Mixture Fraction

In laminar flame analysis, mixture fraction defined by equation (15) and normalised mixture fraction was used to evaluate the thermal structure. The normalised mixture fraction is defined as a form:

$$\xi_n = \begin{cases} \dfrac{0.5}{\xi_{st}+1}(\xi+1) & \xi \le \xi_{st} \\ \dfrac{0.5}{1-\xi_{st}}(\xi-\xi_{st})+0.5 & \xi > \xi_{st} \end{cases} \quad (34)$$

By this definition, stoichiometric mixture condition refers to 0.5 no matter what diluting species and diluting degree is. Also, this normalisation suppresses an asymmetric nature driven by the fact that stoichiometric mixture fraction is generally quite close to 0.

3.1.6 Strain Rates

The formulation of the equation (9) in the background chapter was used for strain rate.

3.2 Experiments

In the present study, OH LIF thermometry is applied to CO_2 diluted oxy-fuel combustion. This section provides the theory of the OH LIF thermometry and the detailed information on a setup of the experiments. In addition, the counter-flow burner and laser pulse stretcher designed in this master study are also explored in this section.

3.2.1 Theory of OH Thermometry

3.2.1.1 Principle of Fluorescence

A simple two energy level diagram for LIF modelling is shown in **Fig.21**. Excited molecules emit light as induced emission, spontaneous emission or quench, going down to ground state. Using the two energy model, the fluorescence signal intensity, S_{FL}, by incident laser irradiance, I_1,is expressed in the form:

$$S_{FL} = \frac{A\ B\ I_1\ N_1}{c\ (A + Q) + 2B\ I_1} \tag{35}$$

where *A*, *B*, N_1, *c* and *Q* is an Einstein A coefficient, an Einstein B coefficient, the number of molecules at ground state, the speed of light and quenching rate constant respectively. Assuming incident laser power is sufficiently weak, the induced light emission can be ignored and then the above equation can be converted to:

$$S_{FL} = \frac{A\ B\ I_1\ N_1}{c\ (A + Q)}. \tag{36}$$

As is obvious from this expression, the fluorescence signal intensity is proportional to the incident laser irradiance. This equation can also be converted to the more practical form:

$$S_{FL} = \eta \frac{\Omega}{4\pi} \cdot F_y \cdot f_B V_c N_1 \cdot \int_{\omega} I_1(\omega) g(\omega) d\omega \cdot \tau \tag{37}$$

where η is an efficiency of collection system, Ω is solid angle, F_y is a quantum yield, f_B is Boltzmann's probability density function, V_c is probed volume, $g(\omega)$ is spectral line width and τ is illumination duration of laser. As with research by Sakiyama et al. [112], the quantum yield is here calculated from the following equation, derived from the experimental results by Hanson et al. [87, 113]:

$$F_y = (7 \pm 1.5) \times 10^{-4} \cdot \frac{1}{P} \tag{38}$$

where *P* is pressure. Also, the number density holds the relation:

$$N_1 = n_1 \frac{P}{kT} \tag{39}$$

where n_1 is mole fraction of OH and k is Boltzmann constant. Substituting equation (38) and (39) to (37), the following relation is obtained:

$$S_{FL} = const \cdot \int_{\omega} I_1(\omega) g(\omega) d\omega \cdot n_1 \frac{f_B(T)}{T}. \quad (40)$$

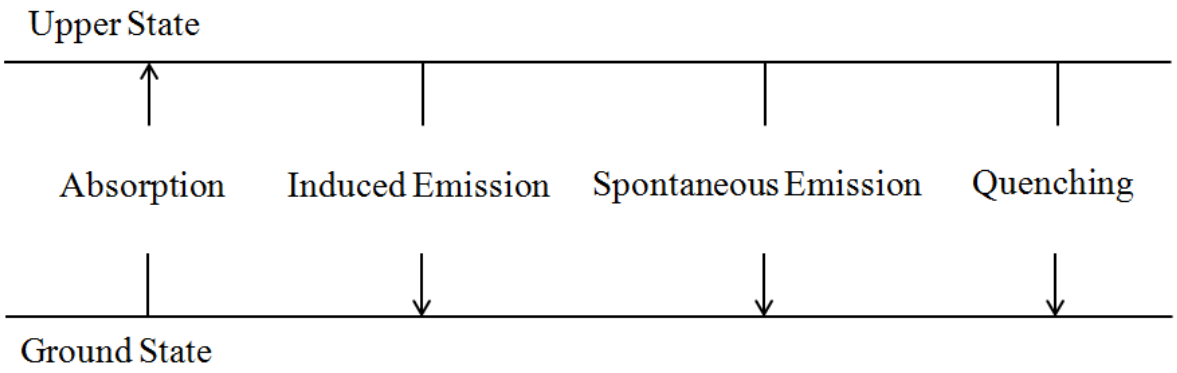

Fig.21. Simple two energy level diagram for LIF modelling.

The transition band of $X^2\Pi$ and $A^2\Sigma^+$ of OH with (1, 0), which is used in the present experiment, is explored more specifically next. In molecules situated electronically and vibrationally at ground state being illuminated, the electronic and vibrational states of the molecules are excited. The excited molecules can change rotational energy level due to collision of other molecules, so-called excitation transfer (ET) in **Fig.22**. After the ET, a portion of the molecules emits light (A11 in **Fig.22**) or quenches (Q1 in **Fig.22**), going down to the ground state. The other is vibrationally de-excited (V in **Fig.22**) and then emits light (A00 in **Fig.22**) or quenches (Q0 in **Fig.22**).

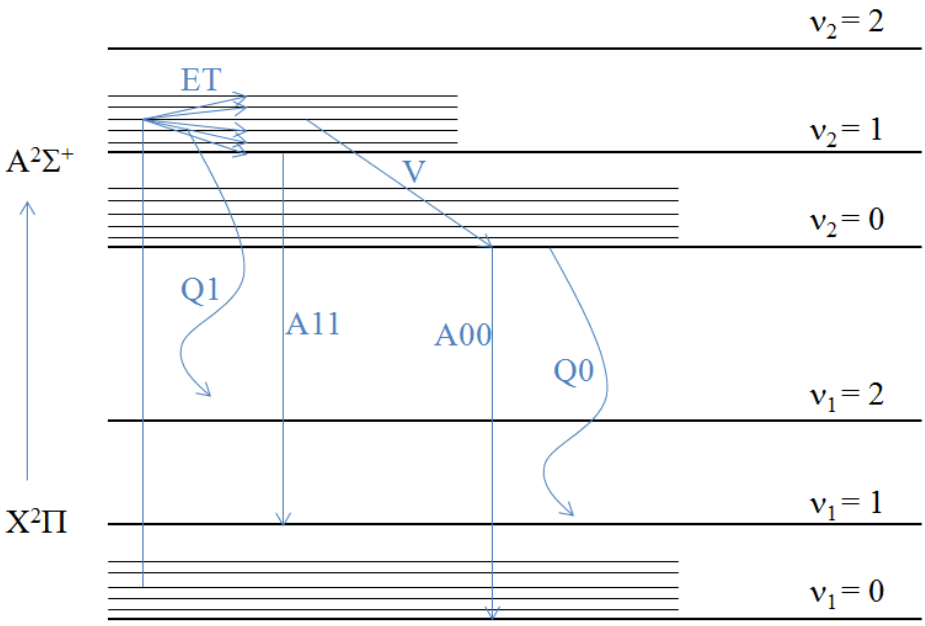

Fig.22. Schematic of transition of $X^2\Pi$ and $A^2\Sigma^+$ of OH with (1, 0).

3.2.1.2 LIFBASE

Theoretical OH excitation spectra of $X^2\Pi$ - $A^2\Sigma^+$ (1, 0) were simulated by LIFBASE version 2.1.1 [114]. All simulation was conducted assuming linear fluorescence regime and thermalised system. In the LIFBASE [114], individual lines of OH are described by a Voigt profile. This Voigt profile arises from the convolution of the Gaussian line shape, led by Doppler broadening and the Lorentzian line shape induced by intermolecular collisions. While the Doppler broadening is dependent on the temperature and can be calculated relatively straightforwardly, the collisional broadening depends on temperature, pressure, composition (collisional partner) as well. That is, the evaluation of the Lorentzian component is more complex. Due to its complexity of predicting exact collisional linewidth, LIFBASE [114] calculates the collisional broadening effect by the following empirical formula:

$$\Delta\nu_{FWHM} = a \times P \times \left(\frac{300}{T}\right)^{b} \tag{41}$$

where T and P is temperature and pressure of environment. The a and b is collisional broadening coefficient. The appropriate values of coefficient a and b alter with composition of interest and the rotational quantum number. The coefficient a and b is of interest in this study. Also, in order to simulate the spectral profile, the instrumental function must be set appropriately. In the LIFBASE [114], the spectral linewidth and Lorentzian of incident laser are prepared as the instrumental function setting parameter.

3.2.1.3 Thermometry

In the present study, three types of OH LIF thermometry are applied to air and CO_2 diluted combustion: spectral fitting, two-line and two-region techniques. The theory and procedure of each technique is summarised briefly in the following.

(a) Spectral Fitting Techniques

The spectral fitting method is based on an excitation scan of laser wavelength over a number of lines and thus the spectral profile at probed volume can be obtained as a result of measurements. The spectral profile is dependent on temperature as is

understood from equation (40). To obtain the temperature at probed volume, the experimental spectral profile is overlayed on theoretical profiles and seeks the temperature that provides the best agreement. For reference, a portion of the theoretical spectral profile in the rotational manifold of the OH $X^2\Pi$-$A^2\Sigma^+$ (1, 0) transition is shown at 2,000 K in **Fig.23**. The theoretical profile was obtained by LIFBASE.

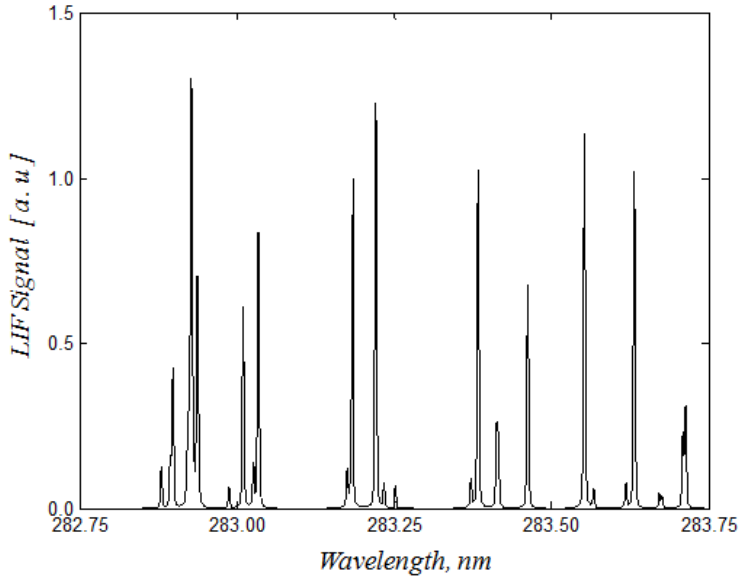

Fig.23. Theoretical spectral profile in the rotational manifold of the OH $X^2\Pi$-$A^2\Sigma^+$ (1, 0) transition at 2,000 K.

In the fitting process, special care must be taken to determine the scaling factor, wavelength adjustment and baseline correction. The scaling factor here is a multiplier to multiply the signal obtained by simulation in the fitting process. The quantity obtained through cameras in the experiment itself, does not represent any physical meanings although the relative intensity of the signal at each wavelength is substantial. Hence, the scaling factor is required and one of the key parameters to seek the best spectral profile. The line position displacement, the wavelength adjustment, is a gap between the wavelength of each signal peak obtained by actual measurement and by simulation. Even if absolute calibration of wavelength of dye laser is conducted with a wavemeter, there is generally still gap in line position between experimental results and simulated datasets. Hence, correct line position must be established by translating the obtained profile before fitting processes for seeking appropriate temperature.

The baseline correction is a zero adjustment between theoretical and experimental data. Even if the background signal is subtracted from the signal, there can be still some signal intensity at wavelength that does not possess any OH LIF lines. This baseline disturbance arises from elastic scattering processes from surface or soot and LIF interference from other species. The baseline correction modifies this baseline difference and makes the measurement system robust. In successfully extracting strong signals from environments of interest, the baseline correction does not affect the result significantly. However, when the signal is relatively weak the baseline correction can affect the consequent result and then is required. The deviation of experimental data from the simulated dataset was evaluated using the following term, and equivalently the best-fitting profile represents the temperature at which the following term hits a minimum (least square method):

$$Dev = \sum_{i=1}^{N} (Pro_{th}(\lambda_i) - (LIF\ signal\ at\ \lambda_i)^2 \tag{42}$$

where Pro_{th} is a theoretical profile and LIF signal at λ_i is an experimental result after multiplication by scaling factor, wavelength translation, and baseline correction. The N is the number of wavelengths monitored in the experiment and λ_i is *i-th* wavelength monitored in the experiment.

(b) Two-line Peak Techniques

In two-line techniques, OH LIF signals are obtained at two-line positions and take a ratio between the two signals. Since the ratio is dependent only on temperature, the temperature at probed volume can be obtained. Using equation (40), the ratio of OH signals with two different excitation wavelengths, *R*, is represented in the form:

$$R \equiv \frac{S_{FL1}}{S_{FL2}} = \frac{\int_\omega I_1(\omega) g_1(\omega) d\omega \cdot f_{B1}(T)}{\int_\omega I_2(\omega) g_2(\omega) d\omega \cdot f_{B2}(T)} \tag{43}$$

Assuming the spectral line width of incident laser is the same as each other:

$$R = \frac{E_1 B_1 f_{B1}(T)}{E_2 B_2 f_{B2}(T)} \tag{44}$$

where E is laser energy per unit area. The Boltzmann distribution function of OH at rotational energy level, J, is represented by:

$$f_B(T) = \frac{2J" + 1}{Z_p} exp(-\frac{E_J}{kT}) \tag{45}$$

where Z_p is partition function, $J"$ is rotational quantum number at ground level and E_J is rotational energy. Substituting the (45) to (44):

$$R = \frac{E_1 B_1}{E_2 B_2} \cdot \frac{2J_1" + 1}{2J_2" + 1} \cdot \exp(\frac{\Delta\epsilon}{kT}) \tag{46}$$

where $\Delta\epsilon$ is the difference in energy between two absorbing states. When excitation wavelengths are chosen, the B and J can be obtained. From the equation, it can be understood that the ratio is dependent only on temperature and then it is possible to obtain temperature by taking the ratio of experimental results and comparing it with theoretical values.

(c) Two-line Area Techniques

The two-line area technique is one developed from the two-line peak techniques. In two-line area techniques, the excitation scans of laser wavelength are implemented over two regions of interest, and each signal is spectrally integrated over the individual region. The ratio of the integrated values at each region is dependent on temperature due to the same reason as two-line techniques. One of the most significant advantages of this method is to enable one to ignore the effect of the broadening phenomenon. The phenomenon of collisional broadening in oxy-fuel combustion environments is unclear thus far. Hence, this technique is of significant assistance to extract the thermal structure of oxy-fuel combustion with high precision. The conceptual idea of the two-region techniques is summarised in **Fig.24**.

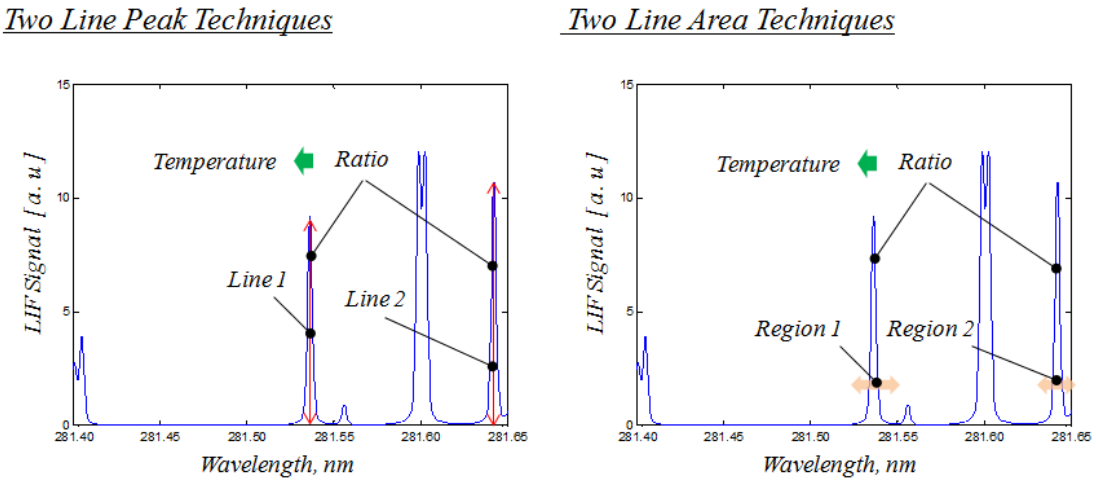

Fig.24. Conceptual idea of two-region techniques, comparing it with two-line techniques. The two-line system takes a ratio of line 1 and line 2 in magnitude and the two-region method take a ratio of values integrated over region 1 and region 2 respectively.

3.2.2 Hardware Setup

Fig.25 illustrates the experimental arrangement used for OH LIF thermometry. In this measurement, a planar sheet of the pulsed laser beam from a dye laser was formed to induce fluorescence from OH in flames. The flames employed in this experiment are Bunsen flame and opposed-flow diffusion flame. The resulting fluorescence from the plane of illumination was recorded with CCD image array attached with an intensifier, filtering flame luminescence with two filters. The intensifier was used for improvement of S/N and the conversion of UV signal to visible light, since the camera cannot detect UV signals. The signal obtained by CCD camera was sent to the computer and the data process was conducted with software, DaVis.7.2 and MATLAB 2011. The laser was tuned to different OH transitions and fires sequentially to separate the fluorescent signals temporally. The synchronisation of hardware was conducted by two pulse generators.

The dye laser was pumped by laser light of 532 nm produced by frequency-doubled Nd:YAG laser, and the output light from the dye laser was frequency-doubled by a frequency conversion unit (FCU) to produce UV light. The pulse energy of the pumping Nd:YAG laser was controlled via Q-switch delay time so that the laser energy of single

pulse at probed volume was 0.74 mJ for Bunsen air flame and 0.29 mJ for counter-flow diffusion flame with CO_2 dilution. The excitation wavelength was 281.9114 – 281.9291 ($Q_1(1)$), 283.3694nm – 283.3956 nm ($Q_2(6)$) and 284.7715nm – 284.7880 nm ($Q_1(11)$) in the experiment. The output beam diameter from the dye laser was approximately 10 mm. The laser sheet was formed by focusing down the laser beam from dye laser horizontally, using a plano-convex cylindrical lens with focal length of 750 mm. The consequent width and thickness of the formed laser sheet was 11.2 and 0.53 mm at probed volume respectively. The collection lens used in the experiment is one with the $f_{\#}$ of 4.5 and focal length of 105 mm.

To correct shot-to-shot variations of laser power, a small fraction (17%) of laser beam was split by a beam splitter and monitored by a CCD camera. In addition, LED was placed between the collection lens and intensifier in order to correct intensifier gain fluctuation shot-to-shot. For reference, an averaged image monitored by a CCD camera is shown in **Fig.26**.

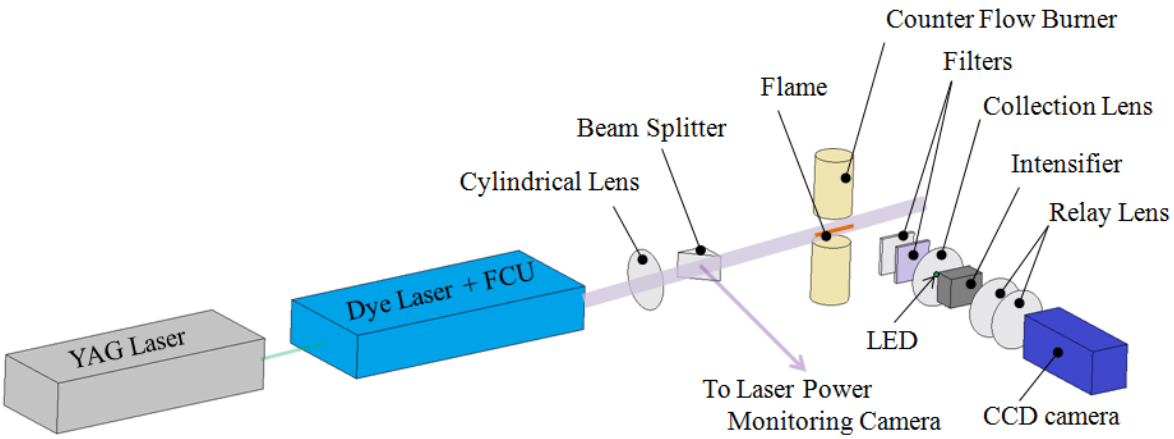

Fig.25. Schematic of OH LIF thermometry. FCU: Frequency Conversion Unit (the output beam from dye laser is frequency-doubled here).

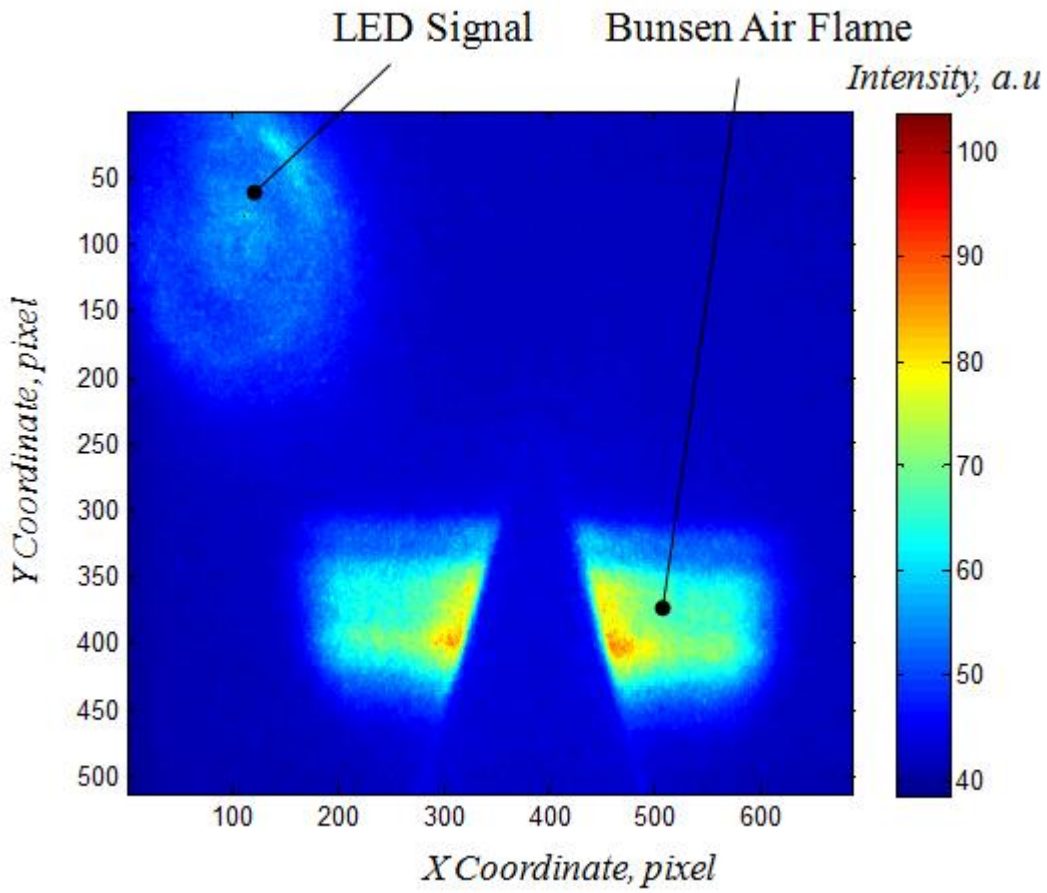

Fig.26. Example of image monitored by CCD camera (LIF).

3.2.2.1 Dye Laser

A Sirah dye laser was used to produce laser pulses with the desired wavelength. The desired wavelength scope in the present paper is 281.9114 – 281.9291 ($Q_1(1)$), 283.3694nm – 283.3956 nm ($Q_2(6)$) and 284.7715nm – 284.7880 nm ($Q_1(11)$). To realise these wavelengths, the dye laser was pumped by 532 nm laser pulse, the output light from the dye laser was frequency-doubled by a FCU and Rhodamine was employed as a laser medium.

The used dye laser possesses capacity to scan. That is, to tune the output wavelength in a well-defined way from an initial to a final value sequentially. The Sirah dye laser has two types of scan modes: constant speed scan and triggered scan. In the experiment, the triggered scan mode was applied. In the triggered scan mode, the system of the laser waits at a fixed spectral position, until a certain number of trigger events have been

counted, before proceeding to next wavelength. The user must set four parameters to use the scan mode: initial wavelength, end wavelength, increment of wavelength, and the number of trigger counts to wait. A more detailed procedure is the following. The laser is initially moved to the specified initial wavelength. When this position is reached, the laser sets the 'Trigger Out' signal to high and begins to count signals arriving at 'Trigger In' port. When the specified number of triggers at the 'Trigger In' port are measured, the 'Trigger Out' signal is set to low and the laser is moved to the next wavelength with specified increment.

3.2.2.2 Nd:YAG Laser

To pump dye laser, 'Quanta-Ray Pro Series Pulsed Nd:YAG Lasers (Model 350)' was used. This Nd:YAG laser was operated with second harmonic generation to produce a 532 nm laser beam. Also, Q-switching was also employed for high quality laser pulse. The specifications are shown in Table 1. The values of the maximum output energy and temporal pulse width at 532 nm were measured in the laboratory. The power control of the Nd:YAG laser was conducted via Q-switching delay time variation. The calibration curve is shown in Appendix 2.

Table 1: Specification of Nd:YAG Laser.

Repetition Rate Hz	Maximum Energy at 532 nm J	Temporal Pulse Width at 532 nm ns
10	1.27	10

3.2.2.3 Cameras

Two 'image intense' from DaVis were used as image arrays in the present study. The photo transfer curve of image intense employed in this study was measured and the result is shown in Appendix 3. The frame size of the image intense is 1376 × 1040, with the pixel size of 6.45 μm × 6.45 μm. Both cameras for LIF signal and laser power monitoring were employed with 2 × 2 hardware binning through the experiment. The

exposure time for the cameras for OH LIF signal was set to be 1 ms, since the intensification process by the intensifier used in this study is completed for 1 ms. The camera for laser energy monitoring was also set to 1 ms, confirming the exposure time long enough to monitor the total energy of single pulse temporally.

3.2.2.4 Intensifier

Intensifier used in the present study was characterised in terms of linearity to the input signal and fluctuation. The characterisation results are shown in Appendix 5. In the entire experiment, the gain voltage was set to be 7.25 V.

3.2.2.5 Synchronisation

To synchronise the optical system, two Berkeley Nucleonics Corporation BNC Pulse Generators (Model 500) and one AND gate were used. The synchronisation starts with the output signal of the flash-lamp from the Nd:YAG laser, and the flash-lamp signal is sent to one pulse generator (pulse generator A). The pulse generator A sends a pulse to the 'Trigger In' of the dye laser and the AND gate without any delay time. The AND gate receives the pulse from 'Trigger Out' port and thus the AND gate creates a pulse and sends it to the other pulse generator (pulse generator B) only when the dye laser emits light. That is, while the dye laser changes wavelength to the next wavelength, the AND gate does not send signals. Using this synchronisation system, the two cameras, LED and intensifier were triggered via the pulse generator B only when the dye laser was fired. In terms of the Q-switch delay, the delay time was simply controlled by pulse generator A (the Nd:YAG laser emitted light all the time). The frequency of the flash-lamp flashing was 10 Hz and then data sampling was operated at 10 Hz as well. The schematic of the system is shown in **Fig.27** and detailed time sequence and delay time is shown in **Fig.28**.

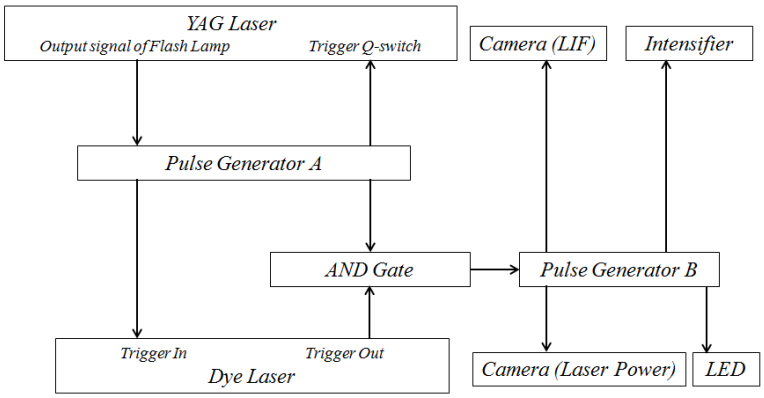

Fig.27. Schematic of the synchronisation system.

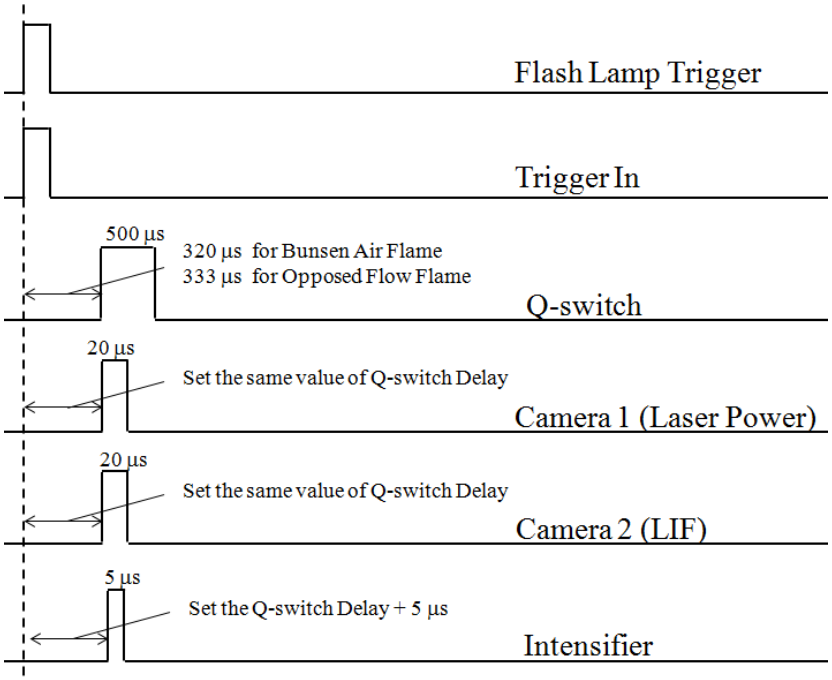

(a)

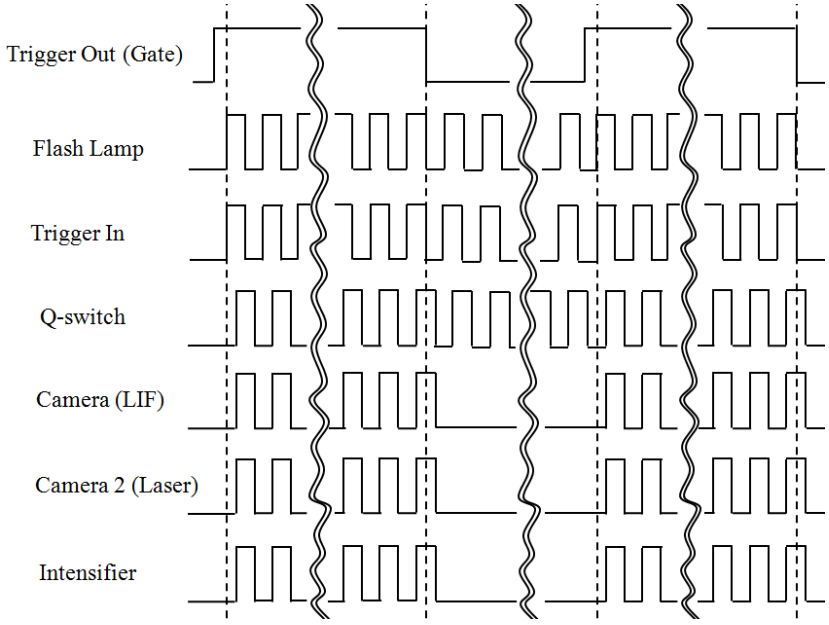

(b)

Fig.28. Detailed time sequence of synchronisation. (a) short time scale (b) long time scale.

3.2.2.6 Filters

Two filters were employed prior to collection lenses to separate visible light from flame, (luminescence). One is CG-UG-295 and the other is CG-UG-1 from CVI Laser optics. The detailed specification provided by the company is shown in **Fig.29** and **Fig.30** for reference.

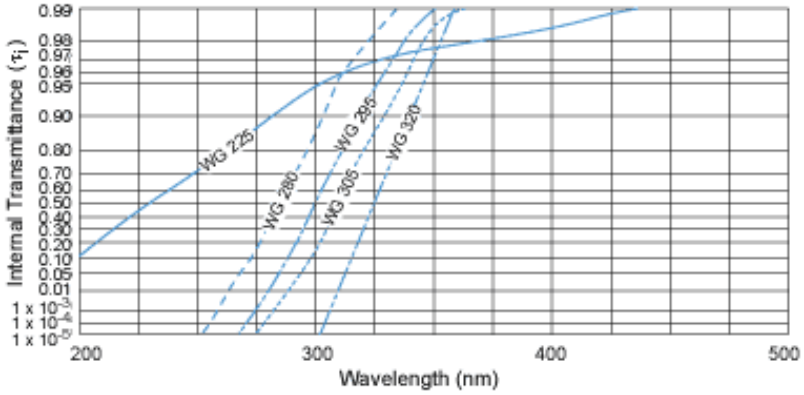

Fig.29. Specification of CG-UG-295.

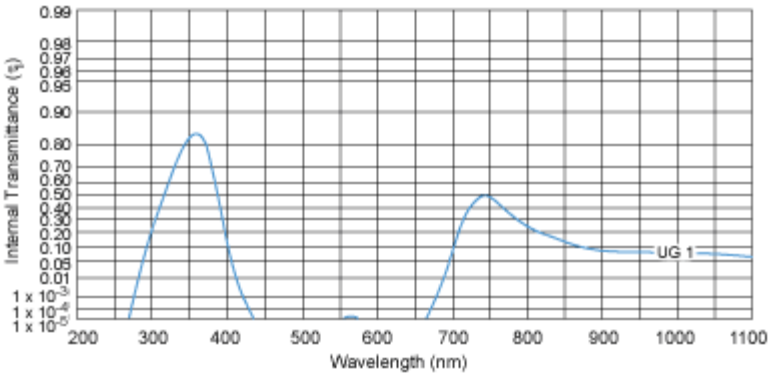

Fig.30. Specification of CG-UG-1.

3.2.2.7 Bunsen Burner

In **Fig.31**, the Bunsen burner used in this study is shown. The inner diameter of main tube is 13.5 mm and the thickness is 0.5 mm. The diameter of the co-flow tube is 77 mm. The actual cross section of co-flow is 1.38×10^{-3} m^2.

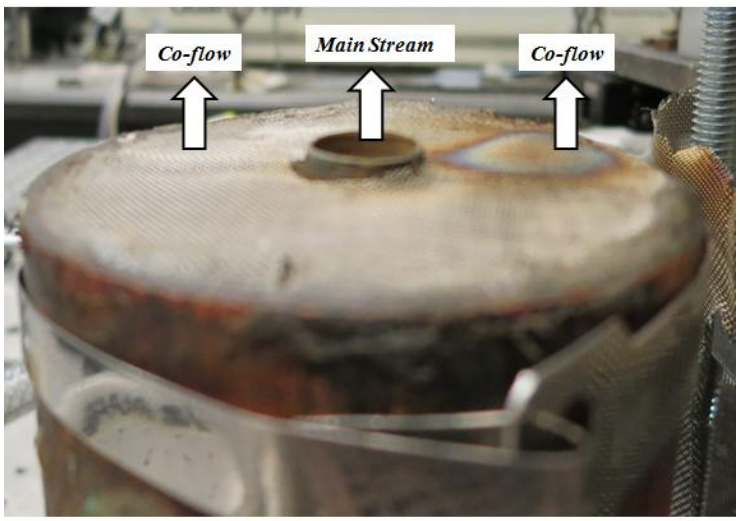

Fig.31. Picture of Bunsen burner.

3.2.2.8 Design of Counter-Flow Burner and Laser Pulse Stretcher

Laser pulse stretchers and counter-flow burners were designed for an advanced future study of the application of Raman-Rayleigh spectroscopy to oxy-fuel combustion. The Raman-Rayleigh spectroscopy enables one to monitor temperature and major species in flame and then grasp temperature structure in mixture fraction space. Equivalently, this future measurement allows for validation of the one-dimensional off-stoichiometric

temperature peaking (1D OTP) characteristics obtained from the simulations in this study. For successful implementation of the Raman spectroscopy, a laser pulse stretcher is needed, since the cross section of Raman scattering is generally small and optical breakdown must be avoided. The designed laser pulse stretcher possesses new geometry, which leads to the better spatial efficiency. That is, it saves more space that the pulse stretcher occupies than the conventional ring cavity developed by Kojima et al. [108]. Besides, the designed counter-flow burner has superiority to the conventional burner, while the burner was employed in the present experiment in common fashion. The one developed in the present study allows for laser beam entry perpendicular to flame between opposed nozzles. This vertical laser entry can realise application of the line measurement axially with counter-flow geometry. In obtaining temperature structure of opposed-flow flame by Raman-Rayleigh spectroscopy, the following steps are generally repeated, putting laser beam parallel with flame [34, 117, 118].

(i) Conduct point measurement at a certain point
(ii) Traverse burner
(ii) Conduct point measurement at another position

The problem of this method is that the spatial resolution is limited by beam waist at probed volume. In general terms, the flame width is sub-millimetre, and thus the detailed evaluation of temperature measurements is not possible by this repetition of point measurements. Due to this, and the fact that the planar imaging of Raman spectroscopy is not possible due to its signal weakness, the vertical laser input is required. The line measurement realised by the vertical laser entry is expected to have much higher resolution, albeit its resolution still being limited by a pixel size of camera and the resolving limit of the collection lens. The conceptual idea of this pixel-by-pixel measurement is shown in **Fig.32**.

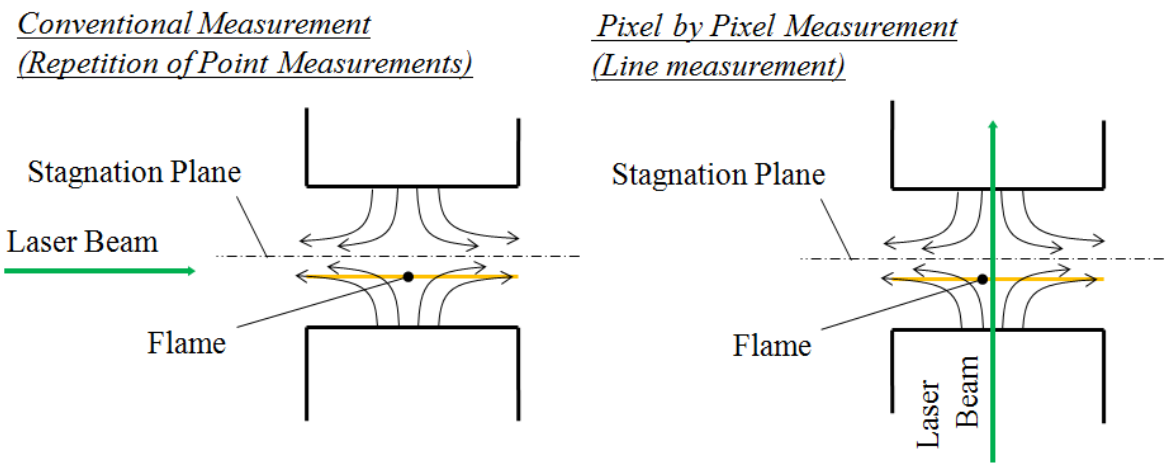

Fig.32. Conceptual sketch of the conventional system and new system (pixel-by-pixel measurement). In the both systems, the collection system is arranged laterally to the counter-flow burners.

3.2.2.8.1 Counter-Flow Burner

A counter-flow burner was uniquely designed. There were two design requirements: realisation of top-hat profile at the nozzle without use of perforated plate, and window attachment at the bottom of the burner. The removal of the perforated plate, which is commonly used in counter-flow burners to enable a near uniform plug flow at the nozzle exit planes, and the window attachment are necessary to enable vertical laser beam entry for future high spatial resolution Raman-Rayleigh spectroscopy. In addition, it is also needed to confirm that the Reynolds's number is sufficiently small at the strain rate of interest, as with usual counter-flow burner.

To realise top-hat profile without any perforated plates, the following contracted geometry was utilised as a burner shape. For better velocity profile at nozzle end, sensitivity analysis was conducted using CFD (ANSYS CFX) [119]. The parameters are shown in **Fig.33**. The best geometry obtained from the sensitivity analysis is also shown in **Fig.33**, and the resultant velocity profiles at jet nozzle are shown in **Fig.34**. As is shown in **Fig.34**, the flat-top profile was realised in the designed burner. The outer flow pass is for shield gas, which prevents external air entrainment. Note that the boundary condition was determined in the sensitivity analysis so that the mass flux of oxidiser

and fuel stream are identical, considering the flame would be set at the centre between the nozzles in the experiment.

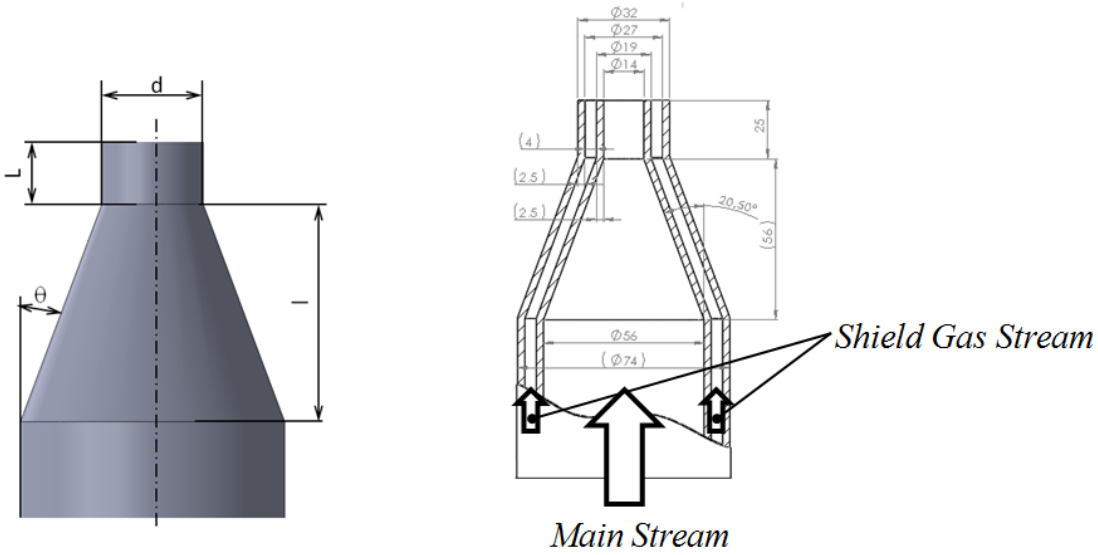

Fig.33. The left picture shows the parameters used in sensitivity analysis (*d*, *l*, *L* and *θ*). The right picture is the best geometry determined by the sensitivity analysis. The outer path is for shield gas.

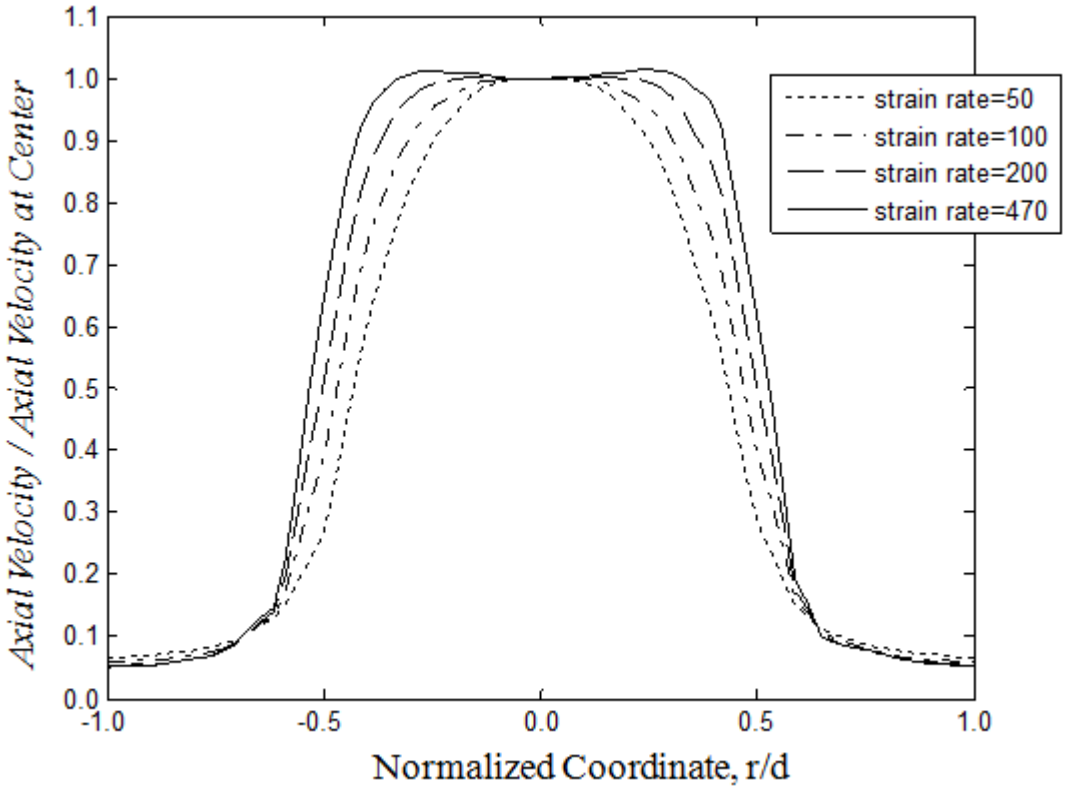

Fig.34. Velocity profile at nozzle end at various strain rates.

The designed opposed-flow burner possesses window attachment at the bottom. Also, to set the lens at the bottom, the gas supply tubes are placed on the lateral surface of burners. The supply tubes are arranged diagonally from four positions, which prevents flow disturbance in the main tube as much as possible. Further, a set of plates shaping a grid is also situated for stratifying the flow in the main tube. The conceptual sketch and actual fabricated burner is shown in **Fig.35**.

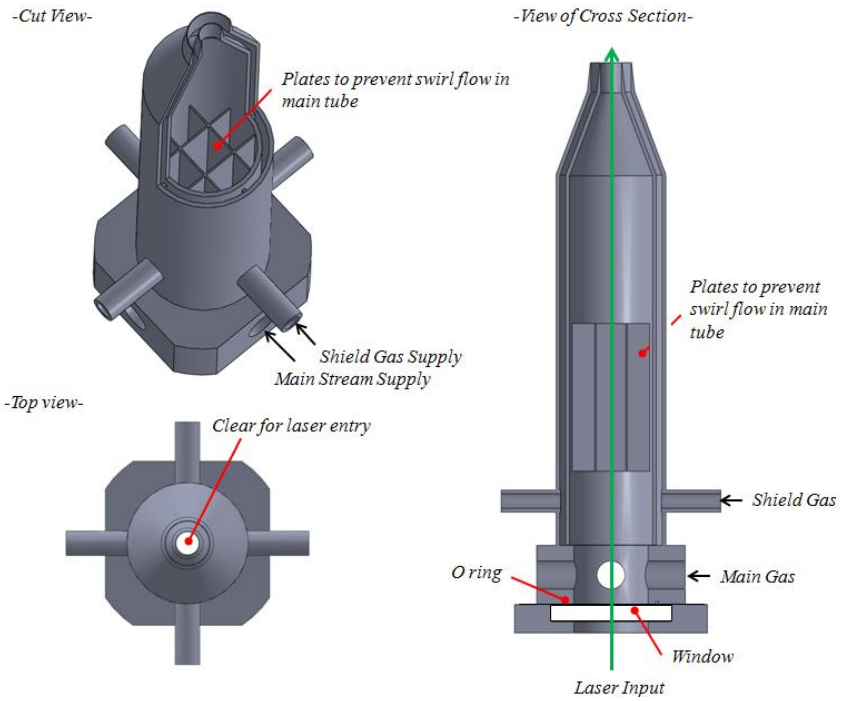

(a)

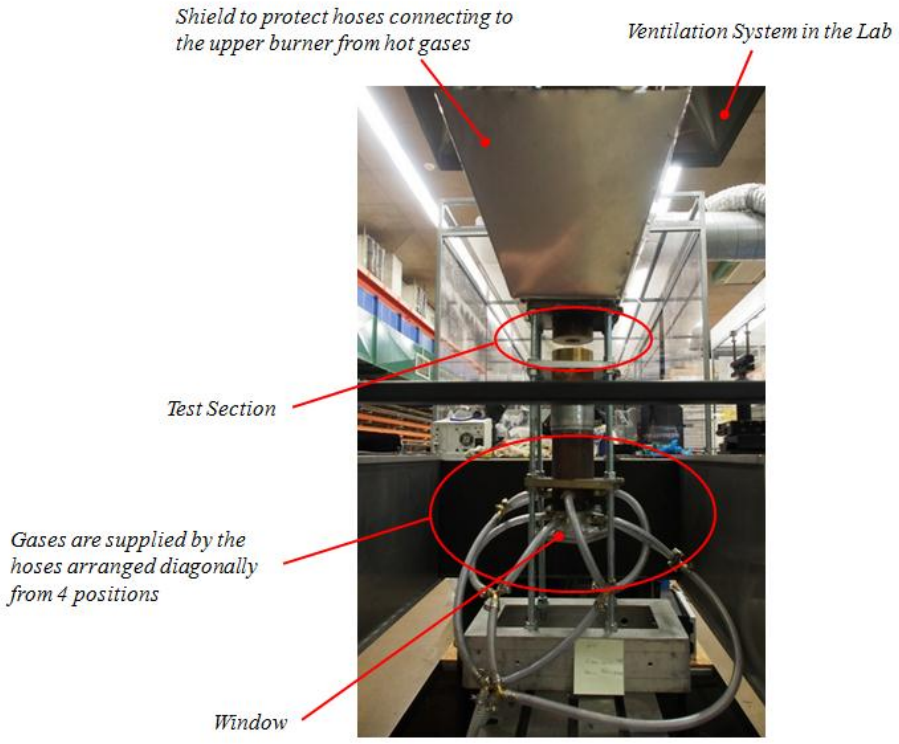

(b)

Fig.35. Conceptual sketch of the counter-flow burner (a) and the picture of actual fabricated burner (b).

Since the flame of interest in this study is laminar, the oxidiser and fuel stream must be laminar. The Reynolds number at the nozzle ends was calculated in the following manner:

$$\mathrm{Re} = \frac{\rho v L}{\mu} \tag{47}$$

where ρ, v, L and μ are density, velocity, representative length and viscosity respectively. The inner diameter of the nozzle of 14 mm end was employed as the representative length in the current case. The calculated results are summarised in Table 2. Since Re<2,300 is laminar region, 2,300<Re<4,000 is transition region and Re>4,000 is turbulent region, the strain rate near extinction of air flame with 20 mm sepration distance resides in transition region. As necessary, the separation distance must be reduced at the strain rate. However, since fuel stream in the experiments was diluted by N_2 for soot suppresion, which reduces strain rate, the inner diameter of 14 mm is fine with the flow condition in the present study.

Table 2: Summary of Reynolds Number Calculation.

Dilution Mode	Strain Rate	Re (Oxidizer Stream)	Re (Fuel Stream)
Air	470 s^{-1} (Near Extinction)	1,700	2,800
CO2 dilution (Y_{O2_oxi} : 23%)	350 s^{-1} (Near Extinction)	1,800	2,600

3.2.2.8.2 Laser Pulse Stretcher Design

The laser pulse stretcher was also designed for future measurements of Rayleigh-Raman spectroscopy. The basic geometry of a cavity designed in this study is one developed from a ring cavity, which is mentioned in the background chapter. The schematic diagram of the designed cavity is shown in **Fig.36**. The cavity possesses two beam splitters (the reflectivity R_{d1} and R_{d2} respectively) and several mirrors. This stretcher with the geometry is called double-ring cavity here. For clarification, the ring cavity mentioned in the background chapter is called a single-ring cavity in the

following. The double-ring cavity is superior to the single-ring cavity in spatial efficiency, defined as best reduction ratio per unit optical length in cavities, while inferior in beam splitter efficiency, defined as best reduction ratio per a beam splitter. The detailed definition of spatial efficiency and beam splitter efficiency is as follows respectively:

$$Spatial\ Efficiency = \frac{1 - Best\ total\ Reduction\ Ratio}{Total\ Optical\ length\ of\ Cavities} \tag{48}$$

$$Beam\ Splitter\ Efficiency = \frac{1 - Best\ total\ Reduction\ Ratio}{The\ Number\ of\ Used\ Beam\ Splitters} \tag{49}$$

The evaluation of these two efficiencies is of considerable assistance for design of laser pulse stretcher. The laser pulse stretcher for Raman spectroscopy generally requires three or four cavities in a pulse stretcher to reduce the laser pulse intensity sufficiently with reasonable total laser energy, which necessitate large space in the laboratory. This space limitation in the laboratory is one of the biggest issues of laser pulse stretchers consisting of beam splitters and mirror. Hence, the better configuration of basic cavity geometry is sought based on this spatial efficiency. In addition, beam splitters are not cheap and thus it is necessary to reduce the number of beam splitters used from a financial perspective. From this standpoint, the beam splitter efficiency is also evaluated.

The output signal, *D(t)*, of a double-ring cavity is mathematically represented as:

$$D(t) = (1 - R_{d1})(1 - R_{d2})Q(t - \tau_{d2}) + R_{d1}R_{d2}Q(t - \tau_{d3}) + \sum_{n=1}^{\infty}\sum_{k=0}^{n} f_{nk} \tag{50}$$

where

$$
\begin{aligned}
f_{nk} = {}_nC_k[&(1-R_{d1})R_{d2}\{R_{d1}(1-R_{d2})Q(t-n\tau_{d1}-(2+k)\tau_{d2}\\
&-(n-k)\tau_{d3})\\
&+(1-R_{d1})R_{d2}Q(t-n\tau_{d1}-(1+k)\tau_{d2}-(n-k+1)\tau_{d3}\}\\
&+R_{d1}(1\\
&-R_{d2})\{R_{d1}(1-R_{d2})Q(t-n\tau_{d1}-(1+k)\tau_{d2}\\
&-(n-k+1)\tau_{d3})\\
&+(1-R_{d1})R_{d2}Q(t-n\tau_{d1}-k\tau_{d2}-(n-k\\
&+2)\tau_{d3}\}](R_{d1}R_{d2})^{k-1}(1-R_{d2})^{n-k-1}(1-R_{d2})^{n-k-1}
\end{aligned}
$$

where *t* is time evolution after an entry of laser pulse to the cavity and Q(t) is the original laser pulse from laser unit. The τ_{d1}, $\tau_{d2,}$ and τ_{d3} refer to a period of time over which the light passes through route 1, 2 and 3 respectively. The definition of route 1, 2 and 3 is in **Fig.36**. The *n* and *k* represent the number of circulations before leaking and the number of times the leaking signal of interest pass the route 2 during *n* times circulation. Note that the *k* is independent of the route of initial and final route, since the *k* refers to the number of times only during *n* times circulations (the total number of times the signal pass the beam splitter two is *n*+2). As with the conventional ring cavity laser pulse stretcher, the reduction ratio limits are determined in the earlier stage of circulation. Therefore, the signal intensities of the following three terms are scrutinised for seeing the reduction limit of the double-ring cavity system, varying combinations of R_{d1} and R_{d2} values:

$$
\begin{gathered}
(1-R_{d1})(1-R_{d2})Q(t-\tau_{d2}), \qquad R_{d1}R_{d2}Q(t-\tau_{d3}),\\
\{(1-R_{d1})^2R_{d2}^2+R_{d1}^2(1-R_{d2})^2\}Q(t-\tau_{d1}-\tau_{d2}-\tau_{d3})
\end{gathered}
$$

Consequently, it is found that the combination of R_{d1} and R_{d2} makes the maximum value of the above three smallest 0.33 and 0.67. The reduction ratio limit with the combination is 0.221. As with a single-ring cavity, the multiple pulses created by each circulation must avoid overlapping as much as possible. Due to this, it was suggested and assumed in this thesis that the individual time delay of τ_{d1}, τ_{d2} and τ_{d3} was set such that $\tau_1 = \tau_3 = dt$ and τ_2= as small as possible where *dt* is a temporal FWHM of original laser pulse. Using this assumption, the spatial efficiency of double-ring cavity is:

$$\frac{1-0.221}{c\,(\tau_1+\tau_2+\tau_3)}=\frac{1-0.221}{c\,(2dt+\tau_2)}\approx\frac{1-0.221}{2cdt}=\frac{0.3895}{cdt}$$

assuming that τ_{d2} is sufficiently small. At the other extreme, the spatial efficiency of two single-ring cavities is:

$$\frac{1-0.38^2}{c\,(\tau_1+\tau_2)}=\frac{1-0.144}{c\,(3dt+\tau_{d12})}\approx\frac{1-0.144}{3cdt}=\frac{0.2853}{cdt}$$

assuming τ_{d12} is sufficiently small, where τ_{d12} is the delay time by the connecting pass from cavity one to cavity two. Due to above results, it can be understood that the double-ring cavity is more efficient in spatial efficiency. However, the beam splitter efficiency becomes smaller in double-ring cavity than in single-ring cavity. The reduction ratio limit of individual ring cavity is 0.38 (the beam splitter efficiency is 0.62). On the other hand, the reduction ratio limit by double-ring cavity is 0.39.

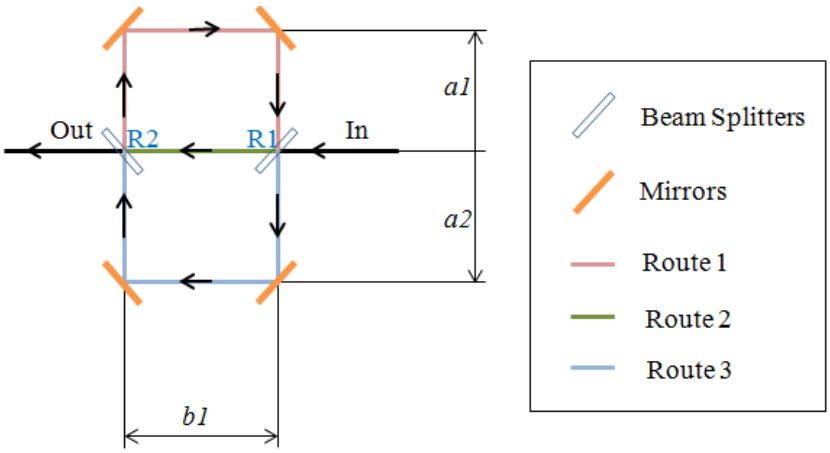

Fig.36. Schematic of double-ring cavity.

To determine the value of each parameter and required cavity number, the information relating to laser intensity inducing significant optical breakdown is necessary. To speculate the value, the experimental results obtained by Cleon et al. [120] were used as a reference. The results are shown in **Fig.37**. From the results, the target maximum intensity was set to be 160 TJ/m^2-s.

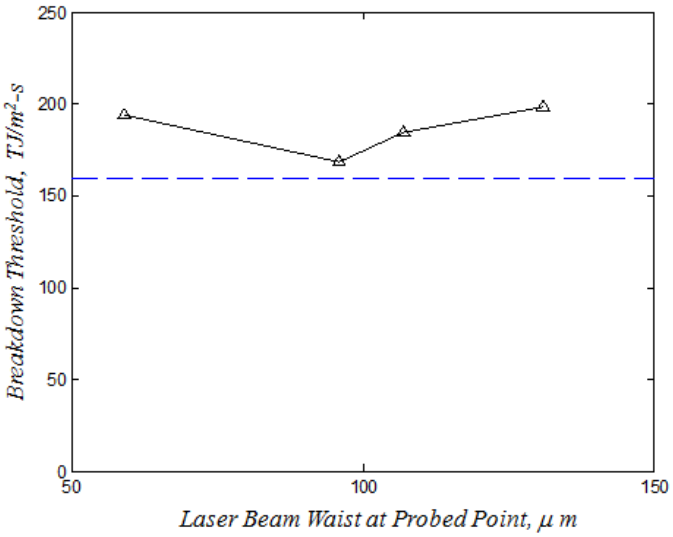

Fig.37. Estimated threshold of optical breakdown obtained by Clemon et al. [120]. The blue line is at 160 TJ/m^2-s.

Considering the above facts, such as the spatial and beam splitter efficiency of single and double-ring cavity, the present laser plus stretcher was designed with a combination of two single-ring cavities and one double-ring cavity. The resultant parameters are summarised in Table 3. The τ_1 and τ_2 represent duration for the first single-ring cavity and the second single-ring cavity respectively. The τ_{d1} and τ_{d2} indicate duration for route 1 and route 2 in the double-ring cavity. The R_1 and R_2 is the reflectivity of the beam splitter in the first and second single-ring cavity. The R_{d1} and R_{d2} is the reflectivity of the beam splitter in the double-ring cavity. The simulated output pulse profile is shown in **Fig.38**. In the simulation, the original laser pulse profile was set to be Gaussian distribution of 10 nm FWHM and 1.3 J.

Table 3: The Parameters Used in the Designed Laser Pulse Stretcher

Parameters	Values
τ_1	10 ns
τ_2	20 ns
τ_{d1}	40 ns
τ_{d2}	40 ns
R_1	0.38
R_2	0.38
R_{d1}	0.68
R_{d2}	0.32

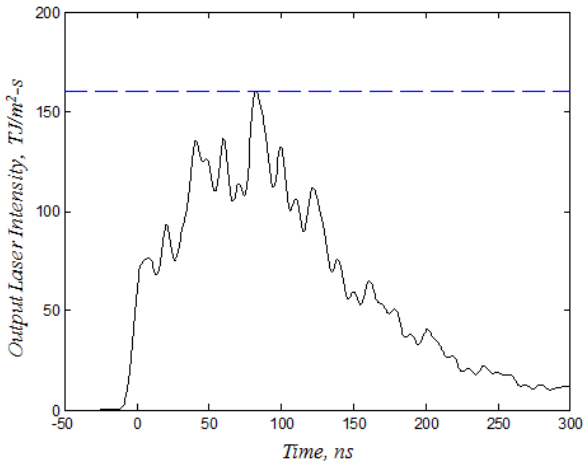

Fig.38. The output signal of the designed laser pulse stretcher. The blue line represents the speculated threshold of optical breakdown of 160 TJ/m^2-s.

Chapter 4
Thermo-Chemical Analysis of Oxy-fuel Combustion

This chapter explores the thermo-chemical structure of oxy-fuel combustion in zero and one-dimensional reactors that do not involve species thermal or mass diffusion. Features such as the maximum adiabatic flame temperature, the degree of zero dimensional off-stoichiometric peaking (0D OTP) and CO emissions are discussed for oxy-fuel conditions and referenced to the results for the conventional air-fuel case. In-depth analysis of the mechanism of 0D OTP in oxy-fuel combustion is conducted and the parametric influence of reactivity, dissociation, heat release and specific heat capacity is ascertained. For all simulations in this chapter, CANTERA was utilised with GRI 3.0 [32] unless otherwise specified.

4.1 Adiabatic Flame Temperature

The constant pressure adiabatic flame temperature for oxy-fuel and conventional N_2 diluted combustion is explored in this section. Specifically, the maximum temperature and off-stoichiometric peaking is evaluated at atmospheric pressure and initial temperature of 300 K. Also, the dominant factor that alters the structure of Tad by the diluting species substitution is identified and the 0D OTP theory developed by Law, et al. is extended by exploring the effect of diluting species replacement in detail. It is noted that in all later analysing processes, flames with the same O_2 mass fraction in the oxidiser, Y_{O2_oxi}, are compared unless otherwise specified. This is because the same O_2 mass fraction with the same equivalence ratio makes the CH_4 consumption mass amount per unit mass of mixture independent of diluting species. It is of considerable importance to fix it in comparison and evaluation in thermal characteristics among flames with dilution of different species, like the present analysis. The CH_4 is a source of thermal energy, retaining energy as chemical energy, and thus it is quite natural and not interested information here to get more heat and higher temperature by more consumption of CH_4 in mixture.

4.1.1 Maximum T_{ad}

Maximum T_{ad} of N_2, CO_2, and H_2O diluted flames are plotted in **Fig.39**, varying the diluting degrees. Maximum T_{ad} of all three combustion modes monotonically increased with Y_{O2_oxi} and the maximum T_{ad} of the three were the most sensitive to dilution degree in the intermediate diluting degree (from 20% to 80%). Also, both CO_2 and H_2O substitution for N_2 led to temperature reduction at a fixed Y_{O2_oxi}. Further, the T_{ad} difference between CO_2 and N_2 was not large, by less than 150 K all over Y_{O2_oxi} while the gap between H_2O and N_2 was as much as approximately 500 K at 35% Y_{O2_oxi}.

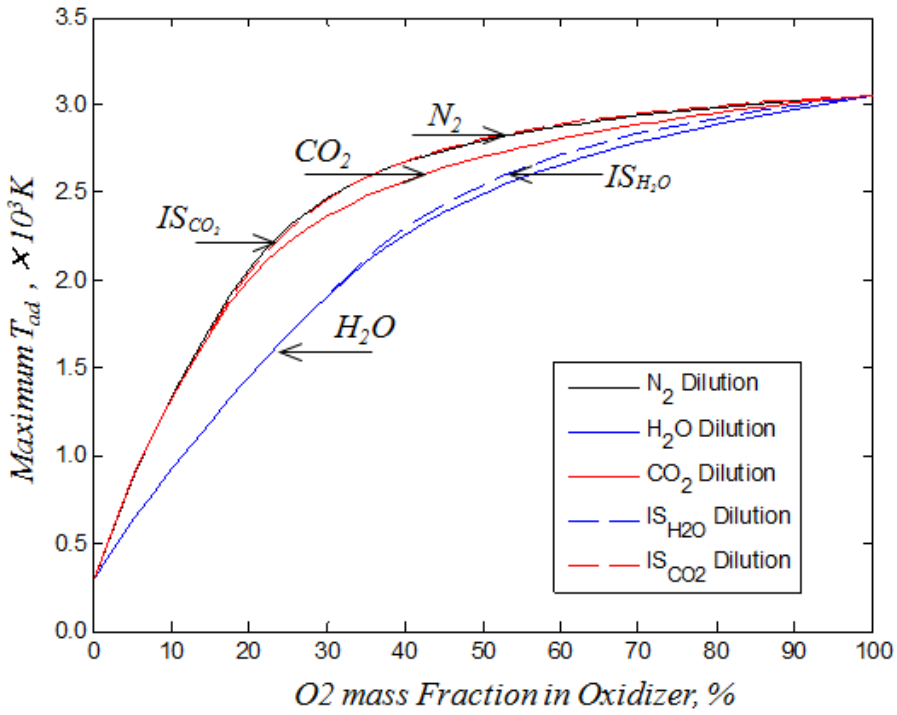

Fig.39. The responses of maximum adiabatic flame temperature to replacement of diluting species and variation of diluting degree. The solid lines represent N_2, CO_2 and H_2O diluted combustion, respectively. The dashed lines are the results with imaginary species dilution (IS_{CO2} and IS_{H2O}). The maximum T_{ad} with pure O_2 combustion was 3,056 K.

The two main differences in properties, between the use of N_2, CO_2 and H_2O as diluents, that influence the constant pressure adiabatic flame temperature are the constant pressure specific heat and the reactivity. The term reactivity here is used to describe the degree and significance of dissociation for the respective diluent. It is noted that although there is a significant difference in the molecular weights of the different

diluents examined here, the molecular weight of the diluent and mixture does not influence the constant pressure adiabatic flame temperature. The molecular weights of the diluents certainly do play an important role in the determination of the constant volume flame temperature, which is not examined here. Where relevant, the constant pressure specific heat is expressed on a per mass basis, making it independent of the molecular weight when comparing diluents and mixtures on a unit mass approach. In **Fig.40** the C_p of pure H_2O, CO_2 and N_2 are shown as a function of temperature. From **Fig.40**, it can be seen that there is a significant difference in both magnitude and variation with temperature of C_p for the three diluents, which will influence the adiabatic flame temperature. In addition to this variation of C_p with temperature, the diluent cannot be considered completely inert, as their reactivity causes different amounts of dissociation. Some of the example dissociation paths are N_2 dissociating to N and NO, CO_2 dissociating to CO and O, as well as H_2O dissociating to H_2, H, OH, O and O_2. Clearly, these dissociation pathways will contribute further towards the variation in the adiabatic flame temperature between diluents.

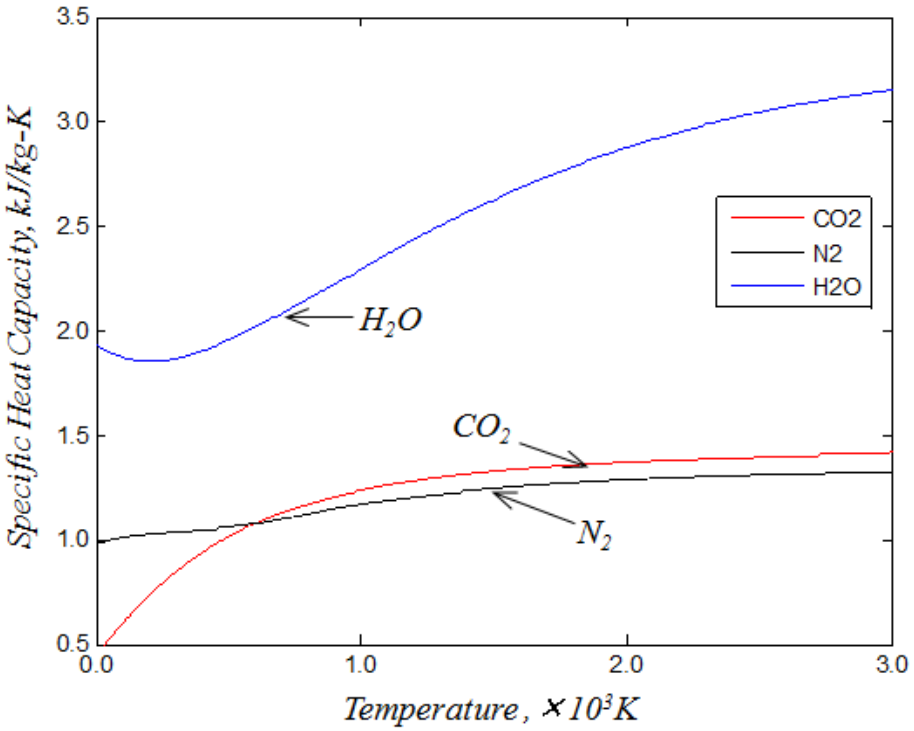

Fig.40. The relation of C_p of N_2, H_2O and CO_2 with temperature.

As an initial step to identify the most significant mechanism that drives the difference of maximum T_{ad} among N_2, CO_2 and H_2O diluted flames, the reactivity, or more

precisely the assumption that N_2 can be considered as an inert in the determination of T_{ad} in air-fuel flames, is assessed. By removing all of the nitrogen-containing molecules from the GRI 3.0 mechanism, with the exception of N2, as well as removing all of the nitrogen-containing reactions that permit dissociation of N2, a new mechanism termed an N2 reaction prohibition mechanism (NPM) was utilised in the equilibrium calculations. The results using this revised NPM and the full GRI 3.0 mechanism with nitrogen chemistry are shown in **Fig.41**, which shows that for the full range of oxygen mass fractions in the oxidiser stream, the influence of nitrogen reactivity has very little impact on the resultant adiabatic flame temperature. For most conditions, the two curves representing the reactive and non-reactive nitrogen cases are indistinguishable and the maximum difference investigated at stoichiometry is found to be 0.41% at the Y_{O2_oxi} of 0.4, which is sufficient for the analysis here to assume that in the determination of the adiabatic flame temperature, nitrogen is effectively inert.

In order to assess the influence of CO_2 and H_2O reactivity on the adiabatic flame temperature, reaction constrained versions of CO_2 and H_2O are utilised in the oxidiser streams, hence termed here as imaginary species, IS_{CO2} and IS_{H2O}. It is emphasised that conventional H_2O and CO_2, formed by the oxidisation of the fuel with the oxygen in the oxidiser, is still allowed to react and hence dissociate. Only the CO_2 and H_2O originating in the oxidiser stream is inhibited from reacting and dissociating, and has the same thermodynamics (specific heats) as the reacting version of the species. The results for the maximum adiabatic flame temperature utilising IS_{CO2} and IS_{H2O} in the oxidiser stream, as well as the conventional CO_2 and H_2O, are shown in **Fig.39**.

It is shown in **Fig.39** that the maximum temperature for the CO_2 diluted case is consistently lower than the IS_{CO2} diluted case. This lower adiabatic flame temperature can be attributed exclusively to the predominantly endothermic reactions resulting from the dissociation of the reactive CO_2 in the oxidiser. It is noted that in **Fig.39**, there is only a small difference between the IS_{CO2} case and the N_2 diluted case, which can be attributed to the similar specific heats of the oxidiser diluents IS_{CO2} (CO_2) and N_2, as both IS_{CO2} and N_2 can be regarded as non-reactive. Thus, it can be concluded that the difference in the maximum temperature between N_2 and CO_2 diluted oxidiser cases is driven by the higher reactivity of CO_2, and not the difference in specific heats.

For the case of utilising H_2O as the diluent, **Fig.39** shows that the maximum flame temperature is consistently lower than when N_2 and CO_2 are used as the diluent in the oxidiser. The difference in the maximum adiabatic flame temperature between N_2 and the non-reactive IS_{H2O} is relatively large, indicating that the larger specific heat value of H_2O relative to N_2 and CO_2 and not the reactivity of H_2O, drives the lower maximum adiabatic flame temperature. This conclusion is supported by the much larger specific heat of H_2O, relative to CO_2 and N_2 reported in **Fig.40**.

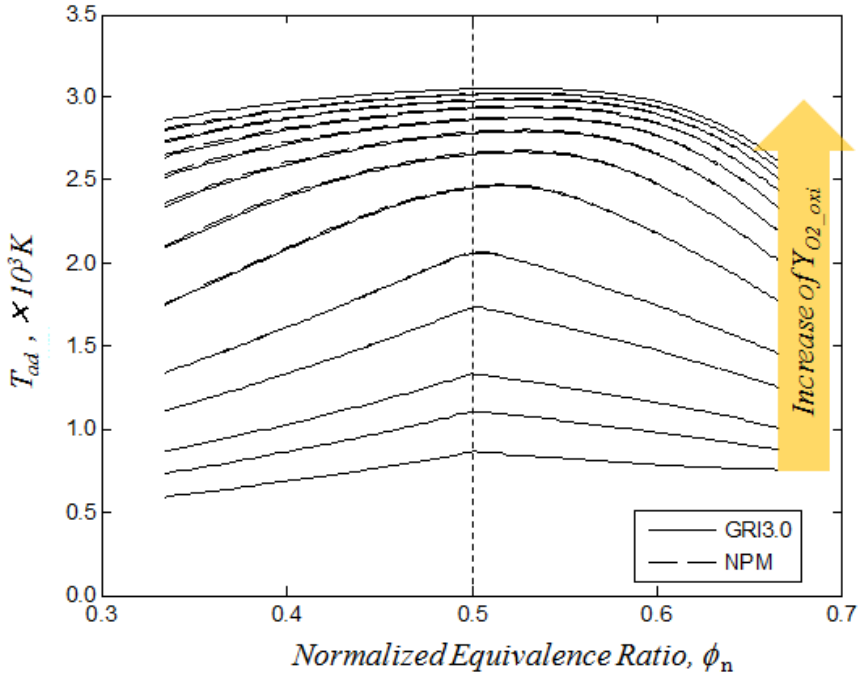

Fig.41. Confirmation of N_2 being inert in T_{ad}. Each curve has different O_2 mass fractions in oxidiser, Y_{O2_oxi} (5, 7.5, 10, 15, 20, 30, 40, 50, 60, 70, 80, 90, 100%). The bottom curve is the result with Y_{O2_oxi} of 5% and the top with Y_{O2_oxi} of 100%. The diluting species used was N_2.

4.1.2 0D OTP

The 0D OTP of CO_2 and H_2O diluted oxy-fuel combustion is characterised here. In addition to that, since the theory of 0D OTP established by Law et al. does not contain the dependence of diluting species on the 0D OTP, the present 0D analysis seeks to extend the 0D OTP theory to the combustion diluted by some species other than N_2. Further, it is also evaluated which species is the most influential to 0D OTP property for further understanding.

4.1.2.1 0D OTP of CO_2 and H_2O Diluted Combustion

The 0D OTP property for the individual dilution modes is shown in **Fig.42** and **43**. **Fig.42** is as a function of O_2 mass fraction in oxidiser, Y_{O2_oxi}, and **Fig.43** is as a function of maximum T_{ad}. The 0D OTP is evaluated via normalised equivalence ratio (ϕ_n) which was defined in chapter 3. It is observed from these graphs that there was no shift of maximum T_{ad} from stoichiometry at less than approximately 1500 K for all diluents types. This is due to their too-low temperature for dissociation occurring. The 0D OTP of CO_2 diluted flame was much richer than N_2 diluted flame all over Y_{O2_oxi} as well as temperature range. Also, the richest shifts of both CO_2 and N_2 dilution modes were at approximately 55% Y_{O2_oxi}. The 0D OTP degree with H_2O dilution was smaller, at less than 65% Y_{O2_oxi}, than N_2 dilution, while the trend became opposite then onwards. Further, the off-peaking property of H_2O dilution flame was more similar to N_2 diluted flame than CO_2 diluted flame at the same maximum T_{ad}.

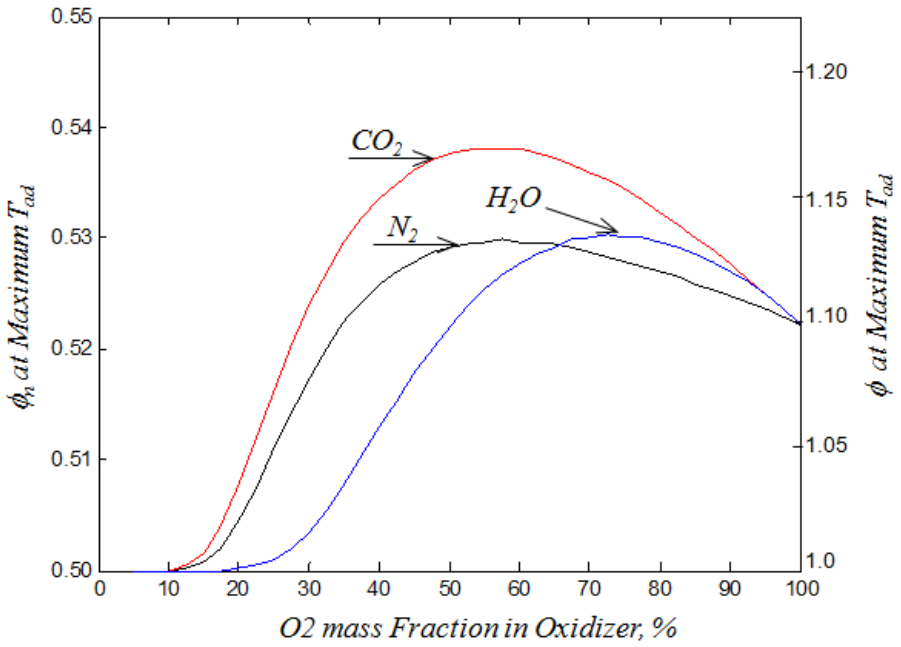

Fig.42. The response of 0D OTP to replacement of diluting species and variation of diluting degree. The degree of 0D OTP is represented by the normalised equivalence ratio, which was defined in chapter 3. For reference, the equivalence ratio is also shown in a right axis in the graph.

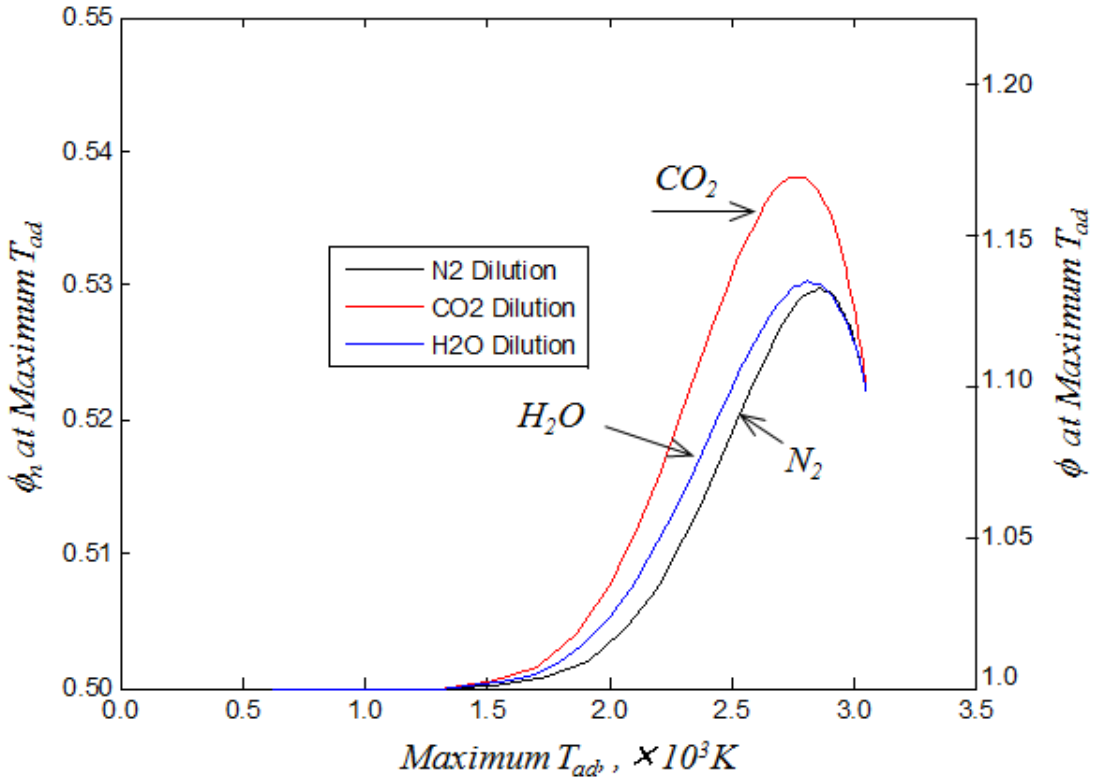

Fig.43. The relation of 0D OTP with Maximum T_{ad}. The degree of 0D OTP is represented by the normalised equivalence ratio, which was defined in chapter 3. For reference, the equivalence ratio is also shown in a right axis in the graph.

4.1.2.2 Extension of 0D OTP Theory

The differences of physical property among CO_2, H_2O and N_2 as diluents are C_p and reactivity. The cause of the discrepancies in 0D OTP among each dilution mode is explored by the same procedure as the above maximum T_{ad} analysis. It is first confirmed whether N_2 reaction affects the 0D OTP phenomenon or not, using the NPM. As is understood from **Fig.41**, N_2 is completely inert in terms of 0D OTP. Second, the difference in C_p among individual diluting species and reactivity of CO_2 and H_2O is examined, employing the imaginary species IS_{CO2} and IS_{H2O}. **Fig.44** shows the 0D OTP property of IS_{CO2} and IS_{H2O} diluted combustion with CO_2, H_2O and N_2 diluted combustion. From the graph, it is found that the IS_{CO2} dilution does not possess a large difference from N_2 dilution in 0D OTP and thus, the effect of C_p difference between CO_2 and N_2 was not significant in discrepancy of 0D OTP property between CO_2 and

N_2 diluted combustion. In contrast, CO_2 diluting mode shows a huge deviation from IS_{CO2} in **Fig.44**, due to which it can be understood that the reactivity difference of CO_2 from N_2 played dominant role in the discrepancy of 0D OTP. On the other hand, the imaginary species IS_{H2O} diluting mode shows relatively a large difference from N_2, while there is no significant gap between IS_{H2O} and H_2O. Consequently, it can be said that 0D OTP deviation of H_2O from N_2 diluted combustion arose from C_p difference between the two.

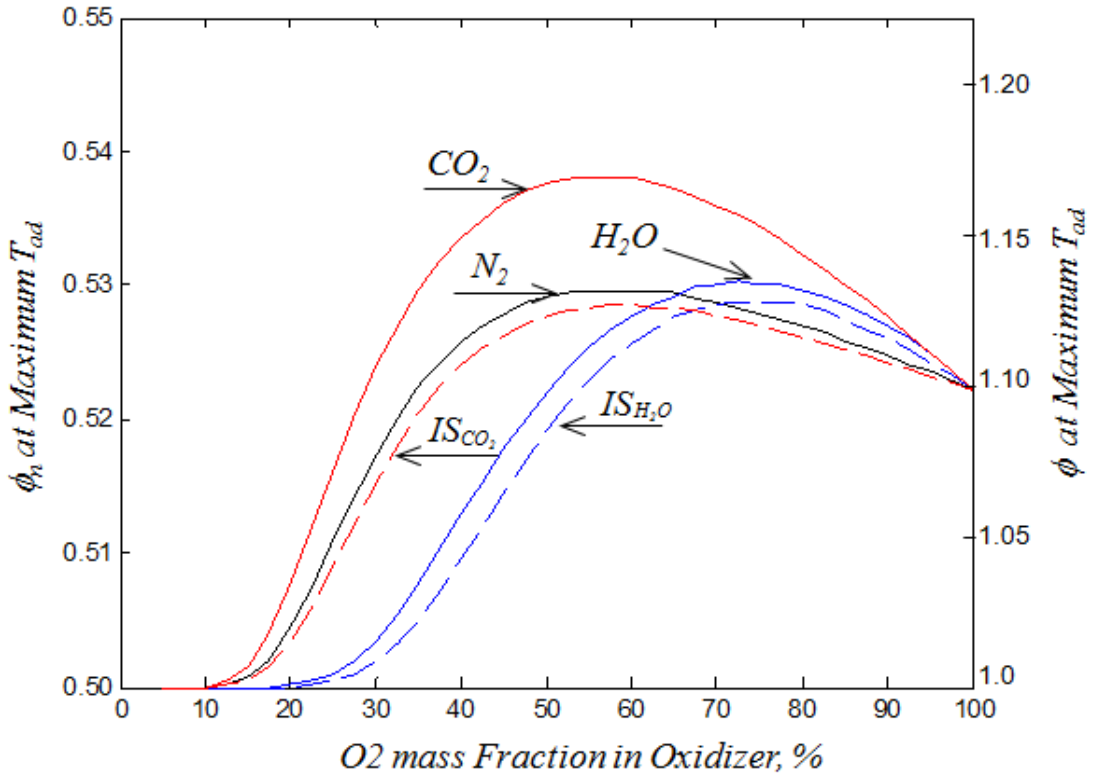

Fig.44. The response of 0D OTP to replacement of diluting species and variation of diluting degree. The solid lines represent N_2, CO_2 and H_2O diluted combustion, respectively. The dashed lines are the results with imaginary species dilution (IS_{CO2} and IS_{H2O}).

From Fig.44, it can be predicted that the C_p of diluting species primarily influences the peak position of 0D OTP curve in the Y_{O2_oxi} space and the reactivity of diluting species mainly affects overall 0D OTP degree. To confirm the first statement, 0D OTP with Ar and He dilution is also explored here. Fig.45 shows the 0D OTP properties of Ar and He diluted combustion with those of N2 and IS_{H2O}. The Ar and He have different C_p quantities, while both are completely inert. Hence, the 0D OTP difference between the

two diluting modes reveals the effect of C_p value of diluting species on 0D OTP. In **Fig.45**, the discrepancy of Ar and He diluted combustion is present only in the condition of Y_{O2_oxi}, in which each 0D OTP curve peaks and then it is true that the C_p of diluting species determines the peak position of 0D OTP curve in the Y_{O2_oxi} space. It is also worth noting that there are slight differences in the maximum 0D OTP degree among these completely inert gases except Ar and He in **Fig.45**. This can be due to the temperature dependence of C_p in individual diluting species. The C_p of Ar and He is independent of temperature since both are mono-atomic, although the C_p of the others differs with temperature.

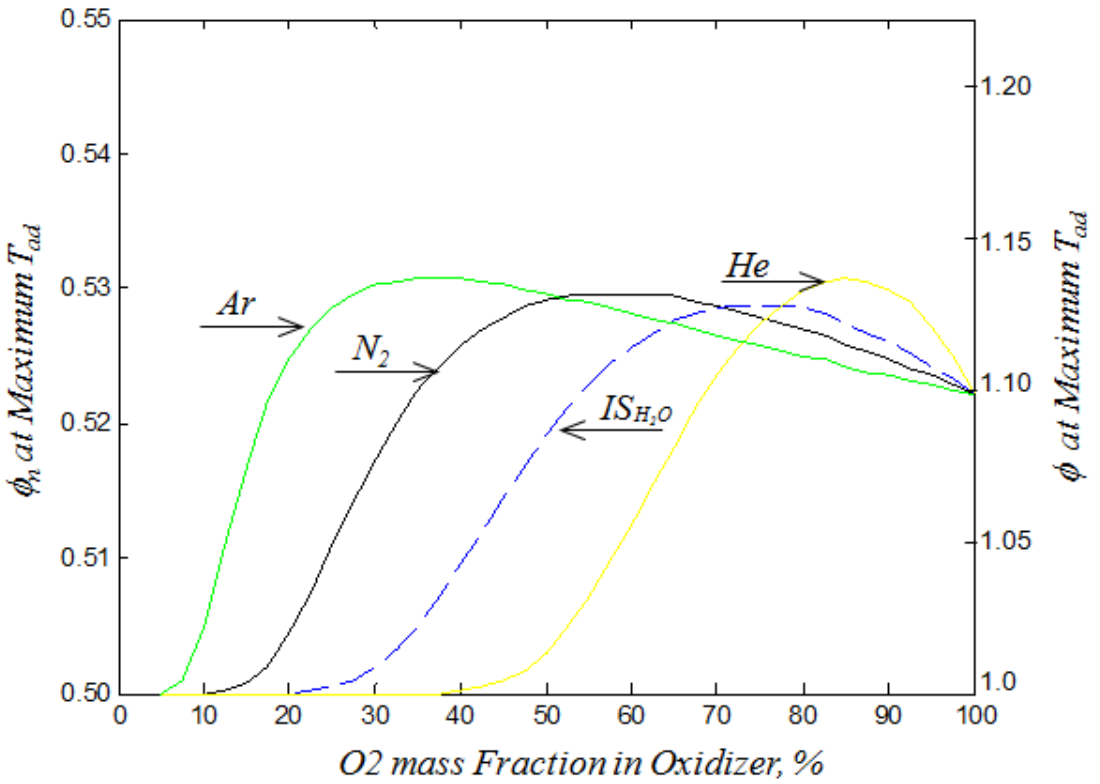

Fig.45. 0D OTP with dilution of other inert species. The degree of 0D OTP is represented by the normalised equivalence ratio, which was defined in chapter 3. For reference, the equivalence ratio is also shown in a right axis in the graph.

Several simplified reaction models are also applied to T_{ad} calculation in order to scrutinise the 0D OTP phenomenon further. Although the significance of dissociation reactions in 0D OTP was reported in a previous 0D OTP study by Law et al., the dissociation reaction of what species is dominant is yet to be clarified. It is quite

arduous to clarify it directly since there is no way to distinguish species of interest produced via dissociation reaction and the species from other reaction paths, using the equilibrium calculation results. Therefore, the following analysis attempts to understand the influential species in 0D OTP degree by the simplified reaction models as preliminary analysis of identification of dominant dissociation reaction.

The used simplified reaction models here are SSM, Two Step Mechanism (TSM) and Diatomic Mechanism (DM). These mechanisms are applied to N_2, CO_2, and H_2O diluted combustion. The SSM permits a presence of CH_4, O_2, N_2, CO_2, and H_2O and equivalently the products created via combustion are considered to be only tri-atom ($CH_4 + 2O_2 => CO_2 + 2H_2O$). The effect of tri-atom (CO_2 and H_2O) formation on 0D OTP can be seen, using this SSM. In the TSM, CO and H_2 are further allowed to be present with CO_2 and H_2O as products, which enable one to see the effect of CO and H_2 presence. The DM allows presence of the other diatom (OH and NO) in the post-combustion composition, in addition to CO_2, H_2O, CO and H_2. The comparison between TSM and DM clarifies the impact of OH and NO, and comparison between DM and GRI evaluates the effect of mono-atom presence such as H and O.

The simulation results are shown in **Fig.46** and **Fig.47**. As is mentioned in Law's paper, there is no off-stoichiometric peaking with SSM in all dilution schemes (T_{ad} peaks at stoichiometry). The results of TSM show a rich side shift of the T_{ad} peak with all diluting species, and the maximum T_{ad} of CO_2 dilution mode resides in the richer side than that of N_2 and H_2O dilution. The peaking position with DM is leaner than TSM, and with GRI 3.0, is leaner than DM. From these results, it can be seen that CO and H_2 formations work as rich shifters, while OH and NO formations/mono-atomic formations function as lean shifters. Also, it is observed that the leaner side movement from TSM to DM is stronger for CO_2 than H_2O and N_2, while the leaner transition from DM to GRI with CO_2 is similar to H_2O and N_2. Therefore, it is found that the rich shift by CO and H_2 and leaner shift by OH and NO with CO_2 is stronger than N_2 and H_2O, while there is not much difference by mono-atomic formation in all three dilution modes. The results here are summarised in Table 4.

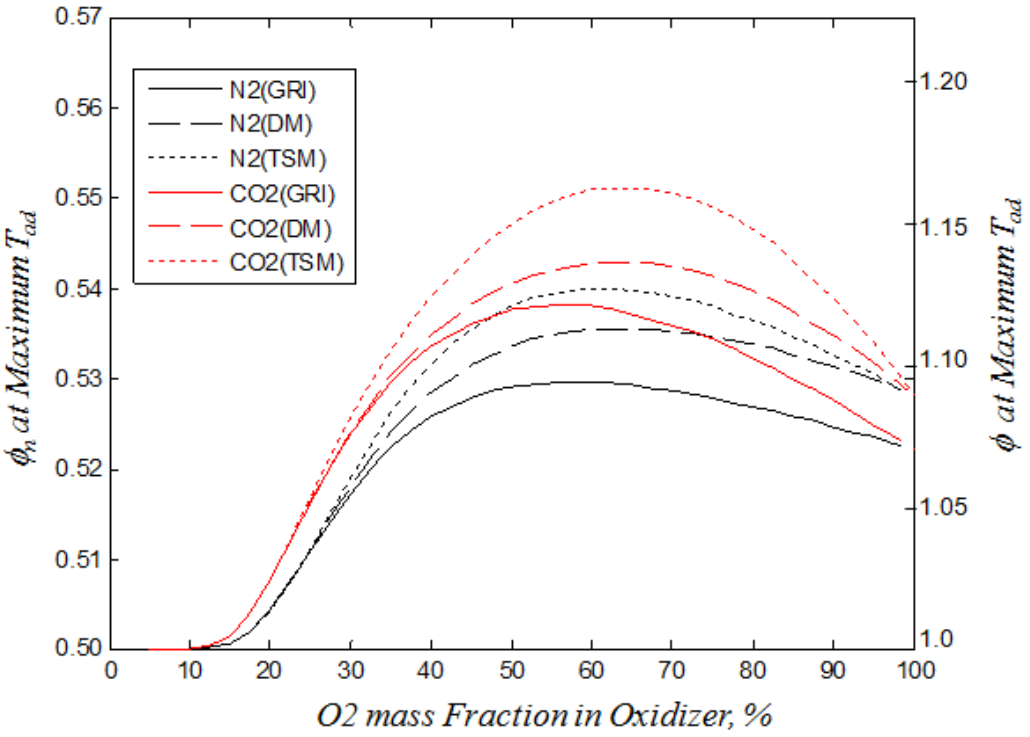

Fig.46. 0D OTP response with various simplified reaction models. The black lines and red lines represent N_2 and CO_2 dilution, respectively.

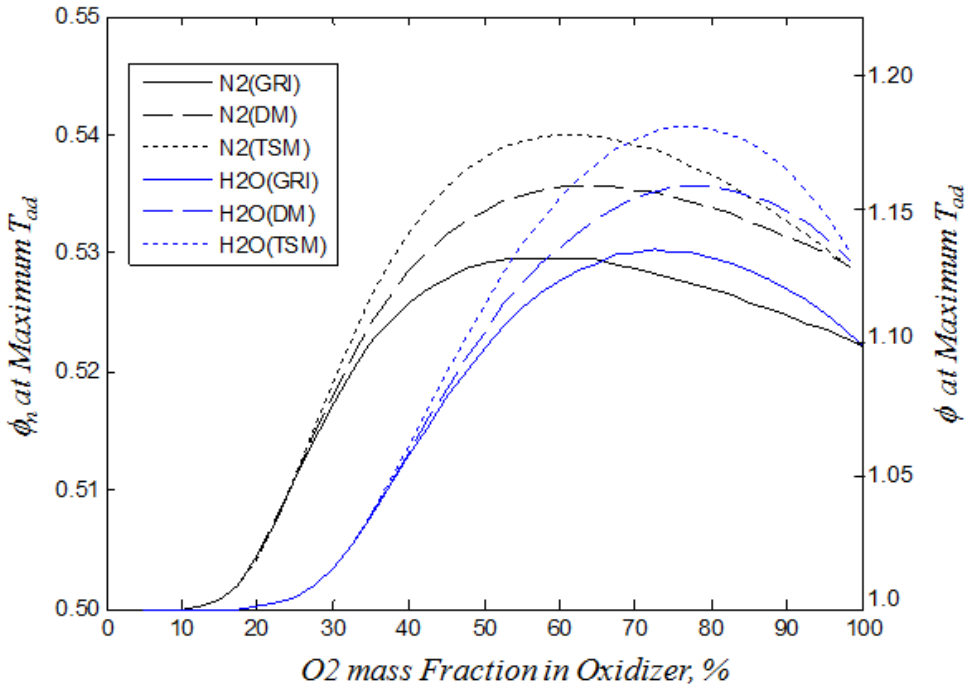

Fig.47. 0D OTP response with various simplified reaction models. The black lines and blue lines represent N_2 and H_2O dilution, respectively.

Table 4: Summary of the Analysis with Simplified Reaction Models

Species	*OTP Motion*	*Trend*
CO and H2 presence	*Rich Shift*	*CO2 dilution > H2O dilution ≈ N2 dilution*
OH and NO presence	*Lean Shift*	*CO2 dilution > H2O dilution ≈ N2 dilution*
Mono-atom presence	*Lean Shift*	*CO2 dilution ≈ H2O dilution ≈ N2 dilution*

Keeping the above results and the fact that methane combustion shows rich shift all the time with GRI 3.0 in mind, it can be said that CO and H_2 are the dominant species in 0D OTP for all H_2O, CO_2 and N_2 diluted combustion. Also, the differences among CO_2, H_2O and N_2 diluted flames mainly come from CO and H_2 presence according to **Fig.46** and **Fig.47**. Further, it is of interest whether the lean shifting via OH and NO/mono-atom presence is caused by C_p related terms or q_p related terms. The C_p and q_p of 60% O_2 mass fraction flame is shown in **Fig.48**, with GRI 3.0, DM and TSM. The C_p does not have much difference among the three kinetic mechanisms, while there is a relatively large difference in q_p. From the result, it can be understood that the main driver of lean shifting via OH and NO/ Mono-atom presence is due to the q_p related term rather than C_p related term.

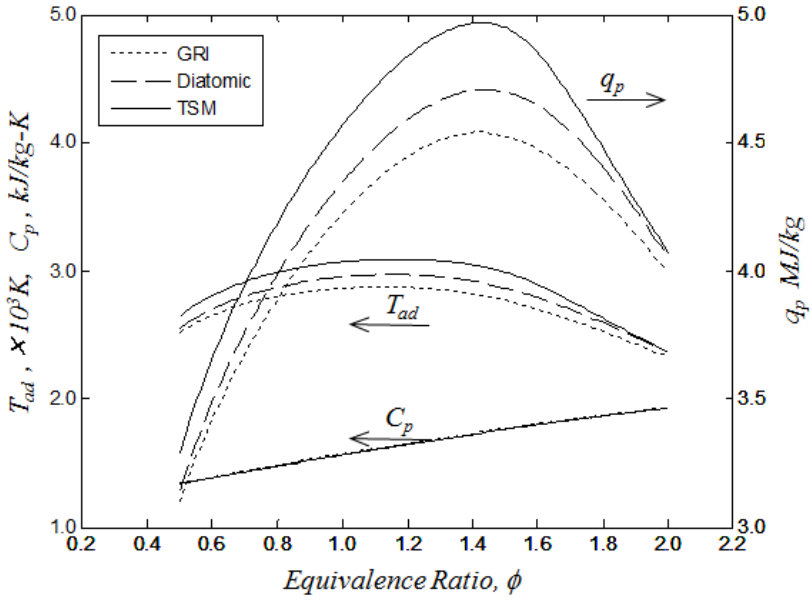

Fig.48. The thermal structure with Y_{O2_oxi} of 60%. The calculation was conducted with N_2 dilution.

4.2 CO Emission

To grasp the general trend of CO emission, the mass fraction of CO in post-combustion mixture, Y_{CO}, is shown with 23.3% Y_{O2_oxi} in each dilution mode as a function of ϕ_n in **Fig.49**. All curves in **Fig.49** hold monotonic increases with ϕ_n, while the magnitudes of Y_{CO} are different from each other. The CO_2 diluted combustion produced the most CO of three, followed by N_2 and H_2O diluted flame. In the next, in order to see the response of CO formation to Y_{O2_oxi} variations, the Y_{CO} at stoichiometry are shown as a function of Y_{O2_oxi} in **Fig.50**. From this result, it can be seen that the CO_2 diluted flame produces the most CO, and H_2O diluted flame forms the least CO formation of three all over the Y_{O2_oxi}.

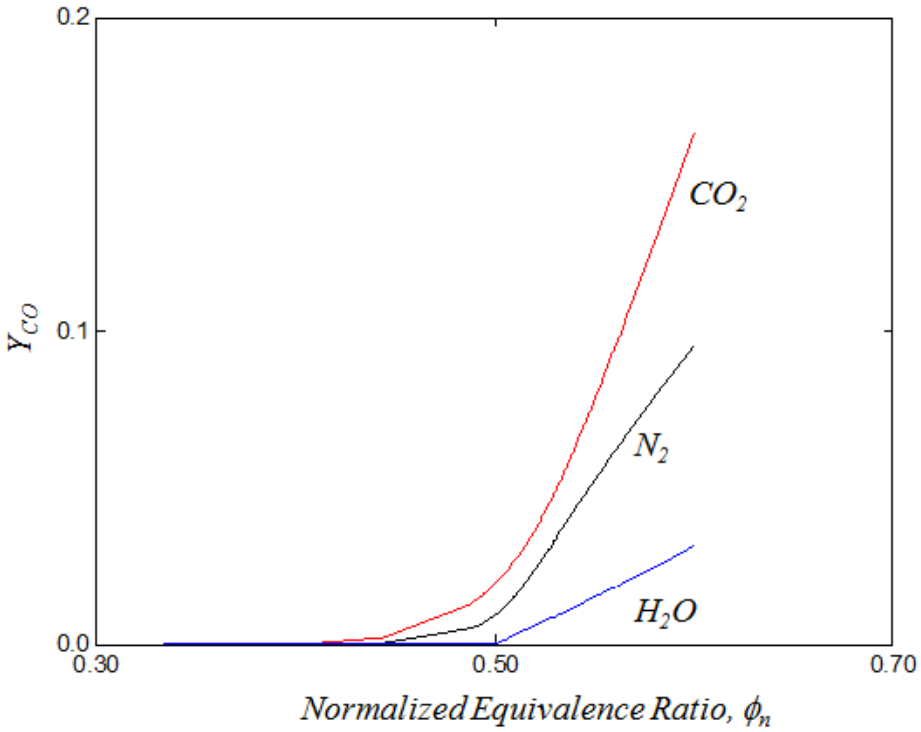

Fig.49. CO emission with distribution with 23.3% Y_{O2_oxi}. The black, red and blue curves represent N_2, CO_2 and H_2O dilution, respectively .

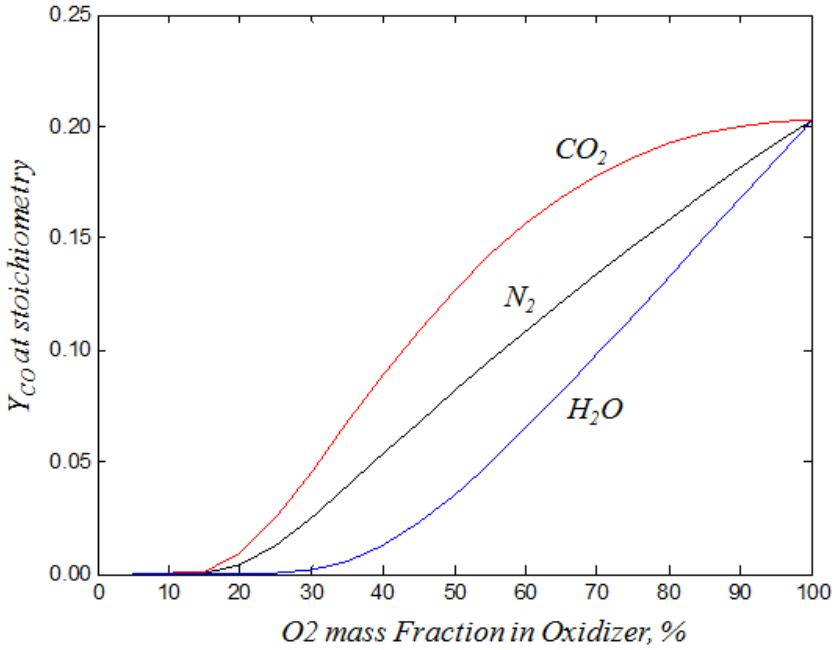

Fig.50. The response of Y_{CO} at stoichiometry to variation of Y_{O2_oxi}. The black, red and blue curves represent N_2, CO_2 and H_2O dilution, respectively.

In the next part, another evaluation of CO is implemented, using an emission index of CO, EI_{CO}, defined by the mass of CO in product per unit mass of CH_4 in reactant. The application of this index to CO_2 diluted flame indicates an interesting result, as is shown in **Fig.51**. While the EI_{CO} of N_2 and H_2O diluted combustion increased monotonically with the Y_{O2_oxi}, as with the above Y_{CO} assessment, that of the CO_2 diluted combustion peaked at Y_{O2_oxi} of 0.64, falling off on the either side. This can be due to the competition between CO dissociation encouragement via an increase of T_{ad} and that of discouragement via a decrease of potential CO_2 in mixture for dissociation. As the Y_{O2_oxi} is increased, the more main forward reaction. That is, the breakdown from CH_4 to product, takes place per unit mass of reactant concomitantly with an increase of T_{ad}, and then the more CO_2 are dissociated. At the other extreme, as the Y_{O2_oxi} increases, the CO_2 in reactants (potential CO_2 for dissociation and consequent CO_2 dissociation), are decreased. Since the dissociation encouragement by the Y_{O2_oxi} increase is dominant in low Y_{O2_oxi}, the CO emission index is increased with Y_{O2_oxi}. On the other hand, in sufficiently large Y_{O2_oxi}, the suppression of dissociation by a decrease of potential CO_2 for dissociation overwhelms. Further, the CO emission index is also evaluated with a few different high ambient pressures. The results are shown in **Fig.52**. From this graph, it is observed that although the curve is flattened more with the pressure increase, the

pressurised combustion system of CO_2 dilution still shows a convex upward parabolic shape.

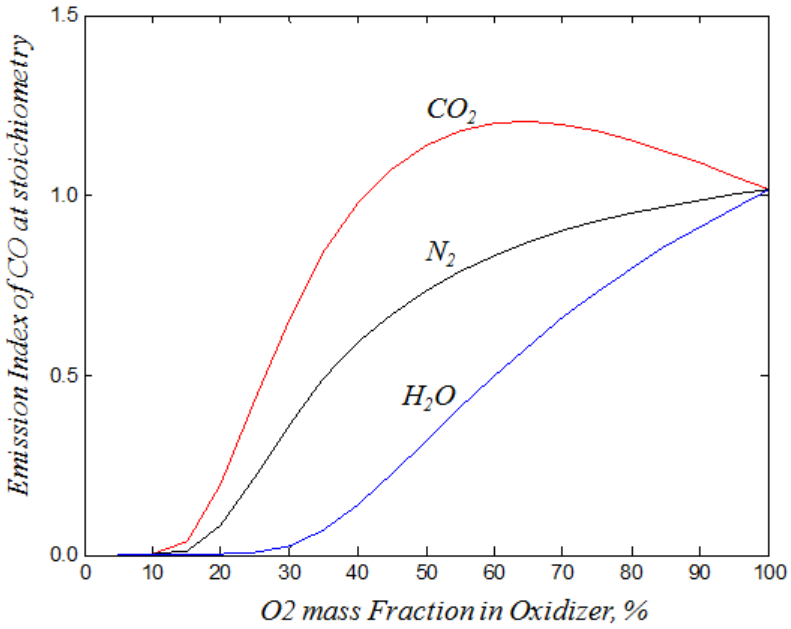

Fig.51. Emission index of CO at stoichiometry with variation of O_2 mass fraction in oxidiser. The black, red and blue curves represent N_2, CO_2 and H_2O dilution, respectively.

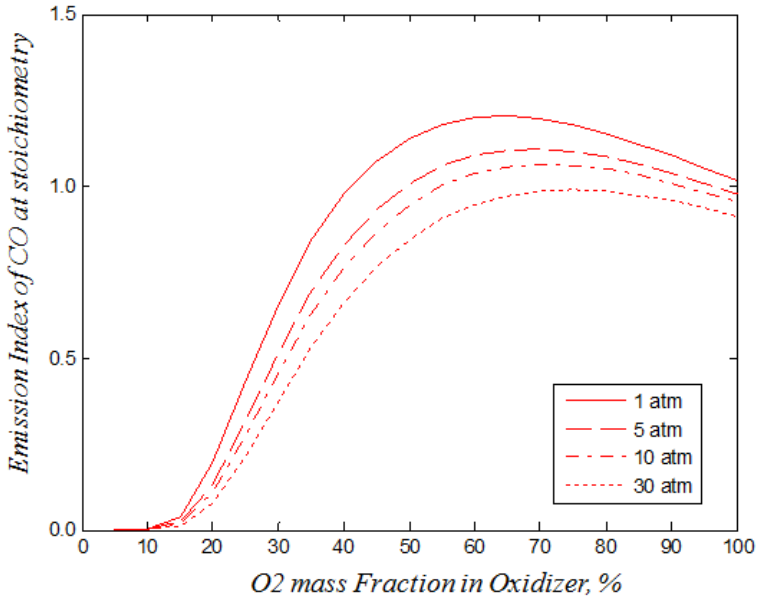

Fig.52. The pressure dependence of EI_{CO} at stoichiometry with variation of O_2 mass fraction in oxidiser.

4.3 CO_2 v. H_2O Dilution

Here, CO_2 and H_2O are compared as diluents alternative to N_2 from practical perspective, using the above discussion of T_{ad} and CO emission. In the above, it was found that the max T_{ad} of CO_2 diluted combustion is comparable to N_2 diluted combustion, while the H_2O substitution of N_2 leads to significant T_{ad} reduction per unit mass of fuel in reactants. Keeping this in mind, it can be understood that to get a given temperature, less fuel is required in CO_2 diluted flame than H_2O diluted mode. As mentioned in the background chapter, it is of considerable importance to fit the temperature of oxy-fuel combustion with that of conventional air mode. The post-combustion temperature with CO_2 dilution equivalent to that of air, can be realised with less fuel than with H_2O dilution. At the other extreme, there is more CO formation in CO_2 dilution cases given that the fuel fraction in reactant is fixed, which is shown in the above CO emission analysis. In **Fig.53**, the EI_{CO} at stoichiometry is plotted as a function of stoichiometric T_{ad}. In **Fig.53**, less CO formation is observed in the case of H_2O dilution than in the case of CO_2 dilution fixing T_{ad}. In conclusion, from the fuel consumption efficiency perspective, the CO_2 diluted flame is preferable, while the CO emission index becomes significantly worse than H_2O dilution mode.

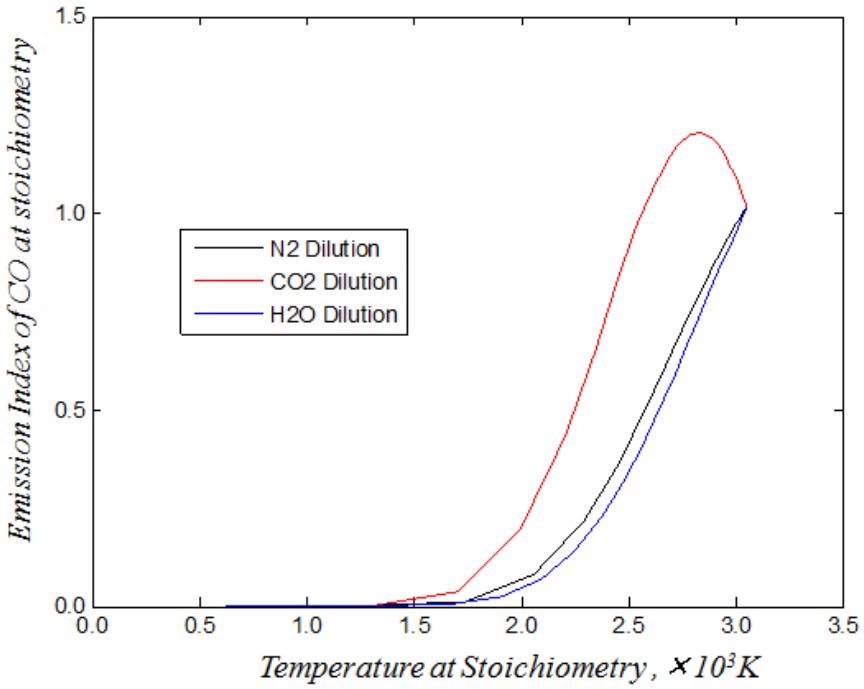

Fig.53. The relation of emission index of CO with temperature. The black, red and blue curves represent N_2, CO_2 and H_2O dilution, respectively.

4.4 Availability of Imaginary Species in Oxy-fuel Combustion Studies

In order to show the capacity of analysis with imaginary species in fundamental oxy-fuel combustion research, the imaginary species is also introduced to auto-ignition calculations. As is mentioned in the background chapter, the CO_2 diluted combustion possesses a longer ignition delay time than that of air, fixing O_2 mole fraction in the oxidiser. Most of the paper expected the cause of the retardation of this ignition delay time to be C_p difference between N_2 and CO_2. In this section, it is evaluated whether this expectation is true or not by imaginary species based analysis.

As criteria, the ambient temperature was set to be 1200 K and the O_2 mole fraction in the oxidiser was set to be 21% by volume for both CO_2 and N_2 diluted combustion. In contrast with the thermal property characterisation analysis, the O_2 mole fraction in the oxidiser was used for comparisons since the reaction rate is not affected significantly by the CH_4 consumption amount. Rather, the chemical reaction rates are influenced directly by molar concentration of each species (mole/m^3) and thus the mole balance among reactant components is more crucial. It is further noted that the difference between CO_2 and N_2 affecting chemical reaction rates are mole based specific heat capacity, C_{pm}, and reactivity. The results of CO_2 and N_2 diluted combustions are shown in **Fig.54** and the retardation of ignition delay time in CO_2 diluted combustions can also be seen there.

To ensure that the difference between the CO_2 and N_2 diluted case is driven by discrepancy in reactivity or C_{pm}, NPM is first applied to auto-ignition calculation of air, and then auto-ignition calculation is conducted with IS_{CO2} dilution. Both results are shown in **Fig.54**. The results of air combustion with GRI 3.0 and NPM do not show any difference with each other, and thus it can be found that the N_2 related reactions do not affect the ignition delay. Also, the IS_{CO2} diluted flame does not have significant differences, due to which it can be understood that the effect of C_{pm} difference is not substantial. On the other hand, there is a relatively large variation between IS_{CO2} and CO_2 diluted cases. The CO_2 diluted mode shows the longer ignition delay from IS_{CO2}. From these facts, it is found that the replacement of one N_2 with one CO_2 leads to overall reaction delay primarily by reactivity of CO_2. For interested readers, reactions

significantly affected by CO_2 substitution to N_2 are identified. To do that, all of the reactions related to CO and CO_2 in GRI 3.0 are deactivated one by one, and each simulation result is compared with that of a normal GRI 3.0. Consequently, it can be clarified that the reactions inducing those ignition delay time differences are the following three reactions. As shown in **Fig.55**, the ignition delay time of CO_2 dilution case with deactivating these three reactions is almost identical to that of IS_{CO2} dilution case.

Reaction 1: $H + CH_2O (+ M) <=> CH_3O (+ M)$

Reaction 2: $2\ CH_3 (+ M) <=> C_2H_6 (+ M)$

Reaction 3: $HCO + M => H + CO + M$

Note that these reaction rates are dependent of the species that used as a third body.

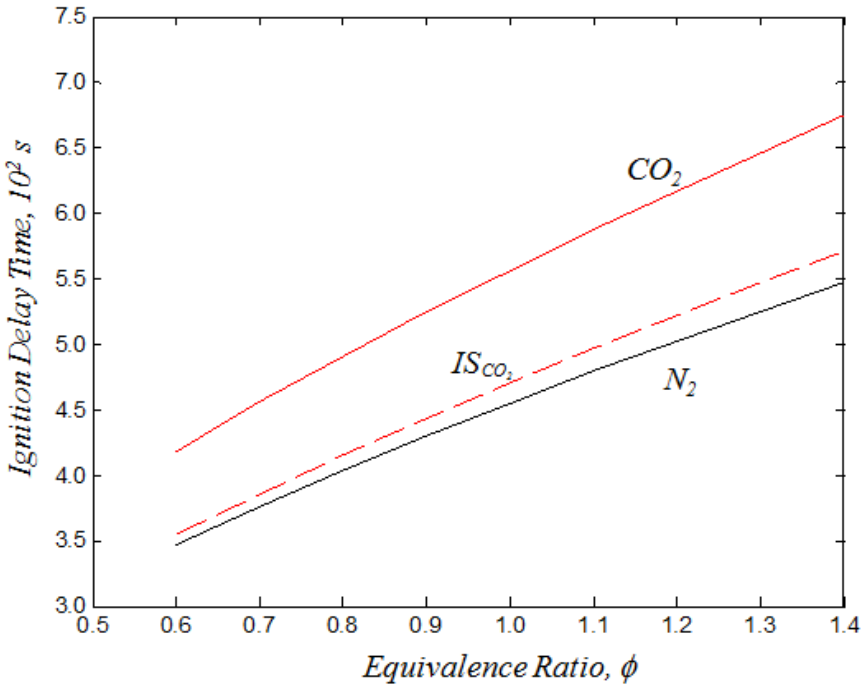

Fig.54. The ignition delay with N_2, CO_2 and IS_{CO2}. The black and solid red lines represent N_2 and CO_2 dilution respectively and the dashed red line is the result of IS_{CO2}.

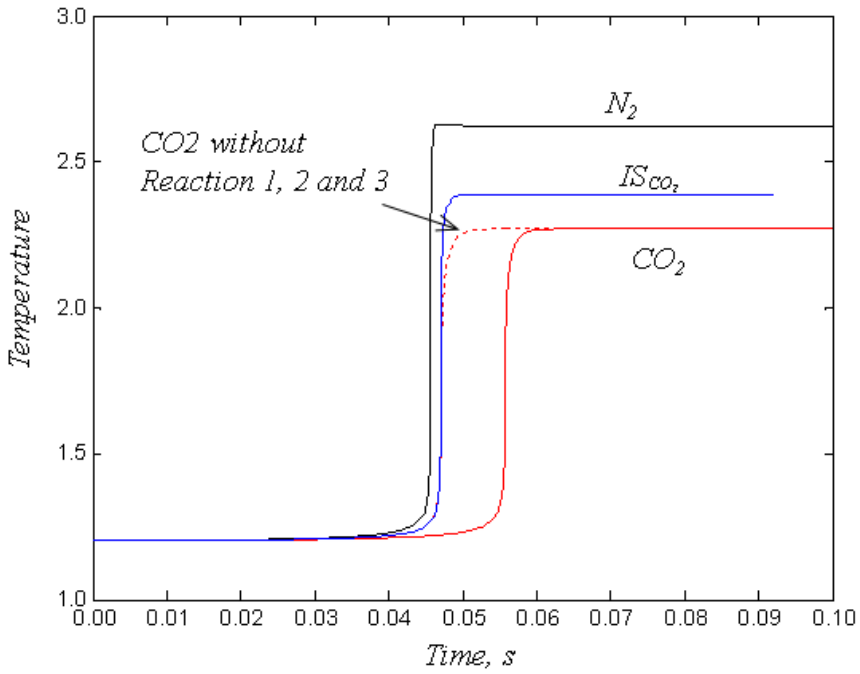

Fig.55. The results of auto-ignition with different dilution modes. The solid line represents N_2, CO_2 and IS_{CO2} dilution. The dashed line is the result with the reaction model, which removes three reactions mentioned in the text from GRI 3.0.

List of Primary Findings in This Chapter

Finding 1: CO_2 and H_2O substitution of N_2 leads to maximum T_{ad} reduction, and the reduction degree of H_2O dilution mode is larger than that of CO_2, comparing fixed Y_{O2_oxi}. The decrease of maximum T_{ad} by CO_2 is due to a discrepancy in reactivity between CO_2 and N_2, while that of H_2O is due to difference in C_p between H_2O and N_2 (section 4.1.1).

Finding 2: The 0D OTP of CO_2 diluted flame is much richer than that of N_2 diluted flame over all Y_{O2_oxi}, as well as maximum T_{ad} range. Besides, the richest shifts of both CO_2 and N_2 dilution modes are observed at approximately 55% Y_{O2_oxi}. The 0D OTP degree with H_2O dilution is smaller at less than 65% Y_{O2_oxi} than N_2 dilution, while the trend becomes opposite then onwards. Further, the off-peaking property of H_2O dilution flame is more similar to N_2 diluted flame than CO_2 diluted flame at the same maximum T_{ad} (section 4.1.2.1).

Finding 3: The deviation of CO_2 from N_2 diluted combustion in 0D OTP mentioned in finding 2 mainly arises from the reactivity difference between CO_2 and N_2, while that of H_2O from C_p difference of H_2O from N_2 (section 4.1.2.2).

Finding 4: The most influential species in 0D OTP is CO and H_2 (section 4.1.2.2).

Finding 5: The fraction of CO emission is the largest in CO_2 diluted combustion, followed by N_2 and H_2O diluted modes. The distinctive feature of CO_2 diluted flame from the other modes is observed in response of EI_{CO} to variation of Y_{O2_oxi}. The CO_2 dilution mode holds a peak, while the others increase monotonically with an increase of Y_{O2_oxi}. This can be due to the competition between CO dissociation encouragement via an increase of T_{ad} and that of discouragement via a decrease of potential CO_2 in mixture for dissociation, by an increase of Y_{O2_oxi} (section 4.2).

Finding 6: From a fuel consumption efficiency perspective, CO_2 diluted flames are preferable to H_2O diluted flames, while the CO emission index becomes significantly worse than H_2O dilution mode (section 4.3).

Finding 7: Analysis through imaginary species is a powerful tool in oxy-fuel combustion.

Finding 8: Ignition delay time of CO_2 diluted flame is larger than N_2 diluted flame at 21% O_2 fraction by volume in the oxidiser, primarily because of reactivity difference rather than the C_{pm} difference between the two (section 4.4).

Chapter 5
Analysis of Oxy-fuel Laminar Diffusion Flames

This chapter explores the thermal structure of oxy-fuel laminar diffusion flames relative to N_2 diluted flames in a counter-flow configuration. The special focus is on OTP in the flame geometry, that is, 1D OTP. The physics behind 1D OTP are clarified here since the mechanism of OTP in 1D flames has not been elucidated in detail thus far.

5.1 1D Off-peaking with N_2 and CO_2 Diluted Flame

This section clarifies the response of 1D OTP property to diluting species replacement and variation of diluting degree. As with 0D OTP, the structure of heat release and specific heat are also explored. There is little literature that focuses on the OTP in one-dimensional flames in depth, even for conventional air flame and thus the 1D OTP response to strain rate variation is explored in detail, using air flame.

5.1.1 Air Flame

The thermal structure obtained by counter-flow diffusion flame simulation is shown in **Fig.56** in ξ space with three different strain rates. The simulation was conducted with multi-component diffusion model and the Soret effect being activated. In **Fig.56**, the T_{ad} is also shown for reference. The graph shows that the 1D temperature peak is on the richer side at low strain rate (15 s^{-1}) than the T_{ad} peak, and is moved further towards the richer side at intermediate strain rate (200s^{-1}), while the 1D OTP degree at near extinction strain rate (470a^{-1}) is almost the same as intermediate strain rate. As with 0D simulation, it is important to evaluate the distribution of heat release amount, q_p, and specific heat capacity per unit mass, C_p, in the mixture fraction field. **Fig.56** also contains the distribution of q_p and C_p respectively. The general trend of both curves is not different from T_{ad} results. The C_p was monotonically increased with mixture fraction and the q_p has parabolic curve with the peak being on the richer side of stoichiometry. From this fact, it can be understood that the temperature structure of counter-flow diffusion flame was skewed to the rich side of stoichiometry, since more heat release was undertaken in the rich region. In addition, the lean shifting of

temperature peak from heat release peak condition arose from the monotonic increase of C_p with mixture fraction. Mathematically, the 1D OTP is determined such that the following equation is established:

$$\frac{\frac{d}{d\emptyset}q_p(\xi)}{q_p(\xi)} = \frac{\frac{d}{d\emptyset}C_p(\xi)}{C_p(\xi)}. \quad (51)$$

The discussion is next developed to a variation of the peak position of q_p by strain rates and its relation between the peaks of q_p and temperature. **Fig.56** shows that the q_p peak position in counter-flow flame at lower strain rate (15 s^{-1}) is on the richer side, comparing 0D simulation results and the further movement towards the rich side occurred as the strain rate is increased. **Fig.57** shows the q_p related term, $(dq_p/d\xi)/q_p$, and C_p related term, $(dC_p/d\xi)/C_p$, in equation (51) as a function of ξ. The gradient of $(dq_p/d\xi)/q_p$ where $(dq_p/d\xi)/q_p$ is zero (at the peak position of q_p), becomes smaller as the strain rate is increased. In particular, the gradient becomes much smaller from intermediate strain rate to high strain rate. In other words, the driving force for which the temperature peak moves away from the q_p peak is enhanced with the increase of strain rate, especially in the transition from intermediate to high strain rate. This could be the exact reason why the peak position of temperature with higher strain rate was almost identical to that of the intermediate strain rate, while the q_p peak at the high strain rate was distinguishingly in the richer region than at the intermediate strain rate.

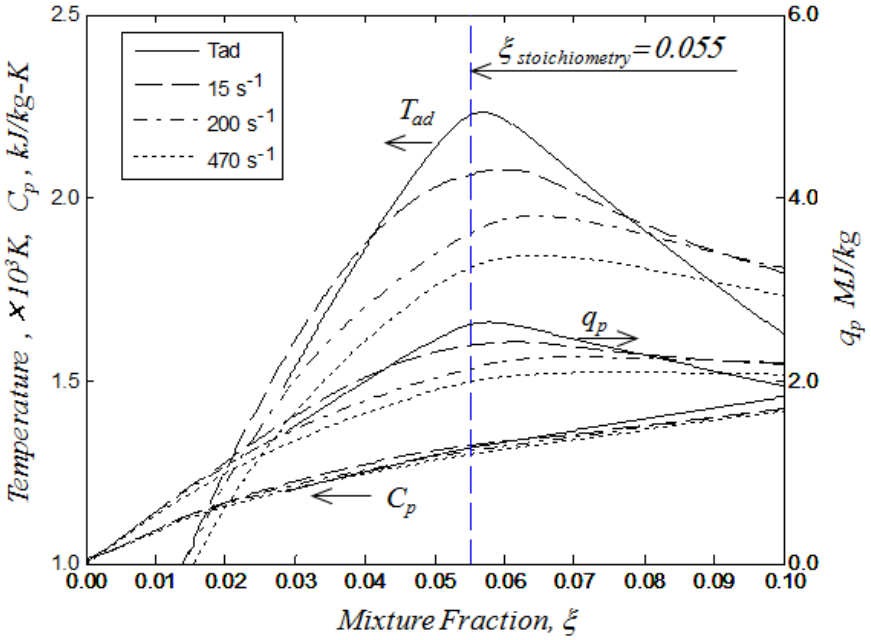

Fig.56. Thermal structure of air flame with various strain rates in counter-flow diffusion flames. The blue line represents stoichiometric mixture fraction of air-methane flame, 0.055.

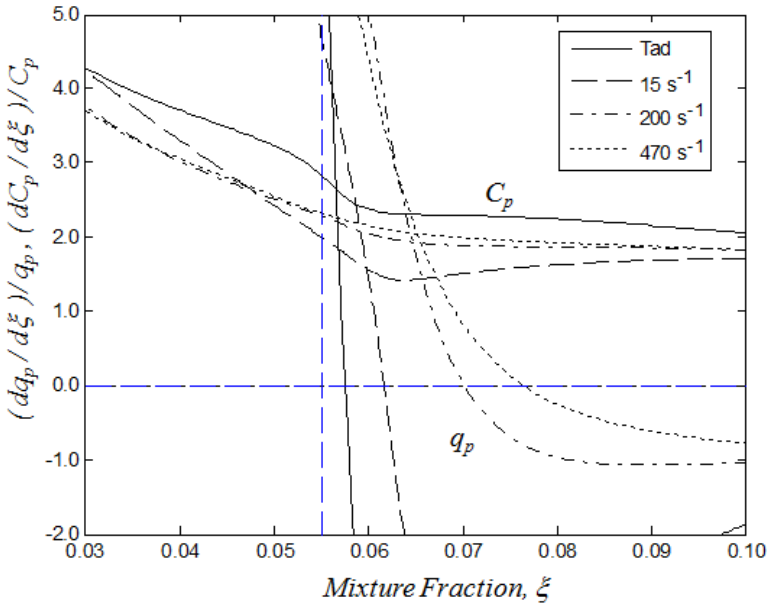

Fig.57. The dominance of q_p and C_p on 1D OTP with various strain rates. The vertical blue line represents stoichiometric mixture fraction of air-methane flame, 0.055. The crossing points of the horizontal blue line and q_p lines with different strain rates means the mixture condition of the q_p peaking.

5.1.2 Flame with Other Dilution Degree

To see the response of 1D OTP to variation of N_2 diluting degree, the counter-flow calculation was conducted with the various amounts of N_2 in the oxidiser. The result is shown in **Fig.58**. To evaluate the 1D OTP with different diluting degree, a normalised mixture fraction, ξ_n, is employed. The result of the low strain rate shows a monotonic movement towards the lean side, with an increase of Y_{O2_oxi} while there is an initial increase and a sequential decrease at the intermediate and high strain rate. It is worth noting that, with the high O_2 content in the oxidiser (O_2 enriched flame), the peak temperature position is present in the lean side of stoichiometry.

In the case of 0D OTP, hydrocarbon flames never peak at the lean side of stoichiometry. As with the previous air flame analysis, the position of q_p peak is of interest. The q_p peak position is shown in **Fig.59** in Y_{O2_oxi} space. Contrary to the temperature structure, the q_p peaks are present in the rich side of stoichiometry all over conditions and hold a further shift towards the rich side as the Y_{O2_oxi} increases. In addition, it can be seen that the gap between the mixing conditions of q_p and temperature peak is larger with the increase of Y_{O2_oxi}. To evaluate these phenomena, the $(dq_p/d\xi)/q_p$ and $(dC_p/d\xi)/C_p$ are explored again. **Fig.60** and **Fig.61** show the results with the different Y_{O2_oxi}. The $(dC_p/d\xi)/C_p$ value becomes smaller with Y_{O2_oxi}, (the role of C_p term becomes smaller). However, the gradient of $(dq_p/d\xi)/q_p$ near ξ of the q_p peaking is decreased with the O_2 addition in the oxidiser. That is, the lean shift force by C_p became more dominant with O_2 content. Considering this, it can be said that the cause of the lean 1D OTP shift is the decrease of $(dq_p/d\xi)/q_p$ gradient with Y_{O2_oxi} increase.

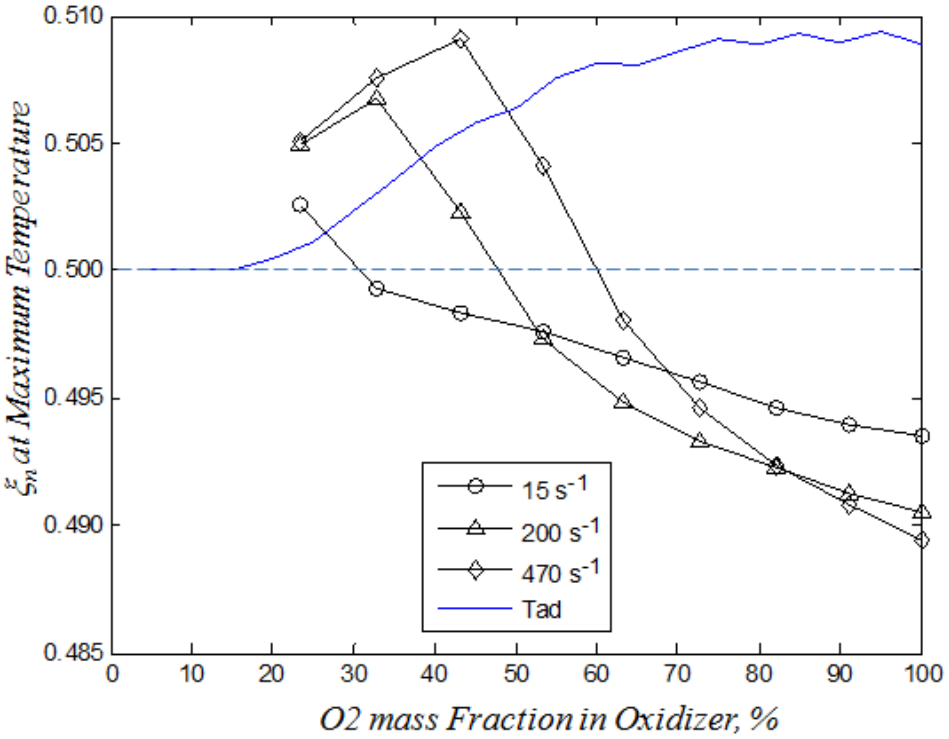

Fig.58. The response of 1D OTP to variation of N_2 dilution degree with different strain rates. The blue line is the result of 0D simulation.

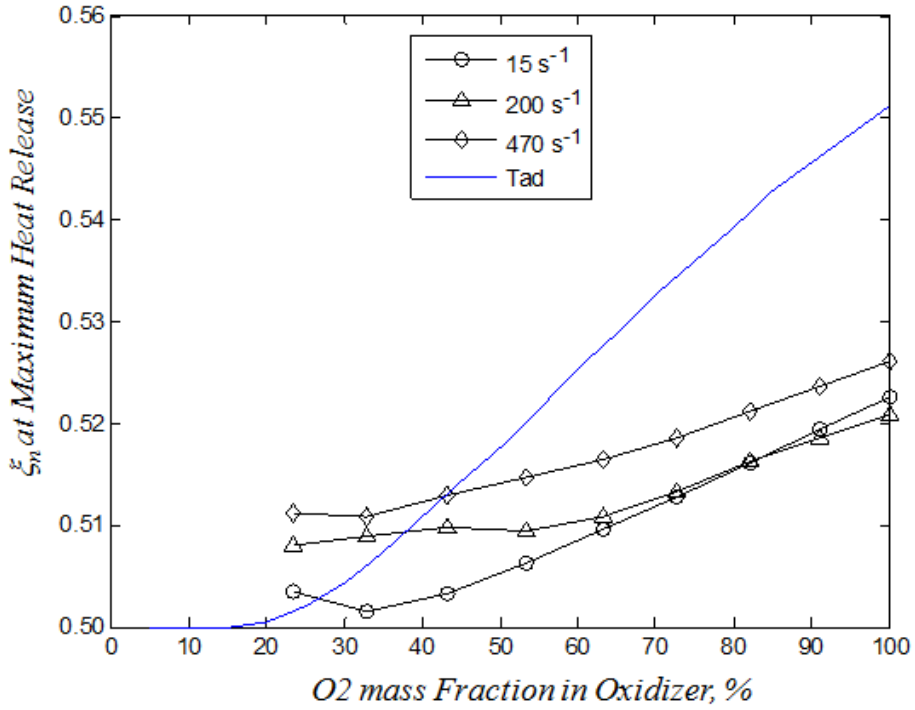

Fig.59. The mixture condition of q_p peaking with different strain rates. The blue line is the result of 0D simulation.

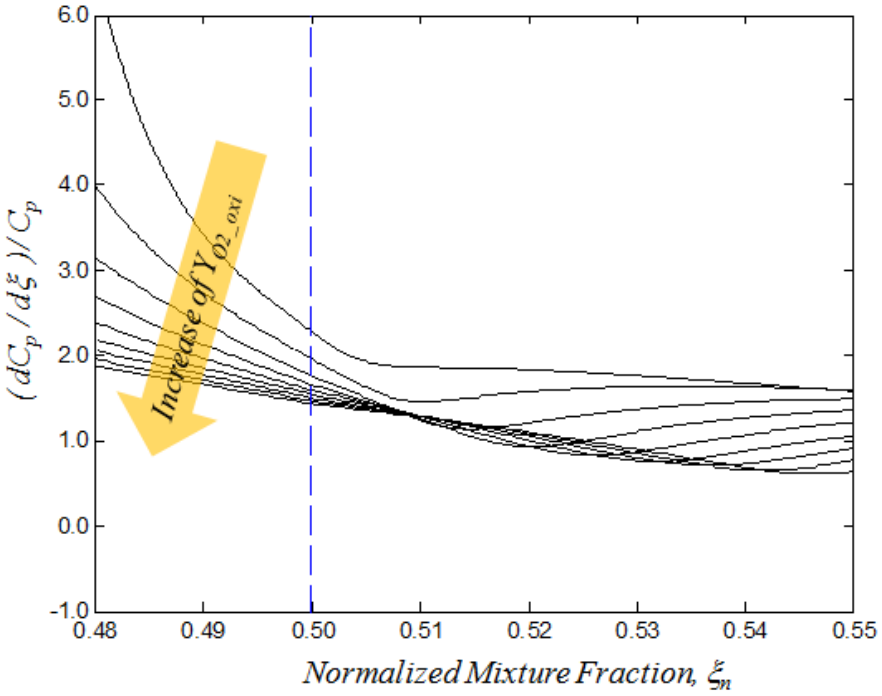

Fig.60. The relation of the distribution of $(dC_p/d\zeta)/C_p$ with different Y_{O2_oxi}. The blue line represents the stoichiometric mixture condition. The top curve is the result of air flames and the bottom is the result of pure O_2 flames.

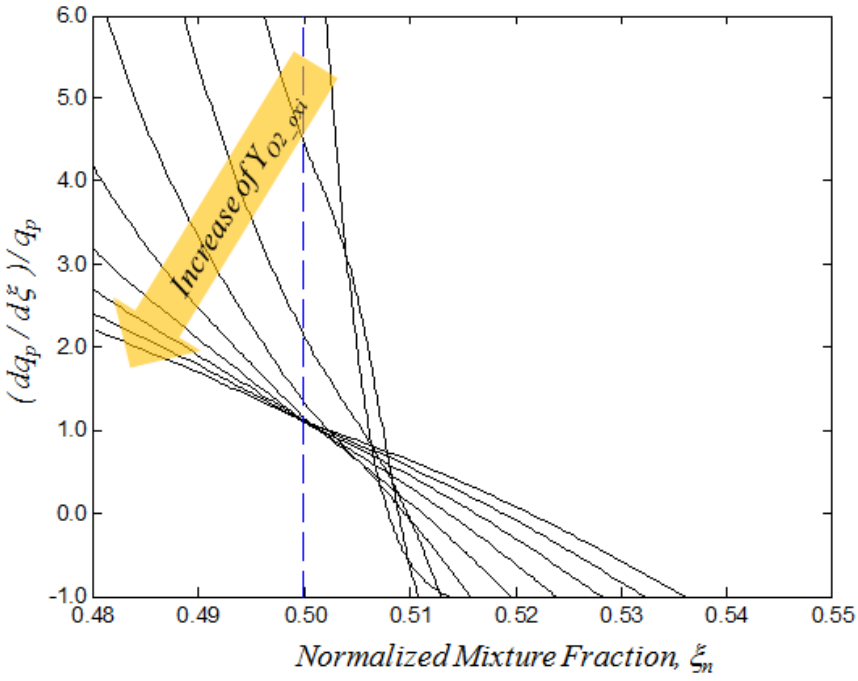

Fig.61. The relation of the distribution of $(dq_p/d\zeta)/q_p$ with different Y_{O2_oxi}. The blue line represents the stoichiometric mixture condition.

5.1.3 CO_2 Diluted Flame

The 1D OTP of CO_2 diluted oxy-fuel flame is characterised here. **Fig.62** shows the structure of temperature, q_p and C_p with 23% Y_{O2_oxi}, which is equalled to Y_{O2_oxi} in air. As with air flame, the temperature peak position is present in the rich side of the stoichiometry and the degree is larger with increase of strain rate. The remark is also applicable to heat release peak. The C_p value does not have significant difference to the strain rate variation. **Fig.63** shows the 1D OTP properties of the CO_2 diluted flames with other Y_{O2_oxi}. In the graph, while the CO_2 diluted flame also peaks in the lean region in temperature in O_2 enriched region, the peak is on the richer side than N_2 diluted flame all over the condition. The condition of q_p peaking with various Y_{O2_oxi} is also shown in **Fig.64**. The peak of q_p situates in the rich side of stoichiometry and is also in the richer side than N_2 diluted flame.

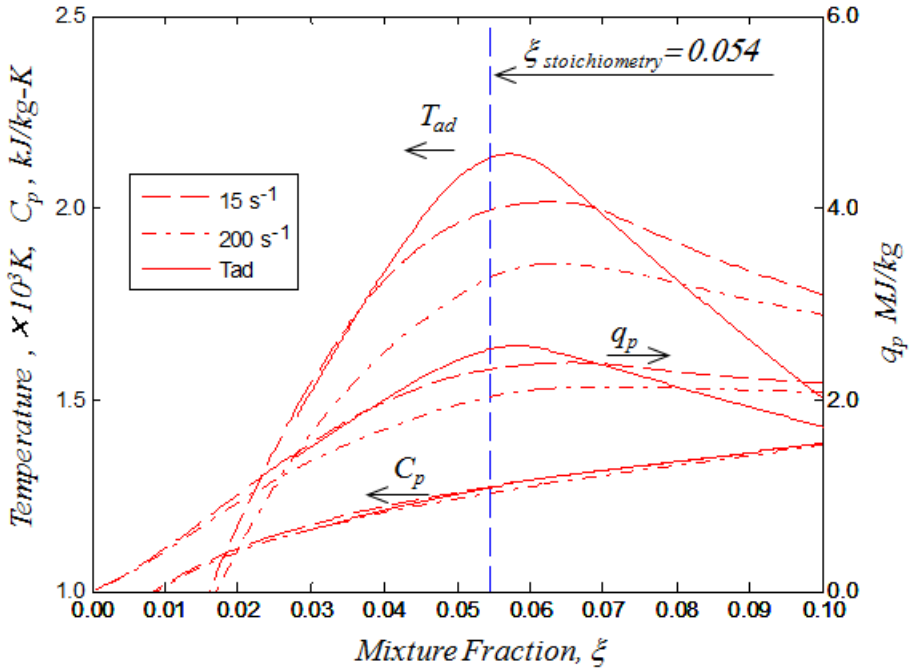

Fig.62. Thermal structure of CO_2 diluted flame with different strain rates in counter-flow diffusion configuration. The Y_{O2_oxi} is 23%. The blue line represents stoichiometric mixture fraction of air-methane flame, 0.054.

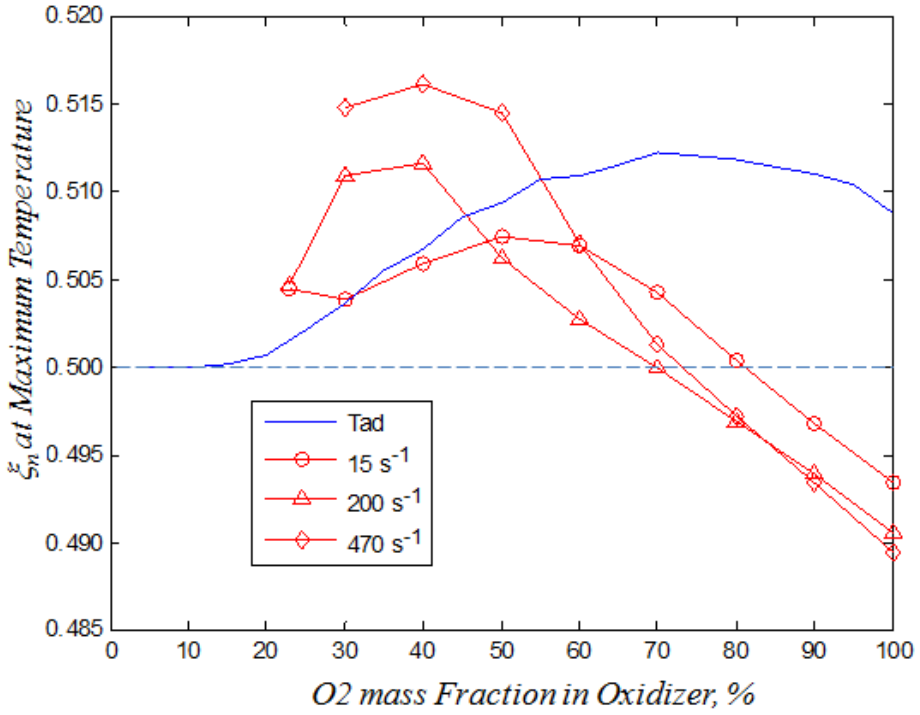

Fig.63. The response of 1D OTP to variation of CO_2 dilution degree with different strain rates. The blue line is the result of 0D simulation.

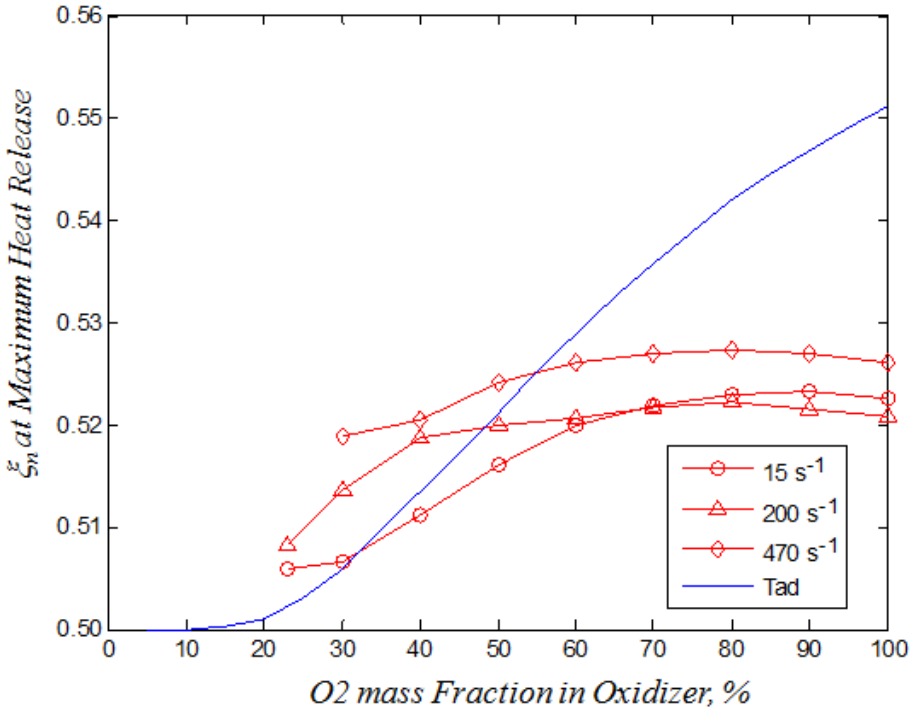

Fig.64. The mixture condition of q_p peaking with different strain rates. The blue line is the result of 0D simulation.

5.2 Clarification of 1D Off-peaking Theory

In the above, the rich and lean shift of temperature peak position in counter-flow flame was observed. In the following, the physics of the both rich and lean shift are explored respectively. For the analysis of rich shift, the air flame is applied and for lean shift, pure O_2 flame is employed at intermediate strain rate. After that, the other O_2 mass fraction with N_2 dilution is evaluated and then the extension of the theory to CO_2 diluted oxy-fuel mode is conducted.

5.2.1 1D Rich Shift Mechanism (Air Flame)

While a rich shift of air flame in 1D simulation was observed as with 0D simulation, it is not necessarily true that the physics are the same as for 0D OTP. This is because molecular transport, conduction and finite-rate chemistry are activated in opposed-flow flame. Hence, the primary cause of the rich 1D OTP may not be dissociation. These factors in the opposed-flow geometry, which is not included in the 0D case, can create three new effects on q_p and C_p distribution: the deviation from chemical equilibrium, the variation of chemical equilibrium state and thermal energy transfer. To clarify the physics of 1D rich off-stoichiometric peaking, each effect is explored in the following.
Before proceeding to each analysis, the q_p distribution in ξ, obtained by equilibrium calculation with pressure and temperature fixed rather than constant pressure and enthalpy, is evaluated briefly. This helps readers to understand the following analysis better, since reactions occur at constant pressure and temperature at each position in space in the opposed-flow configuration, while the T_{ad} calculation above fixed the pressure and enthalpy.

The equilibrium calculation with temperature and pressure constant is called TP equilibrium calculation (TPEC) and with enthalpy and pressure constant is called HP equilibrium calculation (HPEC) for simplicity. **Fig.65** shows the result of TPEC, changing ambient temperature. In the graph, there is no shift of q_p peak from stoichiometry at a temperature less than 1,500 K while the rich shift of the q_p peak is observed above 1,500 K due to start of dissociation reaction in those temperature regimes, as with HPEC.

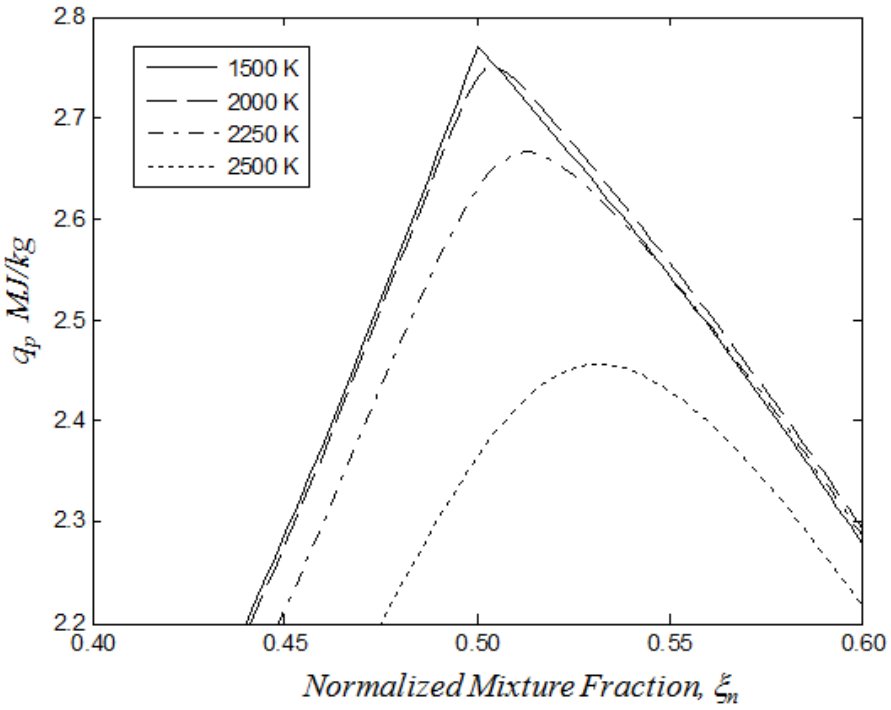

Fig.65. The structure of heat release by TPEC. Each curve has different ambient temperature.

In the counter-flow flame, the time scale of chemical reaction becomes finite and then some reactions may not complete, equivalently the suppression of reaction occurs. As a consequence, the deviation from chemical equilibrium can be observed at each point in the flame. This can affect the thermal structure in flame. Here, the effect of this deviation from chemical equilibrium on 1D OTP is explored at intermediate strain rate. To do that, the composition and temperature of the raw 1D simulation result at each mixture fraction is taken and then the TPEC is implemented using the composition and temperature as an initial condition. This process is referred to as post-equilibrium calculation process (PECP).

If the equilibrium reaches at a certain mixture fraction in flame, no heat release can be seen at the mixture fraction by the PECP. The results are shown in **Fig.66**. To understand the graph easily, the q_p after PECP is shown, being added to the heat release via the raw counter-flow flame (the gap between q_p curves of PECP) and raw counter-flow flame stands for the heat release via PECP. The two important features can be seen in **Fig.66**. First, the q_p after PECP peaks at stoichiometry. Also, the heat release via PECP is greater at stoichiometry than in the slightly rich side of stoichiometry. From

these two facts, it can be said that discrepancy in the deviation from equilibrium state at each position significantly influenced the rich shifting of heat release curve in counter-flow flame. **Fig.66** also shows the structure of C_p of the raw counter-flow flame results and results after PECP. The substantial gap cannot be observed in C_p via PECP. In terms of the shape of the q_p, the heat release curve was flattened by the PECP. Hence, the effect of the $(dq_p/d\xi)/q_p$ becomes smaller relative to the C_p term (the further the distance between the temperature peak and the heat release peak). **Fig.67** shows the structure of $(dq_p/d\xi)/q_p$ with the raw and PECP results for better understanding of the trend.

The molecular transport and the thermal conduction can alter states of chemical equilibrium at each point from that of 0D reactor, and they contribute to thermal energy transfer from one point to another in flame. These two can also affect the thermal structure in flame. To evaluate the combined effects of these on 1D OTP, the TPEC is conducted, taking the resultant temperature of counter-flow flame as initial condition. This process is called PECP only extracting temperature information (PECPT). Note that the composition of initial state in PECPT consists of CH_4 and air, while that of PECP is the resultant composition of counter-flow flame. By comparing the results after PECPT and PECP, the effect of variation of chemical equilibrium state as well as thermal energy transfer, can be revealed on the structure of q_p and C_p. **Fig.66** shows the results of PECPT. As with the result of PECP, the PECPT peaks at stoichiometry. Thus, it can be understood that the mixing condition of heat release peaking was not affected by the thermal energy transfer and variation of chemical equilibrium state. However, there is a difference between the PECP and PECPT curves and the gap can affect the $(dq_p/d\xi)/q_p$, which is also relevant to temperature structure. **Fig.67** shows the structure of $(dq_p/d\xi)/q_p$. It can be understood that the $(dq_p/d\xi)/q_p$ effect becomes more dominant by the variation of chemical equilibrium state and thermal transfer relative to that of C_p. That is, the relatively small distance between temperature peak and heat release peak position, while the degree is not significant.

It is also worth noting that the q_p curves after PECP and PECPT have a sharp gradient at stoichiometry and linear line, in both rich and lean side of stoichiometry, which is characteristic of no dissociation flame. To make sure that the dissociation did not occur substantially at this condition, PECPT is conducted with a dissociation suppressed

reaction model. **Fig.66** shows the result. The curves of PECPT and PECPT with the dissociation suppressed reaction model are almost identical. Consequently, it can be understood that the dissociation did not occur significantly at the current condition.

Considering the above, the rich 1D OTP of air flame was observed mainly due to the discrepancy at each mixture fraction in the degree of the deviation from chemical equilibrium state (the finite-rate chemistry effect, rather than dissociation). Much more heat release was suppressed by finite-rate chemistry at stoichiometry than on the richer region.

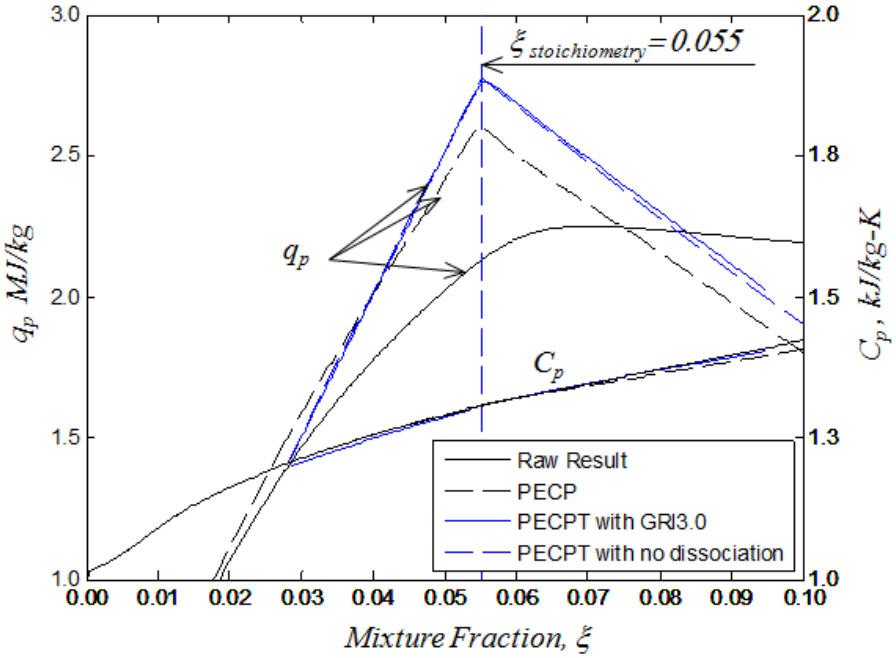

Fig.66. Thermal structure of counter-flow air flames and the post-processed results. The vertical blue line represents stoichiometric mixture fraction of air flame.

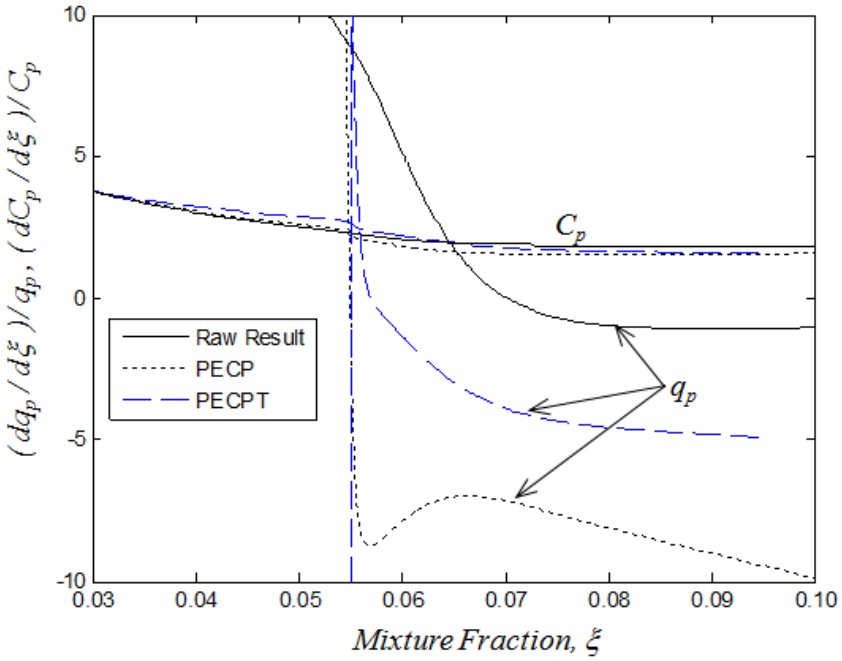

Fig.67. The dominance of q_p and C_p on 1D OTP with counter-flow flame and the results after some post-processing. The vertical blue line represents stoichiometric mixture fraction of air-methane flame, 0.055 .

5.2.2 1D Lean Shift Mechanism (Pure O_2 Flame)

The physics of lean shifting of pure O_2 flame is explored here. The initial interest is in the peak position of the q_p. As with the analysis of 1D rich shifting, PECP is applied to evaluate the deviation from chemical equilibrium state at each position and the results are shown in **Fig.68** with the raw counter-flow flame result. The gap between two curves is relatively small and only a slight shift of q_p peak is observed after PECP. In addition, the PECPT is also employed to explore the effect of heat transfer and the variation of chemical equilibrium state. The result is included in **Fig.68**. Although the gap between the results after PECPT and PECP in q_p is relatively large, the peak position of q_p is not significantly different. Further, PECPT with Dissociation Frozen Mechanism is also conducted for evaluation of dissociation effect and the result is shown in **Fig.68**. As is expected from flame temperature range, a significant amount of dissociation is observed. Also, it can be seen that the dissociation occurs more at stoichiometry than the rich side of stoichiometry as with the T_{ad} structure. Consequently, the rich shifting of pure O_2 flame in q_p was observed due to dissociation. In terms of the C_p, results after PECP and PECPT do not show much difference from the raw output

results. **Fig.69** shows the structure of $(dq_p/d\xi)/q_p$ and $(dC_p/d\xi)/C_p$ terms with the raw, PECP and PECPT results. It is seen that the gradient of $(dq_p/d\xi)/q_p$ near q_p peak is much larger with PECP than the raw result, and thus it is found that the effect of deviation from chemical equilibrium moved the temperature peak significantly away from q_p peak position. The $(dq_p/d\xi)/q_p$ and $(dC_p/d\xi)/C_p$ after PECPT is also shown in the graph. The gradient of $(dq_p/d\xi)/q_p$ near q_p peak is similar to the PECP curve and then the heat transfer and variation of chemical equilibrium state at each position is not dominant in lean shifting.

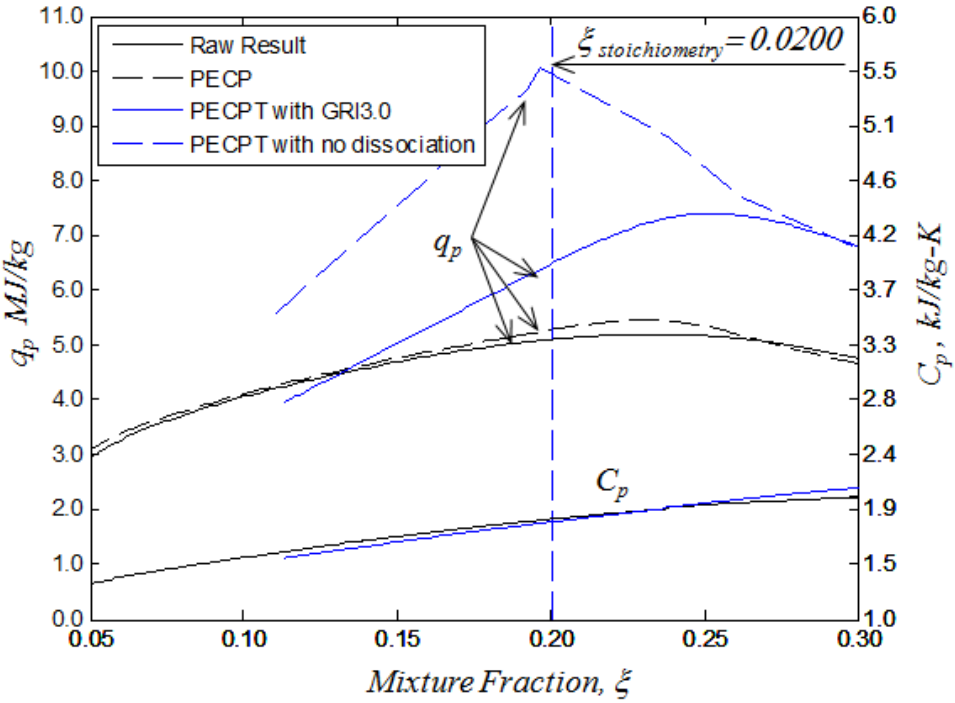

Fig.68. Thermal structure of counter-flow pure O_2 flames and the post-processed results. The vertical blue line represents stoichiometric mixture fraction of pure O_2 flame.

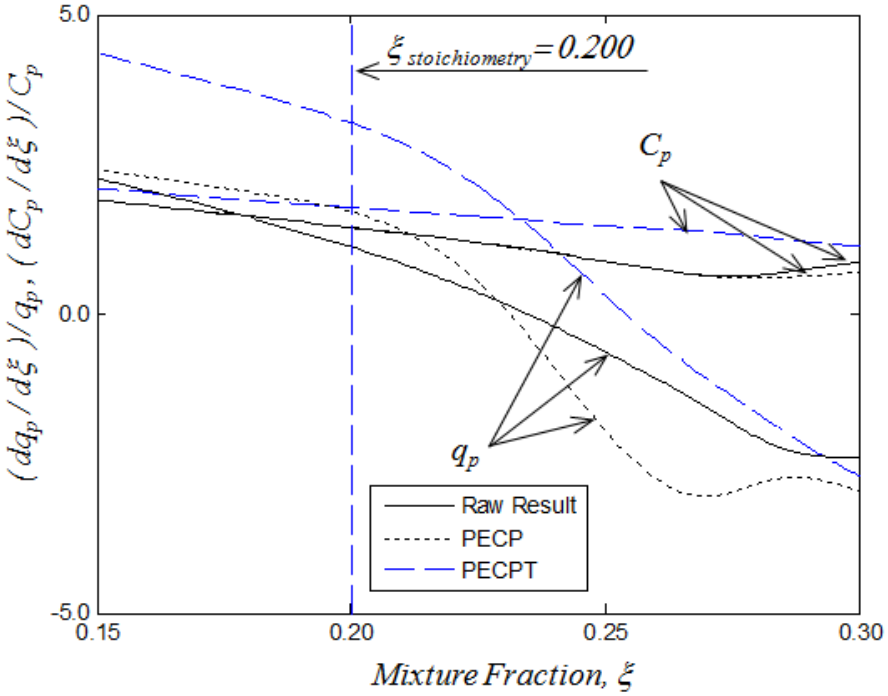

Fig.69. The dominance of q_p and C_p on 1D OTP with counter-flow pure O_2 flame and the results after some post-processing. The vertical blue line represents stoichiometric mixture fraction of pure O_2 flame.

5.2.3 The Extension of Theory to CO_2 Diluted Oxy-fuel Flame

The effect of N_2 replacement with CO_2 on 1D OTP property is explored here. There are some differences between the N_2 and CO_2 in physical property as diluents: reactivity, C_p, thermal conductivity and diffusivity. As with 0D OTP analysis, the dominant factor is identified here. As an initial step, it is confirmed whether the N_2 related reaction such as NO formation is important for 1D OTP or not. To do that, NPM is applied to counter-flow simulation with N_2 dilution. As a result, the 1D OTP properties of GRI and NPM are almost identical and thus the N_2 can be regarded as completely inert gas in the 1D OTP. Next, the imaginary special IS_{CO2}' is employed as the diluting species. This IS_{CO2}' has the same thermo-chemical data and transport data as CO_2, with the molecular weight being 45. Note that in contrast with the previously used IS_{CO2}, the IS_{CO2}' has transport data. By this definition, the IS_{CO2}' behaves in the same way as N_2 in reaction (inert species, while the same as CO_2 in other properties). **Fig.70** shows the 1D OTP properties with N_2, CO2 and IS_{CO2}' diluted flames. The IS_{CO2}' diluted flame and N_2 diluted flame are quite similar to each other and thus it can be understood that

the dominant factor of further rich shifting in oxy-fuel combustion relative to N_2 diluted flame is the reactivity difference between CO_2 and N_2.

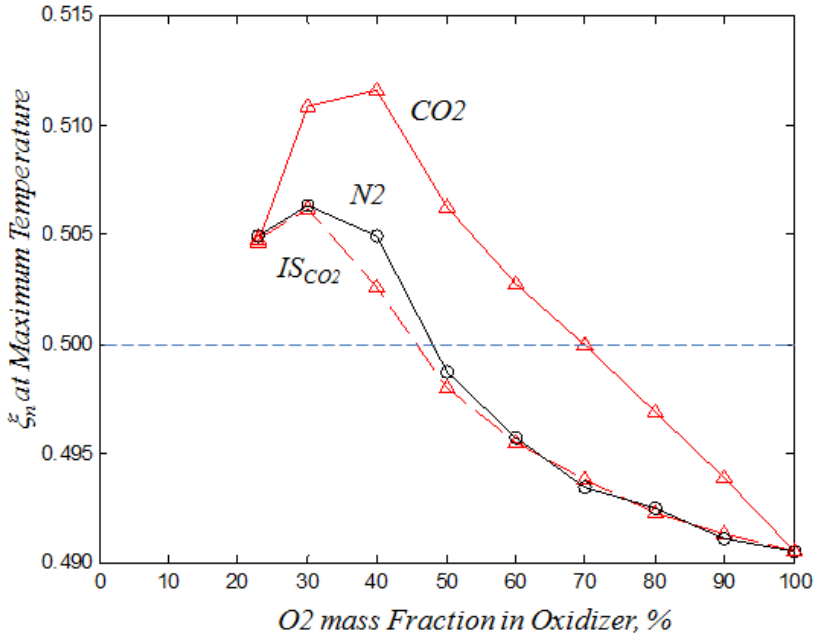

Fig.70. The response of 1D OTP to replacement of diluting species and variation of diluting degree. The solid lines represent N_2 and CO_2 diluted flame respectively. The dashed lines are the results with imaginary species dilution (IS_{CO2}').

Primary Findings in This Chapter

Finding 9: As with 0D OTP, 1D OTP can be elucidated well by discussion based on q_p and C_p distribution (section 4.1.1).

Finding 10: The temperature peaks at lean side of stoichiometry in O_2 enriched regime of both CO_2 and N_2 diluted flame (section 4.1.2 and 4.1.3).

Finding 11: The primary factor of both rich and lean 1D OTP is finite-rate chemistry. The finite-rate chemistry suppresses the heat release more at stoichiometry than on the rich regime and thus the heat release peak position is moved towards richer side. At the other extreme, the finite-rate chemistry flattened the heat release curve and then the C_p force of lean shifting becomes competitive. For rich shift condition, such as highly CO_2 contained flame, the former effect is more dominant than the latter, and rich shift can be

observed. For lean shift condition, such as highly O_2 enriched flame, the latter effect is dominant and then lean shift can be observed (section 4.2).

Finding 12: CO_2 diluted oxy-fuel flame possesses a richer shift of peak temperature than conventional N_2 diluted flame. This is primarily because of the reactivity difference between CO_2 and N_2 (section 4.1.3 and 4.2.3).

Chapter 6

Thermal Structure Measurement of Oxy-fuel Laminar Flames

This chapter provides the results and discussions of thermal structure measurements of oxy-fuel laminar flames. Prior to presenting the primary experiment applied to an oxy-fuel flame, the procedure in the determination of operation conditions and the validation of the used measurement system via a Bunsen air flame is also explored in detail.

6.1 Determination of Operating Condition

6.1.1 Flow Condition

A CNG-air Bunsen flame was utilised as attest case with a mixture and flow speed of the main nozzle set to be ϕ=0.78 and 1.02 m/s respectively. The lean mixture was selected to suppress the diffusion halo around the premixed Bunsen cone, which can produce unnecessary emission for this study. The Reynolds number in the main tube was 8.96×10^2 ($<< 2.30 \times 10^3$) (laminar flow). The flow speed of co-flow was 6.11×10^{-2} m/s. The co-flow flow speed was determined so that the premixed Bunsen cone was more stable and the diffusion halo was removed.

For the counter-flow diffusion flame with CO_2 dilution, the mixture of oxidiser and fuel stream was set to be 36% O2 + 74% CO_2 and 40% CNG + 60% CO_2 by volume, respectively. The fuel stream was diluted by CO_2 to inhibit soot formation. The flow speed of the oxidiser stream and fuel stream was 0.50 m/s and 1.11 m/s and then the global strain rate was 137 s^{-1} (separation distance: 22mm). The shield gas of CO_2 was employed at 8.65×10^{-3} m/s (fuel side) and 0.256 m/s (oxidiser side) to prevent external air entrainment. The determination of the above operation condition was based on stability of the flat flame and appearance/disappearance of the outer flame around flat flame of interest. In addition, in order to reduce the effect of exhaust stream buoyancy induced fluctuations, the counter-flow burner was surrounded by a fine messing sheet of 1.5 mm × 1.5 mm, as is shown in **Fig.71 (a)**. The resultant CO_2 diluted oxy-fuel, counter-flow diffusion flame is also shown in **Fig.71 (b)**.

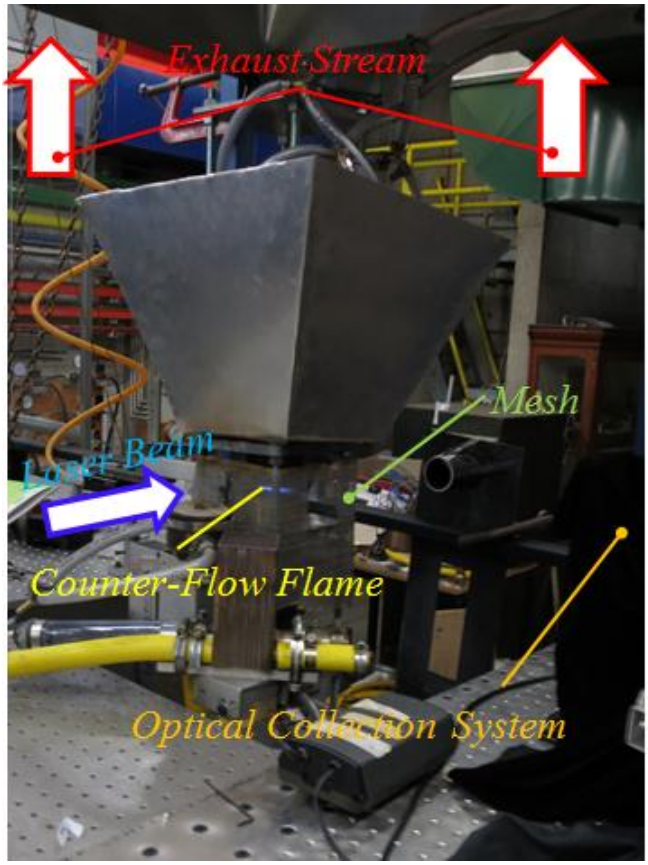

(a)

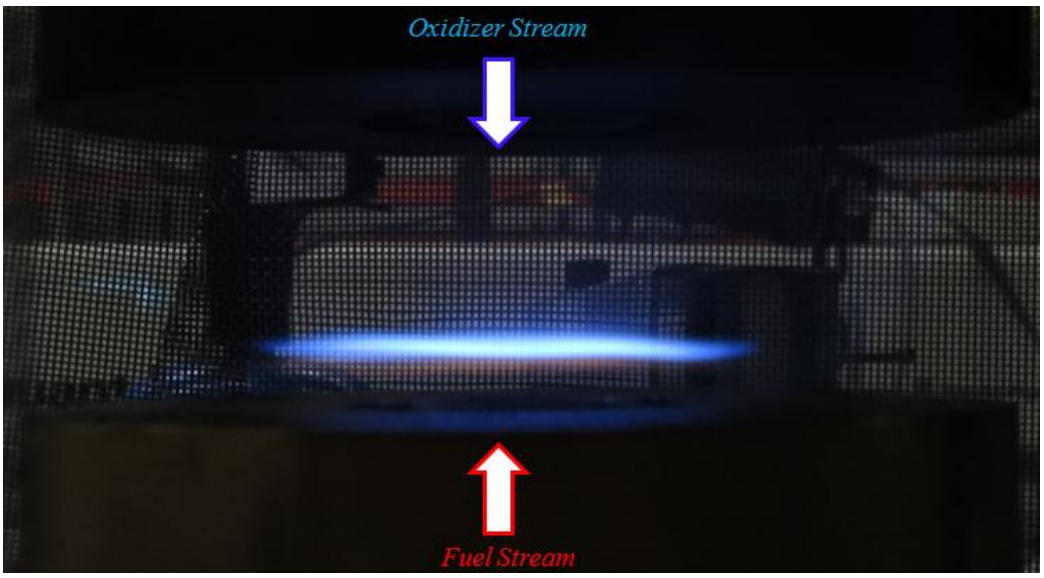

(b)

Fig.71. Pictures of experiments. (a): Schematic picture, (b) Counter-Flow Diffusion Flame with CO_2 dilution.

6.1.2 Input Laser Irradiance (Linearity Check of LIF Signal)

The procedure to determine the laser operational condition is explored here based on the linearity limit of OH LIF signal. The input laser irradiance per pulse used in the experiment must be set so that the consequent OH LIF signal is linear at probed volume, that is, that the OH LIF is in linear regime. The measurement beyond the linearity regime (such as in the saturated LIF regime), poses challenges for the quantification of the LIF signal that will not be explored in this thesis. To confirm the linearity, the response of OH LIF signal to various laser input energies was examined by changing the Q-switch delay time of Nd:YAG laser (320 μs to 250 μs). The Nd:YAG laser used in the present study realises the strongest signal at a Q-switch of approximately 200 μs, and thus the laser power is increased as Q-switch delay goes from 320 μs to 250 μs (Appendix.2). In this process, the wavelength emitted by dye laser was fixed to 283.3852 nm ($Q_2(6)$) and the laser beam was applied to Bunsen air-CNG flame. The result is shown in **Fig.72**.

It was observed that the transition from linear to saturation regime was around 4.3 mJ. Note that when Q-switch delay time is varied, the spatial profile of laser beams also alters and thus it is not always true that the laser energy obtained by the laser energy monitoring camera represents the input laser intensity at volume of interest in flame. In order to compensate for the uncertainty of the result, a spectral profile was obtained with input laser energy and the spectral shape was compared with normalisation. If the result arises from linear regime, the curve shapes are similar to each other. For reference, theoretical spectral profiles in linear regime and partially saturated regime are shown in **Fig.73**. The experimentally obtained result is shown in **Fig.74**. It can be understood that the spectral profiles of 0.7, 2.6 and 4.3 mJ are similar, while the other has a more wide shape. Considering the above, the laser energy of less than 4.3 mJ is in linear regime and then employed in the following Bunsen air flame application.

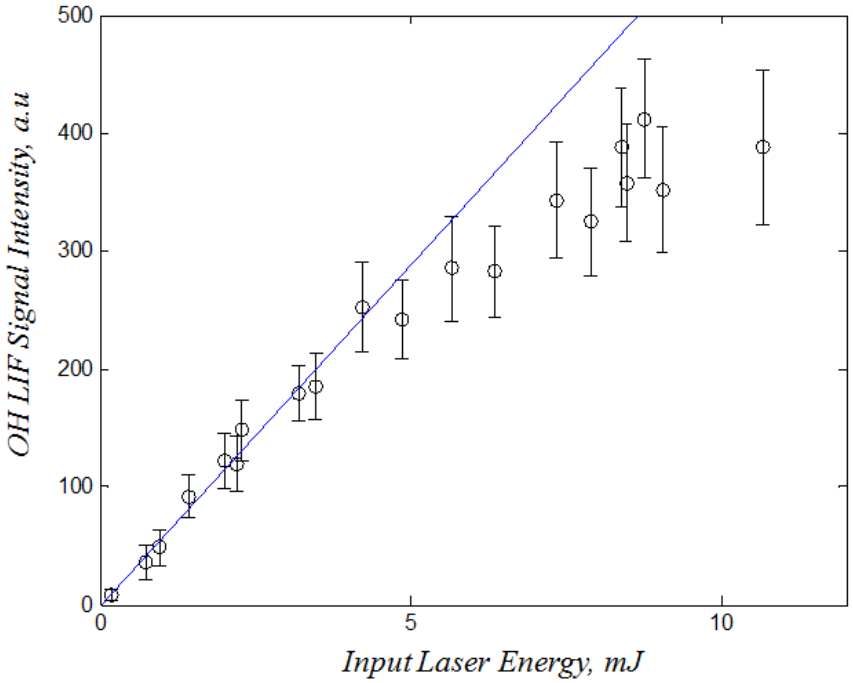

Fig.72. Linearity test results. The error bar represents the confidence interval of 2σ (95.45%). The used wavelength is 283.3852 nm ($Q_2(6)$). The 200 shots were averaged over. The blue line was obtained by least square method using the results of input laser energy less than 4.3 mJ.

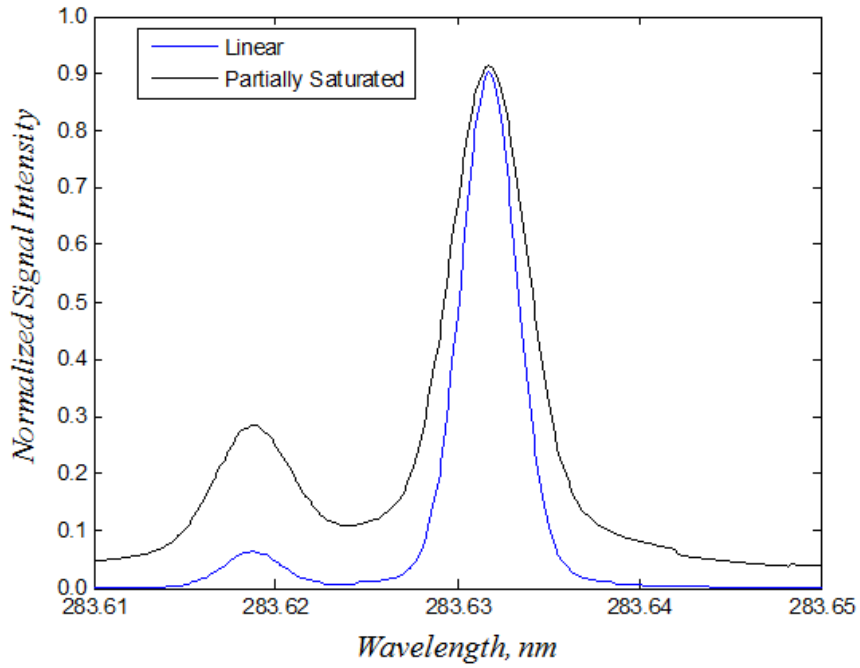

Fig.73. The comparison of theoretical spectral profile of Q1(8) with linear and partially saturated OH LIF.

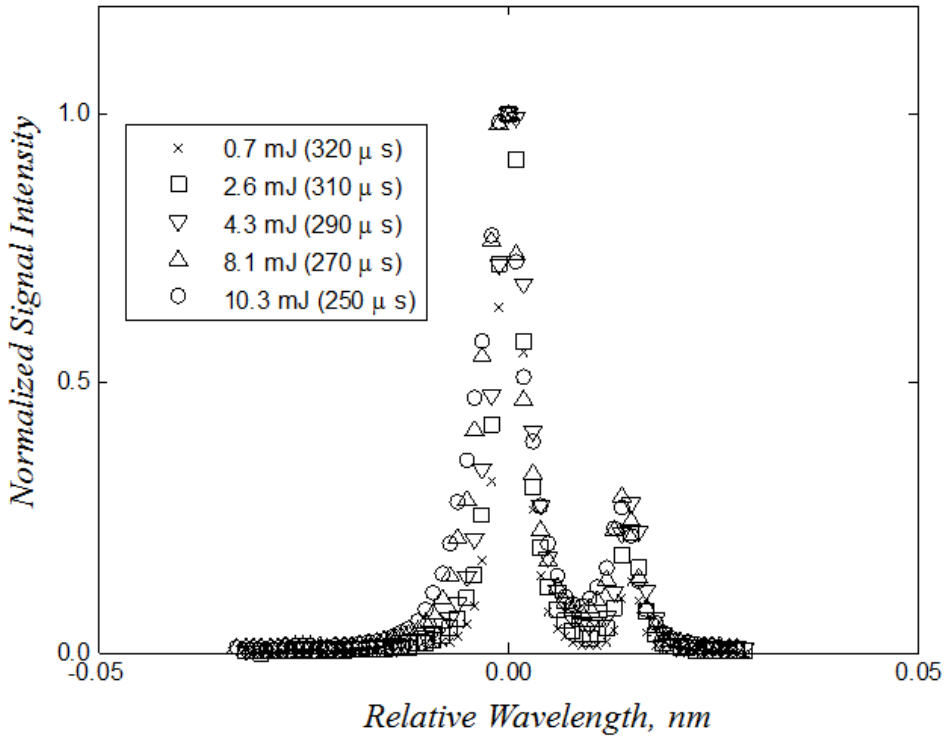

Fig.74. The comparison of spectral profiles of Q1(8) with various input laser energy. To compare the shape of each result, the wavelength at individual maximum signal intensity is set to be 0 and all the signals are normalised by individual maximum signal intensity. The wavelength increment and trigger count was 1.0 pm and 15 shots in this experiments.

In oxy-fuel combustion, the composition can be significantly different from air combustion. The linearity of LIF signal is relevant to collisional quenching, whose degree is affected by types of collisional partners. Hence, the linearity limit may vary even if the laser system is fixed. To this end, the linearity test with the CO_2 diluted flame was also evaluated. In the measurements, the flow condition was completely the same as the main experiment in the following (be 36% O2 + 74% CO_2 and 40% CNG + 60% CO_2 by volume at 137 s^{-1}). The result is shown in **Fig.75**. The linearity limit was around 0.6 mJ. Due to this result, the laser measurement in CO_2 diluted flame was operated at less than 0.6 mJ. It is worth emphasising that the linearity limit of the CO_2 diluted flame with present condition significantly differs from that of air case, which is approximately one seventh of the air flame limit. To this end, it can be said that special care needs to be taken in linearity limit in application of linear OH LIF techniques to CO_2 diluted oxy-fuel combustion.

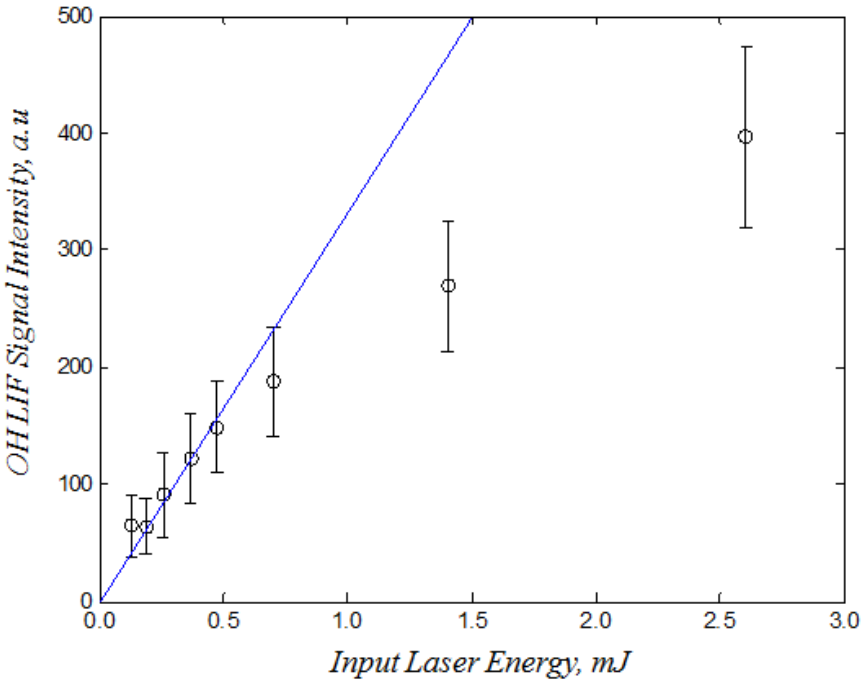

Fig.75. Linearity test results with CO_2 diluted flame. The error bar represents the confidence interval of 2σ (95.45%). The used wavelength is 283.3852 nm $Q_2(6)$). The 200 shots were averaged over. The blue line was obtained by least square method using the results of input laser energy less than 0.6 mJ.

6.1.3 Line Selection

The spectral lines scanned in the present study were selected to be $Q_1(1)$, $Q_2(6)$ and $Q_1(11)$. The ratiometic thermometry, the two-line peak and two-line area method, were implemented with $Q_{21}(1)$ and $Q_1(11)$ and the spectral fitting method was conducted with all three branches. The sequence of choosing the three branches used in the study is as follows. For reference, the pair of $Q_1(1)$ and $Q_1(11)$ is also compared with the other combination used for two-line thermometry in other studies in the following.

In the two-line peak scheme, two peaks at least are necessary to take a ratio, and the spectral profile around the two peaks is required to implement two-line integration techniques. First, two spectral regions were chosen, which are suitable for those ratiometric thermometry. The two spectral bands were determined based on three criteria: sensitivity of temperature, strength of LIF signal and proximity to other potentially interfering peaks. The spectral lines sensitive to temperature are preferable

in this measurement technique compared to those that are insensitive to temperature since the accuracy of measurement is heightened by a greater temperature sensitivity even in the case of modest reductions in signals. Also, the signal must be sufficiently large to secure the reasonable SNR. Further, it was reported by Kostka et al. [101] that the two-line thermometry without sufficient isolation from the other signal can mistakenly obtain temperature by significant quantity. In the Kostka et al. study [101], more than a 4,000 K deviation from theoretical temperature was obtained by $Q_1(9)/Q_2(8)$, which are interfered by each other with 3.4 pm proximity. To see the sensitivity of each transition to temperature, the theoretical spectral profile at 1,500 K and 2,000 K are shown in **Fig.76**, and the signal Intensity Difference is shown at individual wavelength in **Fig.77**. From the graph, it can be understood that the most sensitive transition is $Q_1(11)$. To make sure the $Q_1(11)$ is sensitive in all temperature regions of interest, the $Q_1(11)$ signal peak is shown as a function of temperature and then it can be seen that the $Q_1(11)$ is sensitive to temperature in all temperatures of interest in this study. Also, as can be seen in **Fig.76**, the signal intensity of $Q_1(11)$ is comparatively large. To this end, one of the scanned lines was chosen for $Q_1(11)$.

The root reason to choose a more sensitive transition is to get the ratio of two-line peak or area, which is sensitive to temperature. The $Q_1(11)$, which is chosen in the above, increases signal with temperature. Therefore, the ratio of interest would be more sensitive if the other transition decreases rather than increases with temperature. Considering this, Q1(3) appears to be the best candidature. However, the Q1(3) signal is close to $Q_{21}(3)$ signal with a proximity of 6 pm, and then $Q_1(1)$ was selected alternatively. While the $Q_1(1)$ is close to $Q_{21}(1)$ and $R_2(3)$, the resultant signal is observed as a single peak in actual measurement since the proximity of those branches is less than the order of line broadening by collisional broadening, Doppler broadening, pre-dissociation broadening and spectral line width of incident laser beam. In **Fig.79**, the spectral profiles of $Q_1(1)$, $R_2(3)$, and $Q_{21}(1)$, in absence and presence of those line broadening, are shown. Consequently, the $Q_1(1)$ is still applicable to the present experiment.

As mentioned in the methodology chapter, the scaling factor must be determined appropriately to conduct successful thermometry in the spectral fitting. In determining the scaling factor, the spectral region, which is insensitive to temperature, is expected to

be of considerable assistance since the signal intensity of $Q_1(1)$ and $Q_1(11)$ is varied substantially with temperature as well. Therefore, the presence of spectral region insensitive temperature can prevent the scaling factor from deviating significantly from true value. In this context, $Q_2(6)$ was also scanned in the present research. In addition, this $Q_2(6)$ branch is helpful to evaluate OH distribution in flame, since the $Q_2(6)$ is dependent almost entirely on OH concentration at probed volume.

In order to confirm whether the selection of a line pair for two-line thermometry conducted above is appropriate or not, the pair selected above was compared with the pairs employed in other two-line thermometry studies. In **Fig.80**, the response of the pairs of interest to temperature is shown. In **Fig.80**, the ratio is normalised by the ratio at 1,500 K. From this result, the pair of $Q_1(5)/Q_1(14)$ and $P_1(2)/R_2(13)$ appears to be better than the $Q_1(1)/Q_1(11)$. However, the signal intensity of $Q_1(14)$ and $R_2(13)$ is less than half of $Q_1(11)$ over the temperature range of interest in this study. Due to this, the $Q_1(1)/Q_1(11)$ was used in the present experiment.

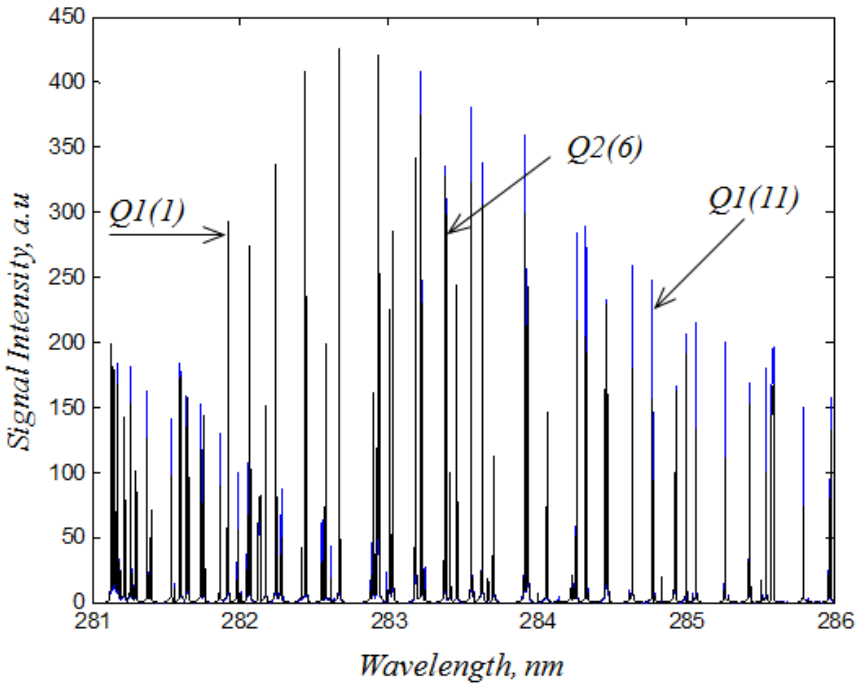

Fig.76. Theoretical spectral profile at 2,000 K (blue line) and 1,500 K (black line) obtained by LIFBASE.

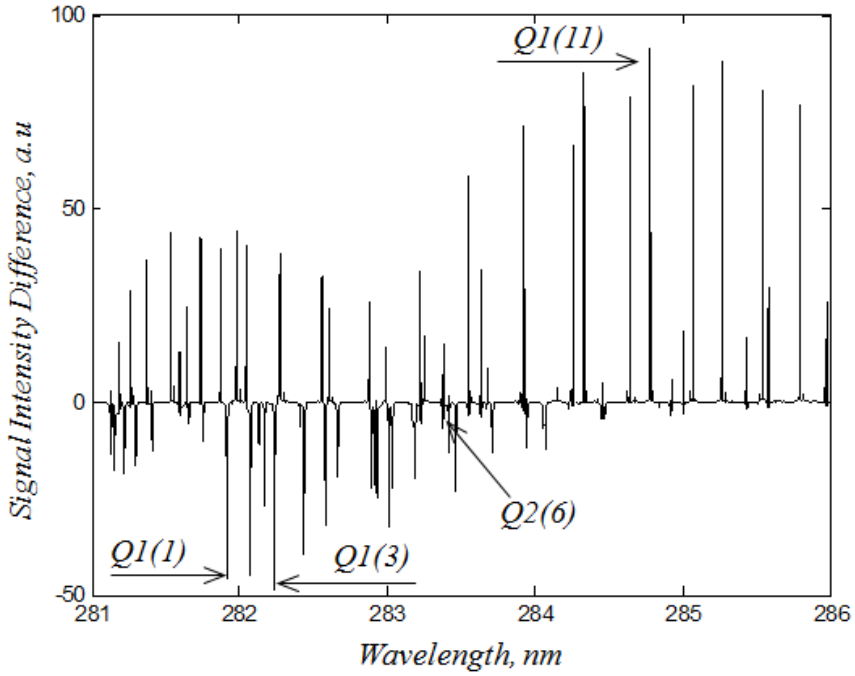

Fig.77. Signal Intensity Difference, i.e., signal intensity at 2,000 K - signal intensity at 1,500 K.

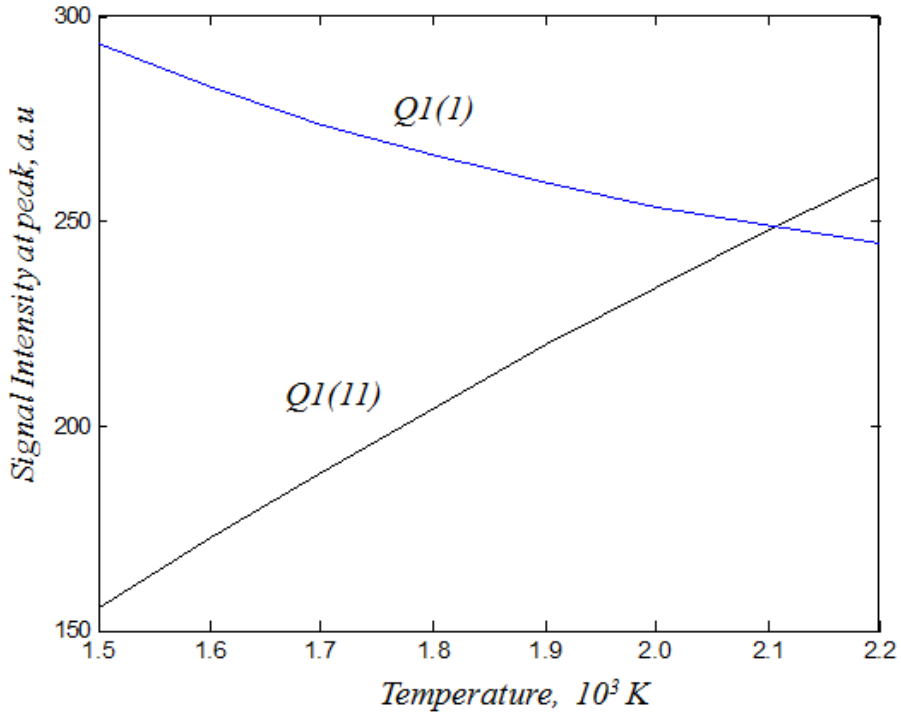

Fig.78. The response of signal intensities at peak of $Q_{21}(1)$ and $Q_1(11)$ to temperature.

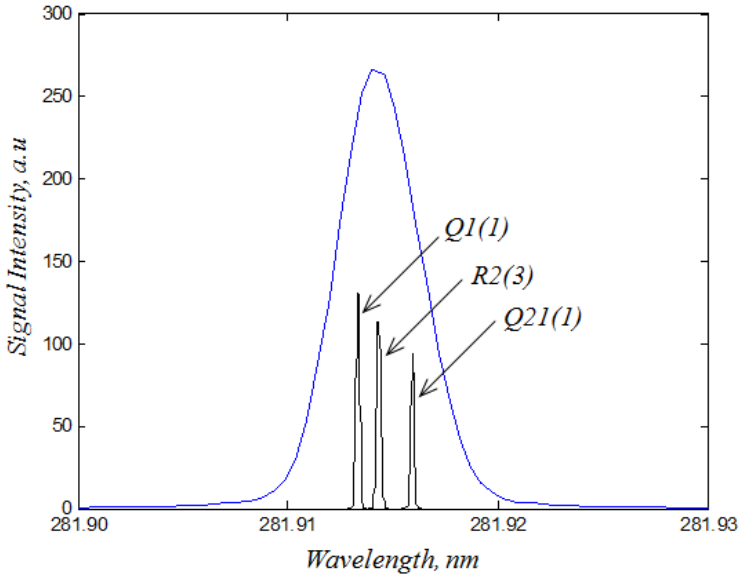

Fig.79. Spectral profile of $Q_1(1)$, $R_2(3)$ and $Q_{21}(1)$ with and without all line broadening, except the line broadening based on instrumental function. The blue line is a simulated result with Doppler broadening, pre-dissociation broadening and collisional broadening activated, using 2.4×10^{-2} Å as resolution of instrumental function. The black line is the result without all line broadening phenomena, except the line broadening based on instrumental function, using 2.0×10^{-3} Å as resolution of instrumental function .

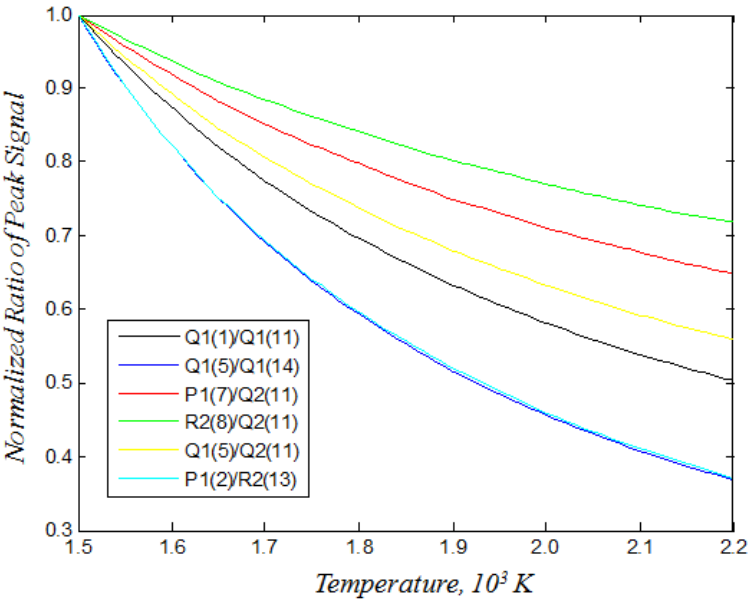

Fig.80. Sensitivity of each pair to temperature. $Q_1(14)/Q_1(5)$ [101], $P_1(7)/Q_2(11)$ and $R_2(8)/Q_2(11)$ [87], $Q_1(5)/Q_2(11)$ [88] and $P_1(2)/R_2(13)$ [121].

6.1.4 Trigger Count and Scan Increment

In the experiments, the trigger count and scan increment was set to be 100 shots and 0.1 pm respectively. The trigger count, which is the shot number per wavelength, must be reasonably large for successful thermometry while more time is needed for completion of the scan as the trigger count is increased. Also, the scan increment, (increment of excitation scan), must be reasonably fine. The spectral profile deviation among different temperatures resides in the peak position of the individual profile, and then the accuracy of thermometry is significantly affected by accurate capturing of spectral profile around the peak. At the other extreme, experimental time increases with the finer spectral resolution of scan. To this end, it is required to take good trade-off conditions in trigger count and scan increment. The sequence of selecting those trigger count and scan increment is as follows.

The trigger count was determined based on confidence interval to signal. In **Fig.81**, the spectral profile of $Q_1(1)$ is shown at 1,900 K, 1,800 K and 1,700 K. In **Fig.81**, the signal intensity is normalised by the maximum value of 1,800 K spectral profile. To separate the spectral profile between the two lines, the confidence interval of the experimental profile around the peak region must be ± 1.42% of signal and otherwise the error of measurement becomes more than 100 K. In this study, this confidence interval of ± 1.42% of signal was set to be target value. This can mathematically represented in the form:

$$\frac{k}{\sqrt{Trigger\ Count}}\frac{1}{SNR} < 1.42 \times 10^{-2} \tag{52}$$

where coefficient k value depends on desired confidence. For example, k=1 with 68.27% confidence (1σ), k=2 with 95.45% (2σ). To obtain the trigger count satisfying the target confidence interval, the SNR of the experimental system in this study is necessary. Thus, the SNR was measured, applying laser beam of wavelength 281.9193 nm ($Q_1(1)$) to Bunsen flame and consequently the SNR was 7.233. Therefore, the trigger count for 68% confidence is more than 68 shots and the trigger count for 95% confidence is more than 365. For reference, the confidence interval is shown in **Fig.82**, as a function of trigger count, using SNR of 7.233.

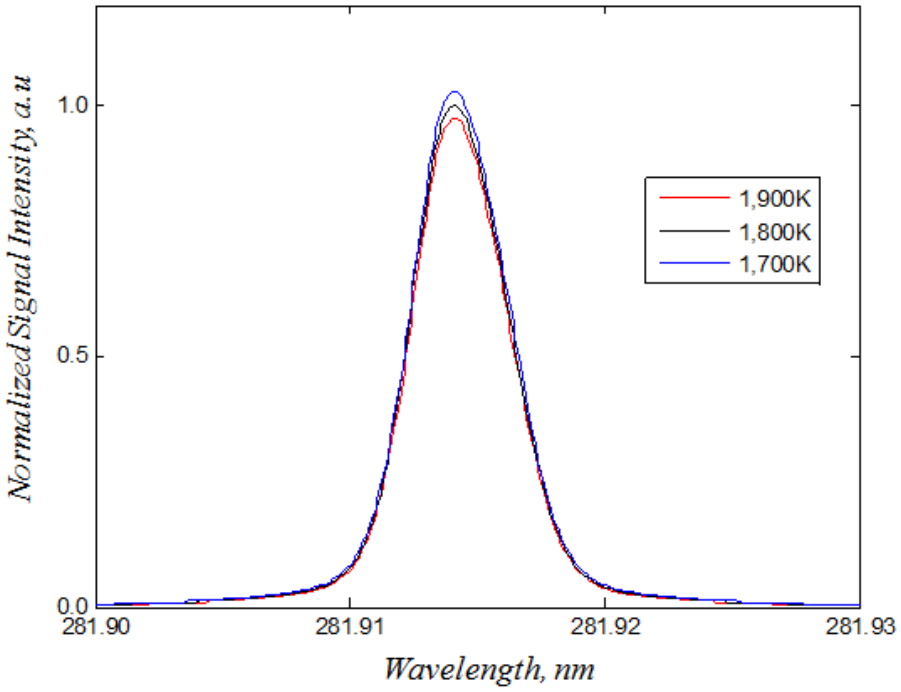

(a)

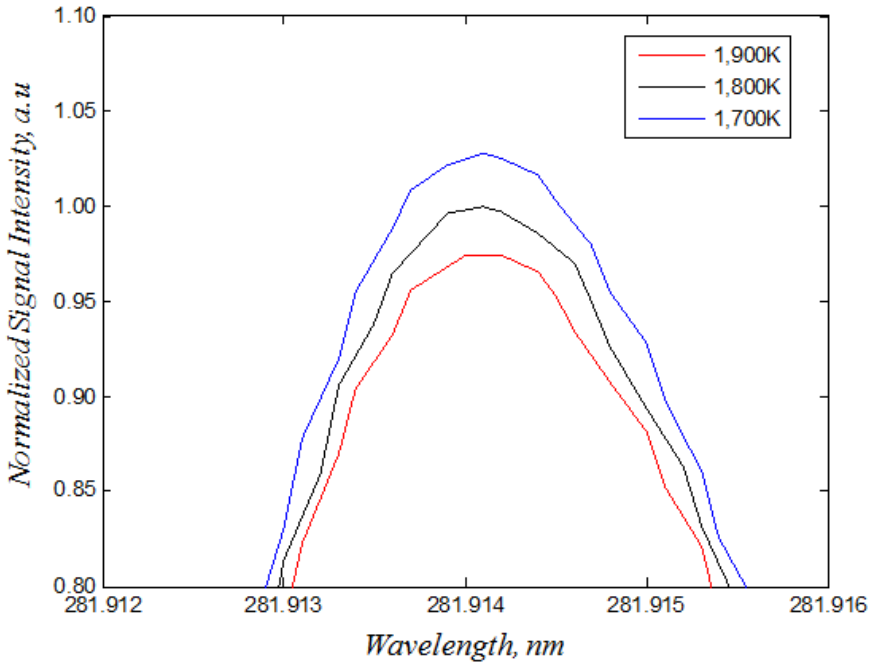

(b)

Fig.81. Theoretical spectral profile at 1,900, 1,800 and 1,900 K. (a) Broad Region, (b) Near Peak.

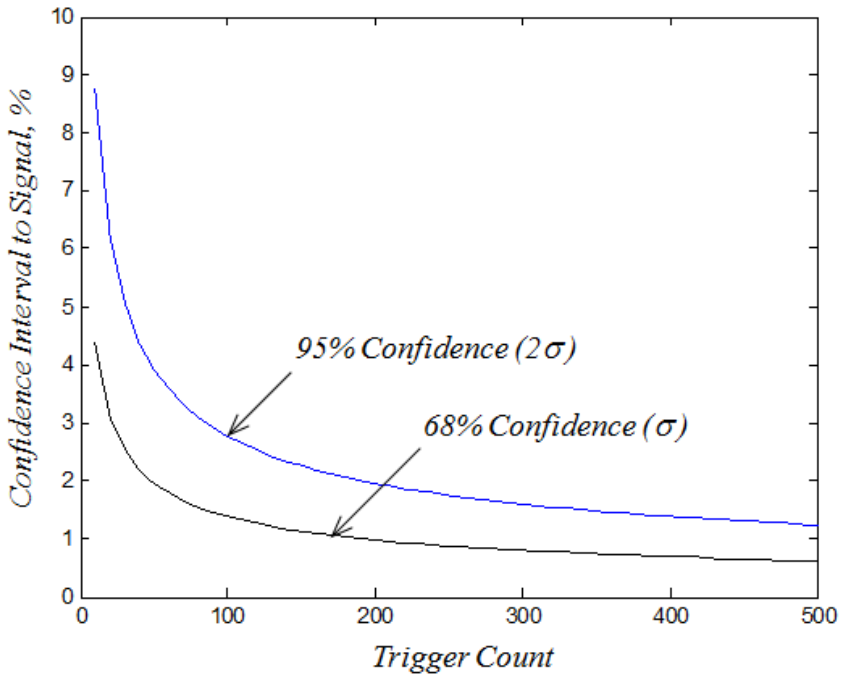

Fig.82. Relation of confidence interval to signal and trigger count. The SNR was fixed to 7.233.

Scan increment must be determined so that the experimental plots capture the peak of spectral profiles, since the spectral difference among different temperatures are present only around the peak, as seen in **Fig.81**. To confirm the operational scan increment, the $Q_1(11)$ profile was scanned with various scan increments. The consequent peak value with individual scan increments is shown in **Fig.83 (a)**, being normalised by the peak vale of 0.1 pm step excitation scan. Also, the actual profile with 0.1, 0.7, 1.1 pm scan increment is also shown in **Fig.83 (b)**. Note that the 0.1 pm wavelength resolution is the finest increment of dye laser used in the present study. It can be seen that even the 0.3 pm scan increment still possessed approximately 2% peak intensity deviation from 0.1 pm. As mentioned above, slight deviation can lead to substantial error from true value in the present thermometry. Therefore, the 0.1 pm scan increment, at least, appears to be required in this study. Also, according to the convergence of fluctuation of curve in **Fig.83 (a)** with approach to 0.1 pm, the 0.1 pm can be considered as reasonably fine increment value.

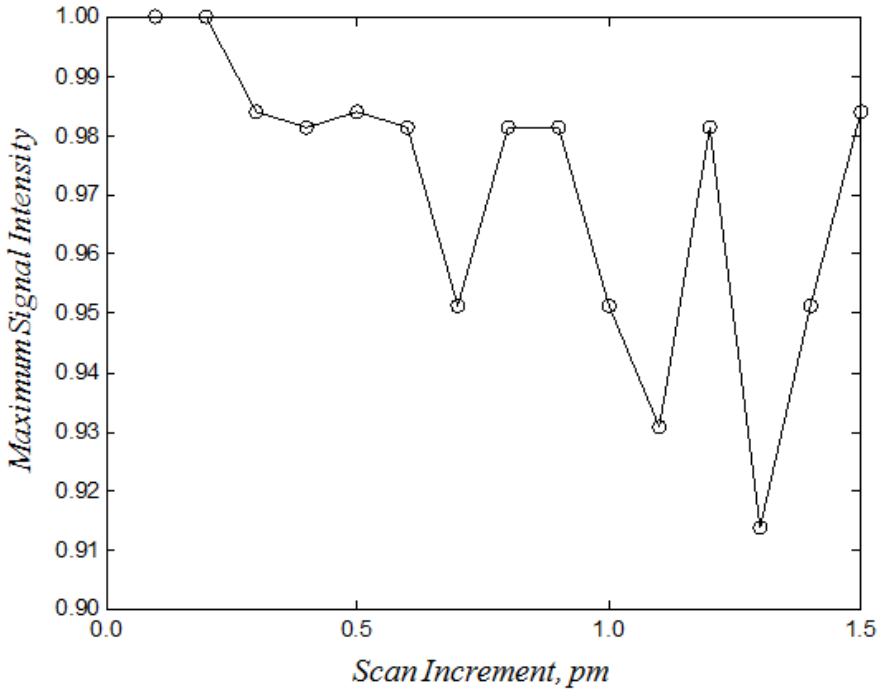

(a)

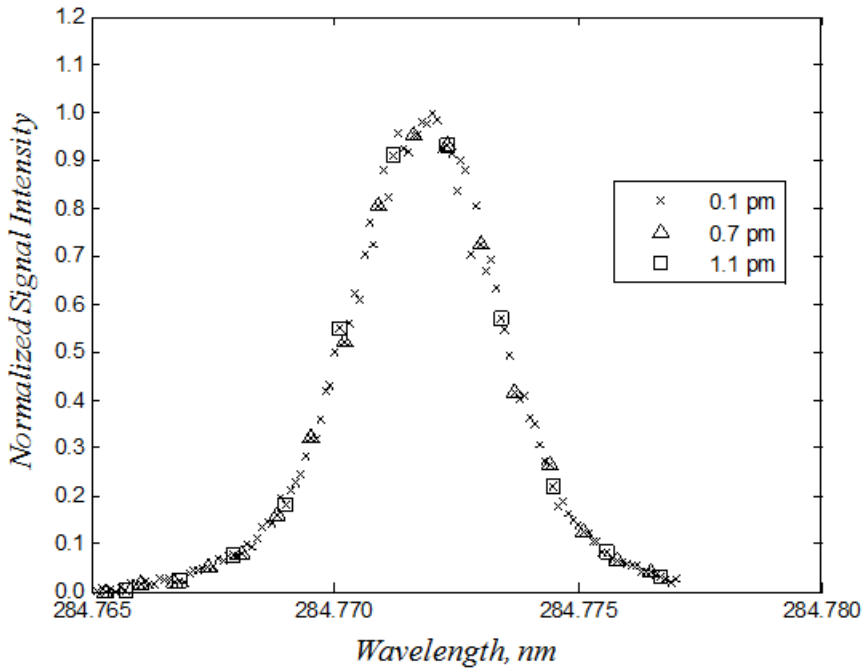

(b)

Fig.83. Confirmation of operational scan increment. (a) Maximum signal intensity v. Scan increment, (b) Spectral profile with scan increment of 0.1, 0.7, 1.1 pm.

Considering the above discussion and time limitation, the operational scan increment and trigger count was determined. Here, the priority was placed more on scan increment since the accurate data plot can be in vain without capturing peak profile. Thus, the scan increment was first decided to be 0.1 pm. In an ideal case, the trigger count must be set to more than 365, equivalent to 2σ confidence interval. However, once the excitation scan with 0.1 pm step and 365 trigger count applies to three spectral region of interest, it takes 368 minutes (six hours and eight minutes). To this end, the target confidence of this study was set to be 68% (1σ). That is, more than 95 shots per each wavelength. Since some synchronisation mistakes are expected to occur in scan process resulting in missed shots and thus acquiring less than the set number of shots, the 100 trigger count was set in the experiments.

6.2 Proof of Measurement System by Bunsen Air Flame

In order to prove the laser measurement system established in this study is reasonable, the OH thermometry was applied to Bunsen air flame. Bennet et al. [122] simulated the Bunsen flame at 0.78 and the maximum temperature was 1,864 K (T_{ad} = 1,966). The temperature was employed as criteria to explore the accuracy of the current experimental system. The obtained temperatures by individual techniques are summarised in Table 5. Considering the accuracy discussed in 6.1.4, it can be said that the measurement system established here is appropriate since the measurement accuracy was within expectations. The detailed procedure of image processing is as follows.

Table 5: Summary of Maximum Temperature Obtained by Bunsen Flame Experiment

	Fitting	*Two-line Peak*	*Two-line Area*
Temperature, K	*1,820*	*1,851*	*1,842*
Discrepancy, K	*44*	*13*	*22*
Discrepancy, %	*2.4*	*0.7*	*1.2*

6.2.1 Image Corrections

To minimise errors obtained in the system, great care was taken in shot-to-shot variation of laser power and intensifier gain. For reference, the averaged image at 283.3805 nm without any correction is shown in **Fig.84**. The algorithm used to correct each instantaneous image of *i* at (*j* , *k*) pixel is:

$$(Corrected\ Image\ of\ i)_{j,k} = (S_{i,(j,k)} - Ba_{(j,k)}) \frac{\overline{La} - \overline{LaBk}}{La_i - \overline{LaBk}} \frac{\overline{In} - InBk}{In_i - InBk} \quad (53)$$

where *S* is an obtained LIF signal intensity, *Ba* is an average background acquired with the LIF signal monitoring camera, *La* is a signal of the laser power monitoring image array, *LaBk* is an averaged background signal of the laser power monitoring camera, In is LED signal and *InBk* is the background signal at LED monitoring pixels.

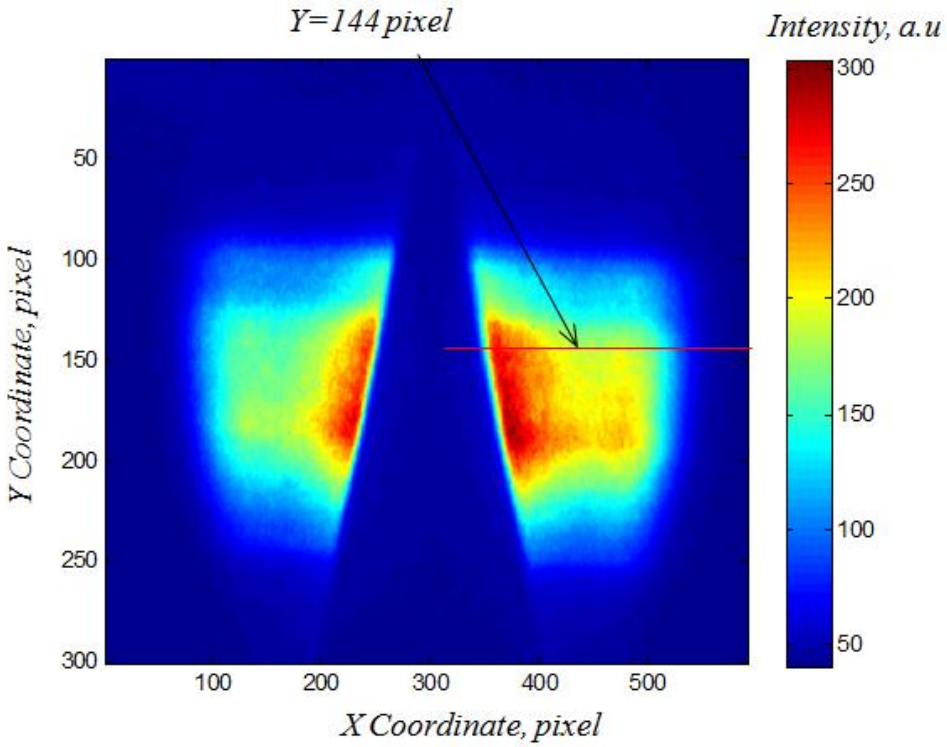

Fig.84. Mean Image at 283.3805 nm without any image correction. Laser beam entered from right to left.

6.2.2 Thermometry

In **Fig.85**, the temperature distribution in radial direction of y=144 pixel, obtained by each thermometry techniques, is shown. In the following, the procedure of obtaining each plot in **Fig.85** is shown, the signal averaged over (364±2,144±2) being taken as example.

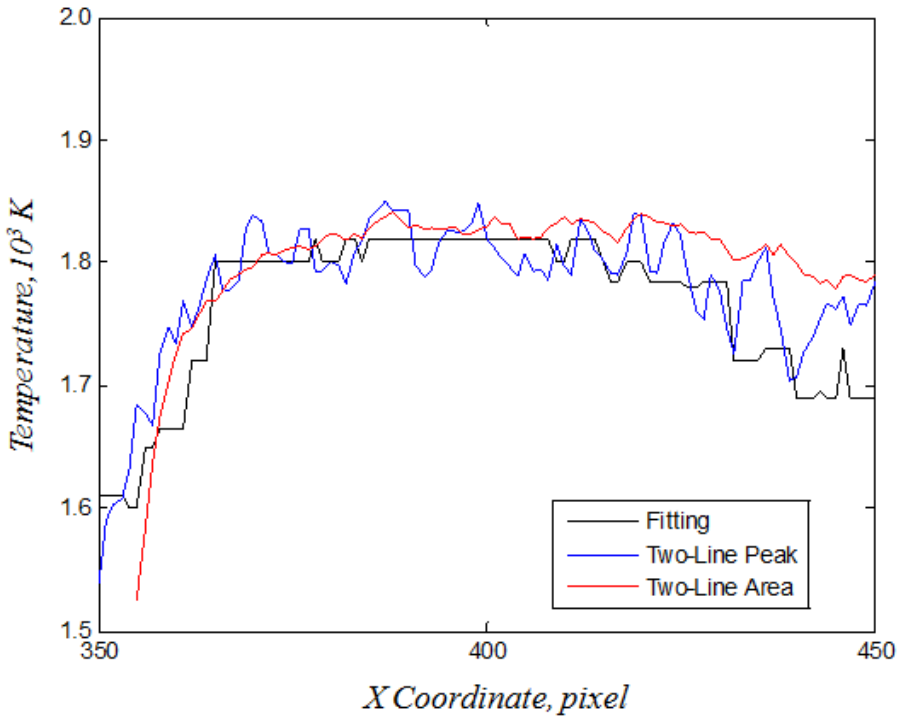

Fig.85. Spatial distribution of temperature in radial direction, obtained by three different techniques.

6.2.2.1 Spectral Fitting Techniques

In spectra fitting techniques, there are several parameters necessary for techniques to be set appropriately: baseline correction, wavelength adjustment, scaling factor, line width of incident laser (instrumental function), Lorentzian of incident laser (instrumental function), collisional broadening coefficient *a* and *b*, and temperature. Each parameter definition was included in the methodology chapter. First, the wavelength adjustment was determined so that the residual of the experimental profile from theoretical profile, was symmetry based on centre of line wavelength. Examples of the procedure are shown in **Fig.86**. After this process, the best combination of baseline correction, scaling factor, instrumental function was determined so that the residual became the smallest.

In the Bunsen air flame, the collisional coefficients *a* and *b* were set to be 0.41 and 0.8 respectively. The values were taken from [123, 124]. The consequent profiles are shown in **Fig.87** with experimental results. The obtained temperature was 1,790 K. In the plots shown in **Fig.85**, the instrumental function was fixed all the time, while the other values were varied with each condition.

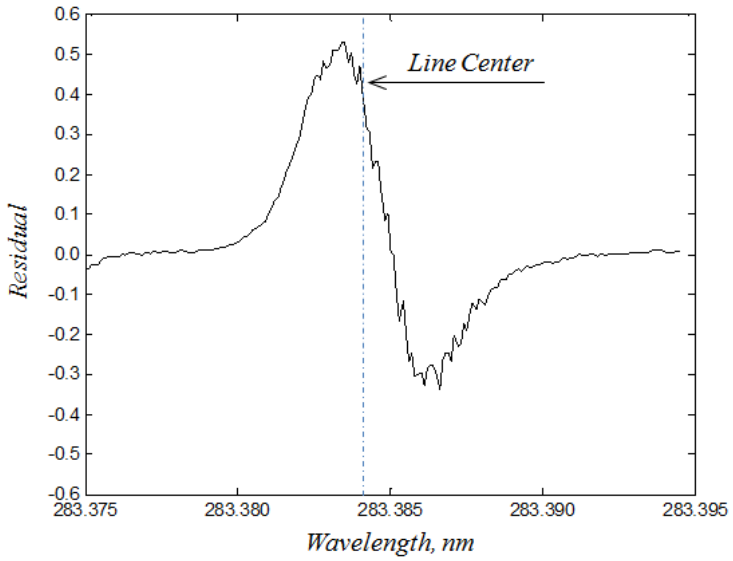

(a)

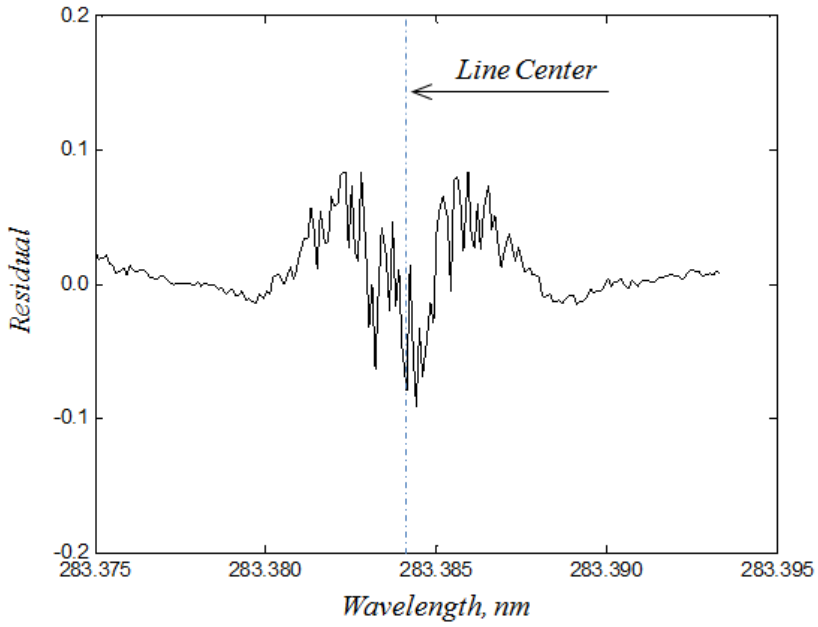

(b)

Fig.86. Examples of wavelength correction. (a) Incorrect Adjustment, (b) Correct Adjustment.

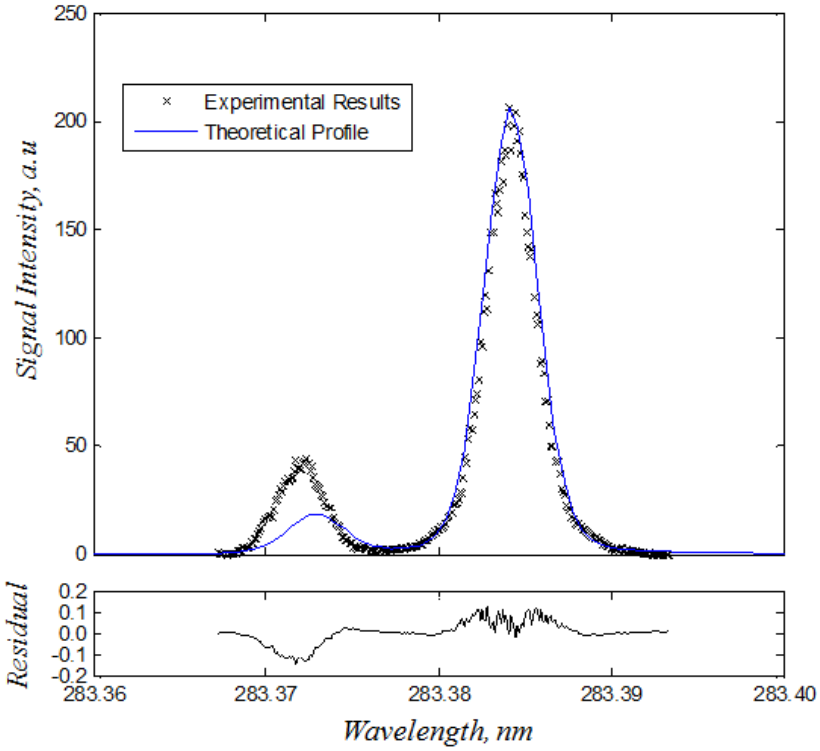
Experimental Results
Theoretical Profile
Signal Intensity, a.u
Residual
Wavelength, nm

(a)

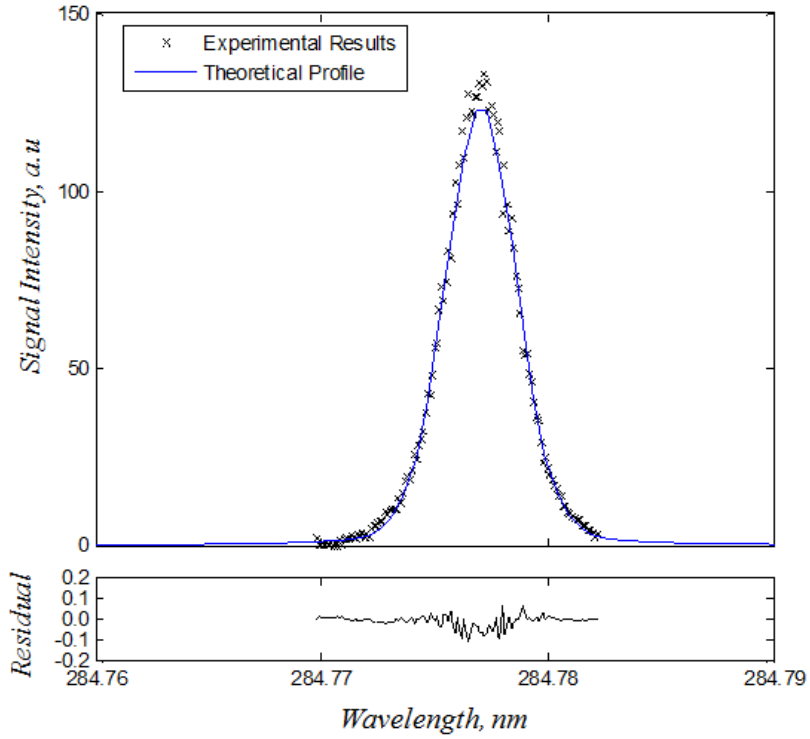
Experimental Results
Theoretical Profile
Signal Intensity, a.u
Residual
Wavelength, nm

(b)

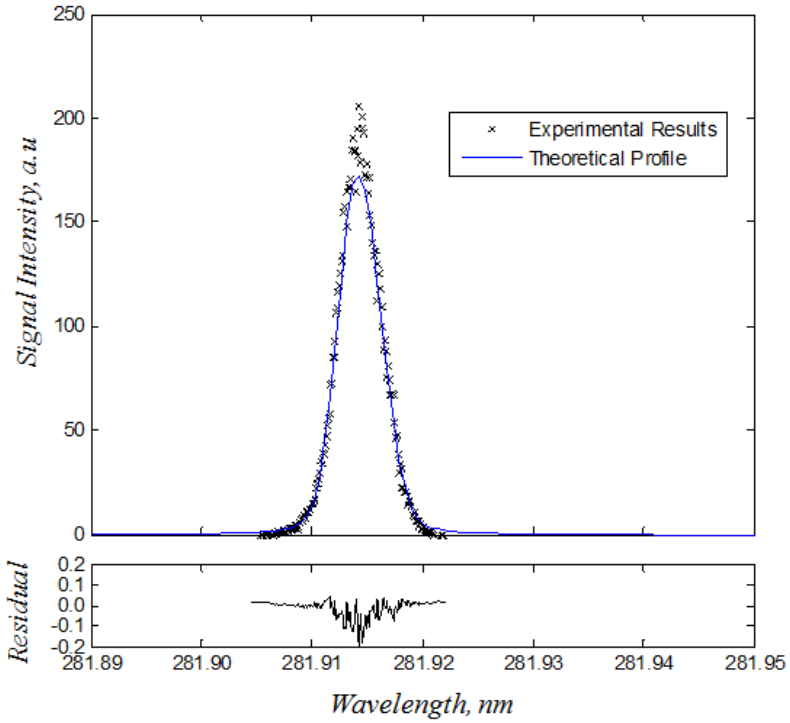

(c)

Fig.87. The best spectral profile with experimental results. (a) $Q_2(6)$, (b) $Q_1(11)$ and (c) $Q_1(1)$.

6.2.2.2 Two-line Techniques

The ratio of the peak values of $Q_1(11)$ and $Q_1(1)$ was taken from experimental results and then the temperature was determined. To take relation of theoretical two-line peak ratio, the instrumental function, a baseline correction was taken from the above result of spectral fitting. The obtained result was 1,680 K.

6.2.2.3 Two-line Area Techniques

In two-line area techniques, the area, S, of each line was calculated by:

$$S = \int_{\lambda_0-\delta\lambda_i}^{\lambda_0+\delta\lambda_i} F(\lambda)d\lambda \qquad (54)$$

where $F(\lambda)$ is the simulated fluorescence line shape function, λ_0 is the centre line position and $\delta\lambda_i$ represents a span for integration (**Fig.88**). To get trustworthy data from

the above integration, care must be taken to integrate wavelength. To confirm the integration span, the relation of integration span and integrated value (area), is shown in **Fig.89**. From this result, it can be seen that 0.5 x 10^{-2} nm $\delta\lambda_i$ is at least necessary and then both $Q_1(1)$ and $Q_1(11)$ spectra was integrated over ± nm from the centre line position. As a result, 1,770 K was obtained.

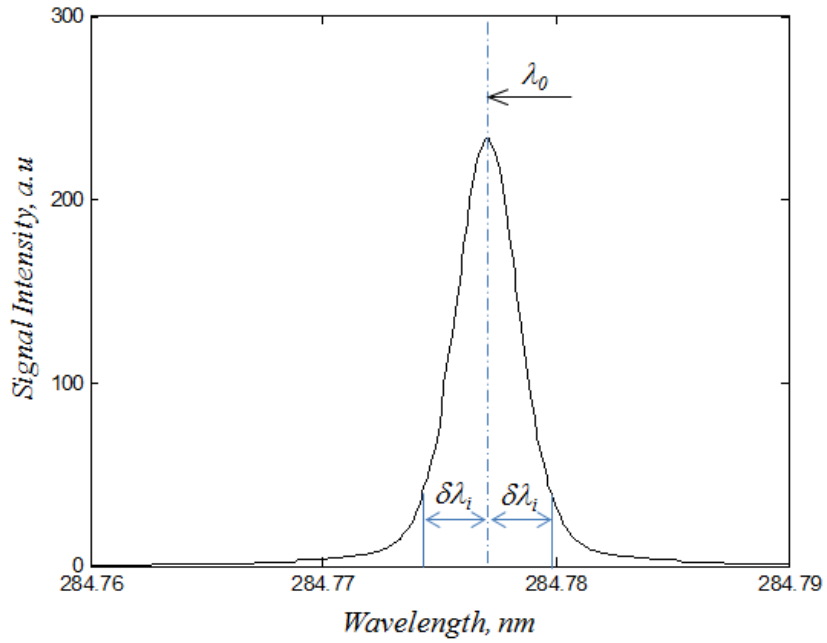

Fig.88. Conceptual idea of $\delta\lambda_i$.

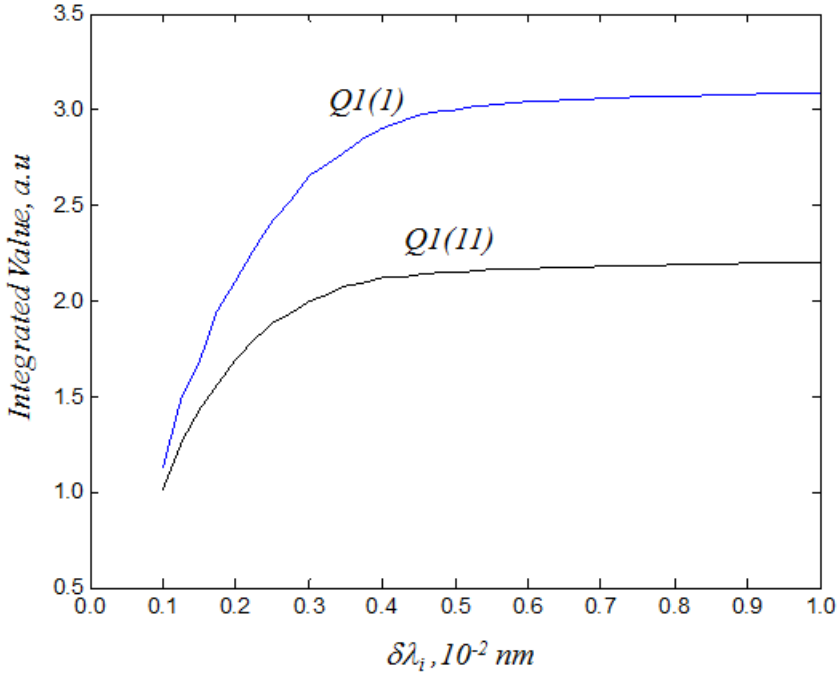

Fig.89. Sensitivity Analysis of Integrated value to $\delta\lambda_i$.

6.3 Application to CO_2 Diluted Oxy-fuel Flame

The OH LIF thermometry validated above was applied to CO_2 diluted oxy-fuel opposed-flow, diffusion flame. The maximum temperature obtained by each technique was compared with theoretical value, calculated by CHEMKIN PRO, and the result is summarised in Table 6. The temperature listed on Table 6 is the result of spectral fitting only by $Q_1(1)$ and $Q_1(11)$ ($Q_2(6)$ spectral profile was ignored). This is because the relatively large discrepancy of $Q_2(6)$ between theoretical and experimental results was observed in the spectral fitting process. This is discussed in more detail later. In all thermometry methods, the deviation from theoretical temperature was less than 2.5%. From this result, it can be understood that the OH LIF thermometry employed in this study is applicable to oxy-fuel combustion at least to extract maximum temperature at current operational conditions.

In Table 7, the deviation of experimentally obtained thermal structure from the simulated thermal structure is also shown above 1,600 K. It can be understood from the graph that all techniques provided agreement with less than 14.9% deviation from theoretical curve, while the best fit of less than 2.4% was provided by the two-line area technique. In contrast with the great agreement at maximum temperature by 1.1% deviation, the relatively large discrepancy of the spectral fitting strategy can be seen in thermal structure.

In the following, the image process implemented here and the more detailed results obtained by each method are explored.

Table 6: Maximum Temperature Obtained by Each Method

	Fitting (Q1(1) and Q1(11))	*Two-line Peak*	*Two-line Area*	*Simulation*
Temperature, K	*1,880*	*1,853*	*1,866*	*1,900*
Discrepancy, K	*20*	*47*	*34*	*N/A*
Discrepancy, %	*1.1*	*2.5*	*1.8*	*N/A*

Table 7: The Discrepancy of Thermal Structure from the Simulated Value Above 1,600 K

	Fitting (Q1(1) and Q1(11))	*Two-line Peak*	*Two-line Area*
Discrepancy, %	*Less than 14.9%*	*Less than 14.9 %*	*Less than 2.4 %*

6.3.1 Image Process

In **Fig.90**, an averaged image without any correction is shown. In counter-flow flame, axial temperature distribution at each radial position is the same as each other, and thus it would be possible to suppress the noise by averaging the signal over radial direction. However, flame flickering was observed to some extent during data collection. To this end, axial alignment was implemented before averaging, based on the peak signal position at individual radial pixel. The conceptual idea of this process is illustrated in **Fig.91**. In this process, the axial position of maximum signal intensity at individual radial point was fixed. After this process, the shot-to-shot variation of laser irradiance and intensifier gain was corrected as with the Bunsen air flame.

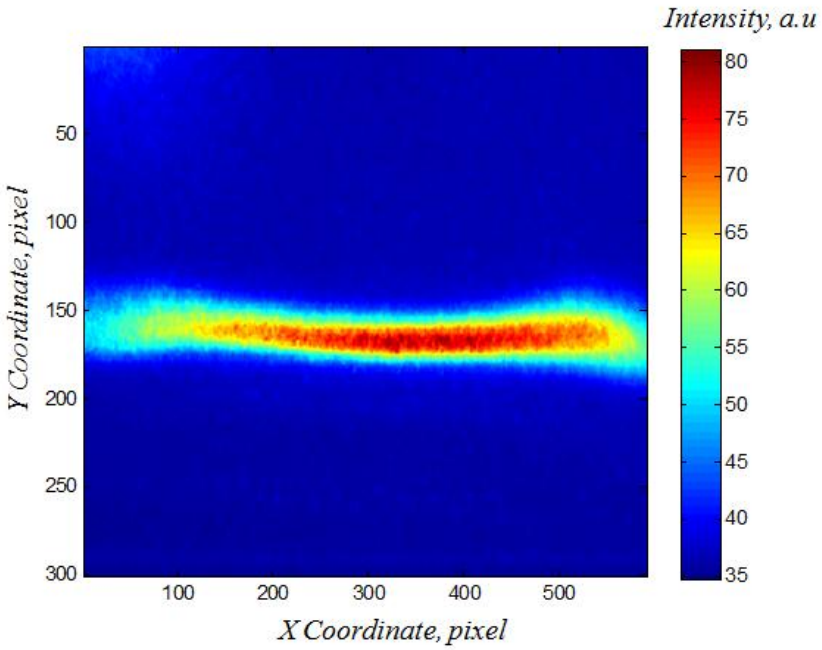

Fig.90. Mean image of counter-flow diffusion flame with CO_2 dilution without any correction. The laser beam entered from right to left. The oxidiser supplied from the top and the fuel stream from the bottom.

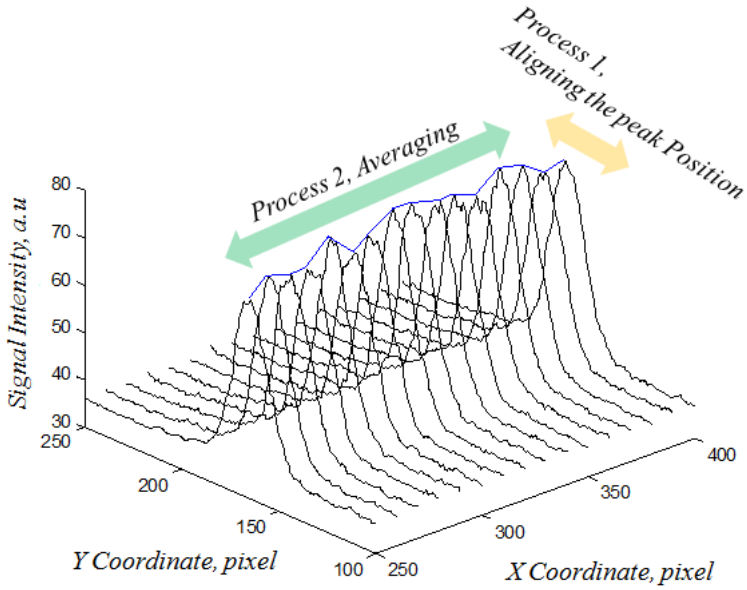

Fig.91. Procedure of axial alignment before averaging. For simplicity, the gap between each profile shown here is set to be 10 pixels in X coordinate. The blue line is a track of maximum signal. The blue line was straightened in the alignment process.

6.3.2 Thermometry

In **Fig.93 (a)**, the thermal structure near temperature peak obtained by each technique is shown. For comparison of the shape among each curve, the temperature obtained by each technique was normalised by own maximum temperature, and the result is shown in **Fig.93 (b)**. The processing conducted here is the same as that of Bunsen air flame. Additional care must be taken only to collisional broadening coefficient *a* and *b* since the collisional broadening phenomenon is affected significantly by collisional partners. Using the experimental spectral profile at the spatial position where the OH LIF signal hits maximum, the best combination of *a* and *b* values were sought. In the fitting process, the instrumental function parameters are fixed to the same values as those obtained by the Bunsen air flame experiment since the same laser system was employed. As a result, the application of coefficient *a* of 0.47 and *b* of 0.77 provided the best agreement. For reference, the result of spectral fit at the spatial position is shown in **Fig.92**. The temperature obtained by the spectral fitting method in **Fig.93** was processed in absence of $Q_2(6)$ since the $Q_2(6)$ spectral profile in **Fig.92** was relatively

large and can lead to larger deviation of temperature from true value. The cause of this large discrepancy observed in the $Q_2(6)$ branch is discussed later.

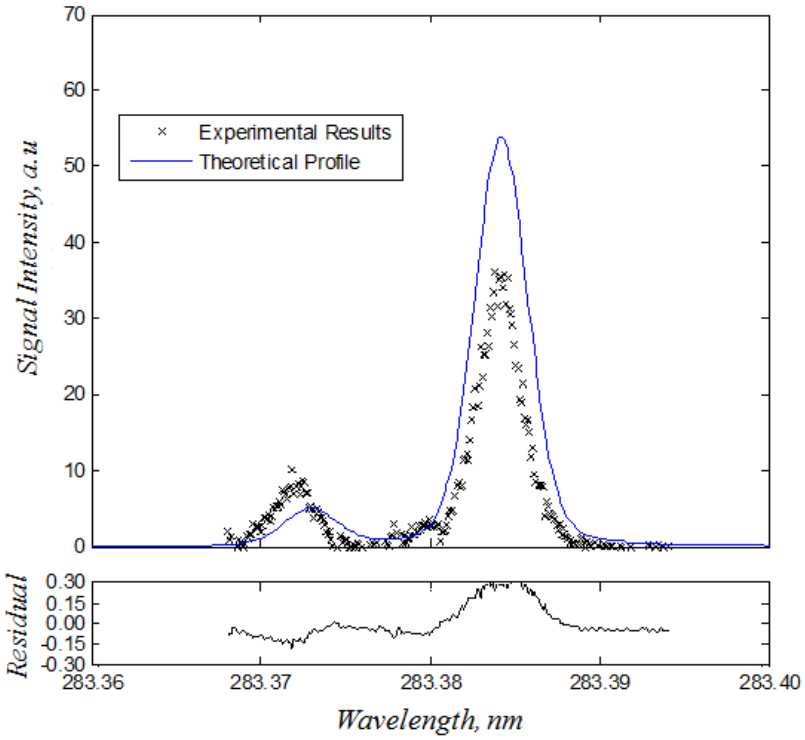

(a)

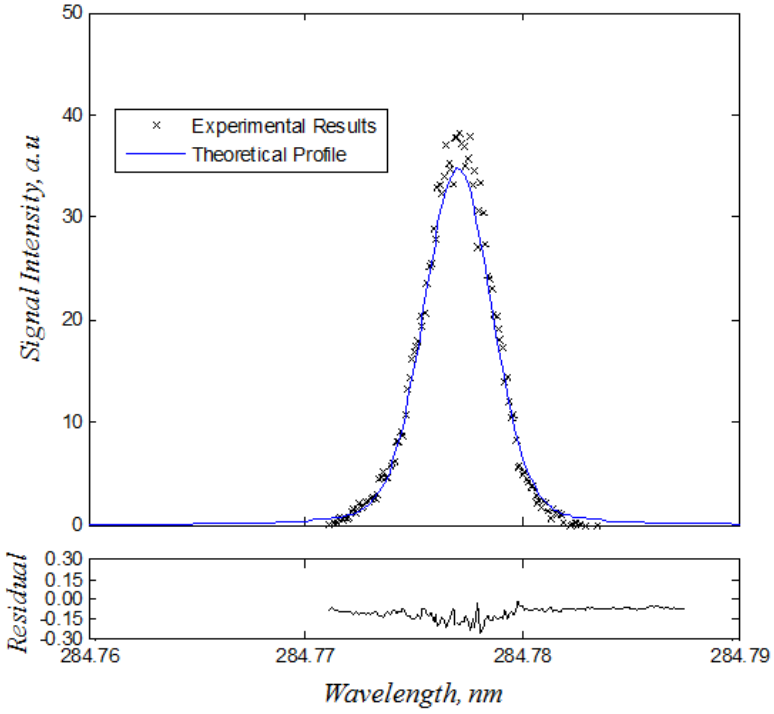

(b)

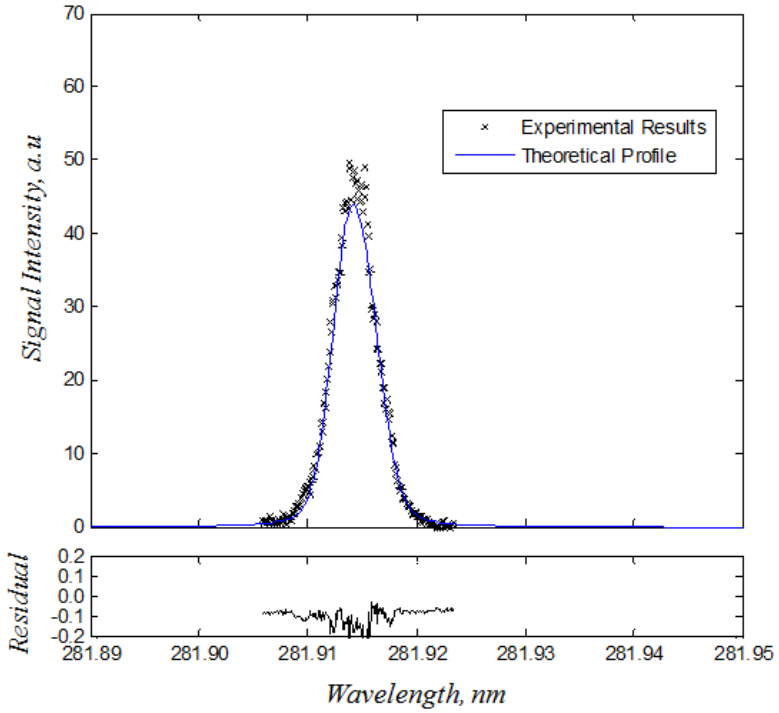

(c)

Fig.92. The best fit of theoretical profile with experimental results at a spatial position where OH signal hits maximum.

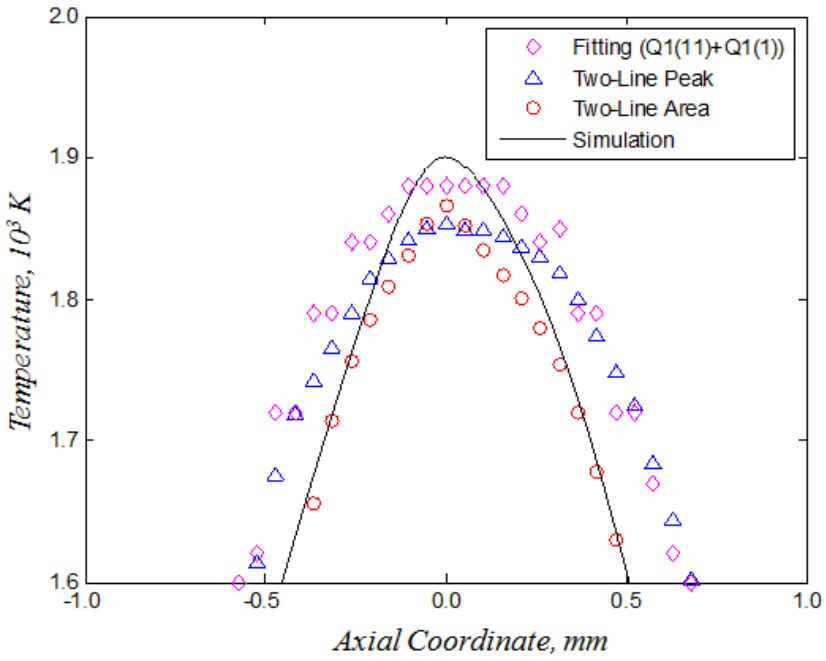

(a)

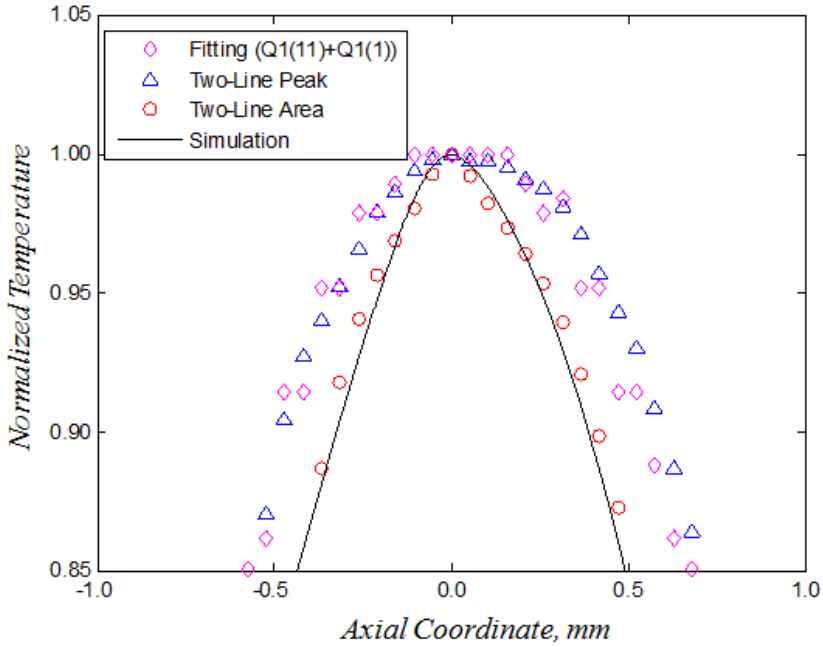

(b)

Fig.93. (a) Spatial distribution of temperature in axial direction obtained by each technique. (b) Normalised distribution of temperature. The axial coordinate of individual peak is set at zero in both (a) and (b).

6.4 Discussion

6.4.1 Discrepancy in $Q_2(6)$ in Spectral Fitting

One of the possible causes for the discrepancy seen in $Q_2(6)$ spectral fitting is that the SNR in $Q_2(6)$ is lower than expected. For confirmation, the SNR of $Q_2(6)$ was calculated from experiment results and the SNR of $Q_2(6)$ at wavelength of peak signal was 5.036. Since the SNR expected in Section 6.1.4 is 7.233, the SNR in $Q_2(6)$ was lower than expected. Using this SNR of 5.036, the confidence interval of 68% and 95% and to signal was calculated by the formula:

$$Confidence\ Interval\ to\ Signal = \frac{k}{\sqrt{trigger\ count}} \frac{1}{SNR} \qquad (55)$$

Consequently, the confidence interval to signal of 68% and 95% was 1.9% and 4.0% respectively. Since the residual of $Q_2(6)$ in spectral fitting was 27%, the confidence interval was sufficiently narrower, while the SNRs were smaller than expected values. Note that the saturation did not occur in the $Q_2(6)$ scan in the present experiment. While the linearity limit varies, being dependent on rotational quantum number, the linearity limit was evaluated using $Q_2(6)$ line as is mentioned in section 6.1.2. Also, the laser power was monitored during the experiments.

At the current stage, the cause of discrepancy in spectral fitting has yet to be identified. However, the cause may be related to CO_2 dilution because the $Q_2(6)$ spectral fitting in the air Bunsen flame was successful. For reference, the thermal structure obtained by the spectral fitting with the $Q_2(6)$ is shown in **Fig.94**.

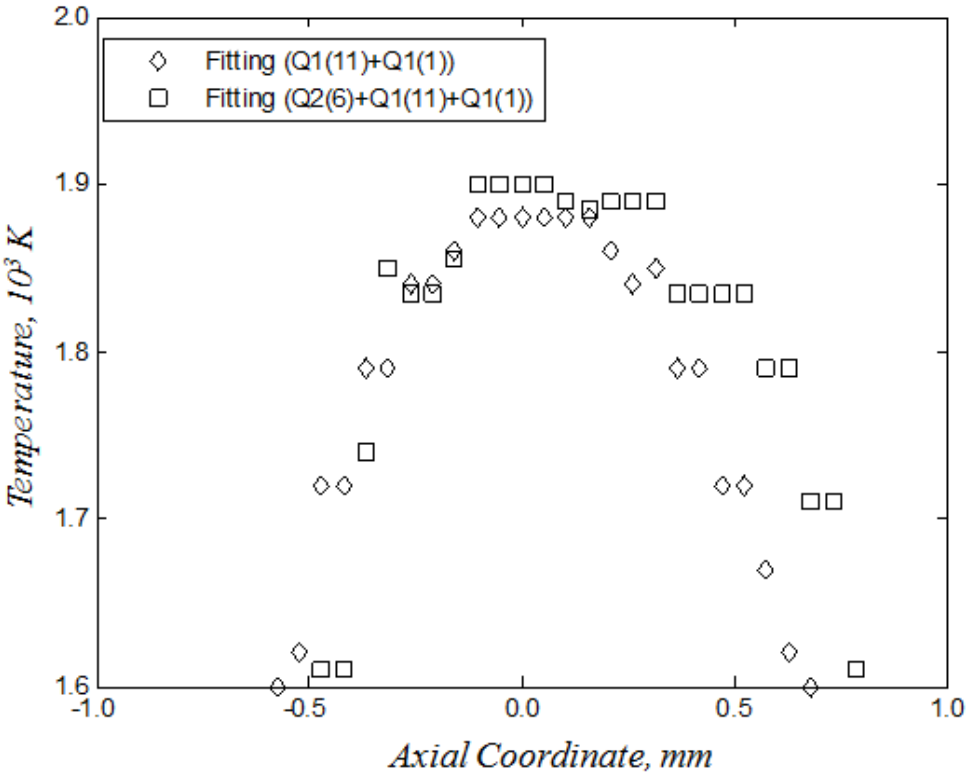

Fig.94. The thermal structure obtained by the spectral fitting methods in presence and absence of the $Q_2(6)$ branch. The axial coordinate of individual peak is set at 0.

6.4.2 The Effect of Baseline Correction

In the above processes, the temperature by the two-line peak technique was obtained using the spectral profile after baseline correction. In the present study, the excitation scan was implemented with the two-line peak method and thus it was possible to implement baseline correction. However, the two-line peak method is employed without excitation scan in most of the cases. As such, the temperature deviation between presence and absence of the correction was examined with the two-line peak method. As a result, the temperature deviation was 20 K at maximum temperature (1.1% deviation). Since the baseline correction represents the removal of the effect of elastic scattering process from surface or soot and LIF interference, it can also be said that those elastic process and LIF interference affected the experimental temperature by 1.1% at maximum temperature conditions.

6.4.3 Collisional Broadening Coefficient

The best combination of *a* and *b* found in the present study was 0.47 and 0.77 respectively. The spatial distribution of temperature with the *a* and *b* combination is compared from the combination used in Bunsen air flame (*a* of 0.41 and *b* of 0.80). The spatial distribution of temperature is shown with the two different sets of *a* and *b* in **Fig.95**. There was a relatively small difference between the two curves. The gap was less than 2.0% at individual temperature. Due to that, it can be said that the adjustment of the *a* and *b* coefficient is not substantial in the present oxy-fuel conditions, while the slightly smoother distribution was observed around temperature peak by the adjustment.

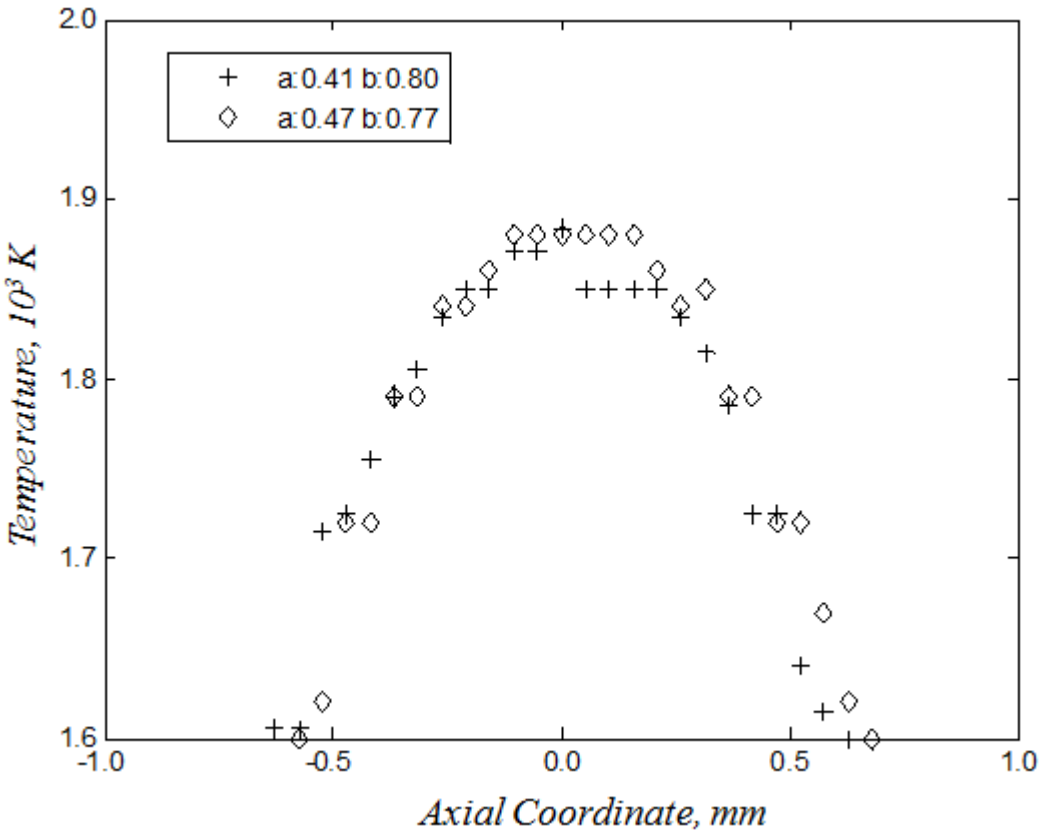

Fig.95. The sensitivity analysis of the thermal structure on the combination of *a* and *b*. The axial coordinate of individual peak is set at zero.

6.4.4 Actual Confidence Interval in Counter-flow Flame

The confidence interval of 68% and 95% to signal with $Q_2(6)$, $Q_1(11)$ and $Q_1(1)$ is summarised in Table 8. The SNR of each line was 5.036, 8.851 and 10.010 at centre of line. The better SNR of $Q_1(11)$ and $Q_1(1)$ than expected value can be due to the spatially averaging process in counter-flow flame. The worse SNR of $Q_2(6)$ than expected value was due to laser power fluctuation around wavelength of the centre line of $Q_2(6)$. The trend of SNR, $Q_1(1) > Q_1(11) > Q_2(6)$, in quantity was also observed in Bunsen air flame.

Using the table, the confidence interval of the temperature obtained by the two-line peak method was also calculated. As a result, the error of temperature was ± 25 K (±

1.3%) with 68% confidence and ± 65 K (± 3.4%) with 95% confidence. Considering the accuracy shown in Table 6, the errors calculated here appear to be reasonable.

Table 8: Actual Confidence Interval to Signal

	Q2(6)	*Q1(11)*	*Q1(1)*
SNR	*5.036*	*8.851*	*10.010*
Confidence Interval to Signal (68 %)	*± 1.99%*	*± 1.13%*	*± 0.99%*
Confidence Interval to Signal (95 %)	*± 3.97%*	*± 2.26%*	*± 2.00%*

6.4.5 Spectral Fitting v. Two-line Peak v. Two-line Area

As shown in **Fig.93 (a)**, the best agreement of thermal structure was provided by the two-line integration scheme. This is a reasonable result since the sampled points of the two-line area method is more than the two-line scheme, and also the two-line area method possesses fewer parameters to be set than spectral fitting. As the number of parameters to be set is increased, the possibility of error can also be enhanced. In addition, the two-line area method provided the great fitting with the simulated result in the shape of the temperature structure. The discrepancy from the simulated result in the full width of 90% of the maximum is as less as 6.8% in the two-line area method, and 50.0% and 51.0% for the spectral fitting and two-line peak techniques. In conclusion, it can be said that the two-line integration is the best strategy of three to extract thermal structure, at least in the present experimental conditions.

Primary Findings in This Chapter

Finding 13: The counter-flow diffusion flame can be stable with 74% CO_2 dilution in oxidiser and 60% CO_2 dilution in fuel stream.

Finding 14: Extra care must be taken to ensure linearity limit is verified in application of OH LIF to CO_2 diluted flames. The linearity limit of the CO_2 diluted flame with

present conditions significantly differs from that of air case, which is approximately one seventh of the air flame limit.

Finding 15: The best spectral profile was obtained with *a* of 0.47 and *b* of 0.77 in the current condition of CO_2 diluted opposed-flow diffusion flame. The correction of *a* and *b* coefficient from Bunsen air flame is not substantial in the present oxy-fuel condition (the gap was less than 2%) while the slightly smoother distribution was observed around temperature peak by the adjustment.

S

Finding 16: The two-line integration scheme provided the best agreement with the theoretical values in the thermal structure of the present counter-flow diffusion flame with CO_2 dilution. The discrepancy was less than 2.4% above 1,600 K.

Chapter 7
Conclusions and Recommendations

While there are many fundamental and interesting differences between conventional air-fuel combustion and oxy-fuel combustion, this thesis focuses both experimentally and numerically on the thermal structural differences in 0D reactors and 1D laminar flows. Numerical calculations focus on the OTP and experimental measurement focuses on the development and application of high precision temperature measurement techniques applicable to oxy-fuel combustion. Although there are many potential fuels that could be used in an oxy-fuel approach such as coal, this thesis focuses on the use of CH_4, which is particularly relevant to modern high efficiency CNG fuelled power generation systems. The key findings, contributions and recommendations from this investigation are summarised below.

(1) The 0D OTP of CO_2 diluted combustion is found to be significantly rich shifted compared to that of N_2 diluted flames for a given mass fraction of O_2 in oxidiser, Y_{O2_oxi}. The 0D OTP degree for H_2O dilution for Y_{O2_oxi} < 65% is smaller than that for N_2 dilution, while this trend reverses for oxygen concentrations greater than 65%. The larger degree of 0D OTP for CO_2 diluted combustion compared to that of N_2 is found to arise predominantly from the reactivity difference between CO_2 and N_2. However, the difference in specific heat capacity, C_p, between H_2O and N_2 is found to be the dominant mechanism in driving the 0D OTP deviation between H_2O and N_2 diluted combustion.

(2) It was found that CO_2 diluted oxy-fuel flames possess a greater degree of rich shifting of the temperature peak than conventional N_2 diluted flames in counter-flow diffusion flames. Intriguingly, temperature peaking of lean mixtures, which generally cannot be seen in 0D OTP with hydrocarbon combustion, is observed in O_2 enriched flames with both CO_2 and N_2 diluted oxidisers.

(3) The primary factor of both rich and lean 1D OTP is finite-rate chemistry for the fuel and diluent compositions examined. Finite-rate chemistry was shown to suppress the heat release to a greater degree at stoichiometry compared to the rich regime, and thus

the heat release peak position and consequent temperature peak position is shifted towards the rich side. As finite-rate chemistry causes the heat release curve near stoichiometry to be near constant rather than displaying a sharp peak, lean shifting of temperature peak driven by C_p variation becomes competitive. For rich shifted conditions, such as highly CO_2 or N_2 diluted flames, finite-rate chemistry is more dominant compared to C_p variations. For lean shifted conditions, such as highly O_2 enriched flames, the C_p variations become dominant and lean shifting is observed. It is further shown that the 1D OTP discrepancy of CO_2 diluted oxy-fuel flames from the conventional N_2 diluted flame is primarily because of the reactivity difference between CO_2 and N_2 as with 0D OTP.

(4) The thermal structure of an oxy-fuel laminar diffusion flame in a counter-flow burner was successfully measured by the spectrally integrated two-line technique. The method was determined to have an error of less than 2.4% above 1,600 K and to be increasingly accurate at higher temperatures. The LIF linearity limit of the CO_2 diluted flame with the present condition significantly differed from that of the air case, which was approximately one seventh of the air flame limit. The optimal collisional broadening assuming an $a(T/300)^b$ model was a= 0.47 and b= 0.77 in the current condition of CO_2 diluted opposed-flow diffusion flame. Modification of the a and b coefficient from air flame versions, a of 0.41 and b of 0.80, did not affect the temperature structure obtained by the spectral fitting method significantly in the present oxy-fuel condition (the gap was less than 2%) above 1,600 K. A slightly smoother residual distribution was observed around temperature peak by this a and b coefficient adjustment.

(5) A counter-flow burner was designed, which features a near uniform exit velleity profile and allows for laser beam entry perpendicular to flame between opposed nozzles. The vertical entry capability of the laser is of considerable assistance for the future advanced experiments employing Raman-Rayleigh spectroscopy to evaluate the thermal structure of oxy-fuel flames in mixture fraction space in greater detail. An original topology laser pulse stretcher to allow Raman-Rayleigh spectroscopy is designed in the present study, referred to as double-ring cavity, and is shown to improve the spatial efficiency (saving space), from the conventional single-ring cavity by 36.5%.

(6) In future studies, it is recommended to characterise the designed counter-flow burner at various strain rates other than the condition used in the present project by applying the OH LIF thermometry developed here. Validation of the nozzle exit profile predicted by CFD simulations would also be useful to be done using PIV. It would be of considerable interest if the thermal structure of a laminar opposed flow flame could be compared over all strain rates to laminar flame calculations. In addition, the realisation and validation of the laser pulse stretcher designed in the current project would be of great interest to allow Raman-Rayleigh spectroscopy to be applied to investigate the thermal structure of oxy-fuel flames in mixture fraction space.

Bibliography

1. Solomon, S., *Climate change 2007: the physical science basis: contribution of Working Group I to the Fourth Assessment Report of the Intergovernmental Panel on Climate Change*2007: Cambridge Univ Press.
2. National Greenhouse Gas Inventory, A.G.O., Canberra., www.greenhouseoffice.gov.au, 2006.
3. Ditaranto, M., J. Sautet, and J. Samaniego, *Structural aspects of coaxial oxy-fuel flames.* Experiments in fluids, 2001. **30**(3): p. 253-261.
4. Croiset, E. and K.V. Thambimuthu, *NOx and SO2 emissions from O2/CO2 recycle coal combustion.* Fuel, 2001. **80**(14): p. 2117-2121.
5. Sevault, A., et al., *On the structure of the near field of oxy-fuel jet flames using Raman/Rayleigh laser diagnostics.* Combustion and Flame, (11).
6. Kutne, P., et al., *Experimental analysis of the combustion behaviour of oxyfuel flames in a gas turbine model combustor.* Proceedings of the Combustion Institute, 2011. **33**(2): p. 3383-3390.
7. Koide, H., et al., *Subterranean containment and long-term storage of carbon dioxide in unused aquifers and in depleted natural gas reservoirs.* Energy Conversion and Management, 1992. **33**(5–8): p. 619-626.
8. Mo, S. and I. Akervoll. *Modeling long-term CO2 storage in aquifer with a black-oil reservoir simulator*. in *SPE/EPA/DOE Exploration and Production Environmental Conference*. 2005.
9. Bergman, P.D. and E.M. Winter, *Disposal of carbon dioxide in aquifers in the U.S.* Energy Conversion and Management, 1995. **36**(6–9): p. 523-526.
10. Abraham, B.M., et al., *COAL-OXYGEN PROCESS PROVIDES CO2 FOR ENHANCED RECOVERY.* Oil and Gas Journal, 1982. **80**(11): p. 68-70, 75.
11. Blunt, M., F.J. Fayers, and F.M. Orr Jr, *Carbon dioxide in enhanced oil recovery*. Energy Conversion and Management, 1993. **34**(9–11): p. 1197-1204.
12. Ferguson, R.C., et al., *Storing CO2 with enhanced oil recovery*. Energy Procedia, 2009. **1**(1): p. 1989-1996.
13. Parker, M.E., J.P. Meyer, and S.R. Meadows, *Carbon Dioxide Enhanced Oil Recovery Injection Operations Technologies (Poster Presentation).* Energy Procedia, 2009. **1**(1): p. 3141-3148.

14. Buhre, B.J.P., et al., *Oxy-fuel combustion technology for coal-fired power generation.* Progress in Energy and Combustion Science, 2005. **31**(4): p. 283-307.
15. Bolland, O. and P. Mathieu, *Comparison of two CO2 removal options in combined cycle power plants.* Energy Conversion and Management, 1998. **39**(16–18): p. 1653-1663.
16. Bolland, O. and S. Sæther, *New concepts for natural gas fired power plants which simplify the recovery of carbon dioxide.* Energy Conversion and Management, 1992. **33**(5–8): p. 467-475.
17. Liu, H., R. Zailani, and B.M. Gibbs, *Comparisons of pulverized coal combustion in air and in mixtures of O2/CO2.* Fuel, 2005. **84**(7): p. 833-840.
18. Glarborg, P. and L.L.B. Bentzen, *Chemical effects of a high CO2 concentration in oxy-fuel combustion of methane.* Energy & Fuels, 2007. **22**(1): p. 291-296.
19. Richards, G.A., K.H. Casleton, and B.T. Chorpening, *CO2 and H2O diluted oxy-fuel combustion for zero-emission power.* Proceedings of the Institution of Mechanical Engineers, Part A: Journal of Power and Energy, 2005. **219**(2): p. 121-126.
20. Kim, H.K., et al., *Emission Characteristics of the 0.2 MW Oxy-fuel Combustor.* Energy & Fuels, 2009. **23**(11): p. 5331-5337.
21. Normann, F., et al., *Emission control of nitrogen oxides in the oxy-fuel process.* Progress in Energy and Combustion Science, 2009. **35**(5): p. 385-397.
22. Stadler, H., et al., *Experimental investigation of NO(x) emissions in oxycoal combustion.* Fuel, 2011. **90**(4): p. 1604-1611.
23. Seepana, S. and S. Jayanti, *Flame structure investigations of oxy-fuel combustion.* Fuel, 2012. **93**(0): p. 52-58.
24. Li, H., J. Yan, and M. Anheden, *Impurity impacts on the purification process in oxy-fuel combustion based CO2 capture and storage system.* Applied Energy, 2009. **86**(2): p. 202-213.
25. Martinez-Frias, J., et al., *Thermodynamic Analysis of Zero-Atmospheric Emissions Power Plant.* Journal of engineering for gas turbines and power, 2004. **126**(1): p. 2-8.
26. Jericha, H., et al., *Design Optimization of the Graz Cycle Prototype Plant.* Journal of engineering for gas turbines and power, 2004. **126**(4): p. 733-740.

27. Marin O, B.Y., Perrin N, Zanno PD, Viteri F, Anderson R., *High efficiency, zero emission power generation based on a high-temperature steam cycle.* 28th International technical conference on coal utilization & fuel systems., 2003.
28. Anderson R, B.H., Doyle S, Pronske K, Viteri F, *Power generation with 100% carbon capture and sequestration.* Second annual conference on carbon sequestration, 2003.
29. Kim, S.-G., J. Park, and S.-I. Keel, *Thermal and chemical contributions of added H2O and CO2 to major flame structures and NO emission characteristics in H2/N2 laminar diffusion flame.* International Journal of Energy Research, 2002. **26**(12): p. 1073-1086.
30. Park, J.-W., C.B. Oh, and O.J. Kim, *Radiation Effects on the Flame Structure and Extinction Limit of Counterflow Methane Partially-Premixed Flames Diluted with Water Vapor in the Air Stream.* Combustion science and technology, 2013: p. null-null.
31. Naik, S.V. and N.M. Laurendeau, *Quantitative laser-saturated fluorescence measurements of nitric oxide in counter-flow diffusion flames under sooting oxy-fuel conditions.* Combustion and Flame, 2002. **129**(1–2): p. 112-119.
32. Gregory P. Smith, D.M.G., Michael Frenklach, Nigel W. Moriarty, Boris Eiteneer, Mikhail Goldenberg, C. Thomas Bowman, Ronald K. Hanson, Soonho Song, William C. Gardiner, Jr., Vitali V. Lissianski, and Zhiwei Qin Available from: http://www.me.berkeley.edu/gri_mech/.
33. Cheng, Z., R.W. Pitz, and J.A. Wehrmeyer, *Lean and ultralean stretched propane–air counterflow flames.* Combustion and Flame, 2006. **145**(4): p. 647-662.
34. Cheng, Z., J.A. Wehrmeyer, and R.W. Pitz, *Lean or ultra-lean stretched planar methane/air flames.* Proceedings of the Combustion Institute, 2005. **30**(1): p. 285-293.
35. CHARLES, K.W. and F.L. Dryer, *Simplified reaction mechanisms for the oxidation of hydrocarbon fuels in flames.* Combustion science and technology, 1981. **27**(1-2): p. 31-43.
36. Bilger, R.W., S.H. Stårner, and R.J. Kee, *On reduced mechanisms for methane-air combustion in nonpremixed flames.* Combustion and Flame, 1990. **80**(2): p. 135-149.

37. Law, C., A. Makino, and T. Lu, *On the off-stoichiometric peaking of adiabatic flame temperature.* Combustion and Flame, 2006. **145**(4): p. 808-819.
38. Katta, V., L. Goss, and W. Roquemore, *Effect of nonunity Lewis number and finite-rate chemistry on the dynamics of a hydrogen-air jet diffusion flame.* Combustion and Flame, 1994. **96**(1-2): p. 60-74.
39. Hirschfelder, J.O., C.F. Curtiss, and R.B. Bird, *Molecular theory of gases and liquids.* Molecular theory of gases and liquids, by Hirschfelder, Joseph Oakland; Curtiss, Charles F.; Bird, R. Byron. New York: Wiley,[1964, c1954]. Structure of matter series, 1964. **1**.
40. Barlow, R., et al., *Piloted methane/air jet flames: Transport effects and aspects of scalar structure.* Combustion and Flame, 2005. **143**(4): p. 433-449.
41. Yang, F., et al., *A mechanistic study of Soret diffusion in hydrogen-air flames.* Combustion and Flame, 2010. **157**(1): p. 192-200.
42. Nabi, M.N., M.S. Akhter, and M.M. Zaglul Shahadat, *Improvement of engine emissions with conventional diesel fuel and diesel–biodiesel blends.* Bioresource Technology, 2006. **97**(3): p. 372-378.
43. Glaude, P.-A., et al., *Adiabatic flame temperature from biofuels and fossil fuels and derived effect on NOx emissions.* Fuel Processing Technology, 2010. **91**(2): p. 229-235.
44. Vidal, M., et al., *Evaluation of lower flammability limits of fuel–air–diluent mixtures using calculated adiabatic flame temperatures.* Journal of Hazardous Materials, 2006. **130**(1–2): p. 21-27.
45. Mashuga, C.V. and D.A. Crowl, *Flammability zone prediction using calculated adiabatic flame temperatures.* Process Safety Progress, 1999. **18**(3): p. 127-134.
46. Sabia, P., et al., *Modeling Negative Temperature Coefficient region in methane oxidation.* Fuel, 2012. **91**(1): p. 238-245.
47. Heufer, K.A., et al., *Shock tube investigations of ignition delays of n-butanol at elevated pressures between 770 and 1250K.* Proceedings of the Combustion Institute, 2011. **33**(1): p. 359-366.
48. Vranckx, S., et al., *Role of peroxy chemistry in the high-pressure ignition of n-butanol–Experiments and detailed kinetic modelling.* Combustion and Flame, 2011. **158**(8): p. 1444-1455.

49. Noorani, K.E., B. Akih-Kumgeh, and J.M. Bergthorson, *Comparative High Temperature Shock Tube Ignition of C1−C4 Primary Alcohols.* Energy & Fuels, 2010. **24**(11): p. 5834-5843.
50. Spalding, D.B., *A Theory of Inflammability Limits and Flame-Quenching.* Proceedings of the Royal Society of London. Series A. Mathematical and Physical Sciences, 1957. **240**(1220): p. 83-100.
51. Mittal, V., H. Pitsch, and F. Egolfopoulos, *Assessment of counterflow to measure laminar burning velocities using direct numerical simulations.* Combustion Theory and Modelling, 2011. **16**(3): p. 419-433.
52. Kee, R.J., et al., *A computational model of the structure and extinction of strained, opposed flow, premixed methane-air flames.* Symposium (International) on Combustion, 1989. **22**(1): p. 1479-1494.
53. Bui-Pham, M.N. and J.A. Miller, *Rich methane/air flames: Burning velocities, extinction limits, and flammability limit.* Symposium (International) on Combustion, 1994. **25**(1): p. 1309-1315.
54. Law, C.K. and F.N. Egolfopoulos, *A kinetic criterion of flammability limits: The C-H-O-inert system.* Symposium (International) on Combustion, 1991. **23**(1): p. 413-421.
55. Egolfopoulos, F.N., P. Cho, and C.K. Law, *Laminar flame speeds of methane-air mixtures under reduced and elevated pressures.* Combustion and Flame, 1989. **76**(3–4): p. 375-391.
56. Zhu, D.L., F.N. Egolfopoulos, and C.K. Law, *Experimental and numerical determination of laminar flame speeds of methane/(Ar, N2, CO2)-air mixtures as function of stoichiometry, pressure, and flame temperature.* Symposium (International) on Combustion, 1989. **22**(1): p. 1537-1545.
57. Kreutz, T.G., M. Nishioka, and C.K. Law, *The role of kinetic versus thermal feedback in nonpremixed ignition of hydrogen versus heated air.* Combustion and Flame, 1994. **99**(3–4): p. 758-766.
58. Seshadri, K. and F.A. Williams, *Laminar flow between parallel plates with injection of a reactant at high reynolds number.* International Journal of Heat and Mass Transfer, 1978. **21**(2): p. 251-253.
59. Chelliah, H.K., et al., *An experimental and theoretical investigation of the dilution, pressure and flow-field effects on the extinction condition of methane-*

air-nitrogen diffusion flames. Symposium (International) on Combustion, 1991. **23**(1): p. 503-511.

60. Sun, C.J., et al., *Response of counterflow premixed and diffusion flames to strain rate variations at reduced and elevated pressures.* Symposium (International) on Combustion, 1996. **26**(1): p. 1111-1120.
61. Law, C.K., et al., *On the structural sensitivity of purely strained planar premixed flames to strain rate variations.* Combustion and Flame, 1994. **98**(1–2): p. 139-154.
62. Kim., J.S., P.A. Libby., and F. A.Williams., *On the displacement effects of laminar flames.* Combustion science and technology, 1993. **87**(1-6): p. 1-25.
63. RNER, S.H.S.T.Å., et al., *Measurements of conserved scalars in turbulent diffusion flames.* Combustion science and technology, 1992. **86**(1-6): p. 223-236.
64. Bilger, R.W., *The Structure of Diffusion Flames.* Combustion science and technology, 1976. **13**(1-6): p. 155-170.
65. Law, C.K., *Combustion physics*2006: Cambridge University Press.
66. Barlow, R.S., et al., *Scalar profiles and NO formation in laminar opposed-flow partially premixed methane/air flames.* Combustion and Flame, 2001. **127**(3): p. 2102-2118.
67. Barlow, R.S. and J.H. Frank, *Effects of turbulence on species mass fractions in methane/air jet flames.* Symposium (International) on Combustion, 1998. **27**(1): p. 1087-1095.
68. Peters, N., *Turbulent combustion*2000: Cambridge university press.
69. Oran, E.S. and J.P. Boris, *Numerical simulation of reactive flow,* 2005: Cambridge University Press.
70. Eckbreth, A.C., *LaserDiagnostics for CombustionTemperature and Species.* 1996.
71. Zhao, F.-Q. and H. Hiroyasu, *The applications of laser Rayleigh scattering to combustion diagnostics.* Progress in Energy and Combustion Science, 1993. **19**(6): p. 447-485.
72. Dibble, R.W. and R.E. Hollenbach, *Laser rayleigh thermometry in turbulent flames.* Symposium (International) on Combustion, 1981. **18**(1): p. 1489-1499.
73. Namer, I. and R.W. Schefer, *Error estimates for Rayleigh scattering density and temperature measurements in premixed flames.* Experiments in fluids, 1985. **3**(1): p. 1-9.

74. Mansour, M.S., *Two-plane two-dimensional Rayleigh thermometry technique for turbulent combustion.* Optics Letters, 1993. **18**(7): p. 537-539.
75. Eckbreth, A.C., P.A. Bonczyk, and J.F. Verdieck, *Combustion diagnostics by laser Raman and fluorescence techniques.* Progress in Energy and Combustion Science, 1979. **5**(4): p. 253-322.
76. Kojima, J. and Q.V. Nguyen, *Strategy for multiscalar Raman diagnostics in high-pressure hydrogen flames.* New developments in combustion research, 2006. **4**: p. 227.
77. Fuest, F., et al., *A hybrid method for data evaluation in 1-D Raman spectroscopy*. Proceedings of the Combustion Institute, 2011. **33**(1): p. 815-822.
78. Daily, J.W., *Laser induced fluorescence spectroscopy in flames.* Progress in Energy and Combustion Science, 1997. **23**(2): p. 133-199.
79. Kohse-Höinghaus, K., *Laser techniques for the quantitative detection of reactive intermediates in combustion systems.* Progress in Energy and Combustion Science, 1994. **20**(3): p. 203-279.
80. Hsu, A., et al., *Mixture fraction imaging in turbulent non-premixed flames with two-photon LIF of krypton.* Proceedings of the Combustion Institute, 2011. **33**(1): p. 759-766.
81. Rothe, E.W., Y.-W. Gu, and G.P. Reck, *Laser-induced predissociative fluorescence: dynamics and polarization and the effect of lower-state rotational energy transfer on quantitative diagnostics.* Appl. Opt., 1996. **35**(6): p. 934-947.
82. Kliewer, C.J., *High-spatial-resolution one-dimensional rotational coherent anti-Stokes Raman spectroscopy imaging using counterpropagating beams.* Optics Letters, 2012. **37**(2): p. 229-231.
83. Bohlin, A. and C.J. Kliewer, *Diagnostic Imaging in Flames with Instantaneous Planar Coherent Raman Spectroscopy.* The Journal of Physical Chemistry Letters, 2014. **5**(7): p. 1243-1248.
84. Vestin, F. and P.-E. Bengtsson, *Rotational CARS for simultaneous measurements of temperature and concentrations of N2, O2, CO, and CO2 demonstrated in a CO/air diffusion flame.* Proceedings of the Combustion Institute, 2009. **32**(1): p. 847-854.
85. Drake, M.C., et al., *Measurements of temperature and concentration fluctuations in turbulent diffusion flames using pulsed raman spectroscopy.* Symposium (International) on Combustion, 1981. **18**(1): p. 1521-1531.

86. Hanson, R.K. and P.K. Falcone, *Temperature measurement technique for high-temperature gases using a tunable diode laser.* Applied Optics, 1978. **17**(16): p. 2477-2480.
87. Seitzman, J.M., et al., *Application of quantitative two-line OH planar laser-induced fluorescence for temporally resolved planar thermometry in reacting flows.* Appl. Opt., 1994. **33**(18): p. 4000-4012.
88. Welle, E.J., et al., *The response of a propane-air counter-flow diffusion flame subjected to a transient flow field.* Combustion and Flame, 2003. **135**(3): p. 285-297.
89. Lucht, R.P., N.M. Laurendeau, and D.W. Sweeney, *Temperature measurement by two-line laser-saturated OH fluorescence in flames.* Applied Optics, 1982. **21**(20): p. 3729-3735.
90. Broida, H.P., *Rotational Temperatures of OH in Methane‐Air Flames.* The Journal of Chemical Physics, 1951. **19**(11): p. 1383-1390.
91. Bessler, W.G. and C. Schulz, *Quantitative multi-line NO-LIF temperature imaging.* Applied Physics B, 2004. **78**(5): p. 519-533.
92. Lee, T., et al., *Quantitative temperature measurements in high-pressure flames with multiline NO-LIF thermometry.* Applied Optics, 2005. **44**(31): p. 6718-6728.
93. Vyrodov, A.O., et al., *Laser-induced fluorescence thermometry and concentration measurements on NOA–X (0-0) transitions in the exhaust gas of high pressure CH4/air flames.* Applied Physics B, 1995. **61**(5): p. 409-414.
94. Lee, M.P., P.H. Paul, and R.K. Hanson, *Quantitative imaging of temperature fields in air using planar laser-induced fluorescence of O2.* Optics Letters, 1987. **12**(2): p. 75-77.
95. Brinkman, E.A., et al., *Optical diagnostics for temperature measurement in a DC arcjet reactor used for diamond deposition.* Applied Physics B, 1997. **64**(6): p. 689-697.
96. Hult, J., I.S. Burns, and C.F. Kaminski, *Two-line atomic fluorescence flame thermometry using diode lasers.* Proceedings of the Combustion Institute, 2005. **30**(1): p. 1535-1543.

97. Burns, I.S., et al., *A thermometry technique based on atomic lineshapes using diode laser LIF in flames.* Proceedings of the Combustion Institute, 2007. **31**(1): p. 775-782.
98. Burns, I.S., et al., *Diode laser atomic fluorescence temperature measurements in low-pressure flames.* Applied Physics B, 2008. **93**(4): p. 907-914.
99. Medwell, P.R., et al., *Instantaneous Temperature Imaging of Diffusion Flames Using Two-Line Atomic Fluorescence.* Applied Spectroscopy, 2010. **64**(2): p. 173-176.
100. Medwell, P.R., et al., *Development of temperature imaging using two-line atomic fluorescence.* Applied Optics, 2009. **48**(6): p. 1237-1248.
101. Kostka, S., et al., *Comparison of line-peak and line-scanning excitation in two-color laser-induced-fluorescence thermometry of OH.* Applied Optics, 2009. **48**(32): p. 6332-6343.
102. Clemens, N.T., *Flow Imaging*, in *Encyclopedia of Imaging Science and Technology*2002, John Wiley & Sons, Inc.
103. Paul, P.H., et al., *High resolution digital flowfield imaging of jets.* Experiments in fluids, 1990. **9**(5): p. 241-251.
104. Paul, P.H. *The application of intensified array detectors to quantitative planar laser-induced fluorescence imaging*. in *AIAA, SAE, ASME, and ASEE, 27th Joint Propulsion Conference*. 1991.
105. Wang, G.H. and N.T. Clemens, *Effects of imaging system blur on measurements of flow scalars and scalar gradients.* Experiments in fluids, 2004. **37**(2): p. 194-205.
106. Kychakoff, G., R.D. Howe, and R.K. Hanson, *Quantitative flow visualization technique for measurements in combustion gases.* Applied Optics, 1984. **23**(5): p. 704-712.
107. Tsurikov, M.S., *Experimental investigation of the fine scale structure in turbulent gas-phase jet flows*2002.
108. Kojima, J. and Q.-V. Nguyen, *Laser Pulse-Stretching with Multiple Optical Ring Cavities.* Appl. Opt., 2002. **41**(30): p. 6360-6370.
109. *CANTERA, Object-Oriented Software for Reacting Flows.* http://www.cantera.org, 2005.
110. CHEMKIN-PRO, R.D., San Diego, 2008.

111. Grcar, J., *The Twopnt program for boundary value problems.* Sandia National Laboratories Report SAND91-8230, 1992.
112. SAKIYAMA, Y., et al., *PLIF Imaging Measurements of OH and Temperature Distribution in Burning Flowfields.* Technical report/National aerospace laboratory (Tokyo), 1999.
113. Seitzman, J.M. and R.K. Hanson, *Comparison of excitation techniques for quantitative fluorescence imaging of reacting flows.* AIAA journal, 1993. **31**(3): p. 513-519.
114. 1999, L.J.a.C.D.R., *LIFBASE: Database and Spectral Simulation Program (version 2.1.1).* SRI International Report MP 99-009.
115. *Davis Software version 7.2.*
116. *MATLAB. version 7.13 (R2011b).*
117. Sung, C., J. Liu, and C. Law, *Structural response of counterflow diffusion flames to strain rate variations.* Combustion and Flame, 1995. **102**(4): p. 481-492.
118. Sung, C., J. Liu, and C. Law, *On the scalar structure of nonequidiffusive premixed flames in counterflow.* Combustion and Flame, 1996. **106**(1-2): p. 168-183.
119. *ANSYS CFX.* Reference Guide. Release, 2010. **13**(0).
120. Cléon, G., D. Stepowski, and A. Cessou, *Long-cavity Nd:YAG laser used in single-shot spontaneous Raman scattering measurements.* Opt. Lett., 2007. **32**(22): p. 3290-3292.
121. Giezendanner-Thoben, R., et al., *Phase-locked two-line OH planar laser-induced fluorescence thermometry in a pulsating gas turbine model combustor at atmospheric pressure.* Applied Optics, 2005. **44**(31): p. 6565-6577.
122. Bennett, B.A.V., et al., *A comparison of the structures of lean and rich axisymmetric laminar Bunsen flames: application of local rectangular refinement solution-adaptive gridding.* Combustion Theory and Modelling, 1999. **3**(4): p. 657-687.
123. Kohse-Höinghaus, K., U. Meier, and B. Attal-Trétout, *Laser-induced fluorescence study of OH in flat flames of 1-10 bar compared with resonance CARS experiments.* Applied Optics, 1990. **29**(10): p. 1560-1569.

124. Rea Jr, E.C., A.Y. Chang, and R.K. Hanson, *Shock-tube study of pressure broadening of the A2 Σ+ - X2 Π (0,0) band of OH by Ar and N2.* Journal of Quantitative Spectroscopy and Radiative Transfer, 1987. **37**(2): p. 117-127.
125. Bohndiek, S.E., et al., *Comparison of methods for estimating the conversion gain of CMOS active pixel sensors.* Sensors Journal, IEEE, 2008. **8**(10): p. 1734-1744.
126. Beecken, B.P. and E.R. Fossum, *Determination of theconversion gain and the accuracy of itsmeasurement for detector elements and arrays.* Appl. Opt., 1996. **35**(19): p. 3471-3477.
127. Suzaki, Y. and A. Tachibana, *Measurement of the μm sized radius of Gaussian laser beam using the scanning knife-edge.* Applied Optics, 1975. **14**(12): p. 2809-2810.
128. Weber, V., et al., *Pixel-based characterisation of CMOS high-speed camera systems.* Applied Physics B, 2011. **103**(2): p. 421-433.
129. Hain, R., C. Kähler, and C. Tropea, *Comparison of CCD, CMOS and intensified cameras.* Experiments in fluids, 2007. **42**(3): p. 403-411.

Appendix

Appendix 1: Temporal Profile of Nd:YAG laser

The temporal pulse shape of the excitation pulse was characterised by measuring the second harmonic of the Nd:YAG laser that was used to pump the dye laser. A 300 ps rise time photodiode connected to a 4GHz, 25 GS/s digital storage scope was utilised to record the temporal pulse shape of the pump laser. As shown in **Fig. A-1**, a resultant pulse with FWHM close to 10 ns was observed. It is noted the dye laser fundamental (~566nm) is expected to be 1-2 ns longer than the pump pulse, however, the doubled output from the dye (~283 nm in the UV) is expected to be 1-2 ns shorter than the dye laser fundamental, resulting in a UV output of pulse duration ~10±2 ns.

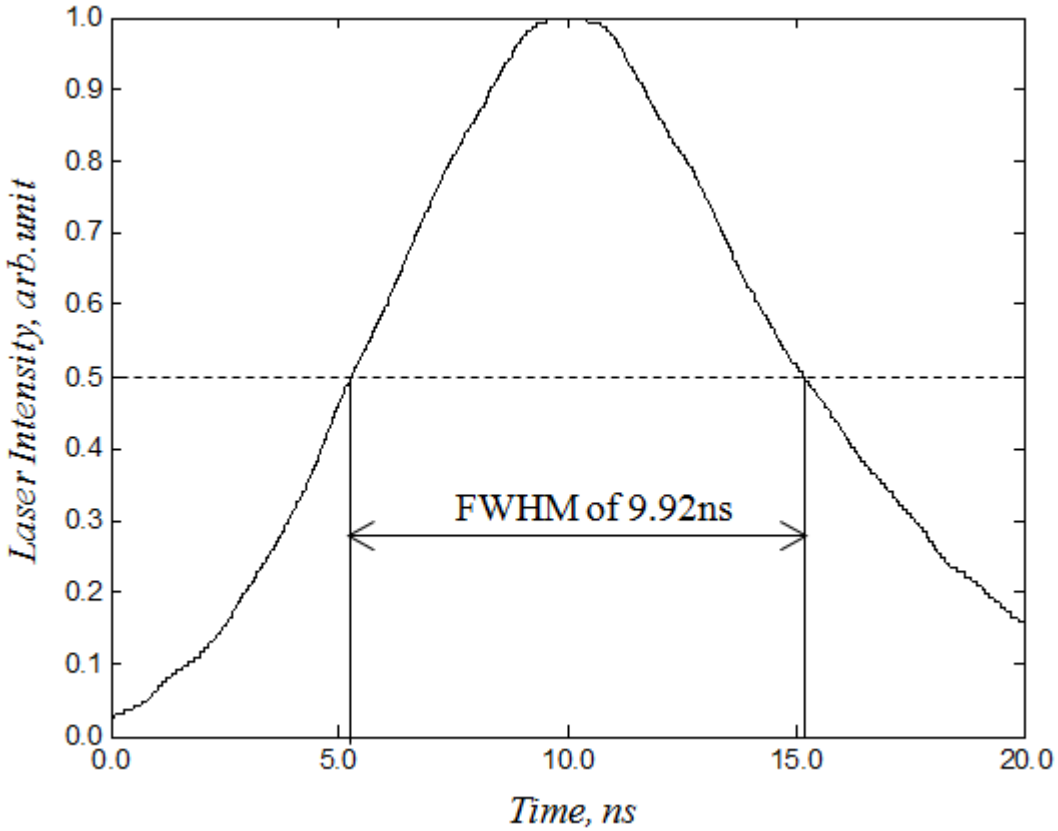

Fig.A-1 Temporal Profile of Nd:YAG laser.

Appendix 2: Relation of Nd:YAG Laser Power with Q-switch Delay

As the primary method to vary the OH LIF UV excitation beam energy, the energy of the Nd:YAG laser pumping the dye laser energy was too varied by changing the Q-switch to flash-lamp delay. The average output pulse energy of the second harmonic of Nd:YAG that pumps the dye laser as a function of Q-switch delay is shown in **Fig. A-2**. Pulse delays longer than 200 μs were utilised as it results in reduced inter-pulse fluctuations for a given energy, compared to Q-switch delays shorter than 200 μs.

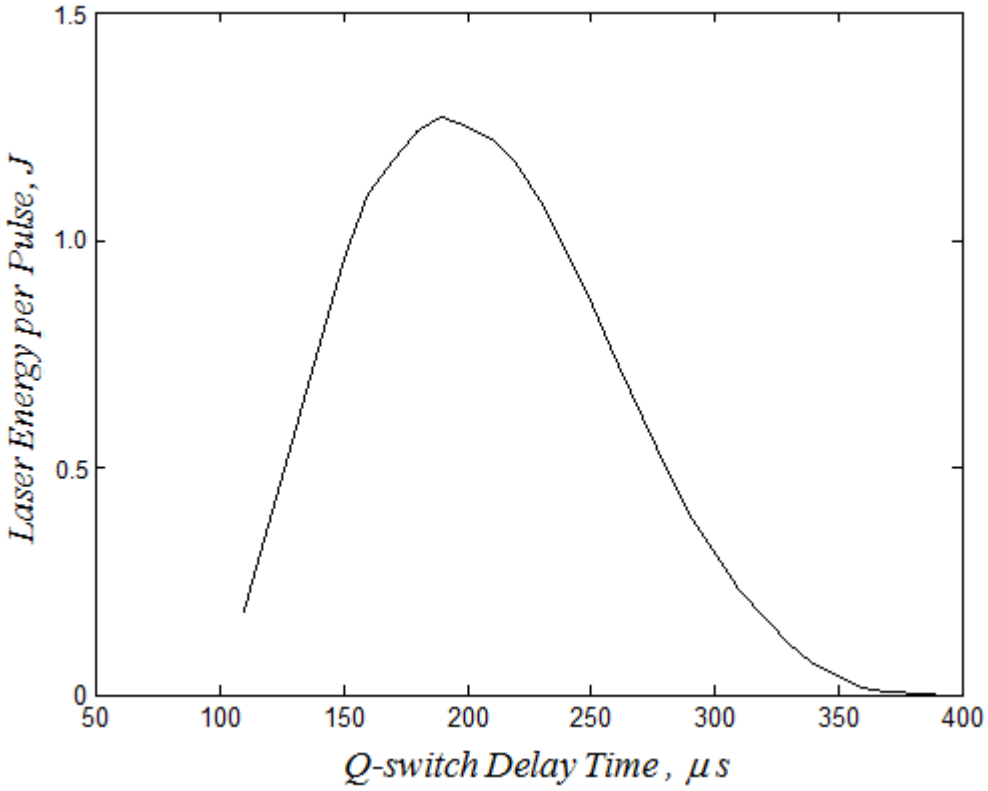

Fig.A-2 Relation of Nd:YAG laser power with Q-switch delay time.

Appendix 3: Photo Transfer Curves of Used Camera

To characterise the CCD camera used in the experiments, the photo transfer curve of the camera was investigated. The setup using a homogeneous light source is show in **Fig. A-4** and the resultant transfer curve is shown in **Fig. A-5**. From **Fig. A-5**, the CCD gain was determined to be 3.85 e^-/ADU when the count was obtained. The more detailed procedure and theory of the photo transfer method can be seen in [125, 126]. For reference, the dark noise of the camera used in the present study was 1.60 ADU.

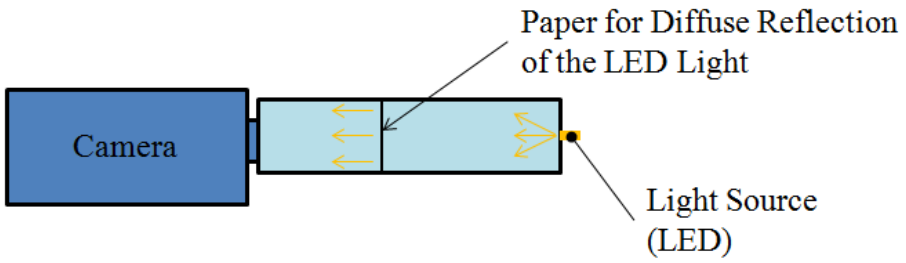

Fig.A-4 Schematic of imaging homogenous light source.

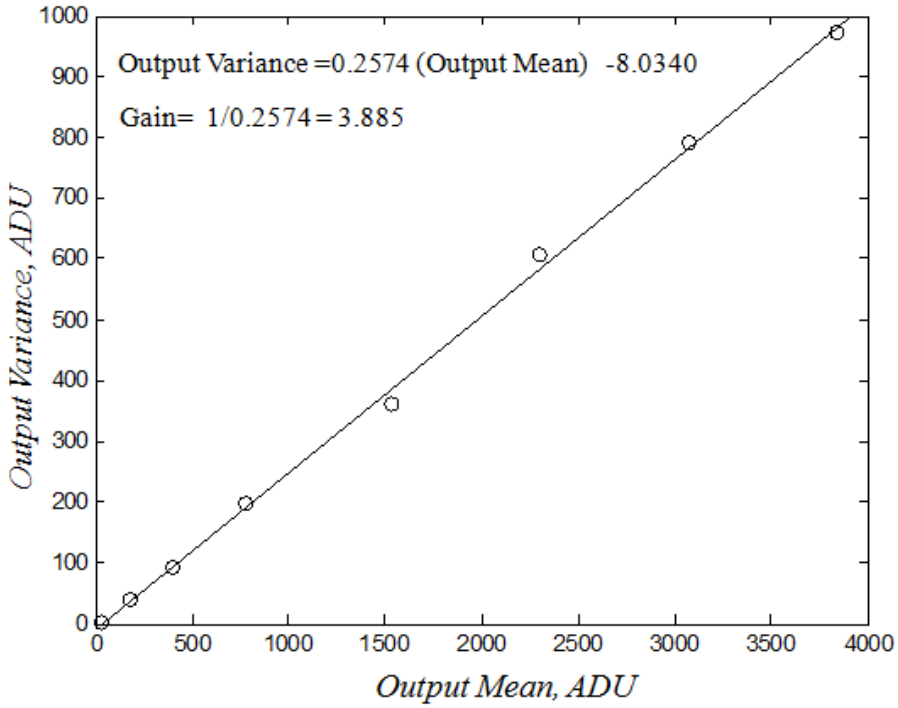

Fig.A-5 Photo transfer curve of camera used in the experiments.

Appendix 4: Measurement of Thickness of Laser Sheet at Probed Volume

The laser sheet thickness at the probe volume was measured using the knife edge scanning technique [127] with the hardware setup shown in **Fig. A-6**. By traversing the micrometer (micro gage) position and recording the transmitted laser energy at each micrometer position, the cumulative distribution function of the laser energy shown in **Fig. A-7** was obtained. Fitting an error function to the experimental data using a least square method, an error function parameterised by width of σ=0.133 mm was obtained as a best fit to the data. Hence, the FWHM of incident laser pulse was 0.31 mm and the full width at $1/e^2$ of the maximum value was 0.53 mm.

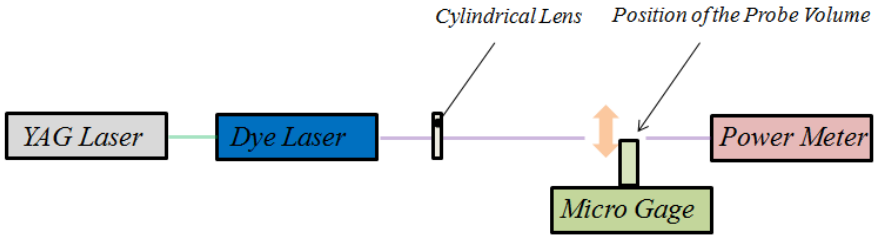

Fig.A-6 Schematic of the laser sheet thickness measurement.

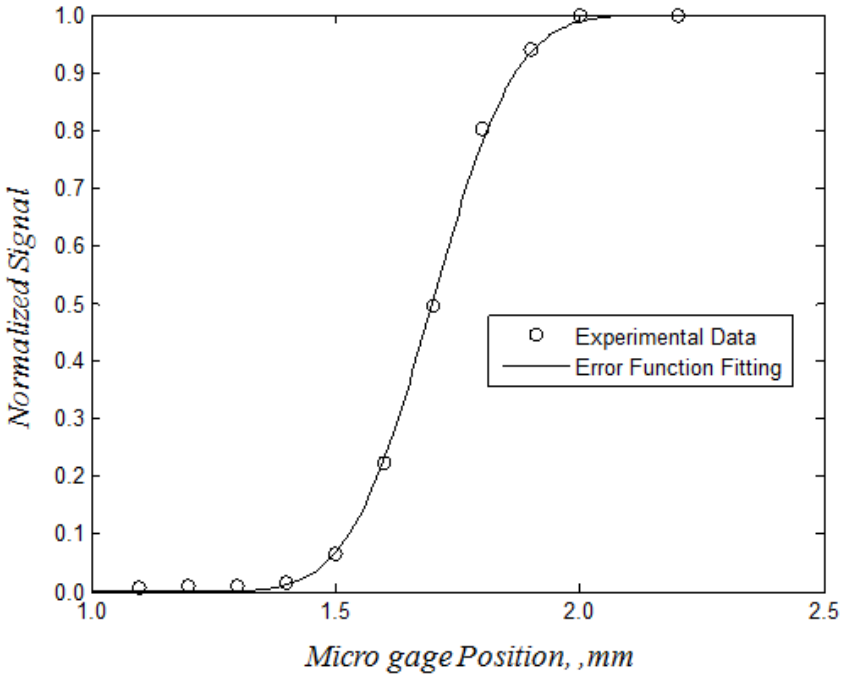

Fig.A-7 Experimental results and the best error function

Appendix 5: Characterisation of Intensifier

Ensuring the linearity of the intensifier employed for the OH LIF is crucial to the accuracy of the LIF thermometry method employed in this thesis. Hence, the linearity of the OH LIF intensifier to input light was investigated for several intensifier gain voltages and incident light levels. The examples of the non-linear response to the incident irradiance level can be seen in [128, 129]. Crucially, this linearity check was conducted using pulsed light of a similar temporal duration as the experimental LIF signal so that any finite spatial charge depletion effects due to the intensifiers multi-channel plate finite capacitance is accounted for. In this measurement, a miniscule fraction of the second harmonic from an Nd:YAG laser illuminated a white card and then the intensified camera monitored the light on the white card. The irradiance level was varied by changing the Q-switch to flash-lamp delay of the laser. A CDD camera with linearity better than 99%, simultaneously monitored the laser pulse energy to give a relative intensity measurement of the incident light levels on the intensified camera. The measurements were implemented with four different intensifier gain voltages. The CCD exposure time on the intensified camera was fixed to 1 ms to ensure the full emission from intensifier rear screen phosphor was collected. The results for these tests are shown in **Fig. A-7**, with the main finding that the intensifier was found to be linear as far as the intensified signal intensity monitored on the camera does not saturate the CCD.

The same setup used to determine the intensifier linearity was used to evaluate the SNR of the intensifier system over a range of irradiance levels for different gain voltages. It is shown in **Fig. A-8** that the best operating condition in terms of SNR was 7.25 voltage.

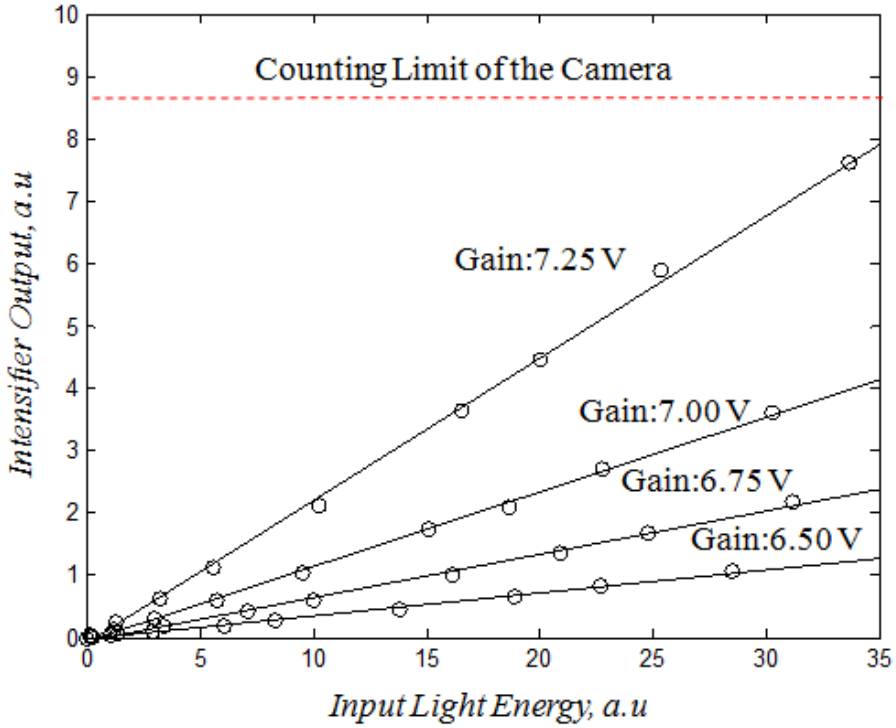

Fig.A-6 Linearity Check of intensifier. The camera exposure time in this test was set to be 1 ms, which is the same value as in the main experiment.

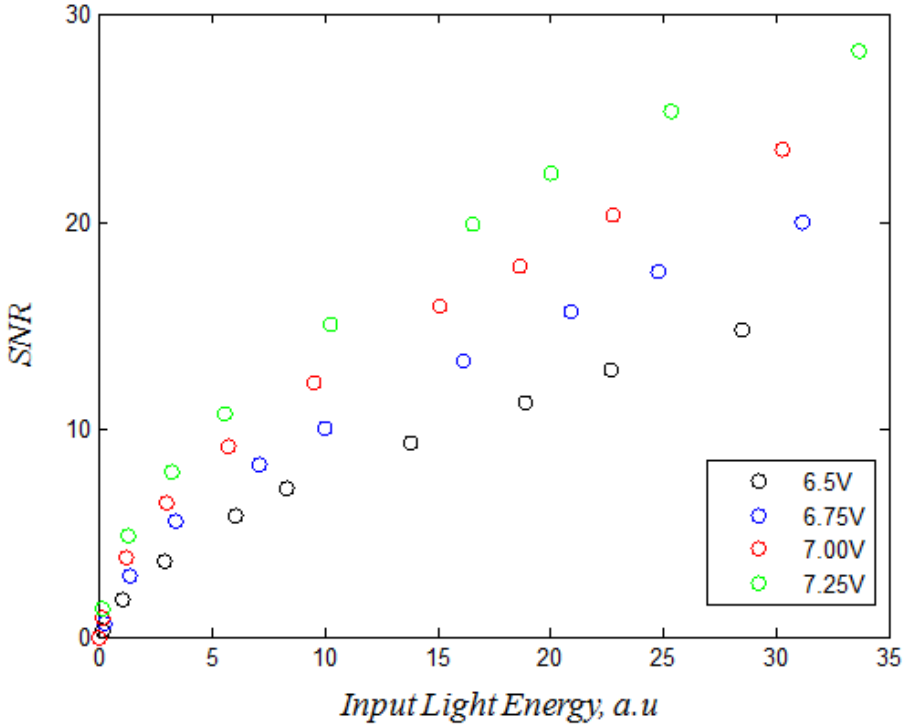

Fig.A-7 SNR with various gain voltage as a function of input light energy.